

Alma Mater Studiorum - Università di Bologna

DOTTORATO DI RICERCA IN  
NANOSCIENZE PER LA MEDICINA E PER L'AMBIENTE

Ciclo 34

**Settore Concorsuale:** 02/B1 - FISICA SPERIMENTALE DELLA MATERIA

**Settore Scientifico Disciplinare:** FIS/03 - FISICA DELLA MATERIA

SMART TEXTILE SENSORS FOR HEALTHCARE MONITORING

**Presentata da:** Luca Possanzini

**Coordinatore Dottorato**

Dario Braga

**Supervisore**

Beatrice Fraboni

**Esame finale anno 2022**



*To my beloveds*



*Nature is pleased with simplicity*



# Abstract

Wearable electronic textiles are an emerging research field playing a pivotal role among several different technological areas such as sensing, communication, clothing, health monitoring, information technology, and microsystems. The possibility to realise a fully-textile platform, endowed with various sensors directly realised with textile fibres and fabric, represents a new challenge for the entire research community. Integrating textile elements and new material with specific functionalisation procedures is crucial to develop non-invasive, adaptable, and comfortable textile sensor systems.

Among several high-performing materials, the intrinsically conductive poly(3,4-ethylenedioxythiophene) (PEDOT), doped with poly(styrenesulfonic acid) (PSS), or PEDOT:PSS, is one of the most representative and utilised, having an excellent chemical and thermal stability, as well as reversible doping state and high conductivity. This semiconducting polymer has been extensively employed during this work to achieve conductive 1-D yarns or 2-D fabrics.

This thesis work relies on combining specific and sensible materials integrated directly into textiles to design, realise, and develop textile chemical and physical sensors. Following an updated description of the latest wearable electronic applications, materials, and experimental techniques used in this work, the main findings on textile human-sweat and wound sensors, pressure and X-ray sensors, and textile thermoelectric generators are presented.

Silver/Silver Chloride and Iridium Oxide nanoparticles synthesis, electrochemical deposition of new compounds as PEDOT:BTB, perovskite single-crystal growth, Bismuth Telluride and Antimony Telluride deposited on single polyester thread are the principal proceedings employed in the fabrication of sensitive, reliable, non-invasive, and wearable smart textile sensors. In particular, sensors with different purposes and working principles are developed as chloride concentration and pH level sensors for human sweat to allow the continuous monitorisation of the wearer's hydration status and stress level. Additionally, a prototype smart bandage detecting the moisture level and pH value of a bed wound is presented, which allows the remote monitorisation of the healing process of severe and chronic wounds. Physical sensors used to monitor the pressure distribution for rehabilitation, workplace safety, or sport tracking are also presented together with a novel fully-textile device able to measure the incident X-ray dose for medical or security applications where thin, comfortable, and flexible features are essential. Finally, a proof-of-concept for an organic-inorganic textile thermoelectric generator that harvests energy directly from body heat has been proposed. Coupling these devices together would allow

the realisation of a self-standing, fully-textile sensor platform consisting of physical and chemical sensors directly powered by the textile system itself.

Though further efforts must be dedicated to overcome issues such as durability, washability, power consumption, and large-scale production, the novel, versatile, and widely encompassing area of electronic textiles is a promising protagonist in the upcoming technological revolution.

# Contents

<b>Abstract</b>	<b>v</b>
<b>Introduction</b>	<b>xiii</b>
<b>Wearable and textile devices</b>	<b>1</b>
<b>1.1 Internet of Things</b>	<b>1</b>
<b>1.2 Wearable devices</b>	<b>3</b>
1.2.1 Transduction mechanisms	5
<b>1.3 Smart textiles</b>	<b>8</b>
1.3.1 Fabrication of conductive textile	9
1.3.2 Electrical connections in textile sensors	11
1.3.3 Sweat monitoring sensors	12
1.3.3.1 Textile glucose sensors	13
1.3.3.2 Textile lactate sensors	15
1.3.3.3 Textile pH sensors	15
1.3.3.4 Textile electrolytes sensors	18
1.3.4 Multi-sensing platforms	22
1.3.5 Wound monitoring sensors	24
1.3.5.1 Textile pH wound sensors	25
1.3.5.2 Textile moisture wound sensors	27
1.3.6 Physical sensors	28
1.3.6.1 Textile electrocardiogram electrodes	28
1.3.6.2 Textile pressure sensors	30
1.3.7 Ionizing radiation sensors	32
<b>1.4 Energy harvesting</b>	<b>34</b>
1.4.1 Textile biofuel cells	34
1.4.2 Textile thermoelectric devices	36
<b>Materials and Methods</b>	<b>39</b>
<b>2.1 Textile materials</b>	<b>39</b>
2.1.1 Yarns	40
2.1.1.1 Cotton and silk fibres	41
2.1.1.2 Synthetic fibres	44

## Contents

---

2.1.2	Fabrics	46
2.1.2.1	Woven fabrics	46
2.1.2.2	Knitted fabrics	47
2.1.2.3	Special fabrics	49
<b>2.2</b>	<b>Materials</b>	<b>50</b>
2.2.1	Conductive polymers	50
2.2.1.1	Doping in conjugated polymers	51
2.2.2	PEDOT:PSS	53
2.2.2.1	Features of EDOT monomer	53
2.2.2.2	Polymerisation of PEDOT	53
2.2.2.3	PEDOT:PSS dispersion and properties	54
2.2.3	PEDOT:BTB	58
2.2.4	Iridium oxide	61
2.2.5	Silver/silver chloride	62
2.2.6	Perovskites	64
2.2.7	Thermoelectric materials	66
2.2.7.1	Bismuth Telluride	67
2.2.7.2	Antimony Telluride	68
<b>2.3</b>	<b>Fabrication technique</b>	<b>70</b>
2.3.1	Deposition methods	70
2.3.1.1	Drop casting	70
2.3.1.2	Spin coating	71
2.3.1.3	Roll-to-Roll	71
2.3.1.4	Screen Printing	72
2.3.1.5	Thermal deposition	72
2.3.1.6	Electrochemical deposition	73
2.3.2	Perovskite crystal growth	74
<b>2.4</b>	<b>Characterisation technique</b>	<b>76</b>
2.4.1	Electrical characterisation	76
2.4.2	Electrochemical characterisation	77
2.4.2.1	Cyclic voltammetry	77
2.4.3	Mechanical characterisation	79
2.4.3.1	TA Instrument DMA Q800	80
2.4.4	Morphological characterisation	81
2.4.4.1	Atomic force microscopy	81

2.4.4.2	Scanning electron microscopy	84
2.4.4.3	FTIR	85
2.4.4.4	DSC	87
<b>Textile sweat sensors</b>		<b>89</b>
<b>3.1</b>	<b>Sweat sensing</b>	<b>89</b>
<b>3.2</b>	<b>Organic electrochemical transistor</b>	<b>91</b>
3.2.1	Working principle of OECT	92
<b>3.3</b>	<b>OECT as chloride sensor</b>	<b>95</b>
3.3.1	Two-terminal configuration	97
3.3.2	Silver/silver chloride nanoparticles	100
3.3.2.1	Fabrication procedure	100
3.3.2.2	Characterisation	100
<b>3.4</b>	<b>OECT as pH sensor</b>	<b>101</b>
3.4.1	OECT with PEDOT:BTB-modified gate	102
3.4.1.1	Electrochemical characterisation of PEDOT:BTB as pH sensing material	102
3.4.1.2	OECT pH-sensor: working principle	103
3.4.1.3	OECT pH-sensor: fabrication	104
3.4.1.4	OECT pH-sensor: characterisation and results	104
3.4.2	From three- to two-terminal configuration	107
<b>3.5</b>	<b>Textile single-thread sensors</b>	<b>110</b>
3.5.1	Fabrication of textile single-thread sensors	111
3.5.1.1	Chemicals	111
3.5.1.2	From pristine yarns to sensing textile threads	111
3.5.2	Morphological and electrical characterisation	112
3.5.3	Liquid sampling volume independency	114
3.5.4	Single thread detection in universal buffer	116
3.5.4.1	Textile Cl <sup>-</sup> sensors	116
3.5.4.2	Textile pH sensors	118
3.5.4.3	Comparison between cotton thread sensors	120
3.5.5	Multi-thread detection in universal buffer	122
3.5.6	Textile platform for sensing in artificial sweat	123
3.5.6.1	Multi-sensing in artificial sweat	126
<b>3.6</b>	<b>Conclusions</b>	<b>127</b>

<b>Textile wound sensors</b>	<b>129</b>
<b>4.1 Introduction to wound care</b>	<b>130</b>
4.1.1 Wound healing process	130
4.1.2 Wound dressings	131
4.1.3 Wound sensing	132
4.1.3.1 pH monitoring	133
4.1.3.2 Moisture monitoring	133
<b>4.2 pH Wound monitoring</b>	<b>134</b>
4.2.1 Textile sensors based on PEDOT:dye compound	134
4.2.1.1 Fabrication of smart dressing pH sensor	135
4.2.1.2 Performance evaluation	136
4.2.2 Non-textile pH sensors based on metal-oxide compound	138
4.2.2.1 Fabrication of PEDOT:PSS/IrO <sub>x</sub> film	139
4.2.2.2 Morphology structure	140
4.2.2.3 Electrochemical characterization	142
4.2.2.4 Two-terminal pH sensors	144
4.2.2.5 Working principle	148
4.2.3 Smart textile dressing for pH monitoring	149
4.2.3.1 Fabrication	150
4.2.3.2 Characterization and comparison	151
<b>4.3 Textile moisture sensors</b>	<b>153</b>
4.3.1 Textile single-layer structure	154
4.3.1.1 Fabrication procedure	155
4.3.1.2 Results	156
4.3.2 Integrated bandage sensor	159
4.3.3 Wireless wound dressing remote readout	161
<b>4.4 Conclusions</b>	<b>163</b>
<b>Textile Physical Sensors</b>	<b>165</b>
<b>5.1 Textile pressure sensors</b>	<b>166</b>
5.1.1 Applications	166
5.1.2 Fabrication procedure	168
5.1.3 Effect of different formulations	169
5.1.3.1 Electrical and morphological properties	169

## Contents

---

5.1.3.2	Textile Pressure sensors characterisation	171
5.1.3.3	Working principle	173
5.1.4	Effect of different fabrics	174
5.1.4.1	Characterisation of fabrics	175
5.1.4.2	Textile pressure sensors performance	180
5.1.5	Real-life applications	185
<b>5.2</b>	<b>Textile ionizing radiation sensors</b>	<b>187</b>
5.2.1	Fabrication of TX-RD	188
5.2.1.1	Conductive electrodes	188
5.2.1.2	X-ray sensing fabric	189
5.2.2	Morphological analysis	189
5.2.3	Results of single TX-RD	192
5.2.3.1	Additional performance of TX-RD	194
5.2.4	TX-RD matrix	195
<b>5.3</b>	<b>Conclusions</b>	<b>197</b>
<b>Further Works: textile thermoelectric generators</b>		<b>199</b>
<b>6.1</b>	<b>Introduction</b>	<b>200</b>
<b>6.2</b>	<b>Theoretical model</b>	<b>201</b>
6.2.1	Preliminary results	205
<b>6.3</b>	<b>Organic-inorganic textile thermogenerator device</b>	<b>206</b>
6.3.1	Fabrication	207
6.3.2	Mathematical model	208
6.3.3	First results and further perspectives	209
<b>Conclusion</b>		<b>213</b>
<b>Bibliography</b>		<b>219</b>
<b>Acknowledgement</b>		<b>243</b>



# Introduction

"Wearable electronics" identifies an emerging category of technological devices that allow a passive, unobtrusive, and continuous monitoring of physiological or biometric parameters. Such sensors are integrated into bracelets, watches, headbands, skin patches, earphones, or garments and are mostly implemented on conventional substrates.

This thesis aims to demonstrate the possibility of realising a sensing platform able to monitor various physical and chemical parameters directly exploiting textile elements, like threads or fabrics, as substrates. The flexible, comfortable, and breathable nature of fabrics makes these substrates ideal candidates for developing large-area wearable devices used in direct contact with the human body. The results collected pave the way for a paradigm change in which wearable and flexible devices are not external elements that are worn, but become an intrinsic part of the garments. This broader vision of the sensor, not just as an integrated and added part, but a fundamental constituent of the cloths or accessories, has led to the realisation of textile fibres and fabrics with intrinsic electrical and sensorial properties. The chapters of this thesis showcase the latest types of textile sensors along with their main performance purpose and examples of real-life applications.

Recently, considerable interest in the research community has been focused on devices realised directly onto textile substrates<sup>1-5</sup>. This is witnessed by electronic textile devices able to change their electrical and/or mechanical properties due to an external stimulus designed to measure biopotentials,<sup>6-8</sup> temperature,<sup>9</sup> movements such as pressure<sup>10</sup> or strain,<sup>11</sup> sweat content,<sup>12-14</sup> or as energy harvesting (thermoelectrics,<sup>15,16</sup> triboelectrics,<sup>17</sup> biofuel cells<sup>18</sup>) and storage platforms<sup>19,20</sup>. In this framework, the examples presented in this thesis are valid candidates to speed up textile devices' diffusion and prove the feasibility of new sensing principles. This work has been completed at the Department of Physics and Astronomy of the University of Bologna, and during a secondment at the Department of Materials, Textile and Chemical Engineering at Ghent University in Belgium. Additionally, fruitful collaborations with the Department of Industrial Chemistry of the University of Bologna, and private companies from Bologna and Treviso aided in the success of these studies.

The first chapter reports an overview of wearable and textile electronics, focusing on the development and rise of smart textiles as a new era in wearable technology. The transduction mechanisms, fabrication techniques, and crucial challenges of the devices present in up-to-date scientific literature are described. Special attention is dedicated to textile physical sensors (e.g., pressure and ionising radiation), textile chemical sensors for sweat or wound bed analysis, and energy harvesting devices directly realised on fabrics.

Chapter two entails a complete description and explanation of textiles and chemical materials used to fabricate the different types of sensors. The conducting polymer, PEDOT:PSS, is employed in almost all of the proposed sensors due to its high versatility and processability, making this material the best candidate for flexible and biocompatible electronics devices. Its physical and chemical properties are presented together with an overview of the features of all materials used. The second part of this chapter describes the fabrication methods and the characterisation techniques employed in the following three chapters containing the results.

Chapter three begins with the explanation of sweat sensing and the description of organic electrochemical transistors (OECT) often used in this area. It demonstrates the feasibility of realising chloride concentration and pH level sensors in human sweat by exploiting the PEDOT:PSS-based OECT working principles. Proper material functionalization and geometry allow designing a two-terminal device based on the electrochemical gating effect, which directly leads to a single textile-thread sensor. The two fully textile sensors are employed to reliably and simultaneously measure the pH level or chloride concentration in a small volume of human sweat sample to perform on-demand and point-of-care epidermal fluid analysis. The possibility to easily knit or sew the thread sensors into fabrics reveals a new way for a textile wearable multi-sensing platform to be achieved in the near future.

In Chapter four, another example of textile-based sensors able to measure the pH and the moisture level of a wound bed is presented. A new mechanism exploiting metal-oxide compounds is employed in a textile to measure the pH of exudate produced by a wound for the first time. In addition, to realise an extensive system for wound monitoring and analysis, a sensor able to measure the moisture level is also integrated into the bandage. A novel approach based on screen-printed PEDOT:PSS on absorbing fabric has been proposed to effectively detect the moisture content, which is a fundamental parameter in the wound healing process. The integration of the textile sensor with RFID technology allows performing the moisture measure wirelessly, paving the way for smart, low-cost, and disposable wound dressing.

Chapter five describes the main results obtained from two different physical sensors employed in healthcare, medicine and sport applications: textile pressure sensors and textile X-ray detectors. The first part of this chapter details the effects of different piezoresistive formulations and different mechanical features of fabrics on the textile pressure sensors performance. Interesting applications in collaboration with a private company are also included. The second part of chapter five introduces a textile X-ray detector capable of measuring the impinging ionising radiation by monitoring the photocurrent signal generated into the sensing layer. It consists of a silk-satin fabric with perovskite single-crystals that directly grow through the textile fibres and two textile electrodes made of PEDOT:PSS to collect the generated current.

Finally, the sixth chapter reports a recent and new example of an inorganic-organic textile thermoelectric generator realised on a single polyester thread coated with PEDOT:PSS, Bismuth Telluride, and Antimony Telluride. This work was carried out during the visiting period at Ghent University. It is motivated by the great interest of the research community to achieve a wearable and textile-based thermogenerator device capable of directly providing the necessary energy to power the textile sensors present in the wearable platform.



# Chapter 1

## Wearable and textile devices

### 1.1 Internet of Things

*In the real world, things matter more than ideas* – with such words may be summed up the core of the expression Internet of Things (IoT), coined in 1999 by Kevin Ashton.<sup>21</sup> The basis of his interpretation is founded on the concept that among the conventional diagrams of the Internet, which typically include servers, routers and so on, people still represent the most numerous and important *routers* of all. So far, computers—and, therefore, the Internet—are almost wholly dependent on human beings for information, and the problems lie precisely on this aspect. People have limited time, accuracy and attention – all features that make them not perfectly suitable at capturing data about things in the real world. According to Ashton, “the economy, society and survival are not based on ideas or information – they are based on things. Yet today’s information technology is so dependent on data originated by people that our computers know more about ideas than things”. The possibility of having computers that know all there is to know about things would lead us to be able to track and count everything, reducing waste, loss and costs. For these reasons, empowering computers with their means of collecting information to let them see, hear and smell the world for themselves will surpass the limitation of human-entered data. This could be achieved by *everyday objects* which are readable, identifiable, locatable, controllable and addressable with the internet via wireless LAN, RFID or WAN. In particular, *everyday objects* should be equipped with sensors and microprocessors, and have to communicate with each other in

## 1.1 Internet of Things

---

order to create a common network and share information independent of human intervention. These everyday objects can spread from household appliances to clothing, including food, luxury items, buildings, roads, etc. In this framework, three significant categories of the Internet of Things can be identified: automotive and transportation application, health and body surrounding monitoring, and tracking and controlling activities in homes and buildings. Due to its widespread use in industry, agriculture, environment, sports, food processing, entertainment, healthcare, and education, IoT is gaining a relevant impact on several aspects of daily life (see Figure 1.1).



**Figure 1.1:** Examples of possible applications in real-life for the IoT.

Its actual implementation could effectively facilitate human lives by using many devices such as smartphones, PCs, tablets and new-gen devices (the things) connected to the internet. The IoT offers flexible solutions by merging technologies such as software and hardware to store, process and communicate the data among groups or individuals. All of this is possible thanks to a well-established device architecture based on four different layers, as reported in Figure 1.2. The base layer consists of IoT devices and includes all components, like sensors, with the ability to sense, compute and detect other devices. The second layer is the IoT gateway, or aggregation layer. This layer significantly aggregates data from various sensors. These two layers form the definition engine and set the rules for data aggregation. The next layer is cloud-based, and is called the processing engine. It has numerous algorithms and data processing elements that are ultimately displayed on a

## 1.2 Wearable devices

---

dashboard. This layer basically processes the data obtained from the sensors layer. The final layer is the application layer or API management. It acts as an interface layer between third party applications and infrastructure. The entire landscape is supported by device managers, and identity and access managers, which are useful for the security of the structure.

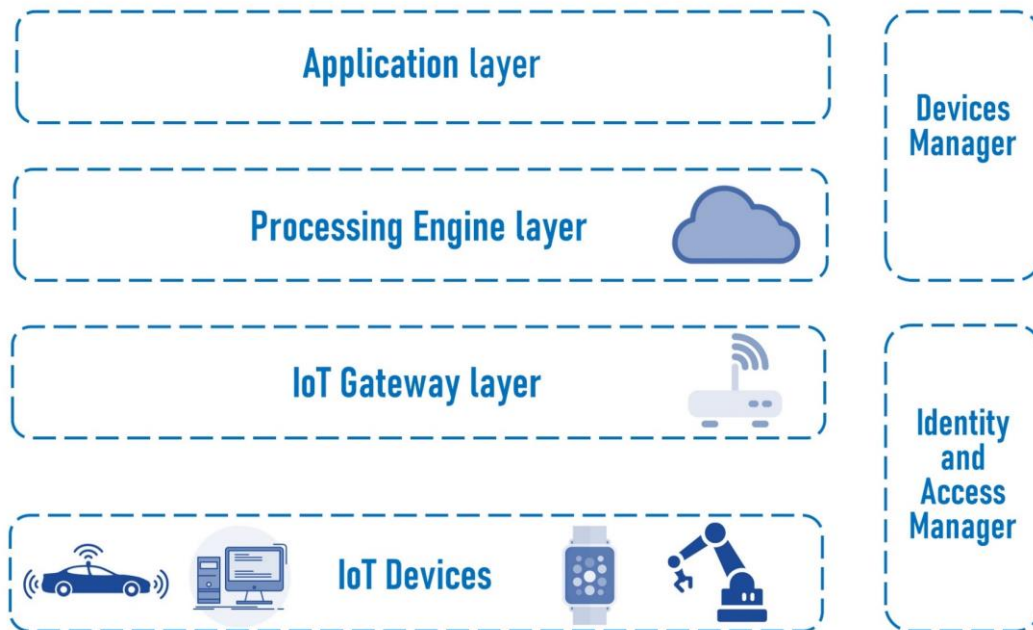


**Figure 1.2:** Four different architecture levels divided among Identity and Access management, and Devices management.

Based on this, the implementation of the concept of IoT is feasible in the real world with the help of low-priced and low-power consumption devices such as sensors, actuators, Radio Frequency Identification (RFID) tags, etc. The wearable devices sense the environment, and analyse, store, transmit and utilise the data based on the final application. The main target of this thesis is to present the latest research results on the development of novel types of IoT devices and sensors to increase the wearable device landscape as much as possible. Namely, it introduces a new, wide range of wearable textile sensors that integrate the sensing element directly into the textile fibres, creating a union between garments and sensors.

## 1.2 Wearable devices

The broad range of IoT devices include smart sensors, actuators, and wearable sensing devices that can be incorporated into daily clothes, worn as accessories or implants. In the

## 1.2 Wearable devices

---

last decade, wearable devices have attracted great attention from the academic community and industry and have become very popular. Wearable devices are defined as “*devices that can be worn or mated with human skin to continuously and closely monitor an individual's activities, without interrupting or limiting the user's motions*”.<sup>22</sup> Sensors seamlessly integrated into textiles, computerized watches, glasses, headbands, belts, etc. can be worn on different parts of the body and are designed for an extensive operational range. In general, the central idea shared by wearable technologies is the wear-and-forget functionality, which automatically reduces the relevance of other approaches with an intrusive nature like, for instance, one that relies on blood samples.<sup>23</sup>

Presently, due to the fast and stressful daily routine that people are subjected to, a large number of individuals tend to completely ignore their health and fitness status. Moreover, even simple appointments with doctors in clinics can require several tests before having a diagnosis, prescription, and final treatment. This means that only the presence of major illnesses prompts people to see a doctor. Therefore, current research in healthcare is seeking alternative monitoring methods such as the use of wearable devices that not only constantly monitor the users' health in real time but also provide timely insights to the users and their doctors in case of altered vital parameters.

Real-time collection and sharing of information regarding body status are significant, not only for hospitalisation situations, but also during daily, routine activities. For instance, continuous monitoring of vital parameters is crucial to take precautionary measures during sports activity or in the wearer's workplace, especially in the presence of diagnosed chronic diseases.

In this view, wearable sensors and smart textiles can be a means to realizing the so-called personalized-medicine, and revolutionizing the way healthcare is managed and medicine is practiced. At the same time, they represent a powerful tool in sports and fitness tracking that can improve the performance and safety of athletes and gain a competitive advantage on the field. The use of wearable devices for sports is still in an early phase, with the majority of the sensors currently used to monitor movement-based parameters or physiological conditions.<sup>24</sup> These devices do not allow team trainers to perform real-time evaluation on the biochemical profile of an athlete with the aim to prevent soft-tissue injuries, cramping or dehydration. However, over the last years, significant progress has been made to develop wearable sensors that detect biomarkers non-invasively from biofluids, easily accessible without impeding the athletes' performance.

In security applications, firefighters, police officers, and paramedics are testing wearable technologies to provide remote communication support and feedback with the ability to access information hands-free while carrying out essential tasks. Additionally, for personal security, lighting technologies and protective clothing are being used to enhance visibility and attract attention. Wearable technologies are also increasingly influencing people's daily activities in terms of gaming and in the tools used to operate household

## 1.2 Wearable devices

---

devices or other gadgets used to communicate. This involves applications related to interacting with computing resource, including data/media access, interactive gaming, responsive learning, and shared experience.

Finally, the application of wearable technology in workplace safety is gaining a lot of attention. Wearable devices may be equipped with sensors to help employees track their behaviours that may increase the risk of injuries. In addition, by monitoring heart rate or other signs of fatigue, wearable devices can alert the users about detrimental practices such as poor posture or overwork. This enables employees to better understand their bodies and possible dangerous habits when performing physically demanding tasks such as bending, lifting, or pushing.<sup>25</sup> Figure 1.3 reports the potential applications of wearable devices divided in three categories based on their location relative to the human body.

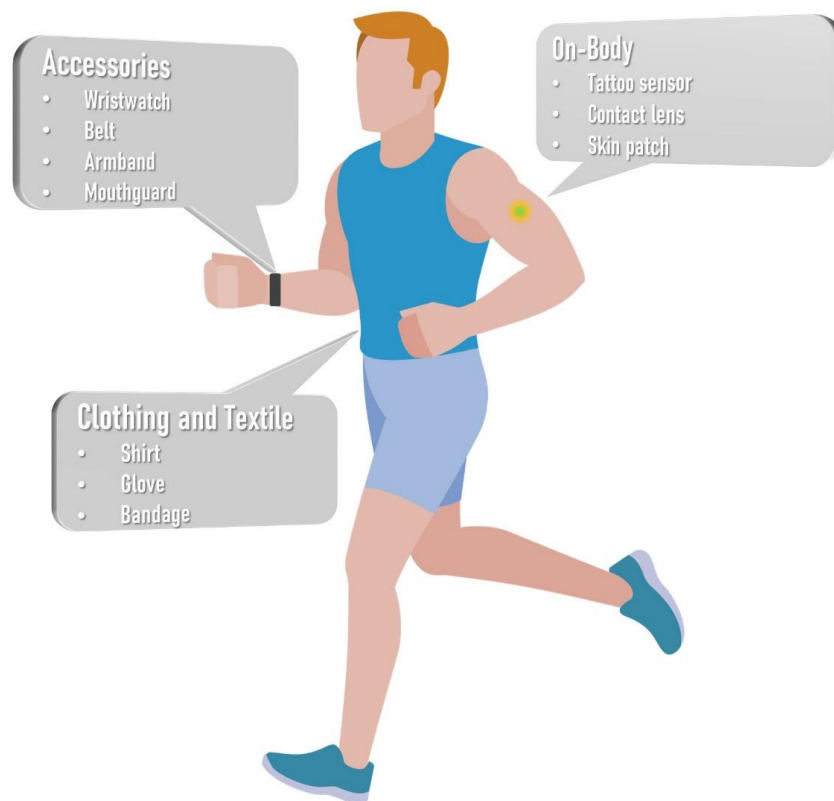


**Figure 1.3:** Applications of wearable devices divided according the placement position.

### 1.2.1 Transduction mechanisms

Wearable sensors rely on different transduction mechanics that can spread from a purely physical to a complex chemical signal. The aim of this paragraph is to present a brief overview of the main working principles on which most wearable sensors, and in particular

the ones presented in this thesis, are based on. The majority of wearable sensors can be classified as piezoresistive, capacitive, electrochemical (in particular amperometric or potentiometric), chemiresistive, transistor-based, or optical.

**Piezoresistive sensors** rely on the piezoresistive effect, which occurs when the electrical resistivity of a material changes in response to applied mechanical strain. In contrast to the piezoelectric effect, the piezoresistivity causes a change only in electrical resistance, not in the electric potential. In semi-conducting materials, the strain from the applied force impacts the material's band structure, which either makes it easier or more difficult for electrons to be excited into the conduction band. Consequently, the density of charge carriers is altered and the material's resistance changes. Usually, the resistance change in metals is mostly due to the change of geometry resulting from applied mechanical stress. However, even though the piezoresistive effect is small in those cases it is often not negligible. Some metals display piezoresistivity that is much larger than the resistance changes due to geometry (e.g., platinum alloys). In the piezoresistive pressure sensors, for example, a combination of geometry deformation and piezoresistive intrinsic behaviour of material, give information about the applied load. Traditionally, active materials for piezoresistive pressure sensors have mainly been based on elastomer composites that contain carbon nano tubes (CNTs),<sup>26-28</sup> metal particles<sup>29,30</sup> and conductive polymers (CPs),<sup>31</sup> which are incorporated into elastomers (e.g., polydimethylsiloxane (PDMS) or polyurethane (PU)) to generate piezoresistive behaviour.

**Capacitive sensors** can monitor the external physical stimuli detecting the capacitance change of a capacitor. A capacitor is a passive electronic component that stores energy in the form of an electrostatic field. It consists of two conducting plates separated by an insulating material, or dielectric. The practical formula to compute the capacitance ( $C$ ) knowing only the geometrical parameters is  $C = \epsilon_0 \epsilon_r A/d$  where  $\epsilon_0$  is the electric constant,  $\epsilon_r$  is the relative static permittivity of the dielectric,  $A$  is the area of the two plates, and  $d$  is the thickness of the dielectric. Therefore, the capacitance between two conductive pads depends on their size, relative position and the properties of the nonconductive material in-between. Changes in  $d$  are commonly used for the detection of pressure in capacitive pressure sensors.

**Potentiometric sensors** consist of an indicator electrode and a reference electrode that must be immersed in the solution under investigation. The analyte is usually quantified by measuring the potential difference between the two electrodes in the absence of current flow. Therefore, the read-out electronics should be designed with a high input impedance. The dependence of the potential of the working electrode on the analyte concentration is described by the Nernst equation:

$$E = E_0 + \frac{RT}{nF} \ln(a_i)$$

where  $E$  is the potential,  $E_0$  is the standard potential,  $R$  is the gas coefficient,  $F$  is the faraday constant,  $n$  is the number of electrons, and  $a_i$  is the activity of the principal ion. The Nernst equation shows that there is a linear correlation between the potential and the logarithm of the analyte concentration. The signal can be generated by redox reactions involving the analyte or through a membrane that selectively allows its adsorption or passage. More complex structures, such as the ion-sensitive field-effect transistor, are described in the literature, but have never been used to produce a textile device.

**Amperometric sensors** measure the current developed by a faradic reaction at a working electrode which is usually biased with respect to a reference electrode with a fixed potential. Both electrodes must be immersed in the analysed sample. Although the most rigorous measurements are carried out in a three-electrode cell endowed with a counter electrode, the simplest devices use a two-electrode configuration. The applied potential is chosen to consume all the analyte at the electrode surface, thus generating a concentration gradient by diffusion from the bulk of the solution. In this way, the recorded current is directly proportional to the concentration of the analyte in the sample.

**Chemiresistors** are a class of sensors that can detect and quantify the target compound due to a change in the electrical resistance of the sensing material. The interaction between the target analyte and sensing material can occur, for example, by creating traps, acting as a dopant, imposing resistive interfacial barriers, and changing the existing intermolecular interactions between molecular subunits.

**Organic electrochemical transistors (OECTs)** are composed of a channel made of a conductive polymer and a gate electrode both immersed in an electrolytic solution. When a voltage is applied to the gate electrode, it stimulates electrochemical reactions at the channel that change the charge carrier concentration and thus the current that flows through it. Each substance that changes the current flow in the channel can be detected by these devices. Since OECTs combine a transducer and an amplifier, the signal is enhanced.

**Optical sensors** exploit the interaction between the electromagnetic radiation and the chemical system. The detection occurs directly for analytes capable of absorbing the radiation or through the use of reagents that modify their absorption spectrum following the reaction with the analyte. In the simplest systems (e.g, the litmus paper for pH estimation) the detection and/or quantification is performed through a visual investigation by the comparison of the resulting colours with a reference scale. More advanced systems use a light source, a photodetector, and a monochromator for quantitative analysis of the absorbed radiation. Recently, signal acquisition has been carried through with a standard smartphone camera for images analysis.

### 1.3 Smart textiles

Among the huge variety of wearable devices, the textile-based sensors represent an excellent example of a non-invasive, low-cost, comfortable, and lightweight point-of-care platform. Fabrics, with their fitting features and comfort, are the best substrates and platforms onto which a wearable sensor device may exist. They can be sensitive to various external stimuli, both physical and chemical,<sup>32</sup> such as the changes in force,<sup>33,34</sup> pressure,<sup>35,36</sup> deformation,<sup>37,38</sup> temperature<sup>39</sup> and the concentration of specific compounds in body fluids,<sup>40</sup> like ion chloride<sup>41</sup> or sweat quantity.<sup>42</sup> Furthermore, it is possible to functionalize fabrics with organic polymers in order to utilise textile electrocardiogram electrodes for the detection of biopotentials.<sup>43,44</sup>

From the wide selection of textile materials and fibres, cotton yarns, acrylic fabrics or elastane-based textiles are the most common substrate to accommodate physical or chemical textile sensors. The choice of the proper textile materials is a relevant aspect in the sensor design since it could affect the sensors' response in terms of sensitivity, stability, or washability, correlated to the interfacing between textile and sensitive materials. The first step to achieving a reliable and reproducible textile sensor platform is to study and investigate the adherence of conductive and sensing compounds with the desired textile substrate. Taking into account the final scope and application of a textile sensor, the proper support to develop and integrate the smart sensor has to be chosen between fibres, yarns, and fabrics.

Fibres are the most basic units of textile technology with a design of flexible, elastic, and stretchable fibres that can be knitted or woven, essential to implement the already existing landscape of fibre-based electronics. According to their application, they can be classified into fibre-shaped energy-harvesting solar cells,<sup>45</sup> thermoelectric<sup>46</sup> or triboelectric nanogenerators;<sup>47</sup> fibre-shaped energy storage devices like supercapacitors<sup>48</sup> or lithium-ion batteries;<sup>49</sup> fibre-shaped electroluminescent devices<sup>50</sup> and fibre-based sensors<sup>51-53</sup> which generally work via physical or chemical processes. Presently, the two relevant strategies to create electronic textiles, or e-textiles, exploiting the soft, deformable and permeable features of fibres rely on their interaction into textiles through standard textile methods or to weave cathode and anode fibre electrodes in an interlaced configuration to realize the e-textile. However, even if they present a real possibility for the production of skin-like pressure sensors<sup>54</sup> or flexible circuits,<sup>55</sup> the mechanical properties of e-textiles are generally lower than those required for automatic manufacturing processes, and the hand-made realisation of these new smart sensors limits their applicability and large-scale production.

Conversely, the yarn-based textile sensors are machine-made and, since the yarns are made by combining different types of fibres, it is possible to produce elastic and conductive yarns.<sup>56,57</sup> Furthermore, many examples of composite structures have been proposed in the last decade based on graphene oxide/nylon yarns<sup>58</sup> and functional

coatings.<sup>41</sup> Cotton yarns were transformed into e-textiles by coating them with a polyelectrolyte-based layer with carbon nanotubes.<sup>59</sup> At the same time, using the melt-spinning method, elastic silicone tubes and stainless-steel yarns has been realised to manufacture stretchable triboelectric yarns.<sup>60</sup> As previously stated, suitable substrates have a vital role in the production of e-textiles.

Different fabrics, such as 100% cotton (woven and knit), 100% polyester and blend substrates (polyester/cotton, cotton/wool, wool/nylon, etc.) have been extensively used. Depending on the sensor type, the less deformable and less porous woven fabric can be used instead of the more stretchable and deformable knitted fabrics. Both knitted<sup>61</sup> and woven<sup>62</sup> fabric-based e-textile sensors are produced using various techniques like dipping,<sup>63</sup> drop casting,<sup>64</sup> coating,<sup>40,65</sup> pad-dry method,<sup>66</sup> screen printing<sup>67,68</sup> and in situ polymerisation.<sup>69</sup> In addition, the different material plays a fundamental role to individuate the textile substrate. For instance, PEDOT:PSS-based sensors (poly(3,4-ethylenedioxythiophene) polystyrene sulfonate) need a hydrophilic substrate such as cotton fabrics.<sup>40,70</sup> On the opposite side, Ag/AgCl ink and carbon ink used for screen printing require a hydrophobic substrate, such as GORE-TEX.<sup>23</sup> Overall, cotton fabrics show high breathability and/or air permeability, which make them preferred for skin-contact sensors,<sup>71</sup> while polyethylene terephthalate (PET) fabrics can be easily functionalized with metallic layers to increase electrical conductivity and electromagnetic shielding.<sup>72</sup> Finally, 100% polyester with a shallow moisture content compared to natural fibres, 100% wool, or a blend of different yarns to optimize textile properties for a specific application have been produced for health monitoring,<sup>73</sup> temperature sensing,<sup>74</sup> motion monitoring<sup>75</sup> and for developing low-cost wearable energy-storage devices.<sup>76</sup>

### 1.3.1 Fabrication of conductive textile

The first step for producing a textile sensor relies on the preparation of conductive filaments or fabrics mainly using polymeric materials due to their compatibility and flexibility. Conductive polymers (CPs) are the most used compounds to make textile fibres conductive and are usually mixed with proper compounds to tune the physical features of the conductive layer. Therefore, the preparation methods usually produce a conductive polymer composite (CPC) since these additives remain entrapped in the films. There are three main ways to realise a conductive textile based on CPs: i) the CPC can be spun in the form of a single fibre by wet spinning, melt spinning, or electrospinning alone or in combination with other polymers, ii) a thin layer of CP can be directly polymerized onto the textile by vapor phase polymerisation, in situ polymerisation, or electropolymerisation, iii) a thin layer of CPC can be deposited onto a commercial textile by printing or coating/dyeing a suspension/solution containing the polymer. It is worth noting that dyeing, coating, printing, and in situ polymerisation are useful to functionalize the surface of fabrics or yarns,

### 1.3 Smart textiles

while spinning allows the creation of fibres to produce conductive filaments. Wet spinning or electrospinning are used to produce conductive fibres. In wet spinning (Figure 1.4.a), the polymer is solubilized in a solvent, and the spinneret is immersed in a bath where the polymer is not soluble. Injecting the solution into the bath, the polymer precipitates in the form of fibres by drying under tension. Zhang et al. have described an interesting approach to wet spin a PEDOT commercial suspension using a strong acidic environment.<sup>77</sup> During the fibre formation, PSS counterions are expelled from the conductive polymer increasing the conductivity of the fibre. On the contrary, electrospinning (Figure 1.4.b) takes advantage from electric forces to stretch the polymer droplets and make the single fibres. CPs can be blended with other types of polymers to improve the mechanical features of the resulting CPC fibres.<sup>78</sup>

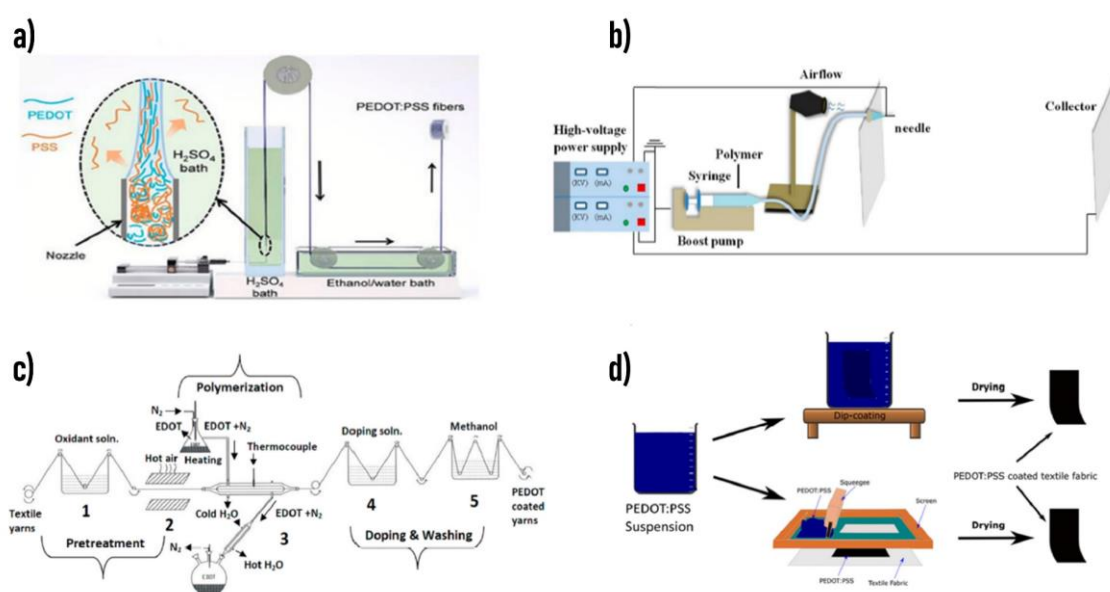


**Figure 1.4:** Fabrication methods for conductive textile: a) Wet spinning, b) electrospinning, c) chemical vapor deposition polymerisation, and d) printing deposition.

The textile surface can also be coated by polymerisation, starting from the basic monomeric units. The first step of a polymerisation reaction is the monomer oxidation, to form radical cations. The following coupling reactions are responsible for the formation of the polymeric chain. During chemical vapor phase (CVP) polymerisation (Figure 1.4.c), the monomer is in the gas phase, while the oxidant is adsorbed on the textile.<sup>79-81</sup> Consequently, the polymerisation takes place only on the fabric surface that will be covered by the CP thin film. The in situ polymerisation is performed by submerging the fabric in the solution containing the oxidant and the monomer. The reaction can be limited to the external surface when the impregnated textile is removed from the reactive solution and the oxidation is induced by a stimulus, such as heating.<sup>82</sup> Electrochemical polymerisation must be performed on a conductive textile soaked in a solution containing the monomers and

electrolytes.<sup>83</sup> The application of an anodic potential between the substrate and a reference electrode leads to the monomer oxidation and thus to the polymer formation.

When the conductive film is prepared by printing<sup>40</sup> or deposition<sup>84</sup> (Figure 1.4.d), a suspension/solution is placed on the textile and, after the evaporation of the solvent, the CP precipitates on the textile. Several commercial products based on conductive polymers are available on the market, but their composition has to be tuned in order to address the peculiarity of the different deposition processes. For example, dip-coating and spin coating are needed for CP solutions with low viscosity because they have to wet the textile to guarantee the continuity of the film.<sup>85</sup> On the other hand, stencils and screen-printing require very viscous inks to hinder the percolation outside the masked area with a consequent reduction of the pattern resolution.<sup>40</sup> Beyond the peculiarity associated to the deposition techniques, auxiliary components are added to impart specific features to the resulting CPC film. For example, secondary dopants enhance the conductivity by acting on the microstructure of the polymer,<sup>86</sup> while plasticizers<sup>87</sup> improve the flexibility of the film and increase the resiliency of electrical features after deformation.

In the dyeing/coating process, the textile is dipped or immersed in the CP solution/suspension; consequently, the conductive film is deposited all over the surface. Conversely, the printing processes, such as ink-jet printing and screen-printing, allow one to deposit the CP film on a selected area of the textile. Both printing and dyeing processes are widely used by the textile industry, and thus offer the advantage of straightforward scalability.

### 1.3.2 Electrical connections in textile sensors

In addition, textile devices require that the electronic and data communication systems be flexible and lightweight to allow their integrability into the textiles themselves. A complete textile system includes not only the textile sensor, but also connections, readout electronics, and power supply. A common way to connect sensors with electronics includes soldering of metallic wires. Buechley et al.<sup>88</sup> tested solder joints as connectors on a metallic fabric circuit. However, this process is limited by the high temperature required (up to 280°C) which damages most of the commercial fabrics. An alternative option includes a mechanical gripping between sensor connectors and rigid connectors or metallic wires of circuits. For example, Leśnikowski<sup>89</sup> et al. integrated rigid poppers on fabric as electronic connectors. Li and Tao explored unique structures to wrap the conductive track around a stainless-steel needle with a diameter of about 1 mm to form a circular helix and achieve a helical connection between knitted interconnect and wire.<sup>90</sup> As opposed to soldering, mechanical gripping could be applied to almost all conductive textiles, but the main drawback is that rigid connections cannot keep stability and may break under extensive deformation. A more flexible solution involves the conductive adhesives. Siegel et al.<sup>91</sup> applied a commercially conductive adhesive on metallic wires on fibre-based substrate and

bonded electronic devices to the metallic pathways attaching sensor electrodes on the adhesive. Finally, non-rigid read-out board systems or wireless communications, such as RFID<sup>92,92</sup> and NFC, are still being researched in order to create fully textile devices and reach the much desired goal of “wear and forget”.<sup>93</sup>

In order to provide a general overview of the current innovations in the field of e-textile sensors, the following sections describe some of the latest examples of physical and chemical textile sensors similar to those mentioned previously in greater detail. The focus will be on those sensors that I have further developed in my PhD research activity and that will be further discussed in detail in the next chapters.

### 1.3.3 Sweat monitoring sensors

Sweat, saliva, interstitial fluids, tears, and exudate are biological fluids that contain abundant information about health status, and are readily accessible and easily sampled for non-invasive monitoring.<sup>94,95</sup> Among all of them, the investigation of chemical compounds in human sweat dates back to the 19th century, with the aim to identify a correlation between physiological states, diseases, and the use of drugs. For instance, the analysis of chloride content in human perspiration is performed for the diagnosis of cystic fibrosis and is the most important application for routine analysis. Doping control is another field wherein sweat tests are employed because they offer some advantages, such as less opportunity for sample adulteration and non-invasive sampling as compared to blood. Finally, the quantification of some toxic metals, such as Cd, Pb, Hg, and As, is important because the rates of their excretion were reported to match or even exceed urinary excretion.<sup>96</sup> The main constraints that hinder a straightforward realisation of a reliable wearable chemical sensor are related to the low analyte concentration, small sampling volumes and fluid stagnation, mechanical resiliency, signal stability, biofouling and biocompatibility issues, together with the need to operate in physiological conditions, adapt to the human body without causing discomfort, and work with low power consumption, thus requiring simple electronic components.

Sweat sensors are attracting increasing interest thanks to the development of new wearable technologies that are overcoming the previous constraints by achieving a real-time sweat collection and analysis.<sup>22</sup> Innovative wearable sensors are placed outside of the body but in close proximity of the eccrine sweat glands that produce a very low, but continuous, amount of biofluids. Its analysis could provide an overview of the chemical composition of the surrounding cells at the time of sweat secretion but it is worthy to note that the sweat analysis cannot reach the medical relevance of blood test, because the human bodies closely control only the blood composition while the sweat can be subjected to multiple variations. In addition, sweat composition is affected by the body region, gender, age, ethnicity, diet, activity level, and acclimation. Liquid human perspiration could be monitored in real time

### 1.3 Smart textiles

by wearable sensors in an easily and non-invasive procedure that cannot be accomplished for blood because of the impossibility of taking samples with this time resolution.<sup>97</sup> Table 1.1 shows the typical concentration of metabolites in human sweat. Among the huge variety of wearable biosensors, the textile-based sweat sensors represent an excellent example for a non-invasive, low-cost, comfortable, and lightweight point-of-care platform.

**Table 1.1:** Typical concentration of metabolites in human sweat. \*\* in  $\mu\text{M}$

Biomarker	Concentration range (mM)	Ref
Ca <sup>2+</sup>	0,07 – 12	98
K <sup>+</sup>	4 – 24	99
Cl <sup>-</sup>	10 – 100	100
Na <sup>+</sup>	10 – 100	101
Ammonium	0.5 – 8	100
Lactate	5 – 60	102
Urea	14.2 – 30.2	103
Glucose	0.01 – 1	104
Ethanol	2.25 – 22.5	105
Pyruvic acid	0.06 – 1.6	106
Amino acids*	303	106
Ascorbic Acid	1.4 – 62.5 **	106

#### 1.3.3.1 Textile glucose sensors

Diabetes is a widely spread disease affecting hundreds of millions of people. This health issue drives technology to develop new glucose sensors for self-testing and monitoring. Commercial portable devices consist of disposable strips with a screen-printed electrochemical sensor and a pocket-size reader.<sup>32</sup> Even if this technology is common and mass-produced, self-testing of blood glucose still suffers from irregular testing frequency; moreover, the knowledge of daily changes of glucose concentration allows for the efficient treatment and improvement of the quality of life for people with diabetes. For this reason, many research groups proposed innovative wearable devices for continuous monitoring, exploiting other body fluids in place of blood. Among them, sweat has been the most studied by far. The main issue still under review, which must be overcome to effectively use this new technology, is the assessment of the correlation between glucose concentration variations in sweat and in blood. With only this fundamental information, it is possible to monitor the glucose concentration directly from the sweat in a non-invasive way. For instance, it is known that the concentration of glucose in sweat ranges between 10

$\mu\text{M}$  and 1 mM, 3 orders of magnitude lower than the concentration in blood.<sup>94</sup> A specific clinical procedure called a “glucose tolerance test”<sup>107</sup> is used to find the direct correlation between the glucose concentration present in blood and in sweat. Mimicking a hyperglycemia event in healthy subjects, the concentration of glucose is simultaneously monitored in both fluids and, as a result, a variation in the range between 50  $\mu\text{M}$  and 120  $\mu\text{M}$  represents an alteration from the normal state to a potentially high glucose level.

Many research groups are working on the development of wearable sweat sensors for glucose concentration<sup>108</sup>, mainly using two different approaches: enzymatic and non-enzymatic sensors. In the first case, the sensors functionalized with enzyme are called “biosensors”, and the presence of GOx catalyzes the oxidation of glucose to gluconic acid as reported in scheme 1:



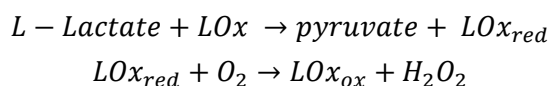
The detection is an indirect evaluation of oxygen consumption, and the sensing element detects the presence of  $\text{H}_2\text{O}_2$  as a product of oxidation reaction, which is directly proportional to the glucose concentration. Most of the textile glucose sensors using this working principle are based on amperometric electrochemical sensors,<sup>109,110</sup> organic electrochemical transistor<sup>111</sup> and, furthermore, on colourimetric sensors.<sup>112</sup> As an example, Wang et al.<sup>111</sup> proposed a fibre-based OECT formed by in situ polymerized polypyrrole (PPy) nanowires and reduced graphene oxide (rGO) (Figure 1.5.a). The gate electrode fibre is functionalized with GOx and Nafion. The large surface area of PPy nanowires increases GOx amount leading to a fast electron transfer and high sensitivity. When glucose is dissolved in the  $\text{LiClO}_4$  gel electrolyte, it oxidizes at the GOx-modified gate electrode and, concurrently, the  $\text{H}_2\text{O}_2$  releases as a side-product reacting with  $\text{LiClO}_4$ , enhancing the channel conductivity of the fibre-based OECT. As a consequence, glucose is detected as an increment in the drain current. The intrinsic amplification of the fibre-based OECT configuration allows it to reach a sensitivity of up to 0.773 decade<sup>-1</sup> and a limit of detection (LOD) down to the nanomolar range.

In the second case, the non-enzymatic sensors approach exploiting the electrocatalytic behaviour of the functionalized working electrode. Several functionalisations have been reported, but just a few of them have been translated successfully on textiles.<sup>113,114</sup> For instance, Peng et al.,<sup>115</sup> proposed an amperometric sensor based on AuNS fibre microelectrode, a fibre of platinum, and a fibre cover with Ag/AgCl to achieve a very low LOD and high sensibility.

### 1.3.3.2 Textile lactate sensors

The concentration of lactate in blood is correlated with the healthy state of cells. This occurs when an insufficient amount of nutrients or oxygen reach a tissue and cells start to generate energy through an anaerobic metabolic pathway leading to an increase in the production of lactic acid. Several factors can determine this condition, including an excessive physical exertion during endurance sports such as running, cycling, or boxing. In a persistent state of anaerobic effort, the accumulation of lactate in the muscles generates muscle fatigue and, monitoring lactate concentration, can help to improve performance in sports activities. Commercial portable devices for lactate detection are already available and are based on standard electrochemical methods<sup>116</sup> while the textile-based technology that continuously detects lactate from human perspiration still represents a forefront application. The typical reference level of lactate in sweat is 25 mM, but this value is strictly dependent on several factors such as age, gender, and area of bodily perspiration.<sup>117</sup>

For such sensors, the functionalisation of the sensing element is always enzyme-based employing mostly lactate oxidase (LOx). The enzyme catalyzes the lactate oxidation to pyruvate and releasing hydrogen peroxide (H<sub>2</sub>O<sub>2</sub>).



This mechanism is at the basis of optical and electrochemical textile-based lactate sensors as highlighted in the Biotex European project,<sup>118</sup> as well as Promptet et al.,<sup>119</sup> Jia et al.,<sup>120</sup> and Baysal et al.<sup>121</sup> Alternatively, Zhang et al.<sup>122</sup> reported a novel approach to fabricate a fibre-based OECT biosensor (Figure 1.5.b). A nylon fibre is first dip-coated with multi-walled carbon nanotubes (MWCNTs) followed by PPy with in-situ polymerisation, leading to a composite material (e.g., PPy/MWCNTs). The PPy-MWCNTs fibre has been used as the OECT channel, while a Pt wire coated with LOx immobilized in a Nafion matrix serves as a gate electrode. The OECT biosensor is biased with a gate voltage equal to 1.0 V and the electrons released at the gate electrode generate a Faradaic current that change the effective gate voltage, which directly affects the channel conductivity. The wide linear response range of 1 nM – 1 mM is suitable for sweat analysis.

### 1.3.3.3 Textile pH sensors

An import parameter that can provide information about the overall body status as well as particular physiological conditions and disorders is represented by the pH in human sweat. For instance, while sweat pH typically ranges from 4.5 to 6.5, a more alkaline sweat (up to pH 9) has been found in patients affected by cystic fibrosis due to impaired

### 1.3 Smart textiles

bicarbonate reabsorption.<sup>123</sup> Sweat pH has been correlated to blood glucose levels,<sup>124</sup> the intensity of physical exercise, and metabolic alkalosis during sport activity<sup>125,126</sup> and due to skin diseases.<sup>127</sup>

The route of optical transduction for the realisation of textile pH sensors has been widely explored in literature with an emphasis on the use of halochromic materials. A halochromic textile changes its colour upon pH variations due to the presence of a pH dye whose reversible acid-base chemistry leads to bathochromic or hypsochromic shifts resulting in visible colour changes. The pH-sensing abilities of dye-functionalised textiles obtained by fibres activation and soaking,<sup>128</sup> layer-by-layer method,<sup>129</sup> electrospinning,<sup>130</sup> sol-gel technique,<sup>131</sup> and photo-grafting<sup>132</sup> have been investigated in relation to the physico-chemical properties of a library of natural and synthetic dyes and fabrics.

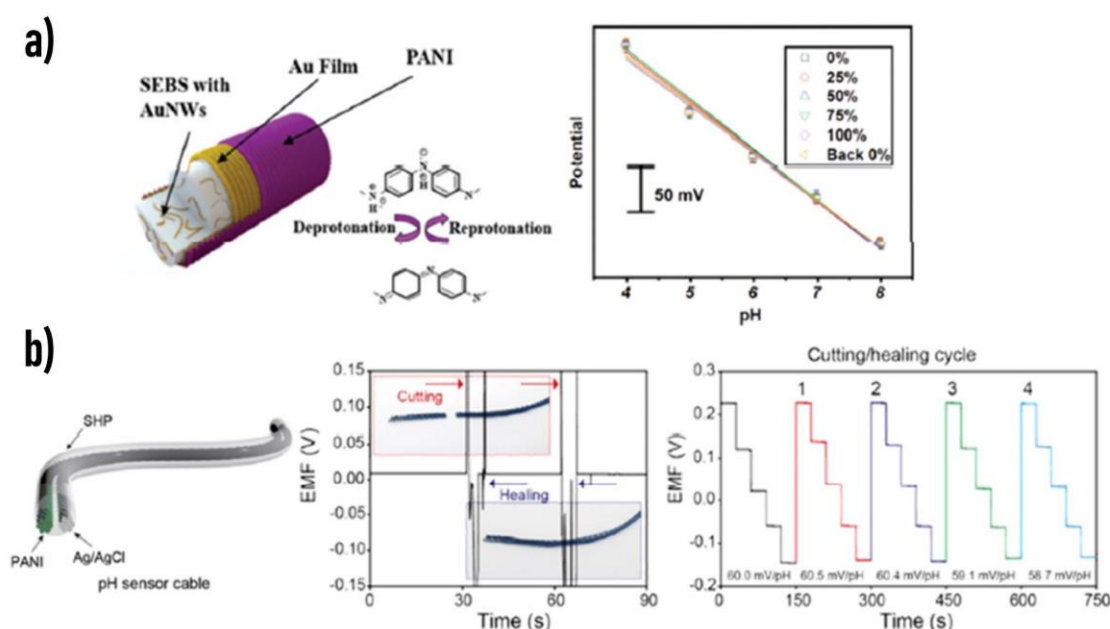


**Figure 1.5:** Fibre-based OECT formed by in situ polymerized polypyrrole (PPy) nanowires and reduced graphene oxide (rGO),<sup>111</sup> and b) nylon fibre-based OECT biosensor based on PPy for lactate concentration detection.<sup>122</sup>

Among textile optical sensors for pH detection in sweat, one of the first examples of textile platforms for on-body trials was reported by Coyle et al.,<sup>133</sup> who developed a smart waistband capable of pH and sweat rate monitoring comprising a sensing area with immobilised Bromocresol Purple and a fabric fluidic channel for passive sweat pumping.

More recently, Rosace's group has thoroughly reported on the encapsulation of Litmusand<sup>134,135</sup> Methyl Red<sup>136</sup> into cotton fabrics by sol-gel method, and equipped the halochromic fabric with miniaturized readout electronics including LED optical detectors and wireless connectivity. Contrary to optical devices, the realisation of textile pH sensors

for sweat analysis based on potentiometric transduction has been introduced only in recent years.

The first example was reported by Zamora et al. with the electrodeposition of an Iridium Oxide film on Nylon-based conducting fabrics and stainless-steel mesh fabric.<sup>137</sup> In the last two years, only one potentiometric sensor for sweat pH detection has been achieved by printing both electrodes (i.e. thick film graphite-polyurethane composite) and the reference electrode on a cellulose-polyester blend cloth showing sub-Nernstian performances,<sup>138</sup> while most works in literature are based on PANI electrodeposition to impart pH sensitivity to the working electrode. Among CPs, polyaniline (PANI) stands out as the most common example of non-redox doping caused by base/acid equilibria between deprotonated (e.g., base, dedoped) and protonated (e.g., salt, doped) forms and has been exploited for the realisation of textile potentiometric sensors. For example, PANI electropolymerisation has been used on wet-spun PEDOT:PSS fibres<sup>139</sup> and elastomeric gold fibres woven into a textile matrix<sup>53</sup> (Figure 1.6.a), both showing good resiliency of the sensing performance during elongation tests. In the first case, treatment with the organic solvent dimethyl sulfoxide (DMSO) increases the conductivity of the PEDOT:PSS fibre, thus facilitating PANi electrodeposition, with the sensor response covering the pH range 3.0 – 7.0 with Nernstian sensitivity ( $-56 \pm 7 \text{ mVpH}^{-1}$ ). In the latter, a  $60.6 \text{ mV pH}^{-1}$  sensitivity is achieved in the pH range 4 – 8 with good selectivity in the presence of  $\text{Ca}^{2+}$ ,  $\text{NH}_4^+$ ,  $\text{Mg}^{2+}$  and  $\text{Na}^+$ , while only a slight decrease in the woven sensor performance is reported during pH detection in artificial sweat. Also worth mentioning is the work by Yoon et al.<sup>140</sup> where a self-healable textile sensor is utilised on PANI-coated carbon fibre threads (Figure 1.6.b), which are eventually sewn into a sport headband for proof-of-concept pH monitoring during physical exercise. The thread-based sensor exhibits Nernstian behaviour (with a sensitivity of  $58.28 \text{ mVpH}^{-1}$ ) within the pH range 3.89 – 10.09 and independent healing capability during four cutting/healing cycles, with no loss in the sensing performance during pH detection in artificial sweat samples. Despite the evident advancements in sensor fabrication and material engineering, the production of stable reference electrode analogues on textile substrates remains a crucial bottleneck in the realisation of potentiometric chemical sensors.

In the next chapters, in congruence with the work of Gualandi et al.,<sup>41</sup> a new two-terminal potentiometric pH transducer made of PEDOT doped with a pH dye will be described, thus demonstrating the possibility to integrate a chemical sensor within a bioactive and elastic textile substrate.

### 1.3 Smart textiles

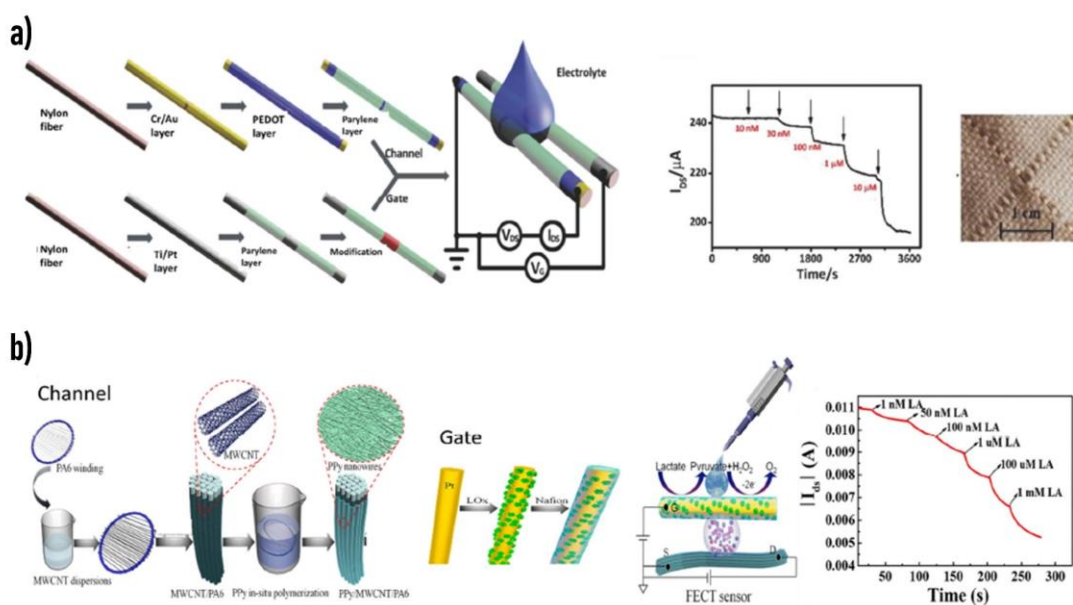


**Figure 1.6:** a) Wet-spinning fibers of PEDOT:PSS fibres<sup>139</sup> and elastomeric gold fibres covered with electropolymerised PANi for pH sensing,<sup>53</sup> and b) self-healable carbon fiber coated with PANi for pH monitoring during physical exercise.<sup>140</sup>

#### 1.3.3.4 Textile electrolytes sensors

Some of the most important components of human perspiration secreted by the eccrine glands are electrolytes ( $\text{Na}^+$ ,  $\text{Cl}^-$ ,  $\text{K}^+$ ,  $\text{NH}_4^+$ ). Numerous clinical- and health-correlated information can be extracted from the electrolyte's analysis. Although the measurement of  $\text{Na}^+$  and  $\text{Cl}^-$  concentration in sweat offers limited correlation with the corresponding values in blood, there is ample evidence regarding the connection between  $\text{Cl}^-$  level and medical status. This evidence is utilised to predict hormonal changes<sup>141</sup> and to non-invasively diagnose cystic fibrosis when the concentration is abnormally high. Moreover,  $\text{Na}^+$  and  $\text{Cl}^-$  concentration can be used to assess hydration level,<sup>142</sup> hyponatremia, and indirectly measure the sweat rate. Conversely, potassium ions concentration in sweat is directly related to the concentration in blood and is independent of sweat rate.<sup>143</sup> Since its concentration in plasma can foretell muscle activity,<sup>144</sup> as well as a vast number of conditions related to hyper- or hypo-kelemia,<sup>145</sup> a huge variety of wearable and textile ion sensors have been studied. Most are based on standard electrochemical techniques, such as potentiometric and amperometric sensors, or they exploit the amplification effect of the organic electrochemical transistor (OECT).

The most common approach concerns the use of ion-selective membranes (ISM), which exclude all ions except for the ion of interest. Although some ISMs are polymeric and do not require other chemical species to sense and immobilize cations, the most used ISMs

are composites formed by matrix/supporting material, anion or cation excluder component, plasticizer, and ionophore. The ability to rapidly and accurately monitor sodium in human sweat using a textile device was first presented by Parrilla et al.<sup>146</sup> They reported a carbon fibre-based sodium ion sensor using commercial carbon fibre (CCF) substrate opportunely modified to realize a potentiometric device in a conventional two-electrode configuration. The ionophore composite is the sensing element of the membrane and is responsible for ion immobilisation producing, in most of the cases, a logarithmic response with a change in analyte-ions activity mediated by the Nernst equation.

Additionally, Parrilla et al.<sup>147</sup> also proposed a variation for the ion-selective membrane cocktail replacing the common PVC matrix with polyurethane (PU) to provide further resistance to mechanical stress and the necessary biocompatibility. These materials can provide exceptional analytical performance when potentiometric techniques are involved and simultaneously minimize adverse physiological effects, such as unwanted inflammation or fouling.<sup>148</sup> Due to the attractive mechanical properties of PU, highly stretchable textile-based sensors able to detect the sodium and potassium concentration in human sweat, even during extreme mechanical stress, were produced.

A breakthrough in the functionalisation of textile fibres was made by Guinovart et al.<sup>149</sup> turning cotton yarns in an ion-selective sensor using CNTs and ISMs. They exploited the good ion-to-electron transduction features of CNTs as potentiometric devices<sup>150</sup> coupled with the excellent electrical conductivity. In their work, they proposed a cotton fibre, properly dipped in an ion-selective membrane solution, able to monitor, in a potentiometric way, pH as well as potassium ( $K^+$ ) and ammonium ( $NH_4$ ) concentration in the liquid.

Following these pioneering works on textile sensors using the ion selective membrane (ISM) as a sensing element to realize textile sensors for ion concentration, Yoon et al.<sup>151</sup> reported high-sensitive wearable sensors endowed with self-healing features based on CNTs, ISMs, PEDOT:PSS, and Poly(1,4-cyclohexanedimethanol succinate-cocitrate) (PCSC). The wearable sweat-sensing device is formed by an indicator and a reference electrode sewn into the textile substrate with Bluetooth communication technology (Figure 1.7.a i). After coating CNTs with the conductive polymer PEDOT:PSS by electrochemical deposition,  $K^+$  and  $Na^+$  ISMs were deposited onto the carbon fibre thread (CFT) electrode by dip-coating the thread in the membrane cocktail. The reference electrode was obtained by coating the CFT electrode with Ag/AgCl ink and polyvinyl butyral (PVB). Both working and reference CFT electrodes were then covered with the self-healing polymer, leading to an electrical healing ability enhancing mechanical properties. The thread-based sensors for  $Na^+$  and  $K^+$  (Figure 1.7.a ii) were tested separately in buffer solution containing the respective ion in the physiologically relevant concentration range (0.1 mM - 100 mM). The thread sensors were stable in a temperature range of 20 - 40 °C under bending or crumpling, and showed good selectivity. Finally, the sensing threads were knitted onto a smart

headband and connected to a flexible PCB, which acquired and transmitted data wirelessly to perform real-time sensing during physical activity.

Besides the great interest inspired by the potentiometric textile sensors, the textile OECT represents a novel class of wearable and portable sensors able to monitor specific analytes in biofluids exploiting the very low operating voltage and absorbed power, coupled with the highest trans-conductance among the transistor-based sensors.

The ground-breaking work of Tarabella et al.<sup>152</sup> in 2012 presented, for the first time, a textile chemical sensor based on an OECT with a single PEDOT:PSS-coated cotton yarn as the transistor channel. The thread was interfaced with a liquid electrolyte, and a silver metal wire was employed as the gate electrode (Figure 1.7.b i), the latter inducing a stable and reproducible modulation of the channel current. The low-cost and simple method was used to effectively sense the NaCl concentration in a liquid electrolyte. The drain current could be modulated in the mA range by gate bias (Figure 1.7.b ii) and the relative current variation directly tuned by the NaCl concentration in the liquid. However, it could not detect the presence of Na<sup>+</sup> and Cl<sup>-</sup> alone.

Recently, Coppedè et al.<sup>153</sup> utilised the remarkable performance of OECTs to achieve a wearable textile device able to selectively detect the concentration of potassium, sodium, and calcium in human sweat. The textile-OECT is composed of a conductive channel made of an acrylic textile covered with the stable, biocompatible, and semiconducting polymer PEDOT:PSS and a gate made with a silver wire (Figure 1.7.c i). The textile threads were made conductive, as previously reported by Mattana et al.,<sup>84</sup> by immersing the yarns in a semiconducting solution formed by PEDOT:PSS, ethylene glycol (EG), and dodecyl benzene sulfonic acid (DBSA). The ion selectivity was achieved by exploiting ISM based on potassium ionophore and calcium ionophore (II). Na<sup>+</sup> is the most abundant electrolyte in human sweat and was employed as the interfering agent to evaluate potassium and calcium sensors' selectivity (Figure 1.7.c ii). Despite the promising results achieved by the transistor configuration based on PEDOT:PSS-functionalized fibres, the requirement of an external and metal gate electrode reduced the flexibility and the wearability of these devices. To overcome such a problem, Gualandi et al.<sup>41</sup> reported a novel and breakthrough approach to fabricate textile sensors inspired by the OECT. They synthesized and achieved a newly composed material based on PEDOT:PSS and Ag/AgCl Nanoparticles integrated into the semiconducting polymer that behave, in a way, as nanogate electrodes (Figure 1.7.d i). The textile sensor is made by a cotton thread coated via a roll-to-roll-like process by a PEDOT:PSS based solution. Consequently, the sensor showed the intrinsic amplification response of a transistor with a simple two-terminal configuration. The sensor behaviour is based on the electronic coupling between the ionic charge and the electrochemically active nanoparticles. The spontaneous and reversible redox reaction between chloride and silver allows wireless monitorisation of the chloride ion concentration in the sample solution with the expected Nernstian behaviour (Figure 1.7.d ii). The real-time electrolytes

### 1.3 Smart textiles

monitoring in sweat, using textile sensors technology, introduces a wide variety of possibilities and new paths to achieve fully-textile multi-sensing platforms for health and sport application.

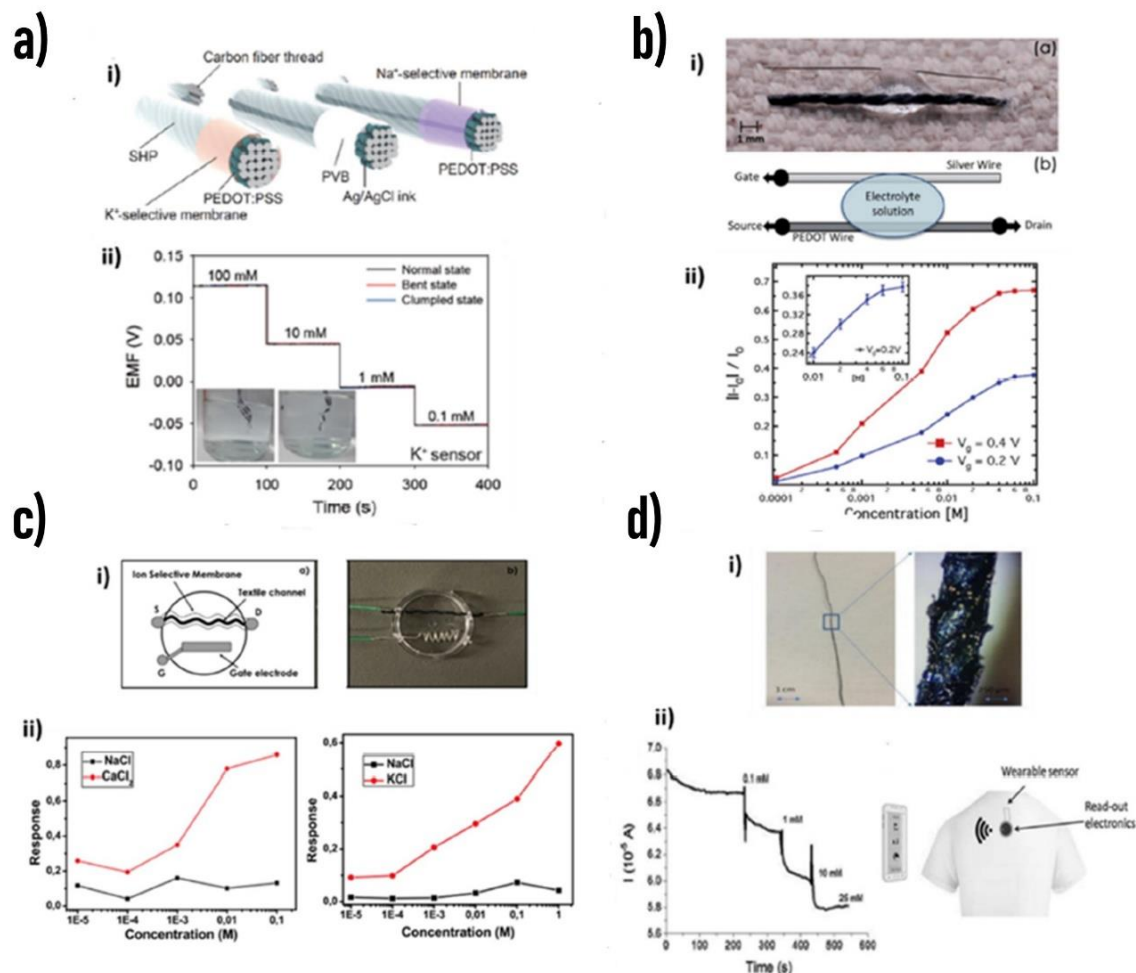


**Figure 1.7:** a.i) Structure of carbon fiber thread covered with PEDOT:PSS and ion selective membranes with a.ii) potential variation according to K<sup>+</sup> concentration changes.<sup>151</sup> b.i) Organic electrochemical transistor based on a cotton thread coated with conducting polymer PEDOT:PSS as channel and a silver wire as gate electrode. b.ii) current modulation after the variation of NaCl concentration in the electrolyte.<sup>152</sup> c.i) Textile OECT configuration with textile thread and metal wire immersed in electrolyte, and c.ii) detection of CaCl<sub>2</sub> and KCl concentration using NaCl as interfering agent.<sup>153</sup> d.i) Cotton thread functionalised by PEDOT:PSS and Ag/AgCl nanoparticles for two-terminals device architecture for Cl<sup>-</sup> concentration.<sup>84</sup>

### 1.3.4 Multi-sensing platforms

The capacity to analyse and measure critical health-related features non-invasively in real-time opens up new scenarios and alternatives to obtain selective, flexible, and highly sensitive multi-sensor platforms. Unconventional substrates such as fibres and fabrics have been used in numerous studies to manufacture flexible and unique wearable biosensors. Examples of textile platforms that combine the possibility to detect various analytes and biomarkers in human sweat with the well-known comfortability of textiles are reported here.

Exploiting the multiple advantages of CPs, together with carbon-based material and enzymes, it is possible to realize textile platforms that are able to monitor numerous parameters such as pH, electrolytes, and metabolites. Incorporating several sensors in the same textile-sensing apparatus makes it possible to perform simultaneous detections from a single sample.

Wang et al.<sup>154</sup> reported the first examples of a multi-analyte platform, exploiting a new approach to produce an electrochemical fabric from a single sensing yarn. Biologically relevant compounds, such as  $\text{Ca}^{2+}$ ,  $\text{Na}^+$ ,  $\text{K}^+$ , glucose or pH, were efficiently detected directly from human sweat exploiting a set of textile fibre sensors, which were stitched into the same fabric, as shown in Figure 1.8.a i. The sensors were set in a coaxial fashion, with the internal core of CNT fibres coated by the sensing layer: PEDOT:PSS or PANI. The electroplating technique was used to fabricate the pH-sensing fibre depositing PANI onto the external surface of CNTs. The glucose-sensitive yarn was made by a drop-casted layer of chitosan/SWCNTs/GOx deposited onto the CNTs and a layer of Prussian Blue (PB) was employed as a redox mediator to increase sensitivity. The ion-sensing fibres were produced utilizing the galvanostatic polymerisation of PEDOT:PSS film and an ion-selective ionophore drop-casted to work as a specific ion detector. Sodium, potassium, and calcium ion-sensing fibres were integrated into the multiplex-sensing electrochemical fabric to monitor the electrolyte concentration in liquids. Reference electrodes made by CNT fibres coated with Ag/PVB layer, were twisted together with pH and ions sensing fibres to allow the potentiometric yarn system to be weaved into a fabric.

The sensors were tested in the respective electrolyte solutions showing a linear and reproducible relationship between the acquired signal and the analyte concentration. Figures 1.9.a ii-iii report two examples of the fibre sensors' response.

He et al.<sup>155</sup> provided an important example of a soft and flexible silk fabric, nitrogen (N)-doped carbon textile (silkNCT), able to measure and detect the level of six different health-related biomarkers in human biofluids. SilkNCT fabric, shaped in circles, was used as the sensing substrate to achieve sensors-array to simultaneously and selectively detect  $\text{K}^+$  and  $\text{Na}^+$ , lactate, glucose, ascorbic acid (AA), and uric acid (UA). For the biomolecules, an amperometric approach was employed with the silkNCT pieces as working electrodes,

silkNCT part as a counter electrode, and Ag/AgCl ink-modified conductive tape as a reference. A two-electrode system was adopted for ion detection while enzyme-based amperometric sensors were employed for lactate and glucose detection. The silkNCT fabrics were coated with Pt Nanoparticles by electrochemical deposition and then functionalized by drop-casting with LOx and GOx. The ion sensors were fabricated exploiting ISM solutions drop-casted onto the corresponding electrode of silkNCT previously coated with PEDOT:PSS. Figure 1.8.b i reports the wearable and flexible patch, while Figures 1.9.b ii-iii show the responses to sodium and glucose, respectively. In all cases, a linear relationship between the electrical signal, either potentiometric or amperometric, and the analytes concentration has been found in the physiologically relevant range for humans.

Additionally, Terse-Thakoor et al.<sup>156</sup> reported a thread-based multiplex sensor patch for real-time sweat monitoring (Figure 1.8.c i). In particular, such textile threads can be conveniently integrated in fabric or adhesive patches to perform on-body and real-time monitoring of essential biomarkers present in human perspiration, such as lactate, sodium or ammonium ions, and pH. The flexible yarns were coated with Ag/AgCl and carbon ink to realize reference and working electrodes, respectively. Na<sup>+</sup> and NH<sub>4</sub><sup>+</sup> sensors were fabricated by dip-coating a carbon/polyethylene (PE) yarn in ISM cocktails and integrated with of a solid-state reference electrode for potentiometric measures. The pH sensing thread was fabricated by potentiostatic deposition of PANI onto the surface of a carbon-coated stainless-steel wire. The lactate sensor was produced with a Prussian Blue-coated PE thread and successively modified with LOx and chitosan by drop-casting. Figures 1.9.c ii-iii report lactate and sodium sensors' responses after separated evaluation in standard solutions. All of the thread-sensors showed good selectivity, reproducibility, wide dynamic range, and low hysteresis. Finally, the sensor patch was coupled with an electronic read-out board for a wireless data acquisition and data processing essential to achieve a wearable sweat monitor platform. Chapter 3 reports the results of the textile sensors developed for chloride concentration and pH.

### 1.3 Smart textiles

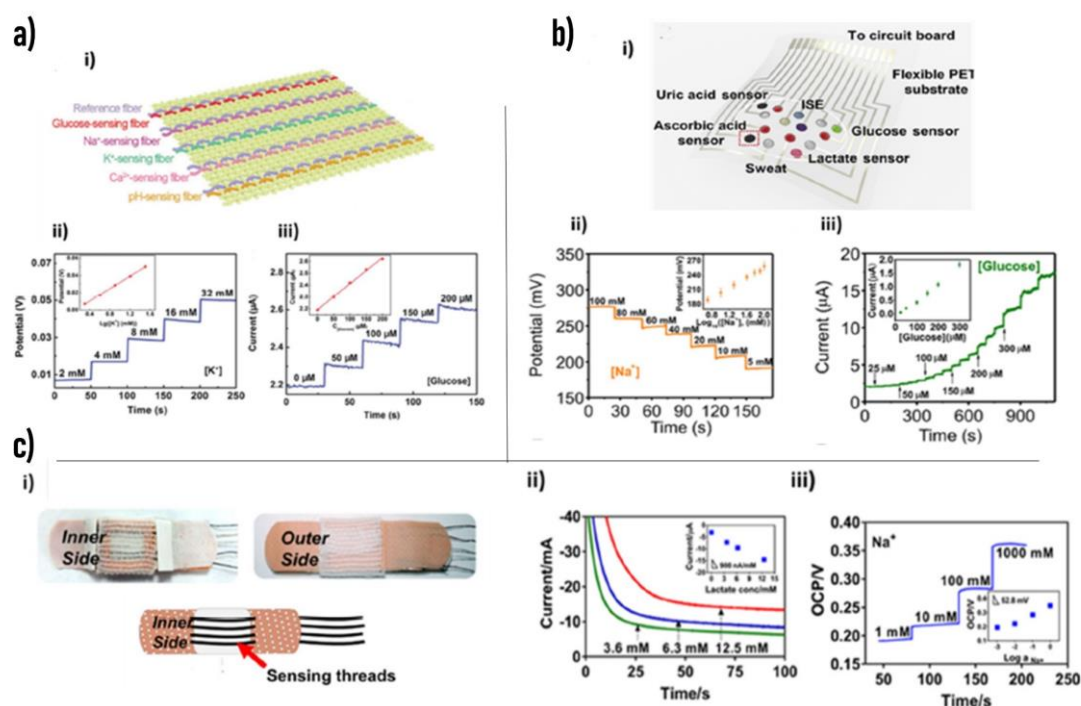


**Figure 1.8:** a.i) Schematic illustration for the fabrication of the electrochemical fabric by weaving sensing fibers, that are made by depositing active materials on CNT fiber substrates; a.ii) The open-circuit potential responses of the K<sup>+</sup> fibers, and a.iii) the chronoamperometric response of the glucose-sensing fiber in PBS solution<sup>154</sup>. b.i) Schematic illustration of multiplex electrochemical SilkNCT-based sensor array integrated in a patch for wearable sweat analysis. b.ii) OCP responses of the Na<sup>+</sup> sensor. b.iii) Chronoamperometry responses of the glucose sensor. Insets show the corresponding calibration plots of the sensors.<sup>155</sup> c.i) Photograph of the patch sensor prototype. c.ii) Chronoamperometric response of lactate and c.iii) potentiometric response of sodium using filter paper soaked in different concentration of respective analyte solution. Inset show the calibration plot of the respective thread sensors.<sup>156</sup>

### 1.3.5 Wound monitoring sensors

Wound exudate is another biofluid that is currently attracting interest in the field of wearable sensing technologies targeting the realisation of smart wound dressings. Upon integration of chemical sensors that are able to non-invasively monitor the wound site, these tools would dramatically impact the current treatment approaches with the potential to improve significantly the wound management and decrease the healing time. Wound healing is the essential physiological process by which damaged tissues repair themselves. If progression through the normal healing phases is delayed or incomplete, the wound enters a state of pathologic inflammation characterised by impaired healing and even eventual chronicity.<sup>157-159</sup> In order to adopt the most appropriate therapeutic strategy,

## 1.3 Smart textiles

---

wound management implicates both wound assessment and evaluation of the healing process. Traditional methods for wound assessment are often based on visual inspection or qualitative systems that may lead to subjective interpretations and biased results.<sup>160-162</sup> However, despite several steps having been taken towards the understanding of normal tissue repair stages and influence of physicochemical parameters, the evaluation of the healing process remains challenging due to its dynamism and complexity, as well as the lack of firmly established and quantitative tools for wound monitoring over time.

In this regard, the choice of the appropriate dressing is crucial to provide moisture, absorb excess wound fluid, and protect the wound site from further trauma, thus accelerating tissue regeneration.<sup>163-166</sup> Dressings can be tailored to the specific healing case and are classified as passive, interactive, advance, and bioactive.<sup>166</sup> However, the need to periodically view the wound site for evaluation of the wound status and therapy efficacy imposes a frequent dressing renewal that is often completed unnecessarily,<sup>167,168</sup> with a risk of disturbing or interrupting the wound healing process, provoking a physiological stress response or even causing a second injury.<sup>169</sup>

In this scenario, point-of-care (POC) and wearable sensing technologies are attracting growing interest with potential to revolutionise wound care practice. In particular, the utilisation of smart dressings comprising chemical and physical sensors, which are specially designed to detect relevant parameters of wound biochemistry, may provide quantitative and real-time information with both diagnostic and theranostic value, thus allowing timely intervention, improved wound management, and decreased healing time.<sup>157,167,168,170</sup> Among the assayable biomarkers, the crucial role of pH, exudate composition, moisture, and temperature in wound healing is largely documented, and are commonly identified as potential indicators of healing rate and wound bed state.<sup>171-174</sup> The exudate is the fluid secreted by the wound and has the function of a healing agent in delivering essential nutrients to the wound bed and providing the moist environment essential to the healing process.<sup>159,174</sup> Relevant exudate biomarkers in wound monitoring are reported in Table 1.2. In this application, monitoring the level of hydration can help to identify whether redressing is due, and assess if the optimal healing condition is present at the wound bed as too little moisture hinders tissue repair and fluid excess leads to skin maceration.<sup>175,176</sup> Due to the relevance of these parameters, the following paragraphs will present the latest example of wearable and textile pH and moisture wound sensors.

### 1.3.5.1 Textile pH wound sensors

One of the most straightforward methods for the preparation of halochromic textiles is electrospinning. pH-sensitive dyes can be directly loaded into the electrospinning solution to generate electrospun nanofibrous materials combining the high porosity and permeability of ultrathin polymer fibres with the pH colour responsiveness of the dye

### 1.3 Smart textiles

---

molecule. Interestingly, halochromic nanofibrous composites have been obtained by mixing hydrophobic and hydrophilic polymers,<sup>177</sup> as well as natural and synthetic polymers<sup>178</sup> leading to smart and highly tailored textiles. De Clerk's group has reported on electrospun nanofibrous blends where different pH dyes were covalently immobilised on a synthetic copolymer<sup>179</sup> and chitosan<sup>180</sup> showing remarkable stability after leaching, migration, and water fastness tests. Focusing on covalent immobilisation of dyes, Mohr's group has significantly contributed to the field by studying the functionalisation of cellulose-based textiles. In particular, covalent immobilisation of synthetic azo-dyes was demonstrated in textiles and non-wovens, including T-shirts, facecloths,<sup>181</sup> and cotton swabs,<sup>182</sup> achieving remarkable stability to washing cycles and sterilisation procedures. In addition, the use of fluorescent dyes has been reported for the preparation of halochromic textiles, including synthetic dyes for covalent functionalisation of cellulose dyes validated for *in vitro* and *in vivo* sensing incorporated in electrospun fibres,<sup>183</sup> and a fluorescent hydrogel coating for wound pads functionalisation.<sup>184</sup> Among optical textile sensors, real-time on-site pH monitoring using a smartphone camera has been demonstrated for halochromic hydrogel microfibrils obtained through microfluidic spinning<sup>185</sup> and halochromic polycaprolactone electrospun fibres. Finally, Kassal et al.<sup>186</sup> recently reported on a commercial wound dressing modified with a pH-sensitive hydrogel incorporating dye-functionalised cellulose particles and equipped with non-contact, flexible electronics enabling real-time monitoring using international wireless standards RFID and NFC.

**Table 1.2:** Relevant exudate biomarkers concentration important for wound monitoring.

Biomarker	Relevant range	Ref
pH	4 - 6 (healing) 7 - 9 (non-healing)	163,169,187,188
K <sup>+</sup> , Na <sup>+</sup> , Cl <sup>-</sup> urea, creatinine	Similar to serum	171,172
Glucose	1.1 - 5.9 mM (healing) 0.6 - 3.7 mM (non-healing)	172,184
Lactate	5.4 - 16.7 mM above ~10 mM (possible inflammation) above ~30 mM (possible infection)	172,189
Uric acid	221 - 751 $\mu$ M	172
Oxygen	5 -20 mm Hg (persistent inflammation)	163,190
Interleukin-6	1.3 pg/ $\mu$ g protein (inflammation)	163,191

Electrochemical textile sensors for pH detection in the wound environment mainly rely on potentiometric sensing. With the combination of lightweight, flexibility, and pH

sensing properties, the conjugated polymer polyaniline (PANI) currently stands out as the gold standard in the realisation of textile, solid-state potentiometric probes. The first work describing a potentiometric pH sensor incorporated into medical textile was reported by Guinovart et al.<sup>192</sup> Screen-printing and electrochemical deposition were used to fabricate reference and working electrodes directly on a commercial adhesive bandage, obtaining Nernstian sensitivity over the 4.35 – 8.00 pH range and excellent resiliency in bending tests. More recently, the electrochemical deposition of PANI has been utilised for the functionalisation of PEDOT:PSS/MWCNTs coated cotton fibres showing antibacterial properties and Nernstian response over a wide pH range (2 – 12) in complex media.<sup>193</sup> Alternative to electrodeposition, textiles can be modified by a simple dip-and-dry process using PANI commercial inks. In this regard, both cotton and polyester threads have been coated with PANI to act as working electrodes and the textile potentiometric systems have been sewn into commercial bandages. In particular, Punja et al. have constructed a pH sensing smart bandage for chronic wound monitoring, which integrates a C/PANI and Ag/AgCl coated cotton threads and is equipped with a wireless data acquisition and transmission setup.<sup>194</sup> Also based on C/PANI coated cotton threads, a smart wound dressing has been reported with an Arduino wireless interface and wireless data transmission that detects bacterial infections by monitoring the wound pH and allows the topical delivery of antibiotics to the wound bed.<sup>195</sup>

### 1.3.5.2 Textile moisture wound sensors

Wound moisture is a crucial parameter to the healing process. Indeed, a low moisture level can desiccate the wound, while too much will lead to its maceration.<sup>196</sup> Maintaining an optimal level of moisture allows wound healing in a shorter time. Commonly, clinicians observe the moisture status by removing the dressing, thus disturbing the healing process. A significant improvement would be the ability to monitor the humidity at the wound bed without removing the dressing and remove only when needed. Several examples of wearable technologies have been developed for this purpose. The first example of a smart bandage integrating a moisture sensor was presented by McColl et al. in 2007.<sup>197</sup> The proposed sensor consists of two Ag/AgCl electrodes insulated with silicon and inserted into a commercial dressing. Exploiting the ionic nature of exudate, they measured the impedance variation across the two electrodes with an AC measurement. They obtained a correlation between the change in impedance and moisture loss, thus enabling a direct comparison among different fabric properties on retained moisture. Following this first approach, various bandage fabrics have been developed with different absorption and retention properties in the last decade,<sup>163</sup> and in 2016, a commercial moisture sensor for wound care was developed called “Wound Sense”<sup>198</sup>. The sensor is based on two wires of silver chloride. The wound exudate is an electrolyte that affects the impedance between the

two electrodes. A low level of moisture generates a high impedance, while a wet wound is responsible for an impedance decrease. An intermediate value between two extremes indicates the optimal environment for the healing process. Other wearable humidity sensors are reported in the literature, and most are fabricated on fabrics due to their intrinsic hydrophilicity that helps to sample moisture.

A recent example of capacitive sensors is based on a polyamide fibre covered with copper threads.<sup>199</sup> Polymer works as dielectric material, and copper as the conductive electrode. The humidity alters the whole capacitance of the yarn shaped sensor showing a 3.5 s response and 4 s of recovery. The main advantage regards the connection of humidity sensors with a fibre inductor coil which allows a RFID monitoring. Another approach enabling wireless connection involves humidity colourimetric sensors.<sup>200</sup> Gong et al. reported a sensor based on structural colourimetric materials which change colour due to alteration of the periodic crystalline structure.

Despite the presence of several examples of textile humidity sensors in literature, only a few of them have been applied to wound monitoring. A relevant example is reported by Zhou et al.,<sup>52</sup> who fabricated fibres based on SWCNT dispersed in a matrix of PVA Poly(vinyl alcohol) (PVA) in which the presence of water molecules, through the presence of the polymer, modifies the conductive network of CNTs with a consequent increment in the fibres' resistivity. Chapter 4 presents a new example of textile sensors for pH level and moisture content using metal-oxide material, and PEDOT:PSS.

### 1.3.6 Physical sensors

The landscape of textile sensors has greatly increased within the last 10 years due to advanced academic and industry studies pursued in this field. The area of application, as already mentioned, is vast and covers a wide range of situations characterizing everyday life. This section reports some of the most relevant examples of physical textile sensors that are nearing actual commercialisation.

#### 1.3.6.1 Textile electrocardiogram electrodes

Early detection of human diseases and health monitoring are the principal aspects of healthcare system research.<sup>201</sup> The long-term monitoring of electrocardiographic (ECG) signals, by the acquisition of biopotentials, is the first stage for a more effective diagnostic procedure able to promptly detect arrhythmias or ischemia episodes. A biopotential is an electrical signal produced by various physiological activities and able to propagate through the whole human body acting as a volumetric conductor. The alteration of the cell resting potential, due to a transient and overwhelming influx and efflux of ions, is well known as the cell action potential. It is the source of the electric activity and when this activity is

correlated to the cell of the heart, the biosignal connected is known as ECG. Achieving an unobtrusive, long-term, and precise ECG biopotential monitoring through a full textile electrode can overcome the main limitation of the extensively used Ag/AgCl disposable electrodes, which require a gel electrolyte to correctly work. This aspect makes them less suitable for long-term recordings, which may result in uncomfortable side effects like irritation or skin rashes. In the case of dry ECG electrodes, the textile-based versions have attracted increased interest in order to create intelligent biomedical clothing to be utilised for elderly monitoring<sup>202</sup> to telehealth,<sup>203</sup> including sports activities<sup>203</sup> and infant monitoring.<sup>204</sup>

Figure 1.9.a shows the screen printing deposition technique of a high conductive silver ink on knitted cotton and polyester fabric for ECG monitoring.<sup>205</sup> The surface resistance, between 1.64  $\Omega$ /sq and 1.78  $\Omega$ /sq for the textile electrodes, reveals the feasibility of the electrodes to be used as an ECG electrode. Placing three electrodes around the wrist of a volunteer, the ECG signal collected shows a comparable waveform to those acquired with standard Ag/AgCl ECG electrodes and, increasing the tightness of the electrode against the skin, the response quality reaches the level of the standard ones. Additionally, even after ten washing cycles, the electrodes response was not affected. In the same vein, using silver as the main transduction material, Arquilla et al.<sup>206</sup> demonstrated the possibility to perform an electrocardiogram monitoring with sewn textile electrodes in a 3-lead, chest-mounted configuration. As reported in Figure 1.9.b, the electrodes are sewn with silver-coated thread in an overlapping zig zag pattern into a woven fabric. The sensors were tested by eight volunteers where categories tested include comfort, stretch, and washing validation, with a further comparison to standard electrodes. No statistically significant difference was found between the traditional and textile electrodes in terms of R peak detectability. Another ECG textile electrode, using a conductive polymer as transduction material, is presented in Figure 1.9.c in which a raw woven cotton fabric is soaked in a high-conductive PEDOT:PSS.<sup>43</sup> The biopotentials recording ability, in terms of both skin contact impedance and quality of ECG signal, at rest and during physical activity, has been tested on human volunteers. Dry electrodes show an acceptable quality signal at rest that greatly increases in wet (saline) electrodes presenting a stable and reproducible behaviour. These PEDOT:PSS electrodes represent an important milestone in wearable technology based on the fact that they can work without the electrolyte, providing a valuable interface with the skin due to its mixed electronic and ionic conductivity.

### 1.3.6.2 Textile pressure sensors

Within the last year, many efforts have been devoted to developing healthcare monitoring devices, sport garments, and accessories to reduce injuries,<sup>207</sup> increase the athlete's performance<sup>208</sup> and comfort,<sup>209</sup> or to improve safety in the workplace.<sup>210</sup> Data on body motion is among the most effective information in order to achieve a comprehensive overview of the user. In this context, the textile pressure sensors play a vital role in achieving the best functionality and sensing performance in a wearable device. During the last decade, the development of textile-based pressure sensors has been aided by their numerous advantages such as low cost, high flexibility, and ease of embedding sensors into wearables objects like garments or accessories. Depending on the specific area of application, the pressure sensors have to show a reasonable sensitivity in their application range. Those with high sensitivity in the low-pressure range (<10 kPa) allow touch detection in human-computer interfaces or to develop, for instance, artificial hands for handling objects. In the same way, sensors working in a high-pressure range (>10 kPa) can be used to monitor the body pressure distribution in standing or sitting positions.

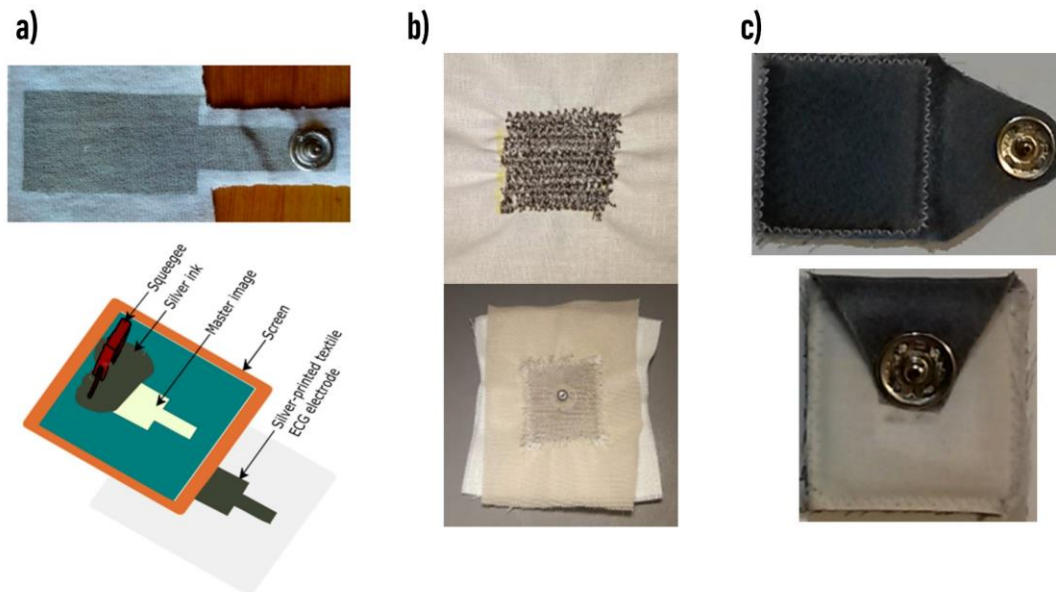


**Figure 1.9:** a) Screen printing deposition technique of high conductive silver ink on knitted cotton for ECG monitoring,<sup>205</sup> b) sewn textile electrodes in a 3-lead, chest-mounted configuration,<sup>206</sup> and c) ECG electrode based on conductive polymer.<sup>43</sup>

The main working principles of textile-based pressure sensors can be grouped into piezoresistive, capacitive and piezoelectric<sup>211-213</sup> sensors which produce an electric signal when an external mechanical force is applied. These sensors are usually made from fabrics knitted with conductive yarns or coated with conductive polymers.<sup>214</sup>

On the one hand, the piezoresistive sensor changes its shape when compressed, resulting in a change in the contact area between the conductive materials, which leads in a resistance variation. Compared with other wearable pressure sensors, the ones based on the piezoresistance effect have been widely studied due to their simple structure and manufacturing process. Since these sensors consume less power, they have a wide range of applications from medical<sup>215</sup> to sports.<sup>216</sup> On the other hand, the capacitive textile pressure sensor displays the change in capacitance when a mechanical stress is applied. These sensors are based on the principle of parallel plate capacitors with a dielectric material sandwiched between plates. A change in capacitance is observed when an external force varies the distance between the plates. Usually, the textile capacitive-based pressure sensors have high sensitivity and wide dynamic range with the further possibility of enhancing their performance, tuning the surface area, thickness, or the intrinsic properties of the dielectric material. Table 1.3 shows a collection of some recent textile pressure sensors based on piezoresistive and capacitive effect with their major outlining characteristics. Furthermore, piezoelectric pressure sensors represent another important class in the pressure monitoring due to their flexibility, easy electrical signal acquisition, and low-cost fabrication. The piezoelectric sensitive materials rely on the physical piezoelectric effect based on the material polarisation able to generate a potential difference when subjected to a mechanical deformation. The material's positive and negative charges' separation due to the external stress is responsible for the potential difference, and its value determines the magnitude of the pressure applied. Recently, several examples of piezoelectric pressure sensors have been developed based on carbon or composite materials for different types of applications. For instance, Yang et al. integrated<sup>217</sup> polydopamine film modified with barium titanate ( $\text{BaTiO}_3$ ) and polyvinylidene fluoride (PVDF) in shoe insole to detect the impact from running or walking. In addition, piezoelectric material can also be used to implement self-powered and multi-functional wearable sensors by electrospinning of PVDF nanofibre with excellent sensing, mechanical, and thermal properties to monitor the biomechanical movements in a human finger, elbow, or foot.<sup>218</sup> In the same vein, Li et al.<sup>219</sup> proposed MWCNTs coating on PVDF nanofibre to improve fibre's conductivity and mechanical properties. They created nanofibres with high bending stability, washability, and breathability to monitor human motion, including tactile stimulation, finger joint, and wrist bending. Exploiting MWCNTs conductive filler ability, Kim et al.<sup>220</sup> enhanced the electrical conductivity, dielectric, and piezoelectric properties of ceramic-epoxy nanocomposite films to obtain an increase in the sensitivity and in the output voltage of the piezoelectric pressure sensors

## 1.3 Smart textiles

**Table 1.3:** Recent examples of textile pressure sensors based on resistive and capacitive principles.

Mechanism	Fabric	Material	Fabrication	Range	Sensitivity	Application	Ref
Resistive	polyester	Thiolated Graphene Oxide	Multilayer stacked structure	0 - 200 kPa	8.36 kPa <sup>-1</sup> (0-8 kPa) 0.028 kPa <sup>-1</sup> (30-200 kPa)	wrist pulses, body motion, voice recognition	221
	Polypropylene fibres, spandex-knitted fabric	Silver-coated fabric	Thermal bonding of fabrics	0 - 8 kPa	3.5 - 1.5 kPa <sup>-1</sup>	Sleeping quality monitoring	222
	Cotton Aluminium Card paper	Stainless steel threads	Sewing	0 - 14 kPa	0.06 kPa <sup>-1</sup>	Breathing rate Muscle activity	223
	Polyester	Graphene films	Dip coating	0 - 800 kPa	0.012 kPa <sup>-1</sup>	In-shoe wireless plantar pressure system	224
Capacitive	Kevlar fibre	SBS Ag NPs PDMS	Dip coating	0 - 20 kPa	0.21 kPa <sup>-1</sup> < 2kPa 0.064 kPa <sup>-1</sup> > 2kPa	Into gloves for human-machine interfaces	225
	Twaron fibre	SBS Ag NPs PDMS	Dip coating	0 - 50 kPa	0.278 kPa <sup>-1</sup> 0-2kPa 0.0186 kPa <sup>-1</sup> 15-50 kPa	Touch panels in robot arms.	226
	Woven fabric	Nickel Copper PDMS	Electroplating	>200 kPa	0.023 kPa <sup>-1</sup>	Finger grabbing Plantar Pressure	227

### 1.3.7 Ionizing radiation sensors

The flexible, comfortable, and breathable nature of fabrics makes these substrates ideal candidates for developing large-area wearable devices in direct contact with the human body. As previously stated, such textile wearable sensors can be placed directly onto textile substrates,<sup>228-230</sup> as witnessed by electronic textile devices that can change their electrical and/or mechanical properties due to an external stimulus. These textile devices are designed to measure biopotential,<sup>70,231</sup> temperature,<sup>232</sup> movements such as pressure<sup>233</sup> or strain,<sup>231</sup> sweat content,<sup>83,154</sup> or can serve as energy harvesting (thermoelectrics,<sup>234,235</sup> triboelectrics,<sup>236</sup> biofuel cells<sup>237</sup>) and storage platforms.<sup>76,238</sup>

Despite the high number of different textile sensors created thus far, textile ionizing radiation detectors have not yet been proposed, mostly due to the incompatibility between conventional materials for radiation sensing and fabric substrates. In Chapter 5 of this thesis, a novel approach for the implementation of a wearable and flexible X-ray detector implanted onto silk-satin and cotton fabrics will be reported. However, the scope of this introductory paragraph is to offer an overview on the latest results about the x-ray detection, spanning from materials to new sensors' concept.

The development of innovative functional materials and low-cost technologies for the detection of ionizing radiations has become an urgent need in the last years due to the relevant increase in the use of ionizing radiation in many aspects of modern society, from medical applications to civil security. In particular, flexible and wearable innovative dosimeters are highly requested in hazardous environments, such as for personnel and patients in medical therapy and for space mission crew. Commercially available personal dosimeters and diagnostic detectors, based on inorganic materials (e.g. silicon-based solid-state devices for dosimeters, a-Si, a-Se, or poly-CZT for large-area flat panels) are heavy, bulky, rigid and uncomfortable to wear. Furthermore, they are difficult to implement in large, pixelated matrices by means of low-cost and low-tech fabrication techniques.

In the last years, a new generation of X-ray detectors has been explored, based on organic semiconductors<sup>239-241</sup> and perovskites<sup>242-244</sup>, two classes of materials that allow for liquid phase deposition methods, enabling an easy device scalability to large areas and the implementation on unconventional flexible substrates, such as thin plastic foils<sup>245,246</sup> and fabrics.<sup>247</sup> The possibility of conforming ionizing radiation detectors and dosimeters onto a non-flat object is one of the primary desired features needed, for example, when detectors have to be integrated inside specific probes during radiation therapy,<sup>248</sup> or in easy-wearable objects (e.g., bracelets, belts) and for potential vignetting limitations. Recently, Zhao et al. proposed a highly sensitive and flexible direct X-ray detector based on a porous nylon membrane with metal halide perovskite loaded by infiltration method. A perovskite-filled membrane such as this has good stability and high sensitivity to X-rays, comparable to those of perovskite single crystals. Excellent results were also presented by Demchyshyn et al.<sup>249</sup> with an ultra-flexible, conformable, and lightweight X-ray detector based on a photodiode architecture, able to stably operate in passive mode (at 0 V) with a sensitivity of  $9.3 \mu\text{C Gy}^{-1} \text{cm}^{-2}$  and a limit of detection of  $0.58 \mu\text{G s}^{-1}$ . Despite these remarkable detection performances, both these flexible devices, together with others in recent literature,<sup>250,251</sup> envisage complex multi-layered structures and fabrication techniques requiring several steps and often oxygen-free environment. In addition, perovskite nanocrystals, polycrystals, or thin films have been proposed for textile photovoltaic applications, such as fibre-shaped perovskite solar cells around Ti wires,<sup>252</sup> carbon nanotubes,<sup>253</sup> or stainless steel wires<sup>254</sup> that may be woven into electronic textile for energy harvesting applications. Perovskite solar cells adopting planar heterojunction configuration were integrated onto textile by Jung et al.,<sup>247</sup>

and Lam et al.,<sup>255</sup> but both examples use the fabric only as a support for the device bottom-up fabrication. Considering the lack of such technology in the broad area of textile sensing, a new solution for intrinsic textile X-ray detector exploiting perovskite nanocrystals will be presented, paving the way for an entirely new class of wearable and textile sensors. Chapter 5 shows the results of the textile pressure and X-ray sensors realized directly integrating the sensing materials into the fabrics.

## 1.4 Energy harvesting

In the past decade, the field of wearable electronics have triggered enormous attention as a novel, revolutionary, and forefront technology for the future of portable electronic devices. Health or medical assistance, together with fitness applications, represent the main fields meeting the highest request for wearable biosensors. The recent trend in personalized healthcare and the great interest to overcome the physical limits in sport disciplines, are leading fast advancements in wearable sensor technology. Such devices usually require energy over extended periods of time for multiparameter detection, complex data processing, and real-time wireless data transmission. Producing high-performance wearable electronic devices always requires the judicious integration of powerful energy sources onto conformal platforms. Despite the accelerated growth of wearable devices, the progress of wearable energy devices has not been fast enough to cope with this rapidly growing power demand of wearable sensing devices. Most of these devices have relied upon rigid and bulky batteries to provide power. Therefore, flexible and stretchable energy-harvesting and energy-storage batteries or supercapacitors have been developed to provide stable and efficient performance for various uses.<sup>256-258</sup> In addition to producing energy from sunlight or from body motion, new alternative energy sources based on thermoelectric materials or epiderma biofuel cells have stimulated considerable interest.

Textile-based energy harvesting and storage devices have been recently developed, representing an astonishing demonstration for a self-powered wearable and textile platform. Different physical and chemical principles can be used in order to create such technology. The following paragraphs present the novel result regarding biofuel cells, and thermoelectric-based devices.

### 1.4.1 Textile biofuel cells

The use of BFCs for producing electric power using body fluids of animals was envisioned first in the 1970's in connection with the use of blood glucose as biofuel.<sup>259</sup> During this half century, enzymatic fuel cells have evolved from large and rigid compartment cells to membrane-less systems, miniaturized implantable devices, and now,

## 1.4 Energy harvesting

---

into flexible wearable energy harvesters. The design and operation of an enzymatic BFC are similar to that of a conventional fuel cell, consisting of the anode and the cathode, as shown in Figure 1.10.a. Initially, the fuel (e.g., glucose) undergoes an enzyme-catalysed oxidation at the bioanode, generating electrons that flow through an external circuit and reach the cathode. Next, when electrons reach the cathode, an oxidant—usually oxygen, present in natural fluids—receives those electrons, leading to a net electrical current.

The Wang's Laboratory of Nanobioelectronics recently developed highly stretchable textile-based BFCs that extract the electrical power from perspiration for probing the sensing events of sweat metabolites (Figure 1.10.b i).<sup>237</sup> The bioanode of the membrane-less BFC was functionalized with a single enzyme (e.g., LOx) and NQ as a redox mediator for the biocatalytic oxidation of biofuels and increase of power density, respectively. Alternatively, as reported on Figure 1.10.b ii, the cathode was realised by a silver oxide/silver ( $\text{Ag}_2\text{O}/\text{Ag}$ ) redox couple electrode. Upon adding a biofuel (e.g., lactate), the biochemical fuel is enzymatically oxidized on the anode and releases electrons. On the cathode compartment, silver oxide accepts those electrons to complete the power circuit. With this approach, they could obtain a printable electronic array on stretchable fabrics with a power density linearly dependent to the lactate concentration in the sweat. The open circuit voltage of the cell is assessed to be 0.46 V. The maximum power density of  $250 \mu\text{W cm}^{-2}$  was obtained in the presence of 20 mM lactate (Figure 1.10.b iii). Such a power density is sufficient to power electronic devices. Moreover, epidermal BFC can generate and deliver power only in the presence of sweat, and since its rate and lactate biofuel level can be variable, this limits a constant power output. To address this issue, an effective storage method based on textile supercapacitor was presented by Lv et al.<sup>76</sup> They used a screen printing approach to fabricate the textile-based SC with a serpentine-shape based on a  $\text{MnO}_2$ -CNT/CNT/PEDOT:PSS ink, reported in (Figure 1.10.c i - ii). The rectangular shape of the Cyclic Voltammetry test, shown in Figure 1.10.c iii, suggests the excellent capacitive behaviour of the SC which has an energy density and power density of  $17.5 \mu\text{W h cm}^{-2}$  and  $0.4 \text{ mW cm}^{-2}$ , respectively. These novel results have a strong relevance and present the possibility to supply textile wearables that require a low operational voltage, paving the way to a possible integration between the textile biosensors and the textile-based energy harvesting and storage.

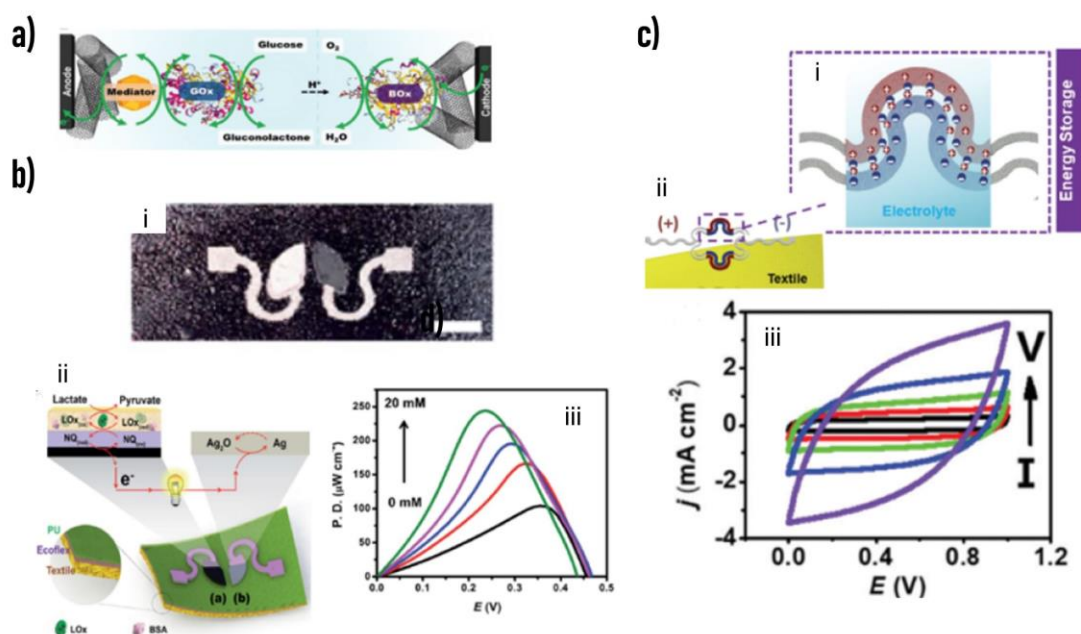


**Figure 1.10:** a) A scheme of the composition and operation of a typical glucose/oxygen BFC consisting of a glucose oxidase (GOx)-mediated bioanode and bilirubin oxidase (BOx) biocathode. b.i) Photograph of the stretchable BFC printed on textile; b.ii): Components of lactate BFC and the redox reaction occur on the anode and cathode; b.iii) Power density vs potential plots of the stretchable nylon-spandex textile-based lactate BFC at varying lactate concentrations (0, 5, 10, 15, and 20 mM).<sup>237</sup> c. i-ii) Schematic illustration of the energy storage mechanism in textile SC; c.iii) CV curves of the SC at different scan rates (2, 5, 10, 20 and 50  $\text{mV s}^{-1}$ ).<sup>76</sup>

### 1.4.2 Textile thermoelectric devices

Thermoelectric energy conversion has emerged as a promising green technology due to its attractive, efficient, and environmentally friendly way to recover energy from industrial waste heat or natural heat. It has numerous advantages, such as solid-state operation, lack of moving parts or chemical reactions, absence of gas emission, silence and durability. Furthermore, a thermoelectric device is versatile since it can be used in the opposite mode, acting as a cooling or heating device when an electric current is applied to the circuit. Exploiting the thermoelectric principle to harvest energy by converting thermal energy, especially from human body heat, has attracted many researchers to investigate this field as an electrical energy source for wearable electronics. There have been many attempts to integrate thermoelectric generators into textiles ranging from non-flexible to flexible materials and through different methods. The thermoelectric generator (TEG) offers a potential application in the direct conversion of temperature difference into electrical power

## 1.4 Energy harvesting

---

via the Seebeck effect. The Seebeck coefficient is an essential indicator of thermoelectric conversion efficiency and is the most widely measured feature from thermoelectric materials. Furthermore, TE materials' performance is expressed as a dimensionless thermoelectric figure of merit,  $Z = S^2\sigma T / k$ , where  $S$  is the Seebeck coefficient,  $\sigma$  is the electrical conductivity,  $k$  is the thermal conductivity, and  $T$  is the absolute temperature. Organic and inorganic materials, such as hybrid or composite materials, have been considered a competitive candidate for solution-based thermoelectric materials due to their high thermoelectric performance and easy manufacturing process. In addition, the individual thermoelectric properties of both organic and inorganic materials can be controlled to realise the optimum thermoelectric properties. This is an attractive and fundamental feature since materials for thermoelectric applications must have a significant Seebeck coefficient as well as high electrical conductivity.

In this framework, the textile thermoelectric generator represents a new class of energy harvesting system that is attracting a lot of attention due to its flexibility, intrinsic wearability, comfortability, and promising performance. However, several efforts are still needed to achieve an output power high enough to drive a wearable device. In this view, a novel and outstanding idea proposed first by Hardianto et al.<sup>234,260</sup> is to realise a fibre-like thermopile directly on a textile yarn that can be directly sewn into cloth exploiting the temperature difference between the body and the surrounding environment. With the out-of-plane configuration, the textile-based thermoelectric generator will be physically seen as a standard fabric, and can be placed directly onto the skin to convert human body heat into electricity. However, it is challenging to fabricate this kind of thermopile pattern on a piece of fabric. For example, metal wires have the disadvantage of being stiff, and therefore, a multifilament yarn with better-bending properties and flexibility is required. A possible solution to alleviate the problem is to use a conductive yarn that is alternately metal-coated at specific areas forming a thermopile. Hardianto et al. reported the first result of a fibre-based thermopile's output power realised with a carbon yarn periodically coated with nickel.<sup>46</sup>

Semiconducting materials show remarkable thermoelectric properties and are widely utilised to fabricate thermoelectric devices on fabric substrates. Kim et al.<sup>261-263</sup> and Lu et al.<sup>264</sup> used the well-know Bismuth Telluride and Antimony Tellurite, n-type and p-type thermoelectric material respectively, to create thermopile on textile substrate, such as silk or glass fabric. Connecting up to 20 couples of n- and p- type material, a Seebeck coefficient of 0.98 mV K<sup>-1</sup> has been extracted. Similarly, organic conductive polymers represent another class of materials for producing thermoelectric device. Polymers such as polyacetylene,<sup>265,266</sup> PEDOT:PSS,<sup>267-271</sup> polyaniline,<sup>268</sup> polypyrrole,<sup>272,273</sup> and poly(3-hexylthiophene),<sup>274-276</sup> have been used in this framework. Du et al.<sup>277</sup> used PEDOT:PSS mixed with dimethyl sulfoxide (DMSO) to dip-coat strips of polyester fabric. The strips were fixed on the untreated polyester fabric with an interval of 5 - 6 mm using silver paint and

## 1.4 Energy harvesting

---

the Seebeck coefficient of the PEDOT:PSS coated polyester fabric was measured to be 15.3 – 16.3  $\mu\text{V K}^{-1}$  at 300 K.

In addition, CNTs represent another example for developing a flexible thermoelectric generator (f-TEG). Choi et al.<sup>278</sup> doped CNT with polyethylenimine and  $\text{FeCl}_3$  to obtain n- and p-type elements for a yarn-based thermoelectric generator. The p-doped coat was on one region and the n-doped was on the successive part of the yarn, and this structure is periodically reproduced. The f-TEG consisted of 60 p-n pairs with a generated output voltage of 0.15 V  $\text{g}^{-1}$  and 1.2 V  $\text{g}^{-1}$  at a temperature difference of 5 K and 40 K, respectively. Another carbon-based thermoelectric generator was reported by Ito et al.<sup>279</sup> They made the thermoelectric generator from carbon nanotube composite threads. Coating the CNT yarn with polyethylene glycol (PEG) exhibits a p-type Seebeck coefficient, while doping the CNT threads with 1-butyl-3-methylimidazolium hexafluorophosphate ([BMIM]PF<sub>6</sub>) results in an n-type Seebeck value. The stitched n-type/p-type thread on fabric reached a thermo-voltage of around 60  $\mu\text{V K}^{-1}$  per cell. Finally, Ryan et al.<sup>280</sup> reported a thermoelectric generator from organic materials covering a PET thread with multiwalled carbon nanotube and Poly(N-vinylpyrrolidone) (PVP) to fabricate the n-type element, and PEDOT:PSS dyed silk thread for the p-type element. The textile-based thermoelectric generator was fabricated by the embroidery technique and could generate a thermo-voltage of 26  $\mu\text{V K}^{-1}$  per couple and total output maximum power of 7 nW with a modulus of 38 elements.

All these cases represent a valid reason to fabricate a new generation of energy-harvesting devices based on the thermoelectric effect, however, further research and studies are needed to improve the outcome performance. Chapter 6 of this thesis reports a proof-of-concept of a new textile-based thermoelectric generator that integrate various fabrication techniques, materials, and device geometry for potential use as a flexible, non-invasive, and efficient wearable energy-scavenging device.

# Chapter 2

## Materials and Methods

This Chapter presents and discusses the details of the materials and the experimental technique employed for device fabrication and characterisation.. In the first section are reported the textile materials used as device substrates both in yarns and in fabrics structure. Section 2 gives an overview of all the chemicals and compounds used to develop the desired sensors with a special focus on the conducting polymers PEDOT:PSS that it is always present in the proposed devices. Section 3 discuss the fabrication methods and the characterisation procedures to realise and study the textile-based sensors. Due to the high number of developed devices present in this thesis, the descriptions here proposed do not pretend to be completely exhaustive, and for further and more specific details, the reader should refer to the corresponding paragraph.

### 2.1 Textile materials

The textile sensors developed in this work are mainly realised on unconventional substrate made of textile single-threads and yarns, or on textile fabrics. From its beginning in mid-18<sup>th</sup> century up to now, the textile industry has made great strides both in the production and in quality domain, allowing the realisation of different kind of products. Exploiting the well-established knowledge in this field, its world-wide diffusion and the intrinsic importance in our society, the textile now have the possibility to make another step

forward realising what is called smart textile. This new way of conceiving fabrics and exploiting their properties represents a further growing possibility for a sector that has been stable for a long time. The new sensors presented in this thesis to realise wearable devices are intrinsically dependent on textile substrates. The following paragraphs provide a description of yarns and fabrics that represent the most common ways to use textile materials in textile electronics.

### 2.1.1 Yarns

A yarn is a strand composed of fibres, filaments (individual fibres of extreme length), or other materials, either natural or synthetic, suitable for use in the construction of interlaced fabrics, such as woven or knitted types. The properties of the yarn employed greatly influence the appearance, texture, and performance of the completed fabric. The yarns can be classified according to the number of strands and can be describe as single, plied or cord.

Single, or one-ply, yarns are single strands composed of fibres held together by at least a small amount of twist; or of filaments grouped together either with or without twist; or of single synthetic filaments extruded in sufficient thickness for use alone as yarn (monofilaments) (see Figure 2.1.a). Single yarns of the spun type, composed of many short fibres, require twist to hold them together and may be made with either S-twist or Z-twist (Figure 2.1.b).

Plied, or ply, yarns are composed of two or more single yarns twisted together. Two-ply yarn, for example, is composed of two single strands (Figure 2.1.c); three-ply yarn is composed of three single strands. In making ply yarns from spun strands, the individual strands are usually each twisted in one direction and are then combined and twisted in the opposite direction. When both the single strands and the final ply yarns are twisted in the same direction, the fibre is firmer, producing harder texture and reducing flexibility. Ply yarns provide strength for heavy industrial fabrics but are also used for delicate-looking sheer fabrics.

Cord yarns are produced by twisting ply yarns together, with the final twist usually applied in the opposite direction of the ply twist (Figure 2.1.d). Cable cords may follow an SZS form, with S-twisted singles made into Z-twisted plies that are then combined with an S-twist, or may follow a ZSZ form.

Although the yarns are the *macro* component in fabric structure, fibres are the building blocks of textile materials and there is a strong correlation between the fibre properties and properties of resultant textile products. A single yarn is usually made by hundreds of single fibres that represent the smaller part in an extended fabric. The following paragraphs show an overview on the main fibres, both natural and synthetic, used in this work.

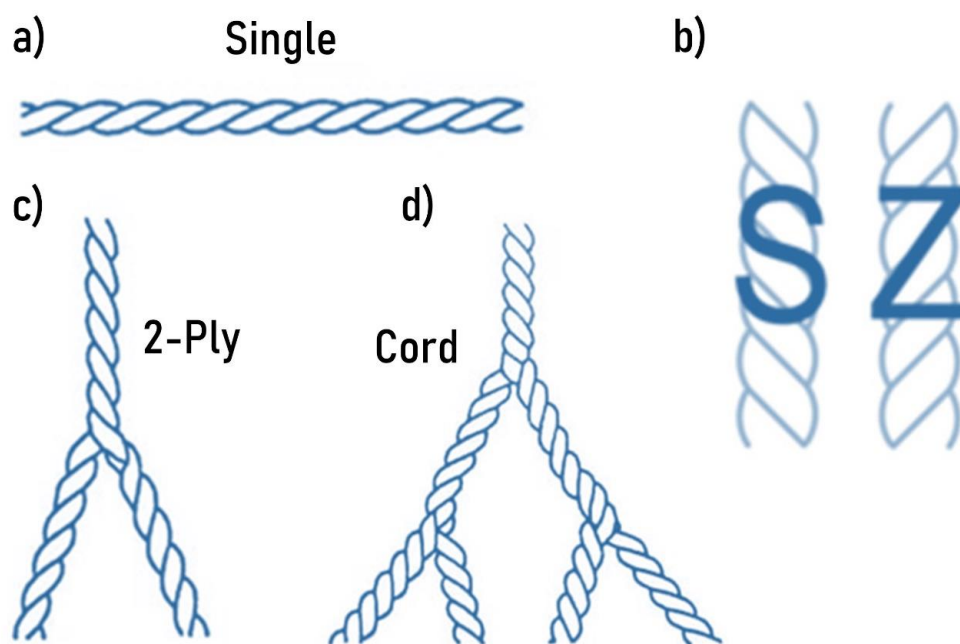


**Figure 2.1:** Schematic examples of a) single (one-ply) yarn composed by twisted fibres, b) S and Z twisted type to better hold the fibres together, c) two-ply yarn composed by two single strands, and d) cord yarn which requires several twisting steps.

### 2.1.1.1 Cotton and silk fibres

Cotton is the most widely used natural fibre, with over 25 million tons produced annually. The combination of strength and good absorbency makes it the most used material for textile production and applications. Cotton is a linear cellulose polymer consisting of glucose ( $C_6H_{12}O_6$ ) linked together to form the cellulose chain molecule. The structural formula of the cellulose chain molecule is shown in Figure 2.2.a with the repeating unit called cellobiose.<sup>281</sup> The number of glucose monomers  $C_6H_{12}O_6$  in the cellulose chain is called the degree of the polymerisation and in cotton it is about 5000.<sup>282</sup> Less than 10% of the weight of the raw fibres consist of waxes, protein, pectate and minerals (see Figure 2.2.b). Cotton fibres have a multilayer structure which consist of a primary wall, a secondary wall and a lumen. The outer surface layer (cuticle) of a cotton fibre has a major influence on fibre properties, processing and use, and it is composed by most of the non-cellulosic materials. Figure 2.2.c shows the cross-section and the schematic structure of a dry cotton fibre.

## 2.1 Textile materials

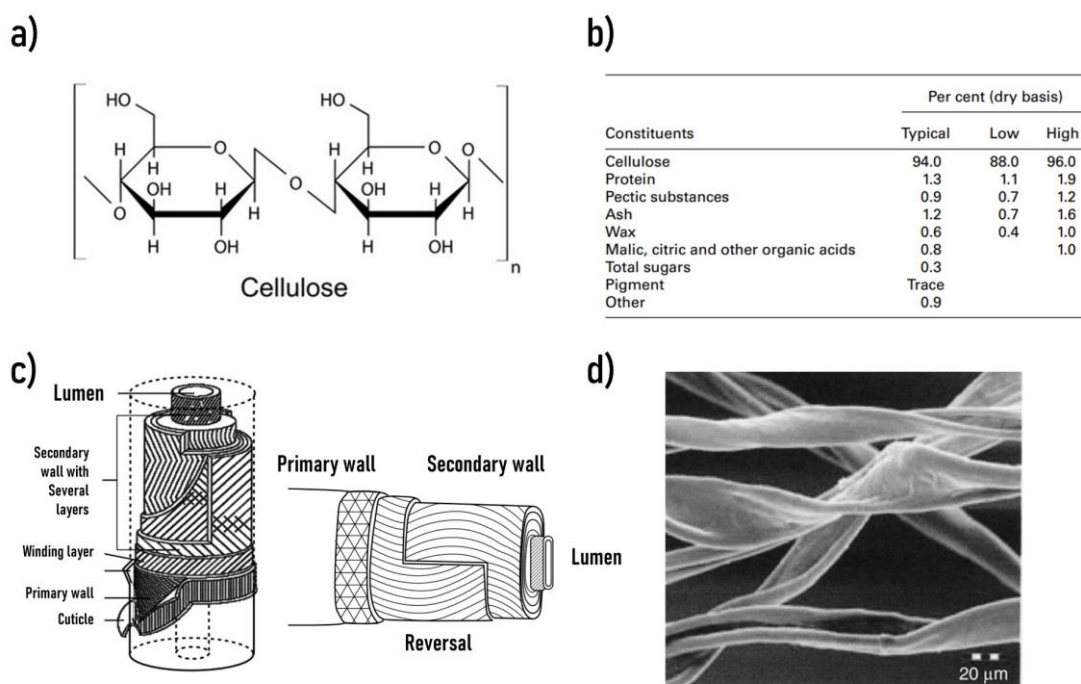


**Figure 2.2:** a) Structural formula of the cellulose chain molecule. b) Specific composition, c) cross-section with schematic structure,<sup>283</sup> and d) SEM image of cotton fibres.<sup>284</sup>

Cotton fibres are moderately strong fibres, with a tenacity of 3 - 5 gm/den and an average fibre diameter of 12.2  $\mu\text{m}$ . It is one of the few fibres which gains strength when wet because the polymer chains in the amorphous regions temporarily improve their alignment. This effect increases the number of hydrogen bonds, with an approximate 5% increase in fibre tenacity. The hygroscopic nature of cotton fibre is due to countless polar OH groups present in its polymers and water molecule can only enter the polymer system through its amorphous regions. The cotton fibres appear as collapsed and twisted tubes that do not stress easily. They have an elongation at break of just 5 - 10 % but show excellent resistance to heat degradation as well as high thermal conductivity. They begin to turn yellow after several hours at 120°C and decomposition happens at 150°C. In this thesis, the cotton are heated at temperatures low enough to avoid this effect. Figure 2.2.d shows a SEM images of typical cotton fibres.

Silk fibres represent the oldest natural fibres known to human produced by different worms to build their cocoons and webs. Silk fibres spun out from silkworm cocoons and they consist of two different proteins: fibroin in the inner layer and sericin in the outer layer. Each raw silk thread has a lengthwise striation, consisting of two fibroin filaments of 10-14  $\mu\text{m}$  each embedded in sericin (Figure 2.3.a-b). The average chemical composition in weight of silk fibres is: 75-83% of fibroin, 17-25% of sericin, about 1.5% of waxes, and 1.0% of other

## 2.1 Textile materials

compounds. They show an irregular triangular cross-section (Figure 2.3.c) and a smooth longitudinal surface (Figure 2.3.d).

Silk fibres are biodegradable and highly crystalline with a well-aligned structure displaying unusual mechanical properties: strength, extensible, and mechanically compressible. It is known that they also have higher tensile strength than glass fibre or synthetic organic fibres, good elasticity and excellent resilience. They also display interesting thermal and electromagnetic responses, particularly in the ultraviolet (UV) range and form crystalline phases related to processing. Silk fibres usually are stable up to 140 °C, and the thermal decomposition starts at a temperature greater than 150 °C. The densities of silk fibres are in the range of 1320–1400 kg m<sup>-3</sup>.

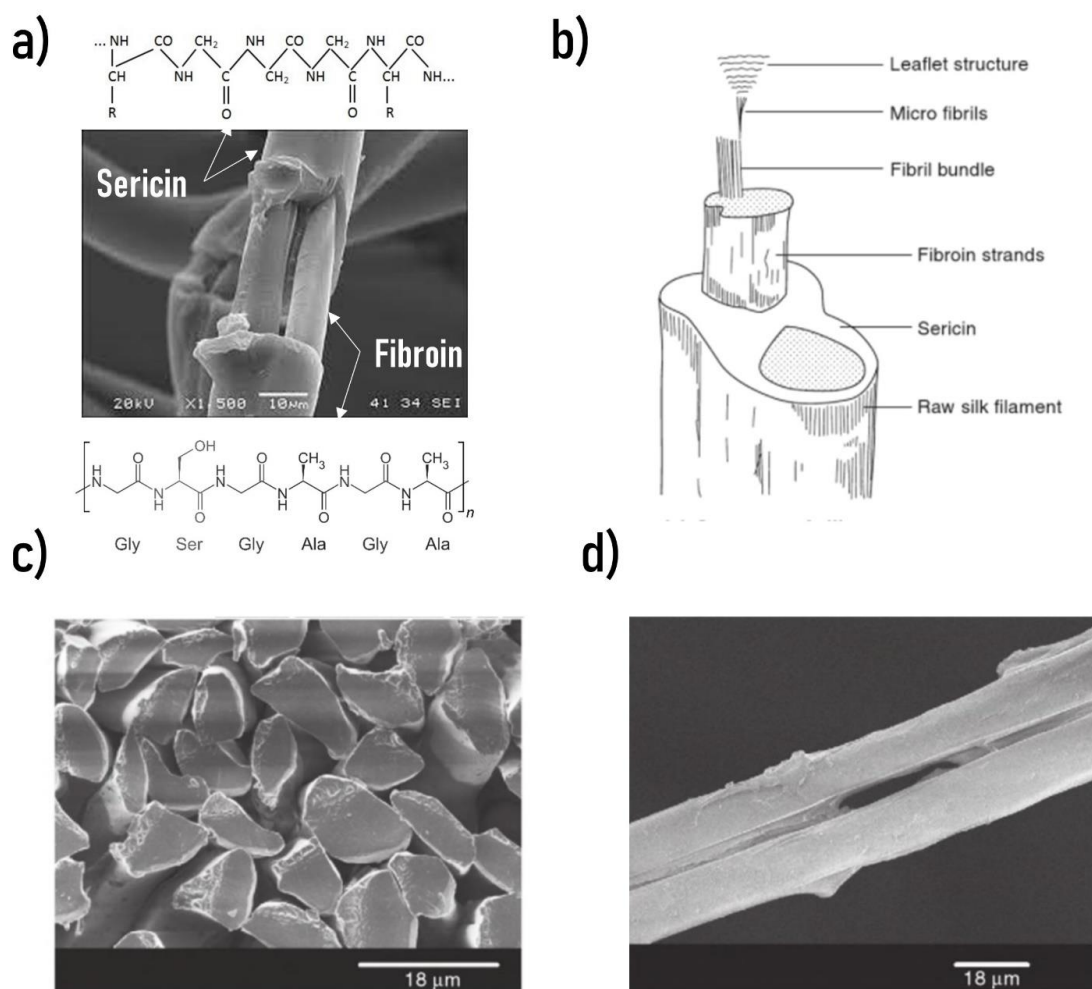


**Figure 2.3:** a) SEM image of silk fibre highlighting the presence of Sericin and Fibroin proteins. b) Schematic cross section of a silk fibre. SEM images of c) irregular triangular cross-section and d) smooth longitudinal surface.<sup>285</sup>

## 2.1 Textile materials

---

Another type of natural occurring fibre used in this thesis is the Rayon fibre. It is composed by the pure cellulose present in cotton or in the cell walls of woody plants. The main characteristic of these fibres is that they are made from cellulose that has been reformed or regenerated, and consequently, Rayon is a manufactured regenerated cellulosic fibre based on wood pulp and cotton lint. Mostly, it's referred with the commercial name of Viscose. As many spinned fibres, variation during the fabrication can provide a wide variety of fibres with different properties. These fibres have a serrated round shape with smooth surface and lose 30–50% of their strength when they are wet. Even direct exposure to sunlight causes loss of strength due to the degradation of cellulose chains. Elongation-at-break is seen to decrease with an increase in the degree of crystallinity and orientation. Rayon fibres are biodegradable, renewable and hygroscopic. Dry and wet tenacity extend over a range depending on the degree of polymerisation and crystallinity, and the higher the crystallinity and orientation of rayon, the lower is the drop in tenacity upon wetting. They exhibit a fair abrasion resistance and lose strength above 149°C and start decomposition between 177 to 204°C. Finally, Rayon fibres are very resistant to bases, while hot dilute acid, bleaches and mildew attack them.

### 2.1.1.2 Synthetic fibres

The presence of synthetic fibres in the textile industry has a stable and leading impact due to the large, fast, low-cost and easy manufacture. Since 1920s, the polymer synthesis, represent one of the biggest achievement in the chemical research. The attention was first settled on several polyvinyl and polyvinylidene fibres but the major breakthrough in synthetic polymer fibres was the synthesis of both polyesters and polyamides. The introduction of melt-spinning has made giant strides in polymer synthesis and up to now, polyester and polyamides represent the most used, versatile and convenient synthetic fibres. Among the polycondensation polymers, polyester is the most important and widely used today. However, this term refers to a huge family of different polymers widely used as packaging materials, film, fibre, filament, fabrics and in photographic applications. The most commercially important thermoplastic and linear aromatic polyester is poly(ethylene terephthalate) and it is the most produced textile fibre, used in a wide variety of applications. Figure 2.4.a reports the chemical structure. The polyester fibres, in particular PETs, have good resistance to weak alkalies and only a moderate resistance to strong alkalies while both weak and strong acid at room temperature do not affect the fibres. In addition, they are generally resistant to organic solvent, synthetic detergents, abrasion as well as sunlight. The moisture regain of polyester fibres is low and they do not have wicking ability, so the moisture can be carried on the surface of the fibres without absorption. These fibres have a density greater than polyamide fibres and lower than rayon. The external surface is usually smoother than the one of natural fabric like cotton (Figure 2.4.b). The melting point

## 2.1 Textile materials

---

of polyester is close to that of polyamide, ranging from 250 to 300°C. Polyester fibres shrink from flame and melt, leaving a hard black residue. The fabric burns with a strong, pungent odour. Heat setting of polyester fibres, not only stabilises size and shape but also enhances wrinkle resistance of the fibres. It is worth to note that a wide range of polyester fibres properties depends on the methods of manufacture like tensile strength and initial Young's modulus. However, poly(ethylene terephthalate) shows nonlinear and time-dependent elastic behaviour. Creep occurs under load with a subsequent delay in recovery on the removal of the load, but compared to that of other melt-spun fibres, creep is small.

Polyamide refers to family of polymers called linear polyamides made from petroleum. The generic name polyamide fibre has the same meaning as nylon fibre first synthesised by DuPont Company in 1931. The polyamide fibres are usually produced from linear aliphatic polyamides, like polycapromide and polyhexamethylene adipamide. The two main polyamide fibres are, indeed, Nylon 6 and Nylon 6,6 which have different performance characteristics and chemical structure (Figure 2.4.c). Furthermore, Nylon 6,6 has highly dense structure whereas polyamide 6 is an open molecular structure as shown in Figure 2.4.e. Figure 2.4.d shows the nylon fibres surface without ruffles and with low roughness compared to cotton fibres. These fibres are characterised by high tensile strength, excellent elastic recovery behaviour, and great resistance to wear and impact. Further, nylons have large extensions to break combined with relatively high strength and thus result in high work of rupture. They are stable to the action on many chemical reagents and biochemical agents, and they have affinity to many dyes. Melting of nylon fibres occur in a range of temperatures. The melting range of nylon 6 is in the temperature range of 215° - 228°C, while the nylon 6,6 melting range is between 250° and 265°C.

These fibres dissolve in concentrated mineral acid, chloroform, phenol and cresol. The polyamide fibres present a low hygroscopicity, poor resistance to thermal oxidation and the action of light, and they easily tend to become electrically charged. Due to good elastic recovery, low initial modulus, excellent abrasion resistance and high resistance to rupture, nylon has been used in a very large number of applications both in apparel and industrial sectors. Light weight and sheer garments are produced from nylon 6 and nylon 66, where low modulus, high strength and good abrasion resistance are of particular importance. Nylon filaments are used in ladies' stockings, socks, technical textiles, carpets, safety belts in cars, hoses, light weight canvas for luggage, tires and ropes just to name a few. Figure 2.4.f resumes the main features of polyester and polyamide fibres relevant in textile applications.

## 2.1 Textile materials

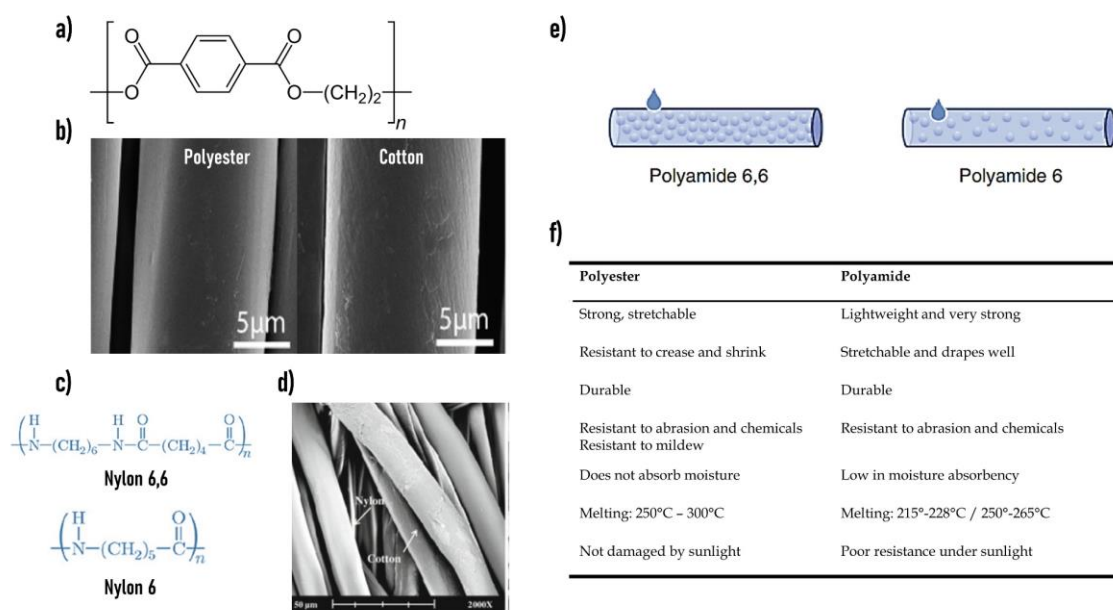


**Figure 2.4:** a) Chemical structure of PET. b) Comparison between external surface of polyester and cotton fibres.<sup>286</sup> c) Chemical structure of Nylon fibre and d) SEM image to comparison the surface roughness with cotton fibres.<sup>287</sup> e) Comparison between molecular structure density of Polyamide 6.6 and Polyamide 6.<sup>288</sup> f) Main features of polyester and polyamide fibres.

### 2.1.2 Fabrics

The natural and synthetic fibres presented above represent the main based material for the fabric used in this work. Examples of textile single-thread sensors will be presented in the following chapter but a lot of attention will be dedicated even to textile sensors based on cotton, polyester, silk, polyamide and rayon extended fabrics. The fabric construction involves the conversion of yarns, and sometimes fibres, into a fabric having characteristics determined by the materials and methods employed. Most fabrics are now realised by some method of interlacing, such as weaving or knitting. Weaving includes the basic weaves, plain, twill, and satin while knitted fabrics include weft types and warp types.

#### 2.1.2.1 Woven fabrics

Woven fabrics are made of yarns interlaced in a regular order called a binding system, or weave. Usually, two components, called warp and weft are combined together in a regular, repetitive manner and, generally, they overlap forming right angles. Woven fabrics are normally much longer in one direction than the other. The lengthwise threads are called the warp, and the other threads, which are combined with the warp and lie width

## 2.1 Textile materials

---

wise, are called the weft. The warp and weft are held in position not by rigid bonding but by friction set up at the areas where they make contact. It is noteworthy that weaving is a completely separated process from warp and weft knitting that use only one set of elements. In addition, there are geometrical differences, one of the most significant being the small angles through which the components of a woven structure are, in general, bent, in contrast with the components of other structures. The binding system, or weave, however, is the basic factor in determining the character of a woven fabric. The three basic systems are plain or tabby, twill, and satin.

Plain weave is the simplest and most common of all weaves and requires only two harnesses and has two warp and weft yarns in each weave unit. To produce it, the warp yarns are held parallel under tension while a crosswise weft yarn is shot over and under alternate warps across the width of the web. The weave unit is completed at the end of the second row, when the weft has been inserted over and under the opposite set of warps, thus locking the previous weft in place as shown in Figure 2.5.a.

Twill weave is distinguished by diagonal lines (Figure 2.5.b). The simplest twill is that created by the weft crossing over two warp yarns, then under one, the sequence being repeated in each succeeding shot, but stepped over, one warp either to the left or right. Twills with more warps than wefts floating on the fabric's face are called warp faced; those with wefts predominating, weft faced.

Satin weave does not have the regular step in each successive weft that is characteristic of twills. Thus, there is no strong diagonal line, and the fabric is smooth faced, with an unbroken surface made up of long floating warp yarns (see Figure 2.5.c). A true satin must have at least five warp and weft yarns in each complete weave repeat and thus requires at least five harnesses. Most satin fabrics are made of smooth, lightly twisted yarns that heighten the effect of light unbroken by visible crosswise bindings. Examples of complex weaves fabrics include multiple plane, inlaid, Jacquard, pile, dobby and gauze weaves.

### 2.1.2.2 Knitted fabrics

Knitted fabrics are constructed by interlocking a series of loops made from one or more yarns, with each row of loops caught into the preceding row. There are two main ways in which yarns can be subjected to the needles for fabric formation: weft and warp knitting.

Weft knitting is accomplished by a loops formed in a horizontal manner by adjacent needles. However, in weft knitting, needles placed next to each other horizontally knit one after another in sequence to produce one row of loops from the same yarn. The Figure 2.5.d shows loops arranged in rows and columns. The horizontal loops produced by adjacent needle during the same knitting cycle is known as a course. The course count measures by the number of courses per linear unit. The vertical loops produced by the same needle

## 2.1 Textile materials

knitting at successive knitting cycles is referred to as wale, and also the wale count is measured by the number of wales per linear length. The standard machines used for weft knitting are the circular knitting machine, that create a tube of fabric in a spiral configuration around a cylinder, and the bed flat machine, with all the needles placed on a flat bed.

Figure 2.5.e shows the structure of a warp knitting fabric. It is accomplished by forming loops in vertical direction. The yarn is intermeshed vertically with two wales. With warp knitting, individual needles knit simultaneously across the width of the machine and the loops are formed by needle knitting a series of warp yarns fed vertically and parallel to the direction of the fabric formation. Compared to woven fabric, knitted fabrics are much more elastic. They can stretch, depending on their material and knitting pattern, up to 500 percent of their original size.

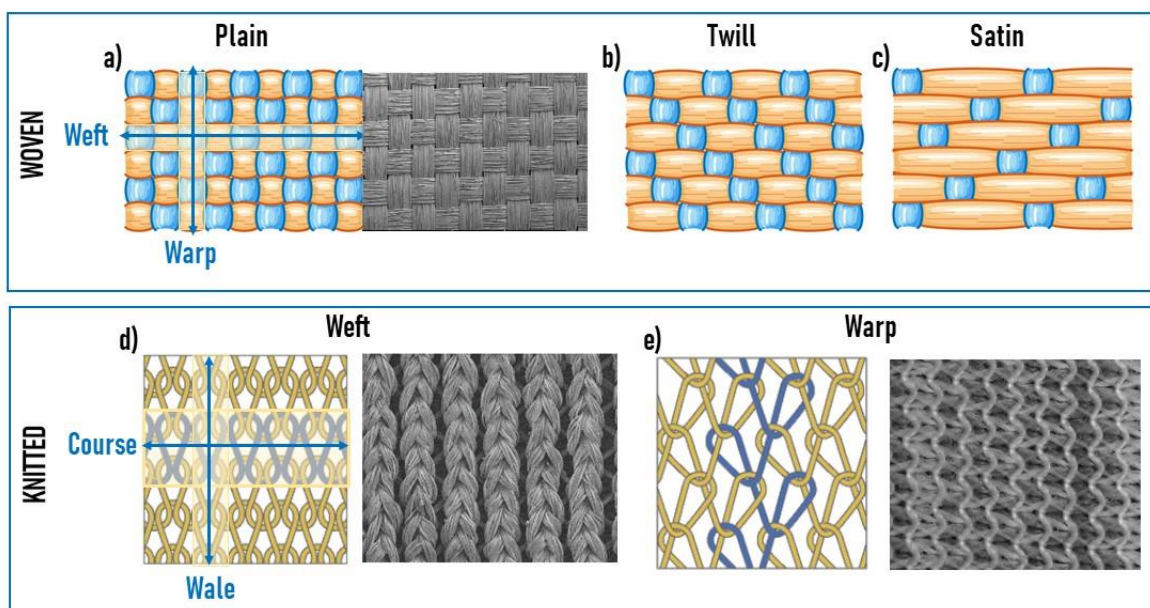


**Figure 2.5:** Different examples of woven (a -c) and knitted (e-f) structure. a) Plain woven structure with a SEM image that shows the simple interlacing of the yarns. Woven b) twill and c) satin structures. Structure and SEM images of knitted d) weft and e) warp structures.

For comparison, woven fabrics typically deform only along their bias direction – for example at  $45^\circ$  to the warp and weft directions – and only by a small amount; only exploiting stretchable material such as elastan, can lead to elastic woven fabric. Knitted fabrics are used in this thesis as deformable and stretchable substrate for textile pressure sensors.

### 2.1.2.3 Special fabrics

Net, or mesh fabric, are an open fabric having geometrically shaped, open meshes, and it is realised with meshes ranging from fine to large. There are a few different versions of mesh fabric, but this type of fabric is typified by its lightweight and permeable texture. Unlike most types of fabric, which feature closely-woven textures, mesh is woven loosely, which results in thousands of tiny holes being present in each mesh fabric. They are now made by knitting machines, and popular types include tulle, made with hexagonal-shaped mesh (Figure 2.6.a) and fishnet, a coarse type with knots in four corners forming the mesh.

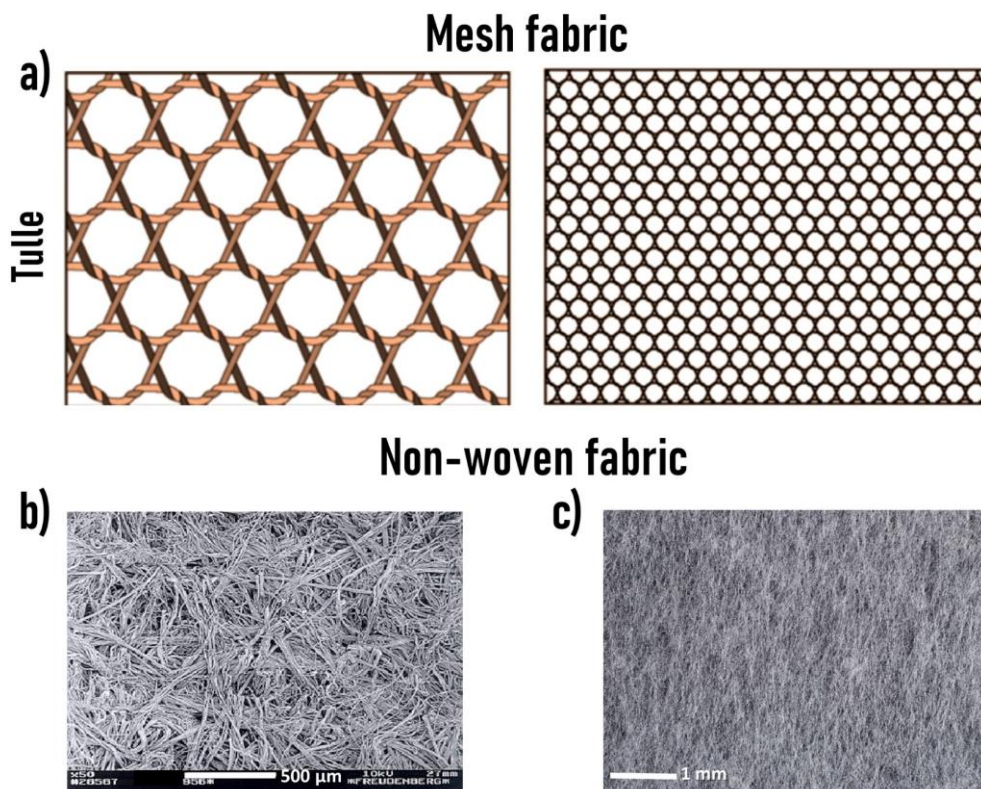


**Figure 2.6:** a) Tulle mesh fabric structure made with hexagonal-shaped fishnet. b) SEM image that shows the random pattern in non-woven fabric,<sup>289</sup> and c) an optical photograph of a medical dressing realized by non-woven structure.

In nonwoven fabric, individual fibres are bound together not by weaving or knitting but by other chemical, thermal or mechanical means by varying the processes and the raw material used. These carefully engineered fabric can create some pretty remarkable advantages. The term is used in the textile manufacturing industry to denote fabrics, such as felt, which are neither woven nor knitted. Non-wovens are flexible, porous, products consisting of one or more fibre layers. The separate fibres may either be preferentially oriented in one direction or may be deposited in a random manner, and they are mainly planar structures. SEM image in Figure 2.6.b shows the random pattern of fibres that

compose the fabric. Nonwovens may be classified as either disposable or durable goods. Disposable nonwovens include such one-time use products as diapers, household wipes, disposable protective clothing and medical dressings (Figure 2.6.c), as the one used in this thesis.

## 2.2 Materials

This section reports a summary about the main chemical materials used in this work highlighting their physical-chemical properties and main features. Chemical agents and compounds employed for fabrication and characterisation that do not participate into the sensing itself, will be describe later as needed.

### 2.2.1 Conductive polymers

Conducting polymers (also called synthetic metals or conjugated polymers) are organic polymers, typically containing a linear backbone with repeated units of conjugated monomers, with highly reversible redox behaviour and properties resembling both metal and plastic ones. Polyaniline (PANI), polypyrrole (PPy), poly(ethylenediothiophene) (PEDOT), polythiophene (PTh) and polyfuran (PFu) represent the most common conductive polymers. The great interest and popularity gained in wearable electronic field in last years is also due to the powerfull electrical and optical features owned by this class of materials. Among the different properties, one of the most remarkable is their ability to be nanostructurally tailored depending on the required application, using innovative synthetic transformations or deposition techniques. Other interesting features are their biocompatibility and “soft” nature, in contrast with the “hard” one for standard inorganic material for electronic applications, easy and low temperature processability, the possibility to control chemical structures and film morphology, together with their tunable conductivity and the corrosion resistance.<sup>290-292</sup> These features enable conducting polymers to have a better mechanical compatibility and structural tunability with unconventional substrate, as fabrics, an easy and wide range control over physical or chemical properties, using surface functionalisations and doping techniques. This resulted in the replacement of traditional inorganic electronic materials with conducting polymers, having a variety of remediation, medical and biomedical applications<sup>293,294</sup> in which they are used as biosensors.<sup>295-297</sup> Table 2.1 summarises the main properties of conducting meaningful applications in a broad range of fields, including energy storage, environmental polymers.

## 2.2 Materials

**Table 2.1:** Main properties of conducting polymers.

Properties	Description
<b>Facile chemical and film morphology modification</b>	Alterations of the $\pi$ -conjugated backbone modify the electronic, mechanical or biological properties. Biomolecules into the backbone improve bio-compatibility
<b>Doping</b>	Either p-type or n-type doped, enabling to achieve a broad range of conductivity. Oxidation/Reduction leads to charge carrier formation, upon charge transfer, in the form of positive or negative polarons, bipolarons or soliton in the CP. p-doping is more common for CPs.
<b>Charges transportation</b>	Organic materials support hole (p-type) or electron (n-type) transport at RT, or both of them. They can transport also ions, which is allowed by the large space between molecules in their structure.
<b>Low Temperature processability</b>	Low temperature processing, exploiting the weak interactions that keep molecular blocks together. Mild heating or solvent addition can overcome these forces, thus allowing the deposition from vapour or solution on different selected substrates.
<b>Swelling</b>	CPs can undergo swelling/de-swelling, according to changing in their redox state. Electrochemical driven expansion/reduction of CP dimensions can lead to a reversible or irreversible swelling.
<b>Reversible Electrochemical Oxidation/Reduction</b>	This electrochemical doping/de-doping capability is based on electrochemical-driven ion uptaking and can be used to affect its electronic conductivity and, subsequently, film morphology and microstructure, together with optical and mechanical properties.
<b>Bulky interaction</b>	CPs can bulky interact with the environment, since not only the surface, but the whole volume of the polymer film is involved in the ion exchange with the electrolyte.

### 2.2.1.1 Doping in conjugated polymers

A primary dopant for a conducting polymer is a substance, a relatively small quantity of which drastically changes the electronic, optical, magnetic and structural properties of the polymer and is accompanied by a large increase in conductivity. This can be brought about by a redox agent that either oxidises (p doping) or reduces (n doping) the polymer chain. Conjugated polymers are composed by organic molecules and there are various approaches to introduce charges into these materials and to radically change their electronic properties. As summarised in Figure 2.7, reversible charge injection by doping can be accomplished in different manners:<sup>298</sup>

- **chemical doping** by charge transfer: it is obtained with a chemical reaction - oxidation or reduction. With this process a semiconducting material becomes conductive thanks to the creation of new electronic states. Both electron donating (n-type) and electron accepting (p-type) dopants, respectively reducing agents and oxidants, have been used to introduce charges into conjugated polymers and render them conductive. In practice, most organic conductors are doped oxidatively to give p-type materials.
- **electrochemical doping**: it attempts to obtain intermediate doping levels using an electrolytic solution (that is a substance that produces an electrically conducting solution when dissolved in a polar solvent, such as water) in which a thin film is dipped. The electrolytic solution contains free ions and with the application of an electric field the electrons could diffuse into the polymer structure. The doping level is determined by the voltage between the conducting polymer and the counter electrode (which is used to close the current circuit in the electrochemical cell); at electrochemical equilibrium the doping level is precisely defined by that voltage. Thus, doping at any level can be achieved by setting the electrochemical cell at a fixed applied voltage and simply waiting as long as necessary for the system to come to electrochemical equilibrium.
- **photo-doping**: the polymer is locally oxidised and (nearby) reduced by photoabsorption and charge separation (electron-hole pair creation and separation into free carriers).

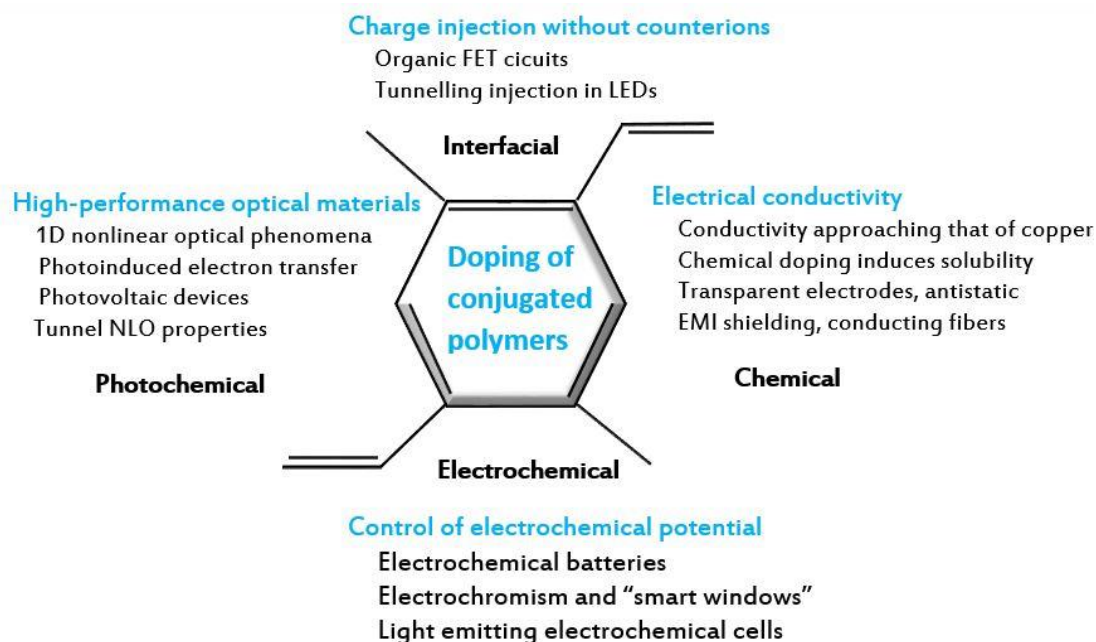


Figure 2.7: Different types of doping methods in conjugated polymers.

### 2.2.2 PEDOT:PSS

Since in the early 1980s, the Bayer's Central Research Department attempts to stabilise polyacetylene in its highly doped form and to achieve processability ultimately failed, several projects were started on polyheterocycles, like polypyrrole, poly(3-alkylthiophenes),<sup>299</sup> etc, but without much success. It was only in the second half of 1980s that the synthesis of 3,4-ethylenedioxythiophene (EDOT) monomer led to a technical breakthrough, particularly due to its polymerised form poly(3,4-ethylenedioxythiophene) (PEDOT), which exhibited high conductivity and stability in the doped state (the only state available at the time).<sup>300</sup> PEDOT is an intrinsically conductive conjugated polymer, formed by a chain of its EDOT monomers, that are visible in Figure 2.8.a, and it can be prepared using standard oxidative chemical or electrochemical polymerisation methods. Several electrolyte can be used for EDOT polymerisation, including polyelectrolytes, as proved by Yamato and co-workers,<sup>301-303</sup> that can lead to the formation of PEDOT:PSS.

#### 2.2.2.1 Features of EDOT monomer

EDOT chemistry started in 1930s, after the synthesis of the corresponding 2,5-dicarboxylic acid esters.<sup>304</sup> Gogte et al.<sup>305</sup>, introduced the actual synthesis method for pure distilled EDOT monomer that appear a nearly colorless liquid with unpleasant odor. A small change to pale yellow is possible after long storage time (especially in daylight), without significantly affecting its purity. On the contrary, air and light exposure makes it turn dark due to partial oxidation.<sup>306</sup> The main physical EDOT properties are reported in Figure 2.8.b. The purification procedure for EDOT is vacuum distillation. Moreover, the melting point at 10.5 °C permits a very efficient low temperature recrystallisation from solvents like methanol, ethanol and their mixtures. Regarding the chemical properties, EDOT main reactions are its oxidation, that typically result in conductive oligomeric to polymeric materials when charge balancing is possible, i.e. when there are doping counterions (anions). These reactions are at the basis of the one needed to realise PEDOT:PSS.<sup>307</sup>

#### 2.2.2.2 Polymerisation of PEDOT

The synthesis of PEDOT derivatives can be divided into three main types of polymerisation reactions:<sup>306</sup> oxidative chemical polymerisation of EDOT-based monomers,<sup>308,309</sup> transition metal-mediated coupling of dihalo derivatives of EDOT<sup>310,311</sup> and electrochemical polymerisation of EDOT derivatives. The latter method is based on electrochemical oxidation of the electron-rich EDOT-based monomers and requires low amounts of monomer, short polymerisation times and can give electrode-supported or free-standing films, according to the required application/purpose. For EDOT, this method

results in a highly transmissive sky-blue and doped PEDOT film at the anode.<sup>312,313</sup> Several electrolyte can be used for EDOT polymerisation, including polyelectrolytes, as proved by Wernet and co-workers<sup>301-303</sup>, and even aqueous micellar medium.<sup>314-316</sup>

Even though PEDOT is an insoluble polymer, it exhibits some very interesting properties that justify its wide-spread use in industry and academic research.<sup>317</sup> PEDOT can be reversibly and repeatedly doped and undoped. A PEDOT thin film is almost transparent and light blue in its oxidised state, while it can be turned into opaque and dark blue upon switching it to the neutral state. The color variation according to its doped state may be used as a suitable property for optical applications, such as electrochromic displays.<sup>318</sup> It has good chemical and thermal stability: thermal studies proved that a continuous degradation only occurs over 150 °C and a complete decomposition above 390 °C. Moreover, electrical conducting properties seem to be unaltered after aging in environmental conditions. PEDOT low band gap (1.5-1.6 eV) is thought to originate from the influence of the electron-donor ethylene dioxy groups on the energies of the frontier levels of the  $\pi$  system.<sup>319</sup> Thus, PEDOT presents high electrical conductivity (up to 550 S/cm) in the doped state. Synthesised PEDOT films have low redox potential and excellent stability in the doped state, when compared to other conducting polymers.

### 2.2.2.3 PEDOT:PSS dispersion and properties

One of the main reason for PEDOT success as conducting polymer is its availability in aqueous dispersion. Although PEDOT is an insoluble polymer, combined with poly(styrenesulfonic acid) (PSS) as a counterion, it creates a polyelectrolyte complex (PEC), that can be prepared in stable aqueous dispersions, produced on industrial scale and used through several deposition techniques. PEDOT:PSS chemical structure is reported in Figure 2.8.c: it must be noted that PEDOT chains are much shorter compared to PSS ones (Figure 2.8a): the molecular weight of PEDOT molecules is between 1000 and 2500 Da (for 6 to 18 repeating units), resembling an oligomer nature of these segments,<sup>321</sup> while PSS average molecular weight is usually 70 kDa at least.

Polyelectrolyte complexes are typically formed mixing aqueous solutions of polyanions and polycations, resulting in a compound that can be either water-soluble or insoluble, depending on the parameters.<sup>300</sup> PSS was the first polyelectrolyte to be used with PEDOT in 1990, creating a water-soluble PEC and remaining an industrial standard ever since. PSS is commercially available with different molecular weights and polydispersities. It is soluble in water and forms durable and transparent films.<sup>306</sup> As PEDOT counterion, PSS is always used in excess, thus as host polyelectrolyte (HPE). In standard PEDOT:PSS dispersions the molar ratio between thiophene groups and sulfonic acid groups is in the range of 1:1.9 to 1:15.2 (weight ratio range 1:2.5 up to 1:20). Since there is one charge every

## 2.2 Materials

three to four thiophene rings,<sup>322-324</sup> the charge excess of PSS is between 6-fold and 46-fold.<sup>300</sup> According to the delocalisation of positive charges in PEDOT, the weak polar groups and the different spacing of PEDOT charges compared to PSS ones, there is no molecular or supramolecular order in PEDOT:PSS, but only a random interaction between polymer chains giving the so-called pancake-like structure, as shown in Figure 2.8.d.<sup>325</sup> PSS is thus used in combination with PEDOT for two main reasons: first, it is used as counterion, balancing the positive PEDOT charges; second, it is used to keep PEDOT segments dispersed in water owing to its high hydrophilicity.<sup>321</sup> Indeed, water is the solvent chosen for PEDOT:PSS synthesis, due to the fact that it is inert to most oxidation or reducing agents, it is highly polar and a good PSS solvent. Even though EDOT presents poor solubility in water (at 20 °C only 0.21 g of EDOT can be dissolved in 100mL of water), it increases with PSS presence and with increasing temperature. As shown in Figure 2.8.d, PEDOT:PSS final structure is a cross-linked and highly swollen polymer gel, composed of gel particles with 90-95% of water content, with the maximum solid content that grows with decreasing PEDOT to PSS ratio. This ratio also influences other physical parameters of the polymeric film, such as bulk conductivity, sheet resistance and surface roughness. For example, higher relative concentrations of PSS give less conductive and flatter films because of a size reduction of PEDOT particles in the PEDOT:PSS dispersion.<sup>326,327</sup>

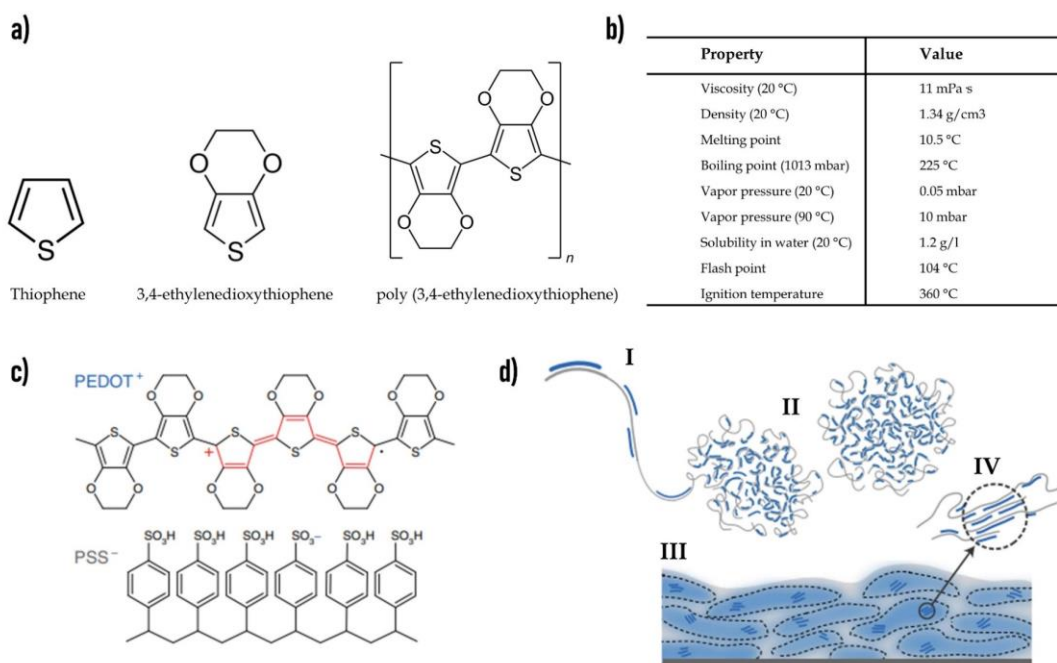


**Figure 2.8:** a) Chemical structure of EDOT and PEDOT with b) the main physical and chemical properties.<sup>306</sup> c) Representation of PEDOT:PSS chemical structure. d) PEDOT:PSS microstructure with PSS in grey and PEDOT in blue: I) synthesis onto PSS template; II) colloidal gel particle formation in dispersion; III) PEDOT:PSS films with PEDOT-PSS-rich (blue) and PSS-rich (grey) phases; IV) aggregates/crystallites supporting enhanced electronic transport.<sup>325,328</sup>

## 2.2 Materials

---

This is in accordance with the observation that films with smaller particles present lower conductivities.<sup>321</sup> The average particle size in a PEDOT:PSS dispersion is typically in the range between 10 and 100 nm.

PEDOT:PSS dispersion in water can be deposited using all the main common techniques employed for depositing waterborne coatings, namely slit coating, drop-casting, bar coating, spin coating, electrospinning and spraying. If there is the need of a structured deposition, other techniques, such as screen printing, nozzle printing, inkjet and several forms of contact printing, are employed.<sup>329</sup> Other structured deposition methods for PEDOT:PSS relied on a modification of the surface wetting properties, depositing of water repellants<sup>330</sup> or employing photo-lithographical<sup>331</sup> techniques. PEDOT:PSS, like other polymers with sulfonic acid groups, is hygroscopic and takes up moisture in ambient conditions. Flexibility is another important PEDOT:PSS film properties which is highly advantageous since PEDOT:PSS films do not crack upon bending,<sup>332</sup> differently from their inorganic metal oxide counterpart.

As already stated before, PEDOT represents a conductive polymer that can experience a modification of its property following a doping process. Unlike primary doping, which consists of the addition of small nonstoichiometric quantities of material to conducting polymers, secondary doping refers to additive further enhancing the conductivity of a primary-doped polymer.<sup>333</sup> The secondary dopant substances are widely refer as conductivity enhancement agents (CEA). PEDOT:PSS films after secondary doping with some organic inert solvents, sugars, polyols, ionic liquids, surfactants and salts such as sorbitol,<sup>334,335</sup> (poly)-ethylene glycol,<sup>336</sup> dimethyl sulfoxide (DMSO) and tetrahydrofuran<sup>337</sup> undergo a conductivity increase of 2-3 orders of magnitudes. Charge hopping through the polymer chain is believed to be the dominant conduction mechanism in almost all conducting polymers and, increasing the inter-chain interaction facilitate the charge hopping. One of the main observations that needs to be done is that the conductivity increase is not proportional to the additive concentration, as proved by Crispin et al.<sup>338</sup> and by Zhang et al.<sup>339</sup> works. As can be seen in Figure 2.9.a, after a certain concentration, the further addition of secondary dopant does not enhance the conductivity of the film, but either it remains constant, or it could be even reduced.<sup>339</sup> Moreover, as shown in Figure 2.9.a, under a certain concentration, there is no effect of the CEA on the conductivity. Thus, it can be noted that there are small concentration ranges, depending on the conductivity enhancing agent itself, where their effect on the conductivity is almost linear with the concentration. Worth note is the work of Kim et al.<sup>337</sup> that reported the conductivity trend with temperature for pristine film compared to those films prepared with THF (tetrahydrofuran), DMF (dimethylformamide) and DMSO (dimethyl sulfoxide) as additives. The plot of the conductivity shows its increment with the temperature highlighting the different behaviour with or without additives. The pristine sample follows a quasi-one-dimensional variable range hopping (VRH) model while the sample prepared

## 2.2 Materials

with DMSO, THF and DMF follow the power law. Figure 2.9 b reports the measured trend with the model equations.<sup>337</sup> In addition, if PEDOT:PSS with solvents receives a post-coating heat treatment, called annealing, an increase in electrical conductivity is obtained due to an increment in the orientation of the domains which promote an ordered structure. The morphological model of the PEDOT:PSS films before and after the addition of solvents is reported in Figure 2.9 c.<sup>340</sup> In the film without any solvent, the oblate ellipsoidal-shaped PEDOT nanocrystals, surrounded by PSS chains, are embedded in the PSS matrix with the PSS chain network largely aligned along the surface. The cores of PEDOT nanocrystal are composed of linear chain network of quionoid components and near the grain boundary regions are enclosed by randomly oriented coil-like benzoid components. When a contact is realised on the film, the higher number of PSS chains on the surface reduces the ohmic contact points to the top electrode which reduces the front surface carrier collection. Addition of a solvent enhances the packing density of PEDOT and produces clustering with reduced PSS content at the surface.

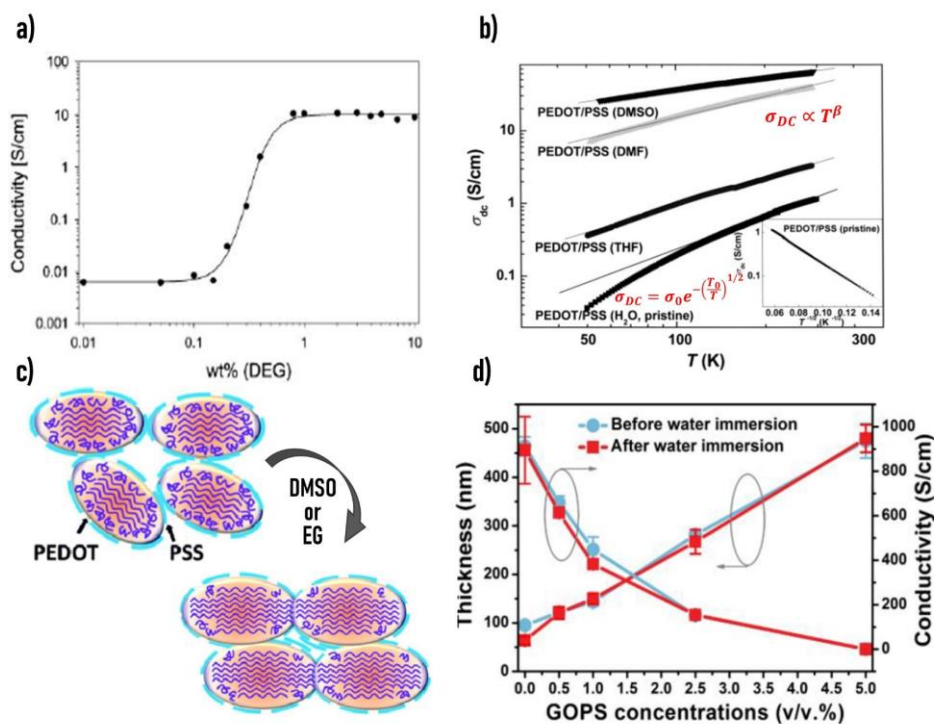


**Figure 2.9:** a) Plot of PEDOT:PSS film conductivity as a function of dyethylene glycol introduced in the water emulsion.<sup>338</sup> b) Temperature dependence of  $\sigma_{DC}(T)$  of PEDOT:PSS films prepared from various organic solvents.<sup>337</sup> c) Schematic model of structural modification in PEDOT:PSS with the addition of co-solvents.<sup>340</sup> d) Thickness (left y scale) and conductivity (right y scale) changes for films made with mixtures containing 94.5 v/v% of Clevios<sup>TM</sup> PH1000, 5 v/v% glycerol and 0.5 v/v% DBSA with increasing GOPS concentration.<sup>339</sup>

## 2.2 Materials

---

The defect generation is also suppressed at the interface because the PSS chain network is rearranged to form closely packed domains of PEDOT nanocrystal. The increase in the PEDOT nanocrystal size upon the addition of the solvent suggests an internal re-ordering inside the nanocrystals, which is likely mediated by hydrogen bond formation between the solvent and PSS. This solvent mediation stabilises the PSS chains and realigns them along the PEDOT grain boundaries to form an intermediate connection with PEDOT nanocrystals.<sup>340</sup> The solvent effects appear to saturate after the addition of a sufficient amount of solvent (i.e. upon reaching a certain wt%). Further addition of solvents does not contribute significantly to the internal structural re-ordering of the PEDOT:PSS, possibly because of saturation of all the available bonding sites. A confirmation of this is reported by Crispin et al.<sup>338</sup>, which found that the conductivity increase is not proportional to the additive concentration. As shown in Figure 2.9.a, no effect is observed at concentrations below 0.2% diethylene glycol in the dispersion. For concentrations between 0.2% and 0.8%, the doping effect becomes stronger and finally reaches a plateau for concentrations above 0.8%. Therefore, the conductivity increase is the combination of different factors such as: high solubility in water, high boiling point and a high dielectric constant that leads to a good secondary dopant for PEDOT:PSS. A combination of all the aspects shown above can give a conductivity greater than 900-1000 S/cm for the Clevios PH 1000 when DMSO or ethylene glycol are used as a conductivity enhancement agent.

A different class of additives are the cross-linkers, which increase the formation of covalent bonds between the polymer chains, thus changing their physical features. Since PSS is highly hydrophilic, PEDOT:PSS films exposed to water usually delaminates. The addition to the mixture solution of the cross-linking agent 3-glycidoxypropyltrimethoxysilane (GOPS) has proved to enhance the PEDOT:PSS film stability in aqueous solutions,<sup>339,341</sup> as reported in Figure 2.9.d. Even though GOPS addition induces good mechanical and electrical stability, it gives thicker films with lower conductivities: thicker films have a larger amount of PSS units, not removed by the water, due to the GOPS cross-linking effect. The PSS excess absorbs larger water amounts and causes irreversible morphological changes in the film, resulting in decreased conductivity.<sup>339,342</sup>

### 2.2.3 PEDOT:BTB

Different doping agents are used to changing the main properties of PEDOT, such as metallocarborane,<sup>343</sup> heteropolyacids,<sup>344</sup> and iron oxalate.<sup>345</sup> The composite PEDOT with organic counterions has been reported in various applications as sensitive electrodes and, exploiting the electrochemical doping of PEDOT with electroactive anions during the polymerisation, can lead to novel classes of materials.

## 2.2 Materials

---

Bromo-thymol blue is a pH-sensitive material used as a pH indicator. It is typically in solid form and acts as a weak acid in a solution. It can thus be in protonated or deprotonated form, appearing yellow or blue, respectively. Acid–base equilibria involving BTB and correspondent UV–vis spectra of the dye dissolved in different pH buffers are shown in Figure 2.10.a. pKa value for BTB is equal to  $7.1 \pm 0.1$ , whose acidic (yellow) and basic (blue) forms present maximum absorbance peaks at 435 and 616 nm, respectively. The BTB dye can be exploited to synthesise PEDOT:BTB material on glassy carbon electrodes<sup>346</sup> by linearly scanning the potential with the substrate in an aqueous solution containing the precursor in a three-electrode cell. The polymerisation solution (PS) needed for PEDOT: BTB electrodeposition contains EDOT monomers, BTB dyes power, PBS (pH 7.0) and  $\text{KNO}_3$  dissolved in water. Example of a deposition curve for PEDOT:BTB from Mariani et al.<sup>347</sup> work is reported in Figure 2.10.b. The figure shows that in the range 0–0.8 V, the recorded current is mainly due to the redox process involving the conductive polymer because its increase after consecutive cycles is ascribed to the polymer growth at the electrode surface, demonstrating that the dye can act as a counterion for PEDOT. Indeed, the film-forming process is driven by the oxidative polymerisation of EDOT, which is in turn allowed and assisted by the electrostatic interaction established between the available negatively charged sulfonate group of the dyes and the growing polycationic chains of PEDOT, as depicted in Figure 2.10.c. As further proof of dyes intercalation within the polymer matrix is given by FTIR-ATR spectroscopy (Figure 2.10.d). Looking at the fingerprint region of BTB, the bands at 1190 and 1051  $\text{cm}^{-1}$  are attributed to the stretching of the sulfonate group<sup>348</sup>, and corresponding signals at 1183 and 1047  $\text{cm}^{-1}$  are found in PEDOT:BTB. Since none of these diagnostic bands is present in the spectrum of a PEDOT:PSS electrode, the new spectroscopic features of the composite films are originated from the functionalities belonging to the embedded dye. As further demonstrated,<sup>347</sup> the absorbance spectra of PEDOT:BTB is pH-dependent, changing its behaviour from acidic to basic, according to the pH buffers solution. It is worth mentioning that if PEDOT is doped with counterions involved in weak acid–base equilibria as BTB, this leads to the formation of a new HOMO–1 level. As confirmation of this statement, Figure 2.11.a shows a CV under two different pH conditions (pH 2.2 black; pH 8.6 red) of a PEDOT:PSS and PEDOT:BTB electrode. From a careful analysis of the shape of this curve, the energy of frontier orbital levels can be estimated. On the one hand, PEDOT:PSS films are dominated by a capacitive behaviour while the PEDOT:BTB film presents evident faradaic features highlighted by the presence of one or more well-defined peaks. In addition, the synthesised PEDOT:BTB materials exhibit considerable pH-induced changes in their electrochemical response, and no redox processes occur for BTB in the scanning range.

On the other hand, the faradaic features are correlated to in-situ rearrangements of PEDOT electronic bands. Indeed, it is well-known that PEDOT has three fundamental redox states,<sup>349</sup> that are neutral, polaronic, and bipolaronic forms, the last two originating from

## 2.2 Materials

electrons extraction/holes injection into the highest occupied molecular orbital (HOMO) of PEDOT. Polaron and bipolaron formation induces a local relaxation of the polymer lattice and creates new electronic states within the energy gap due to local upward or downward shifts of the HOMO and LUMO (lowest unoccupied molecular orbital) levels, respectively.<sup>350</sup>

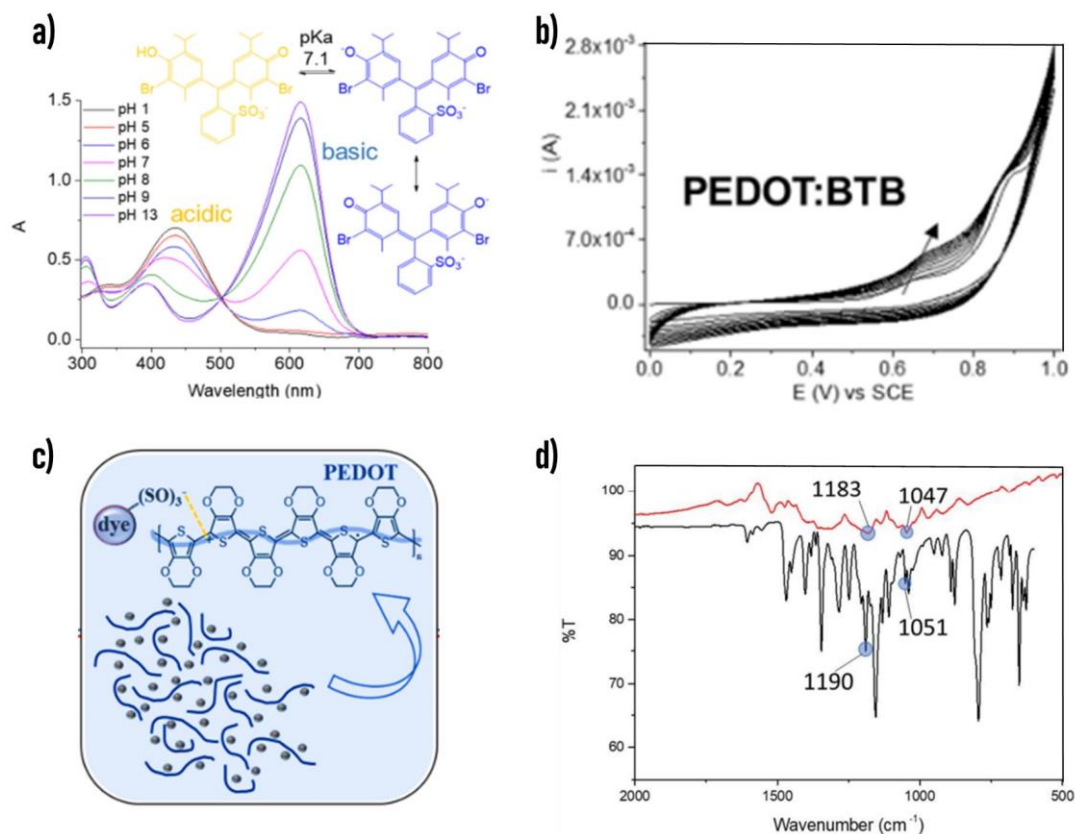


**Figure 2.10:** a) Absorption spectra of 0.02 mM BTB dissolved in different pH buffers and correspondent acid–base equilibrium. b) Electrodeposition curve of PEDOT:BTB at a GCE. c) Proposed interaction between the doping dye and the polymer. d) FTIR-ATR Spectra of PEDOT:BTB with the fingerprint regions between 2000 and 5000  $\text{cm}^{-1}$ .<sup>347</sup>

The HOMO energy level,  $E_{\text{HOMO}}$ , extracted from the onset oxidation potential,  $E_{\text{OX}}^{\text{onset}}$  (circled in blue) is reported in Figure 2.11.b. HOMO levels of PEDOT:PSS do not change significantly upon pH buffer variation while PEDOT:BTB display additional HOMO–1 levels, that is,  $-4.4$  eV at pH 2.2 and  $-3.7$  eV at pH 8.6. Indeed, the dye is deprotonated at a different extent upon pH variation and consequently interact in a pH-susceptible fashion with PEDOT. At high pH (red curve) the dye is deprotonated at its maximum extent, that is,  $\text{BTB}^{2-}$ , consequently making electron extraction easier. On the other hand, when the pH is low (black line),  $\text{BTB}^-$  is monoanionic, thus providing an energetic barrier to further

## 2.2 Materials

oxidise PEDOT. However, since the couple of HOMO-1 levels shows a variation of 0.7 eV in PEDOT:BTB depending on the electrolyte pH, the BTB shows a strong interaction with PEDOT (Figure 2.11.c). Since the energy of the HOMO-1 level in PEDOT:BTB is strongly affected by the pH of the electrolyte solution, this material is used as pH-sensitive coating to develop textile sensors both in plain fabric, and in a single-textile thread to monitor the pH level in human sweat and wounds.

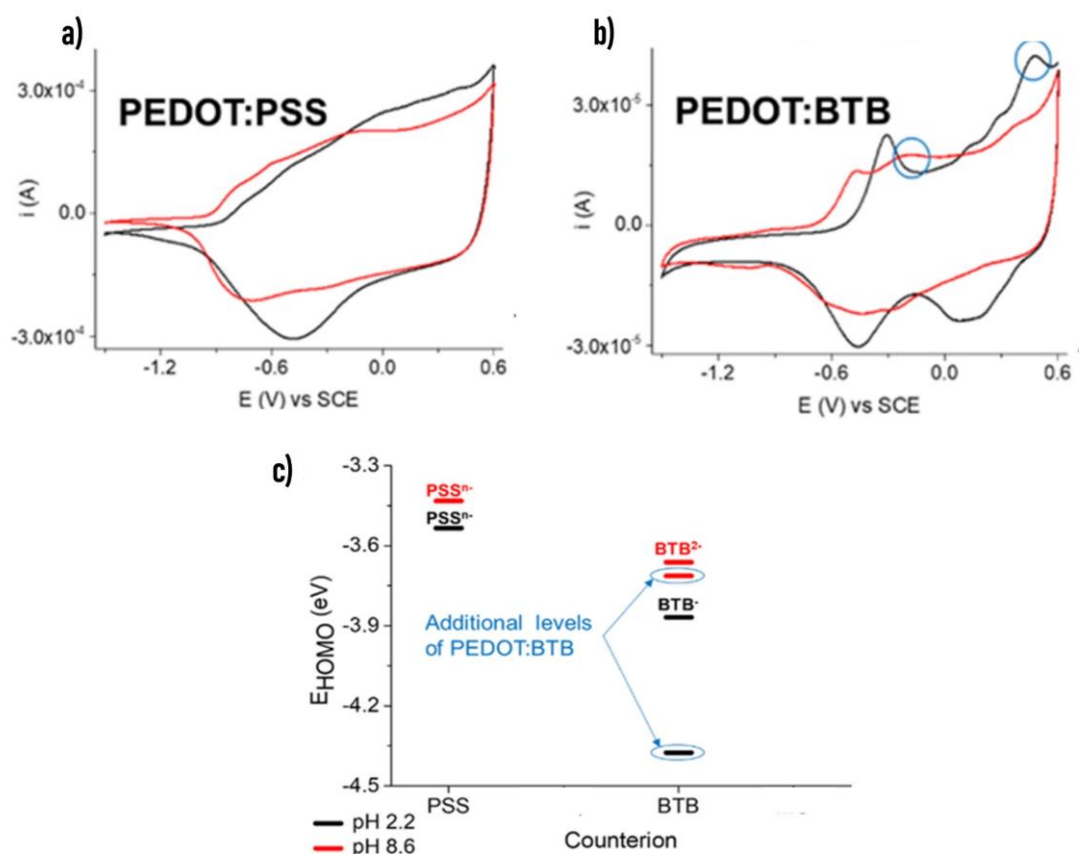


**Figure 2.11:** Cyclic voltammograms obtained at  $50 \text{ mV s}^{-1}$  in buffers at pH 2.2 (black) and 8.6 (red) for the a) PEDOT:PSS and b) PEDOT:BTB films deposited on GCEs. c) Energy diagram of the HOMO levels calculated from the CV of each film at the two pH values.

### 2.2.4 Iridium oxide

Iridium oxide is a highly insoluble and thermally stable source of iridium, suitable for applications in optics and ceramics. IrO<sub>x</sub> is the only well-characterised iridium oxide and occurs as a black powder. Like other metal-oxide compounds, IrO<sub>x</sub> is a basic anhydride capable of reacting with acids and strong reducing agents in redox reactions. Nanoscale elemental powders and suspensions are used in various applications in both industry and research.

## 2.2 Materials

The first example of the synthesis of a stable, blue-coloured colloidal suspension of  $\text{IrO}_x\text{-nH}_2\text{O}$  nanoparticles dates back to 1908.<sup>351</sup> This process was based on thermally assisted basic hydrolysis of the  $\text{Ir}^{\text{IV}}$  complex  $[\text{IrCl}_6]^{2-}$ . Subsequently, various techniques for synthesis of both capped<sup>352</sup> and ligand-free<sup>353–355</sup> NPs of  $\text{IrO}_x\text{-nH}_2\text{O}$  were reported, which were eventually combined with spin coating,<sup>355</sup> self-assembly,<sup>356</sup> and inkjet printing<sup>357</sup> techniques to obtain functional electrochemical interfaces for water splitting and pH sensing. It is this feature that will be exploited in the present work to realise a pH sensor on fabric. Figure 2.12.a shows as an example a (UV-vis) spectrum of a dark blue aqueous suspension containing  $\text{IrO}_x\text{-nH}_2\text{O}$  particles attenuated by basic hydrolysis and subsequent acidification of  $\text{Ir}^{\text{IV}}$  solution. An isosbestic point around 370 nm highlights the coexistence of two species, namely  $[\text{Ir}(\text{OH})_6]^{2-}$  and  $\text{IrO}_x\text{-nH}_2\text{O}$  colloid, which absorbs at 304 and 574 nm, respectively, and are in equilibrium depending on the pH of the solution. The absorption band at 574 nm increases in intensity with acidification due to the promoted formation of  $\text{IrO}_x\text{-nH}_2\text{O}$  colloids.<sup>358</sup> In such acidic suspension solution containing ligand-free  $\text{IrO}_x$  particles, it is possible to measure the particle size by dynamic light scattering (DLS) showing, in general, an average diameter of  $(1.1 \pm 0.5) \mu\text{m}$  (Figure 2.12.b).

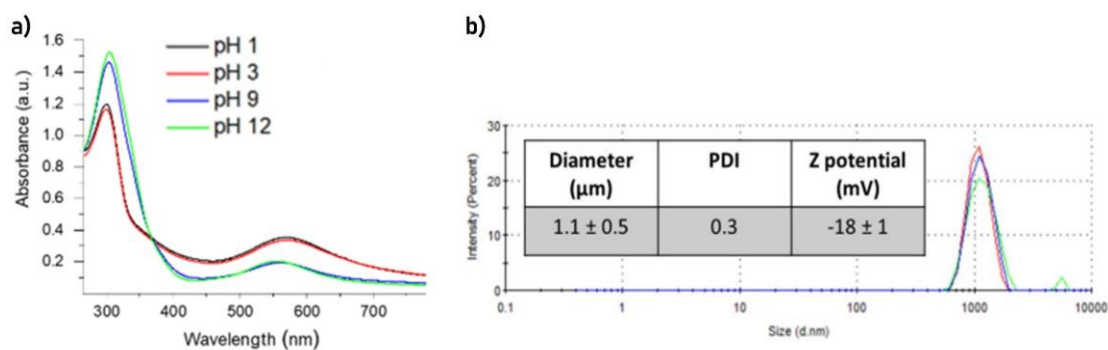


**Figure 2.12:** a) UV-vis characterisation of the  $\text{IrO}_x$  P's suspension at different pH values. b)  $\text{IrO}_x$  particles diameter distribution ( $N = 3$ ) obtained by DLS characterisation. Average diameter, polydispersity index (PDI) and Z potential are reported in the table.<sup>358</sup>

### 2.2.5 Silver/silver chloride

Silver chloride is a white chemical compound known for its low solubility in water with the chemical formula  $\text{AgCl}$  (Figure 2.13.a). When exposed to light or a heat source, silver chloride converts to silver (and chlorine), changing to a grey-black or purple coloration. It also occurs naturally in the form of the mineral chlorargyrite. Unlike most chloride salts,  $\text{AgCl}$  has low solubility, making it easy to synthesise by metathesis: a chemical reaction based on the exchange of two or more ions between elements and groups having the same valence. By combining an aqueous solution of silver nitrate with a soluble chloride salt, such as sodium chloride or potassium chloride, silver chloride can be formed

## 2.2 Materials

---

by precipitation. In recent years, great interest has been aroused in the production of silver-based composites. Its ions can inhibit bacterial multiplication by binding and denaturing bacterial DNA, thus stopping bacterial cells' growth.<sup>359,360</sup> Thus, the use of silver ions as a broad-spectrum antibacterial agent has enabled its wide-spread use in disinfectants and wound healing, medical implants and instrument sterilisation. Expressly, these antibacterial abilities are conferred by the silver ion, and as a result, silver chloride (AgCl) is a potentially sustainable silver resource. In addition, AgCl in the form of nanoparticles, given their smaller size, is more effective in penetrating through cell membranes, thus leading to greater accumulation of silver in the cells.<sup>361</sup>

The term nanoparticle usually identifies a class of particles of different shapes (spherical, cubic, and so on), made of atomic or molecular aggregates with a size ranging from 1 to 100 nm. Various materials, including biopolymers and metals (nickel, chromium, gold, silver) can be exploited to make NPs used in bandages,<sup>362</sup> food containers,<sup>363</sup> disinfectants, and makeup/cosmetics.<sup>364</sup> While having various applications, the preparation of AgCl nanoparticles with controlled size is limited to methods such as microemulsion technique, ultrasonic irradiation, matrix-based technique, or mixing silver nitrate (AgNO<sub>3</sub>) with hydrochloric acid in the presence of Poly (vinylpyrrolidone).<sup>365,366</sup> Figure 2.12.b shows a SEM image of AgCl nanoparticles formed via the biogenic synthesis of metallic nanoparticles, a bioredox mechanism using cellular enzymes, secondary metabolites and other cellular components for NPs synthesis.<sup>367</sup> Furthermore, Ag/AgCl NPs are another silver-based compound that can be prepared exploiting the standard electrodeposition method using a three-electrode cell configuration. Ag NPs are first deposited using an AgNO<sub>3</sub> solution, and then a KCl solution is used to cover the Ag NPs surface with an AgCl layer. Figure 2.13.c shows the atomic force microscopy image of Ag/AgCl nanoparticle electrodeposited on a conductive polymer with an average size of  $300 \pm 80$  nm. The electrodeposition method can be exploited to realise particles with a bigger size changing the deposition time. The so-realised particles are able to react with chloride present in the surroundings and are presented later in this thesis to develop wearable and textile sensors for monitoring the chloride concentration in human biofluids.

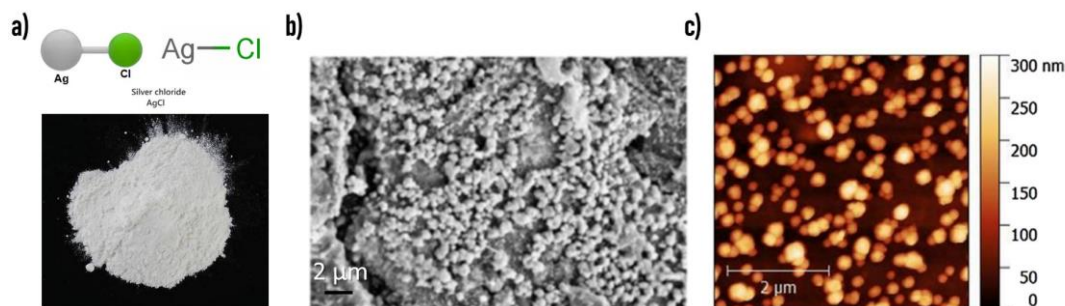


**Figure 2.13:** Silver Chloride powder. b) SEM image of synthesized silver chloride nanoparticles.<sup>1</sup> c) AFM image of Silver/SilverChloride nanoparticles deposited on conducting polymer PEDOT:PSS:<sup>41</sup>

### 2.2.6 Perovskites

The term perovskite refers to a calcium titanium oxide mineral composed of calcium titanate (chemical formula  $\text{CaTiO}_3$  but more in general, a perovskite is any material with a crystal structure similar to the mineral itself. Many different cations can be embedded and arranged according to a perovskite structure, allowing the development of diverse engineered materials. The general chemical formula for perovskite compounds is  $\text{ABX}_3$ , where  $A$  and  $B$  are two cations, often of very different sizes ( $A$  atoms are generally bigger than the  $B$  atoms), and  $X$  is an anion (frequently oxide) that bonds to both cations.

As one of the most abundant structural families, perovskites are found in many compounds with wide-ranging properties, applications, and importance. The organic-inorganic Methylammonium hybrid  $\text{MABX}_3$  ( $\text{MA} = \text{CH}_3\text{NH}_3^+$ ) ( $B = \text{Sn}, \text{Pb}, X = \text{Cl}^-, \text{Br}^- \text{ or } \text{I}^-$ ) materials with perovskite crystal structures have attracted great interest in the optoelectronic device fields, such as solar cells, light-emitting diodes, photoelectric detectors and X/gamma-ray detectors. Figure 2.14.a report a schematic representation of the Methylammonium halides family. The general crystal structure of these materials is shown in Figure 2.14.b. The main physical properties of this novel kind of synthesised material include superconductivity, magnetoresistance, ionic conductivity, and a multitude of dielectric properties, which are of great importance in microelectronics and telecommunication. The most studied application areas for perovskite structure are the photovoltaic cells and the X-ray dosimeters thanks to the large optical absorption coefficient, high carrier mobility, long carrier lifetimes, tunable resistivity and large X-ray attenuation coefficient, they could reach a theoretical peak efficiency of 31%.<sup>368</sup> Figure 2.14.c reports examples of two stacked structures for perovskite photovoltaic cell and x-ray detectors using the two most common Methylammonium halide structures.

In the growing perovskite photovoltaic cells field, Methylammonium lead iodide ( $\text{CH}_3\text{NH}_3\text{PbI}_3$ ) represents the most studied Methylammonium halides material <sup>369,370</sup> since their first appearance in 2009 by Kojima.<sup>371</sup> Spin-coating technique can be used to deposit

## 2.2 Materials

thin films at low temperature (usually  $< 100^\circ\text{C}$ ) or vapour deposition can be exploited for planar heterojunction perovskite solar cells.<sup>372</sup> Methylammonium lead iodide is a semiconducting pigment with a direct bandgap of 1.55 eV corresponding to an absorption onset of 800 nm.<sup>373</sup> The weak binding energy of about 0.03 eV of the produced excitons is responsible for their rapid dissociation into free carriers at room temperature.<sup>374</sup> The mobilities of electrons and holes produced in this material range from  $7.5 \text{ cm}^2 \text{ V}^{-1} \text{ s}^{-1}$  for electrons<sup>375</sup> to  $12.5 - 66 \text{ cm}^2 \text{ V}^{-1} \text{ s}^{-1}$  for holes.<sup>376</sup>  $\text{MAPbI}_3$  presents a long carrier-diffusion length ranging between 100 nm and 1000 nm.<sup>377</sup>

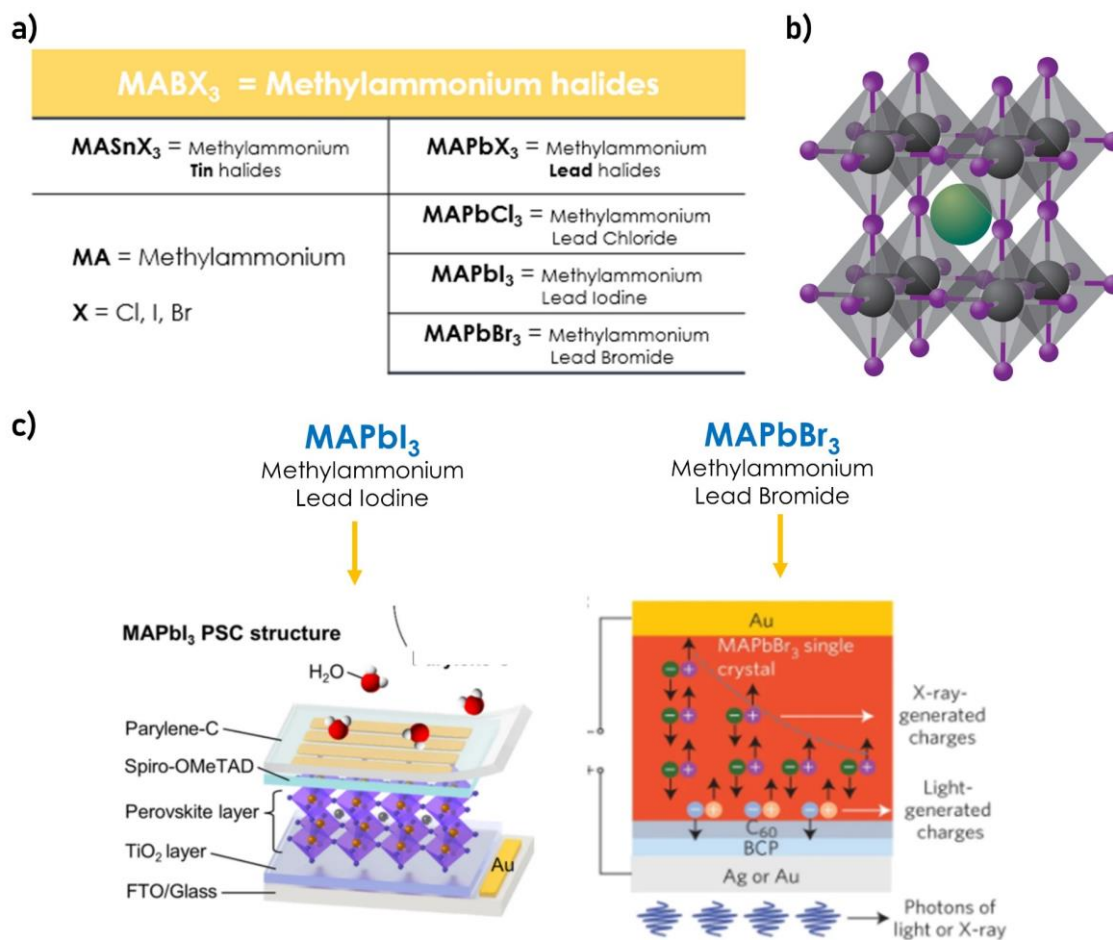


**Figure 2.14:** a) Schematic representation of the Methylammonium halides family. b) General crystal structure of cubic metal halide perovskites with the generic chemical formula  $\text{ABX}_3$ . Organic or inorganic cations occupy position A (green), whereas metal cations and halides occupy the B (grey) and X (purple) positions, respectively.<sup>378</sup> c) Schematic of the  $\text{MAPbI}_3$  PSC structure with Parylene-C encapsulation and the chemical structure of Parylene-C (left),<sup>379</sup> and single-crystal radiation detector structure. The charge generation regions are located close to the surface for visible light excitation and deeper inside the single crystal for X-ray excitation, respectively (right).<sup>380</sup>

Another popular application of perovskites is the realisation of ionising radiation sensors. In this thesis, another popular class of perovskites, methylammonium lead bromide

## 2.2 Materials

(MAPbBr<sub>3</sub>) will be used to realise textile x-ray sensors using single crystals directly grown through the fibres of the fabric. The use of MAPbBr<sub>3</sub> single crystal for X-ray detection relies on the strong stopping power of halide perovskite (high atomic number of Pb<sup>2+</sup> on Br<sup>-</sup> of 82 and 35, respectively) and the relatively high resistivity of about 1000 Ω cm that is responsible for small dark current and noise. The better defect tolerance than other semiconducting materials give at this class of detectors a greater radiation tolerance.

Figure 2.15.a shows the typical XRD spectrum of MAPbBr<sub>3</sub> single crystals with the main four diffraction peaks, corresponding to (100), (200), (300) and (400) crystal planes, respectively. The schematic diagram of MAPbBr<sub>3</sub> crystal structure shows the cubic symmetry and the space group Pm $\bar{3}$ m with a lattice constant of 0.59062 nm. The band gap for a MAPbBr<sub>3</sub> single crystal is approximately 2.23 eV.<sup>381,382</sup> It is usually estimated using a UV-Vis-NIR transmittance spectra of MAPbBr<sub>3</sub> and the absorption law as reported in Figure 2.15.b.

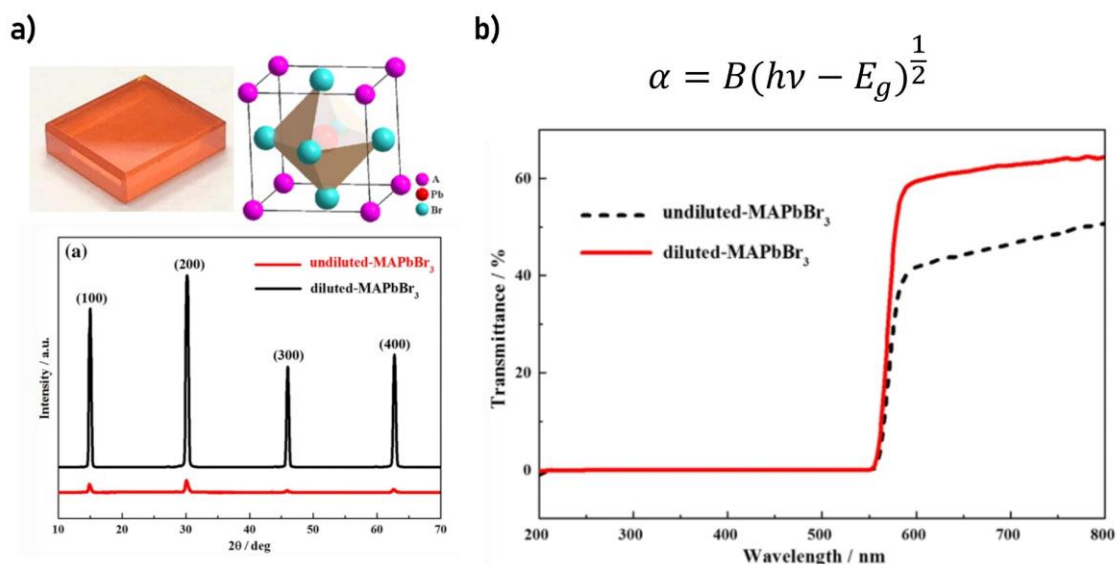


**Figure 2.15:** a) XRD results and UV-Vis-NIR transmittance spectra of MAPbBr<sub>3</sub> single crystals.<sup>382</sup>

### 2.2.7 Thermoelectric materials

Thermoelectric materials convert thermal energy into electrical energy based on the Seebeck and Peltier effect. They can be applied in energy recovery, highly efficient cooling and refrigeration, sensing and thermo-power systems. This leads to re-use the wasted thermal energy in production applications in the most efficient way. Since most energy from fossil sources is lost as heat in engines or industrial processes, the use of thermoelectric materials that can recover this energy can make considerable contributions to helping solve the global energy crisis. Thermoelectric generators (TEGs) enjoy the advantage of being able

to recover waste heat over a wide range of temperatures while operating without producing noise, vibration or gas emissions. They also do not require refuelling or maintenance over a long period of time. The only limitation is related to the modest heat conversion efficiency, which is characterised by the figure of merit  $ZT$  expressed as:  $ZT = S^2\sigma T/k$  with Seebeck coefficient  $S$ , thermal conductivity  $k$ , electrical conductivity  $\sigma$  and absolute temperature.

Therefore, materials with low thermal conductivity and high electrical conductivity are required to achieve high  $ZT$  or higher material efficiency. Bismuth compounds with tellurium and antimony represent the best room temperature thermoelectric materials known today. This thesis used organic and inorganic thermoelectric materials to develop textile thermoelectric generators using single polyester strands. A power generator able to supply the energy without the use of external batteries in a textile sensors platform remains the main goal to spread the use of textile wearable technologies massively.

### 2.2.7.1 Bismuth Telluride

Bismuth telluride ( $\text{Bi}_2\text{Te}_3$ ) is a compound of bismuth and tellurium, which occurs as a gray-colored powder. It is a semiconductor and an efficient thermoelectric material for refrigeration or portable power generation. Bismuth telluride crystallises in the tetradymite crystal structure shown in Figure 2.16.a.  $\text{Bi}_2\text{Te}_3$  has a hexagonal HCP arrangement of Te layers. The Te - Bi bonds are polar-covalent while only weak van der Waals type bonding exists between the neighboring,  $\text{Te}^{(1)} - \text{Te}^{(1)}$  planes.

The lattice thermal conductivity along the basal planes is almost double that in the perpendicular direction.<sup>383</sup> The Seebeck coefficient for both n- and p-type  $\text{Bi}_2\text{Te}_3$  is nearly isotropic. However, it should be considered that the Seebeck coefficient and electrical conductivity have a trade-off: a higher Seebeck coefficient corresponds to decreased carrier concentration and decreased electrical conductivity.

Coupled with its inherently low lattice thermal conductivity,  $\text{Bi}_2\text{Te}_3$  is an excellent thermoelectric material because of its complex electronic band structure. Bismuth telluride has a narrow indirect gap of 0.14 eV that decreases with temperature like most covalent semiconductors<sup>384,385</sup> at a rate of  $0.95 \cdot 10^{-4}$  eV/K. The electronic transport of  $\text{Bi}_2\text{Te}_3$  can be generally described as that of a small bandgap semiconductor where the conduction band has a higher mobility than the valence. When the electrical conductivity is low,  $\sigma$  below  $\approx 500 \text{ S cm}^{-1}$ , there is a sharp reduction of thermopower  $S$  and change in sign which corresponds to the intrinsic regime where carriers in both conduction and valence bands contribute significantly to transport (Figure 2.16.b). Recently, it has been reported that materials with one or more dimensions reduced, as nanowires or thin film, can improve the overall material efficiency.<sup>386</sup> Thin film of bismuth telluride deposited by radio frequency magnetron sputtering can lead to an n-type thermoelectric material with a Seebeck coefficient of  $-287 \mu\text{V/K}$  at  $54 \text{ }^\circ\text{C}$ .<sup>387</sup>

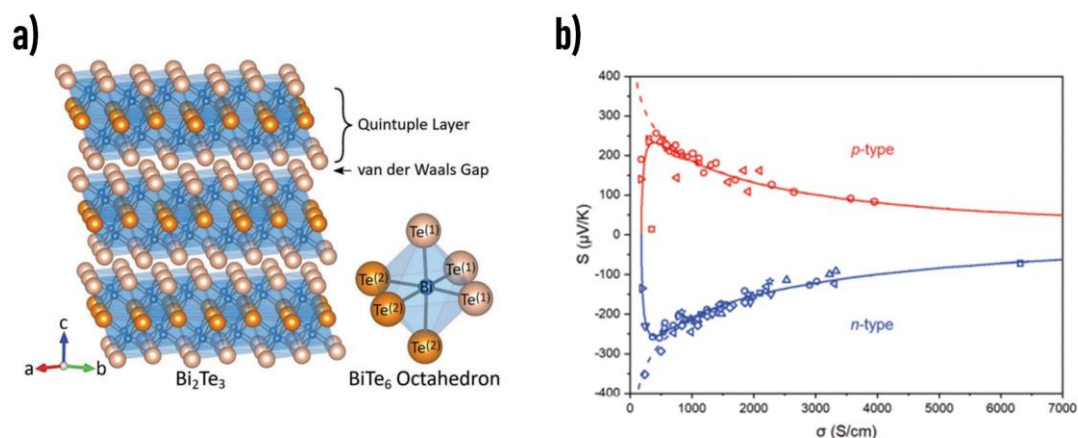


**Figure 2.16:** a) Layered structure of Bi<sub>2</sub>Te<sub>3</sub>. Bismuth atoms are octahedrally coordinated by tellurium atoms residing on two inequivalent sites, distinguished here by tone and notation. Each quintuple layer lamella is separated by weak van der Waals bonding between adjacent Te(1) layers. b) Room temperature trend of Seebeck coefficient varying the materials conductivity. The two-band effective mass models (solid line) describe the data well and illustrate the limiting effect of minority carriers at low conductivity values.  
383

### 2.2.7.2 Antimony Telluride

Antimony telluride is an inorganic compound with the chemical formula Sb<sub>2</sub>Te<sub>3</sub>. It is a grey crystalline solid with layered tetradymite crystal structure. Layers consist of two atomic sheets of antimony and three atomic sheets of tellurium and are held together by weak van der Waals forces. Sb<sub>2</sub>Te<sub>3</sub> has a rhombohedral crystalline structure with space group R3m. The lattice constants for the hexagonal cell at 29°C are:  $a=4.264$  and  $c=30.458$  for Sb<sub>2</sub>Te<sub>3</sub>. Schematic atomic structures of Sb<sub>2</sub>Te<sub>3</sub> depicting mixed ionic-covalent bonded quintet layers held by interlayer van der Waals bonding are reported in Figure 2.17.a.

Crystallisation of antimony tellurite are directly dependent on the temperature<sup>388</sup> and microstructure, surface morphology, and thermoelectric properties can be modified changing the working temperature. X-Ray diffraction on Sb<sub>2</sub>Te<sub>3</sub> sample (Figure 2.17.b) shows the widened peaks in XRD patterns with indicate the general fine crystalline grain size. Sb<sub>2</sub>Te<sub>3</sub> is a narrow-gap semiconductor with a band gap 0.21 eV. Furthermore, it is also a topological insulator, and thus exhibits thickness-dependent physical properties.<sup>389</sup>

The room-temperature Seebeck coefficient and electrical conductivity range from 55  $\mu\text{V/K}$ <sup>390</sup> to 140  $\mu\text{V/K}$ <sup>391</sup> changing the deposition methods (from electrochemical deposition to thermal evaporation). Figure 2.17.c shows the temperature dependence of the Seebeck coefficient for a thin film of antimony telluride with different percentage of tellurium. However, the deposition technique, the substrate temperature, the annealing procedure and

## 2.2 Materials

eventually doping, can largely modify the Seebeck coefficient up to a six-time value.<sup>390</sup> Even the morphology structure of  $\text{Sb}_2\text{Te}_3$  samples can differ changing the fabrication methods but when a substrate at high temperature is used, the  $\text{Sb}_2\text{Te}_3$  has a homogeneously distributed and well-defined polycrystalline grain structure with large-sized grains, corresponding to a continuous, well-crystallised layer <sup>391</sup>(Figure 2.17.d). Thanks to its crystallographic structure, antimony telluride presents an overall good thermoelectric properties and it has been commonly applied as a low-temperature thermoelectric material, because of its relatively high value of ZT parameter.<sup>392</sup>

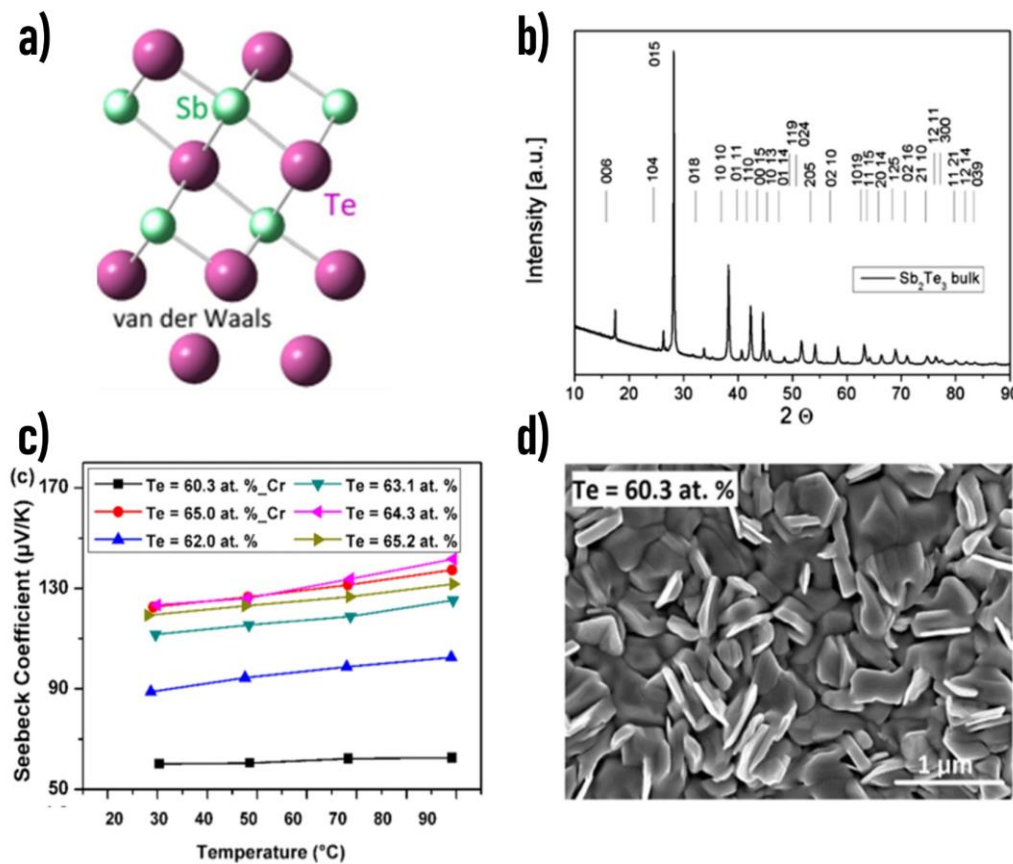


**Figure 2.17:** a) Schematic atomic structures of  $\text{Sb}_2\text{Te}_3$  with Wyckoff site labels depicting mixed ionic-covalent bonded quintet layers held by interlayer van der Waals bonding in the undoped, defect free configuration. <sup>392</sup> b) Diffraction pattern for  $\text{Sb}_2\text{Te}_3$  layer.<sup>393</sup> c) Temperature variation of the Seebeck coefficient of the Sb-Te thin films prepared at high substrate temperatures.<sup>391</sup> d) Scanning electron microscopy (SEM) images showing the surface and (inset) cross-sectional morphologies of Sb-Te thin films prepared at high substrate temperatures.<sup>391</sup>

## 2.3 Fabrication technique

---

Finally, it is worth to note that values for the Seebeck coefficient and the figure of merit of thermoelectric material in real application, can not be considered absolute but considerable variations are correlated to the deposition technique, type of substrate and temperature. In this thesis, the p- and n-type thermoelectric material based on  $\text{Bi}_2\text{Te}_3$  and  $\text{Sb}_2\text{Te}_3$  respectively, are synthesised on a textile thread to present the first example of an organic-inorganic textile single-thread thermoelectric generator.

## 2.3 Fabrication technique

In this paragraph, a brief overview of all the fabrication methods employed to realise the different devices present in the following thesis is reported. All the precise details and exact information about the fabrication procedure used can be found in the corresponding section.

### 2.3.1 Deposition methods

Generally speaking, the sensing layers for the textile sensors presented in this thesis, have been realised with different deposition, and patterning techniques. The deposition methods are usually divided in two categories: coating and printing methods. The main difference between them lays on the fact that the former technique covers all the available surface, while the latter method transfers the ink (namely the conductive solution) only over a predefined pattern. The most used coating methods are drop casting, spin coating, dip coating, roll-to-roll, spray coating, and electrodeposition, while for printing they are screen printing, pad printing, ink-jet printing and nozzle printing. The most suitable deposition technique is chosen taking into account various factors as the shape, dimension and surface features (roughness and wettability) of the substrate; the solubility, polarity and nature of deposited material, and the uniformity and thickness chosen for the final layer.

#### 2.3.1.1 Drop casting

The drop casting procedure is a very simple method that allow a very low material waste. The solution is dropped onto the target substrate, and the spontaneous solvent evaporation lead the surface coated by the active material. When a conductive solution is employed, the samples are usually annealed in order to speed up the solvent evaporation, and enhance the conductivity (Figure 2.18.a). The typical disadvantages of this technique are the difficulty to get a uniform, large area coating with a controlled thickness. In the present thesis, the technique is only exploited to fabricate the pressure sensing layer on cotton fabrics since this consent to locally turn conductive an extended piece of fabric.

### 2.3.1.2 Spin coating

Spin coating process is a very common and widely used coating method in which the substrate spins around an axis which is normal to the coating area. The spinner is designed to coat thin films onto the surface of the substrate. The thickness of layer is controlled by spin speed, spin time and viscosity of the solution. The spin coating process involves four stages: deposition, spin up, spin off and evaporation, as shown in Figure 2.18.b. In the deposition process, an excessive amount of fluid is deposited at the center of the substrate and, during the spin up, it is accelerated up to the final spin speed. In the liquid, rotational forces are exerted on the upward direction causing the formation of a wave front. This wave front flows from the center to the edge of the substrate thanks to the centrifugal force, and results in a uniform layer. During the spin off phase, the excess solvent is removed from the substrate surface, while the excess portion of solvent is let evaporated during a final annealing step. This technique allows to realise highly uniform films, and thoroughly tune the thickness of the film by varying the spin speed or using different viscosity solution. In contrast, large substrate cannot be spun at a sufficiently high rate, it causes a great waste of material and the fast drying procedure provides less time for molecular ordering.

### 2.3.1.3 Roll-to-Roll

Roll-to-roll processing is a fabrication technique used in manufacturing that coats, embeds, prints or laminates different fluid materials onto flexible rolled substrates that are continuously fed from one roller to another. The roll-to-roll method typically consists of numerous rollers, named the web path, which winds the substrate material thorough and over the rollers while it carries out various operations. The technique applies materials onto substrates with different width, as it moves along the web path. The final thickness and aspect of the deposited thin film is mostly determined by the type of applicator roller, the type of the fluid, and the relative speed of the two rotation surfaces.

For the purpose of this thesis, a simplified roll-to-roll like technique is exploited to uniformly coat with conductive polymer various types of textile threads (Figure 2.18.c). In the home-made setup here used, a single yarn is pulled and span around a round glass stick and meanwhile is dipped in the conductive solution. Applying this process four different times, followed by annealing, it is possible to homogeneously coat a single fibre with a conductive ink. This process, however, does not use a real roll-to-roll instrumentation but is based on the same roll-to-roll principle in order to continuously apply a coating layer on thread.

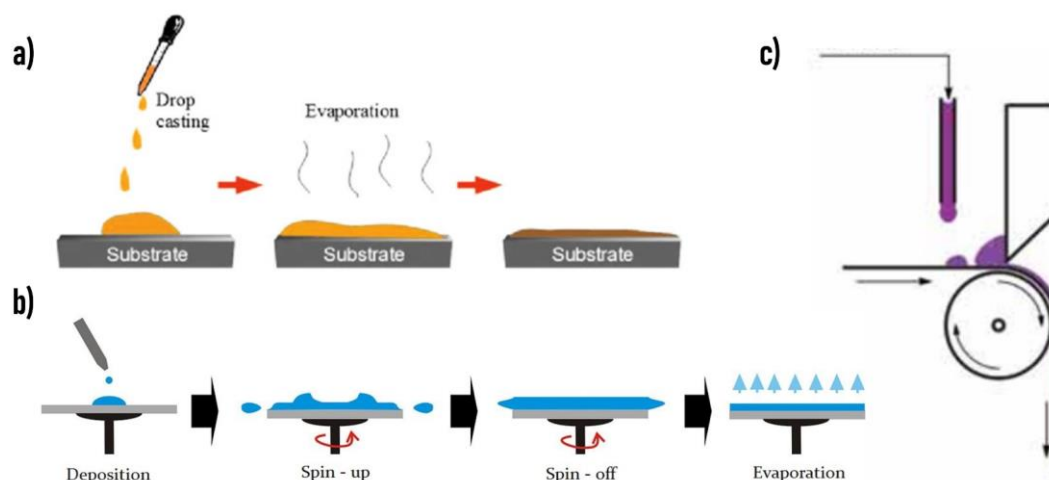


**Figure 2.18:** a) Drop-casting procedure composed by the drop of the solution on the substrate and the subsequent annealing . b) Schematic representation of spin coating steps: the PEDOT solution is drop casted on the glass substrate; then, spin coating rotation spreads the solution onto the whole substrate, getting rid of the excess solution, while the evaporation of the solvents leads to the final film formation. c) Roll-to-roll deposition method to coat textile single-thread with conductive ink solution.

### 2.3.1.4 Screen Printing

The screen printing technique is based on a stencil process where a silk screen frame or an open mask can be used to impress a conductive pattern onto the substrate. The conductive solution should have the right density in order to cover only the region under the unmask part, without diffusing to the surroundings. Usually, the final mass of the solution is halved to better coat the substrate with the ink (Figure 2.19.a).

Figure 2.19.b report the working principle of the screen printing method used in this thesis to coat different types of fabric with inks based on conductive polymer. The paste is squeezed by a moving blade over a screen formed by a monofilament polyester mesh. The solution passes through the interlocked mesh and the conductive pattern does not penetrate to the bottom side of the textile. The method is simple but has a limited thickness resolution and requires highly viscous pastes.

### 2.3.1.5 Thermal deposition

Thermal evaporation is another useful method to deposit a thin layer. The source material evaporates in a vacuum chamber due to high temperature heating, which facilitates the vapor particles flowing and directly reaching the substrate where these vapors again change to a solid state. In this method, a resistive coil is exposed to a large direct current (DC = 20 A), in order to reach the high melting points typical of metals. The evaporation

## 2.3 Fabrication technique

---

chamber is kept in high vacuum (below  $10^{-4}$  Pa) in order to support the evaporation of the metal. This technique is especially applicable for materials with low melting points and in this thesis is used to deposit chromium and gold thin layer (10 nm and 50 nm, respectively) on glass substrate to realise the electrical connections of the polymeric thin film. A schematic of the thermal evaporation system is exhibited in Figure 2.19.c.

### 2.3.1.6 Electrochemical deposition

Electrochemical deposition is a technique by which a thin and tightly adherent desired coating of oxide, salt, or metal can be deposited onto the surface of a conductive substrate by simple electrolysis of the solution containing the desired metal ion or its chemical complex. The electrochemical deposition allows a precise control over the quantity of the deposited material and provides an easy way to functionalise the samples.<sup>394</sup> The limitation of this procedure is the need of an electrically conductive substrate on which the film is formed: for this reason, evaporated gold substrate and PEDOT:PSS thin film on glass or textile are used as substrates to functionalise the surface with proper sensing ability.

The schematic in Figure 2.19.d shows a three electrode electrochemical cell, equipped with a saturated calomel electrode (SCE) as reference electrode (RE), a Pt wire as counter electrode (CE) and the chosen conductive substrate acting as working electrode (WE). The inert atmosphere can be assured inside the chamber in order to limit polymer reduction that can lead to sample delamination. The electrochemical deposition is a viable technique to control polymeric layer thickness and amount deposition (tuning the deposition cycles). A constant magnetic stirrer is used to avoid mass diffusion limit in the region close to the WE.

The depositions can be realised with two different procedures: the first employed a cyclic voltammetry (CV), with the potential varied between two values,  $E_{low}$  and  $E_{high}$ , at a fixed scan rate for various cycles. On the other hand, the second method uses a potentiometric control, applying a constant potential  $E$  while counting the total amount of the material deposited, thus its thickness. This fabrication process is employed for the realisation of the textile thread sensors for chloride and pH sensing in sweat presented in chapter 3.

## 2.3 Fabrication technique

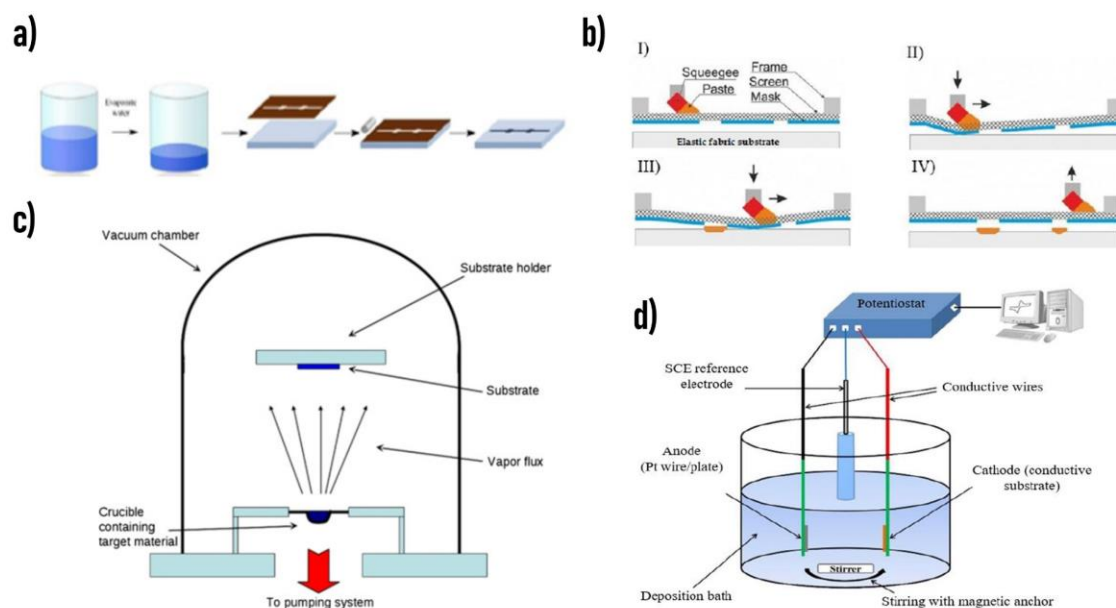


**Figure 2.19:** a) Solution preparation and screen printing phases. b) Different steps in the serigraphy printing method using a proper serigraphy frame. c) Vacuum chamber for metal thermal deposition method. The target material is heated in the crucible and the metal gases condensate onto the cold substrate. d) Electrochemical deposition method using an electrochemical cell with three electrodes, namely a saturated calomel electrode (SCE) as reference electrode (RE), a Pt wire as counter electrode (CE) and a conductive substrate as working electrode (WE). The stirrer is constantly used to have a uniform solution and avoid depleted region during deposition.

### 2.3.2 Perovskite crystal growth

Perovskite single crystals (PSC) have been grown onto the surface of silk fabric to realise the textile X-ray detectors reported in chapter 5. Overall, the controllable synthesis of high-quality PSC is of fundamental importance for its applications in photovoltaic and photoelectric fields. Obtaining high-quality and large-size crystals remains a challenge that requires several efforts from the research community. However, different approaches have been developed up to now in order to fabricate stable and regular crystals as solution temperature lowering (STL), anti-solvent vapour-assisted crystallisation (AVC), and inverse temperature crystallisation (ITC).

STL method utilises the difference of solubility of the perovskite precursors in solvents under various temperatures. The perovskite precursors are melted into the solvents at high temperatures. Then, the solution's temperature is gradually reduced to reach a super-saturated state, resulting in single-crystal growth (Figure 2.20.a).<sup>395</sup> A specific example of an STL method is the top-seeded solution growth (TSSG) that allow to prepare large single crystals. As reported in Figure 2.20.b,<sup>377</sup> many small crystals are collected at the

## 2.3 Fabrication technique

bottom of the saturated perovskite growth solution, which is kept at a fixed temperature around 75 °C. A silicon wafer is then immersed into the precursor solution. Thanks to the lower temperature at the top of the glass vessel, small crystal will form on the Si wafer. The higher concentration at the bottom, allows the convection process between the bottom and top of the solution, which provide enough material for large single-crystal growth.

AVC is a temperature independent and reproducible method to realise high-quality single crystals by exploiting the solubility of the precursor solution in different solvents. The precursor is placed into a sealed bottle containing antisolvent. The solubility of the mixed solvent decreases when the antisolvent is slowly diffused into the precursor solution, resulting in the growth of crystals (Figure 2.20.c).<sup>396</sup>

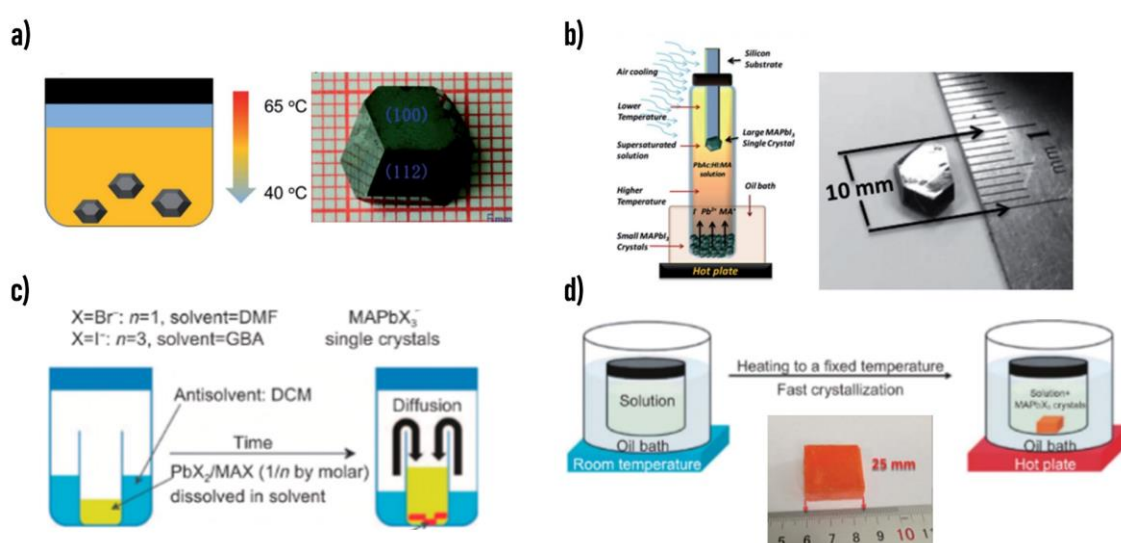


**Figure 2.20:** a) Solution temperature lowering method and image of  $\text{CH}_3\text{NH}_3\text{PbI}_3$  oriented to exhibit its natural facets  $\{100\}$  and  $\{112\}$ .<sup>395</sup> b) Schematic representation of top-seeded solution growth with the large  $\text{MAPbI}_3$  immersed in the supersaturated solution and the image of a piece of as-prepared  $\text{MAPbI}_3$  single crystal.<sup>395</sup> c) Schematic diagram of AVC process using a solvent with high solubility and moderate coordination (like DMF or GBA), and an antisolvent in which perovskite precursors are completely insoluble (DCM).<sup>396</sup> d) Inverse temperature crystallisation method to fast growth single crystals.

Inverse temperature crystallisation method is directly used in this thesis and it consists of a precursor solution inserted in a bottle, and heated at a fixed temperature ( $\sim 80$  °C) to grow single crystals. During the growth process, illustrated in Figure 2.20.d, at the beginning, the solution surface is in a saturated state due to of the volatilisation of the solvent, while the solution below is unsaturated. As the amount of the solvent decreases, the concentration will exceed the solubility of precursors because of the convection inside the bottle. This condition leads to the growth of single crystals. Large single crystals of  $\text{MAPbBr}_3$  are commonly synthesised by this method. The growth could be faster if the

temperature is higher, but the crystal will lose regularly, or tiny crystals will be formed. The details of the fabrication of single perovskite crystals are explained in chapter 5.

## 2.4 Characterisation technique

The most relevant experimental techniques used to characterise the textile sensors developed in this thesis are discussed and explained here. The following paragraphs will provide a theoretical overview of the working principles at the basis of the characterisation methods used in the following chapters to study the electrical, mechanical, morphological and optical properties of both materials and devices.

### 2.4.1 Electrical characterisation

Electrical characterisation has primary importance in producing chemical and physical sensors that respond to changes in the surrounding environment through a variation of the electrical properties of the composite materials. In this work, sensors based on different physical principles, such as piezoresistivity, electrochemical gating, impedance variation or electron-lacuna pair generation, will be presented. A first validation of the electrical response of the developed devices is generally performed with laboratory instrumentation such as source meter unit (SMU), oscilloscopes and, in the case of small signals, lock-in amplifiers. In addition, depending on the nature and geometry of the device, various types of measurements can be performed in order to directly extract the resistance, current or voltage generated.

Thin films of semiconductor materials are electrically characterised by measuring the surface resistance, or sheet resistance, using the Van der Pauw 4-probe method. It is a technique commonly used to measure the resistivity of a planar material with the electrodes placed on its perimeter. The Van der Pauw method employs a four-point probe placed in the four corners of a squared sample (Figure 2.21). During a measure, the current flows along one edge of the sample (for instance,  $I_{12}$ ) and the voltage is applied across the opposite edges (in this case,  $V_{34}$ ). From these values, using Ohm's law, it is calculated a resistance  $R_{12;34} = V_{34}/I_{12}$ . Then, by exchanging the contacts from  $I_{12}$  to  $I_{34}$  and  $V_{34}$  to  $V_{12}$  one obtains the reciprocal value  $R_{34;12}$ . The same approach is employed to calculate the resistance  $R_{23;14}$  and  $R_{14;32}$ . To obtain a more precise measure, these four resistance values are averaged.

For thread-like sensors, measurement of the current variation flowing through them is generally done by applying a constant potential via an SMU such as the Keithley 2400, Keithley 2600, or Keysigth B2902A. On the other hand, AC impedance measurements are made using the MFLI Zurich lock-in amplifier by applying a sinusoidal voltage signal and measuring the current through the device. Custom programs developed in Labview allow

interfacing with the instruments and the acquisition of data necessary for the characterisation of the devices.

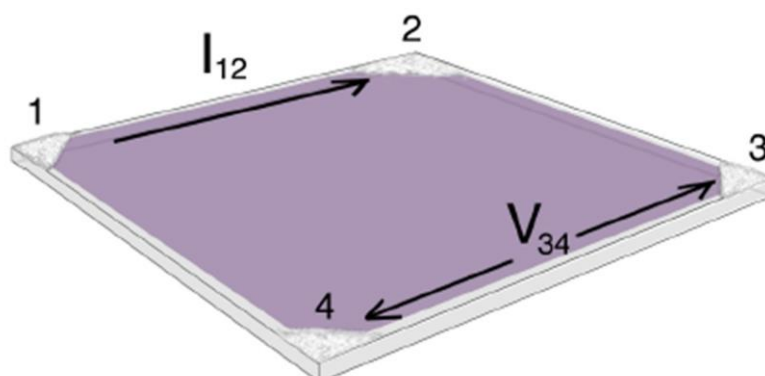


**Figure 2.21:** Conductive contacts on a conductive thin film to realize a Van der Pauw measurement in a four-probe configuration.

### 2.4.2 Electrochemical characterisation

Electrochemical characterisations enable to achieve information on the kinetics and charge transport involved in electrochemical reactions and doping mechanisms, together with the electrode/electrolyte interfacial properties. The measurements are usually carried out using CV (mainly exploited for polymeric electrochemical deposition, rather than a characterisation technique) and electrical impedance spectroscopy (EIS). Both employ an electrochemical cell with three electrodes, namely a WE, a RE and a CE, dipped in an electrolyte solution to electrically connect them. The sample under investigation are placed as working electrode, and their potential is measured with respect to the RE, represented either by a saturated calomel electrode (SCE) or by a silver/silver chloride (Ag/AgCl) one. The counter electrode is used to generate a current flowing between WE and CE, which keeps the working electrode at the selected potential. The CH Instrument 660C and a Metrohm Autolab PGSTAT204 potentiostat have been here used.

#### 2.4.2.1 Cyclic voltammetry

In cyclic voltammetry, the electrochemical potential of the samples is swept linearly (as shown in Figure 2.22.a) over time at a fixed scan rate  $v=dE/dt$  up to the switching potential,  $E_{\lambda}$ , reaches a time  $t = \lambda$ , then the scan rate is switched, and the electrochemical potential is brought back to its initial value,  $E_i$ . The potential during each cycle can be mathematically represented by the following:

## 2.4 Characterisation technique

$$E = E_i - vt \quad (0 < t \leq \lambda)$$

$$E = E_i - 2\lambda t + vt \quad (t > \lambda)$$

This sweep reversal method is very powerful and useful, and it is widely practiced as an electrochemical method.<sup>397</sup>

In CV experiments, the shape of the resulting curve ( $I-t$ , but more commonly  $I-E$ , as reported in Figure 2.22.b) represents the superposition of a capacitive current and a faradaic one. The former is related to the charging of the electrical double layer at the electrode/electrolyte interface, while the latter comes from the mass transfer due to the eventual electrochemical reaction  $O + ne \leftrightarrow R$  at the electrode. The charging current during a potential sweep can thus be written as:<sup>397</sup>

$$I_c = vC_d \left[ 1 - \exp\left(-\frac{t}{R_s C_d}\right) \right]$$

with  $R_s$  being the electrical resistance of the solution and  $C_d$  the double-layer capacitance. This time-dependent current saturates when  $t \gg R_s C_d$ , having a steady-state current of  $I_{c,ss} = vC_d$ . If the sweep has a triangular shape (not just a linear one), then the steady-state current changes from  $vC_d$  during the forward scan (the potential  $E$  is increasing) to  $-vC_d$ , during the reverse scan (decreasing  $E$ ), due to the change of sign of the scan rate  $dE/dt$ .

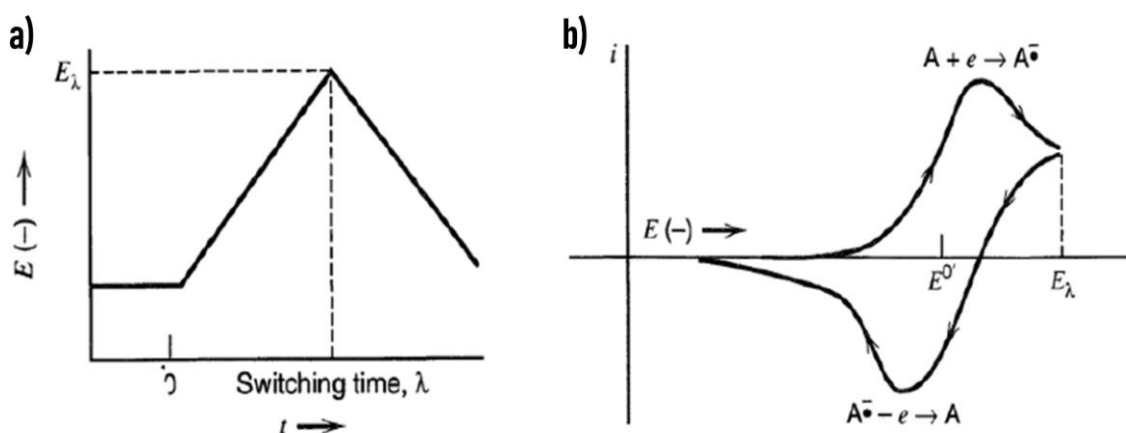


**Figure 2.22:** a) Cyclic potential sweep (triangular shape); b) Resulting cyclic voltammogram,  $I-E$ .<sup>397</sup>

The faradaic current depends on two laws, namely the Fick's law of diffusion for the planar electrode, and the Nernst equation:

$$\frac{d[O]}{dt} = D \frac{d^2[O]}{dx^2}$$

$$\frac{[O]_{x=0}}{[R]_{x=0}} = \exp \left[ \frac{nF}{RT} (E(t) - E_0) \right]$$

Fick's law governs the mass transport process towards the electrode, where  $D$  is the diffusion coefficient, and  $x$  is the parameter denoting the distance from the electrode surface. On the other hand, Nernst equation is related to the surface concentration of oxidised and reduced forms of the redox agents as a function of  $E(t)$  and  $E_0$ , that are the applied and formal potentials, respectively.<sup>398</sup> In Nernst equation,  $t$  is the time,  $n$  the number of electrons transferred per molecule of  $O$  reacting at the surface of the electrode,  $F$  the Faraday constant,  $R$  the constant for ideal gas and  $T$  the absolute temperature.

For a reversible, diffusion-controlled process, where the reaction rate is limited by the transport rate of the reactants to the electrode surface, the current response at each potential may be calculated for a reversible cyclic voltammogram, with  $E(t) = E_i - vt$  using a mathematical procedure called semi-integration ( $d^{1/2}y/d^{1/2}x$ ) or convolution:<sup>399</sup>

$$I(t) = -nFA[O]_{bulk}\sqrt{D} \frac{d^{1/2}}{dt^{1/2}} \left( \frac{1}{1 + e^{\frac{nF}{RT}(E_i - vt - E_0)}} \right)$$

where  $A$  is the area of the electrode. To verify the hypothesis of the diffusion-controlled process, the Randles-Ševčík equation can be used, expressed as:

$$I_p = 0.446nFA[O]_{bulk} \sqrt{\frac{nFvD}{RT}}$$

### 2.4.3 Mechanical characterisation

Mechanical characterisation allows to investigate and assess different features related to the intrinsic nature of the material as elasticity, elongation, tensile strength, hardness and fracture toughness. Dynamic Mechanical Analysis, otherwise known as DMA, is a standard characterisation technique where a small deformation is applied to a sample in a cyclic manner while measuring the sample mechanical response to study composition and viscoelastic properties. The response to the deformation can be monitored as a function of temperature or time. It allows characterisation of the composition and viscoelastic properties. DMA works by applying an oscillatory (sinusoidal) deformation to a sample of known geometry. The sample can be subjected to controlled stress or a controlled strain.

## 2.4 Characterisation technique

---

Where stress is applied, the sample will deform a certain amount and it is measured. A force motor generates the sinusoidal stress wave and this is transmitted to the sample via a drive shaft. Applying a sinusoidal force, the stress in a dynamic experiment is a complex stress  $\sigma^*$  and can be separated into two components (with phase angle  $\delta$ , the difference between deformation and response):

**real part**  $\sigma' = \sigma^* \cos\delta$ , is the degree to which materials behaves like an elastic solid;

**imaginary part**  $\sigma'' = \sigma^* \sin\delta$ , is the degree to which it behaves like an ideal liquid.

In the same way, the modulus can be expressed as an in-phase component, the elastic (storage) modulus  $E'$ , and an out-phase component, the viscous (loss) modulus  $E''$  (Figure 2.23.a).

The storage modulus  $E'$  is the measure of the sample's elastic behaviour and the ability of the material to store energy. The ratio of the loss to the storage modulus is the  $\tan\delta = E''/E'$ , and it is often called damping. It is a measure of the dissipation energy of material under cyclic load, and it indicates how well a material can get rid of energy.

### 2.4.3.1 TA Instrument DMA Q800

For the analysis and tests on the textile materials, the TA Instrument DMA Q800 has been employed. The Q800 utilises non-contact, linear drive technology to provide precise control of stress and air bearings for low friction support. Optical encoder technology measures strain and provides unmatched sensitivity and resolution. Figure 2.23.b reports the different parts that compose the DMA Q800. The motor is formed of high-performance composites that ensure low compliance. It is thermostated to eliminate heat build-up even when using large oscillation amplitudes and high deformation forces. Sophisticated electronics enable the motor current to be rapidly adjusted in small increments. The motor can deliver reproducible forces from  $0.1 \cdot 10^{-3}$  N to 18 N and the force can be changed rapidly, up to 200 Hz. This motor transmits force directly to a rectangular air bearing slide (that connects to the driveshaft and sample clamp), and pressurised air flows to the bearings forming a frictionless surface that permits the slide to "float." A high-resolution linear optical encoder is used to measure displacement, and it is based on diffraction patterns of light through gratings (one moveable and one stationary). Due to the excellent 1 nanometre resolution of the optical encoder, very small amplitudes can be measured precisely.

The Q800 features a variety of sample clamps that provide for multiple modes of deformation. The clamps have high stiffness, low mass, and each one is individually calibrated to ensure data accuracy. The high stiffness minimises clamp compliance, and the low mass ensures rapid temperature equilibration. There are different modes of deformation that need a specific clamp for each of them: dual/single cantilever, 3-Point bending, shear sandwich, compression and tension mode. In compression mode, the sample

## 2.4 Characterisation technique

is placed on a fixed flat surface and an oscillating plate applies force, while, in tension mode, the sample is placed in a tension between a fixed and moveable clamp.

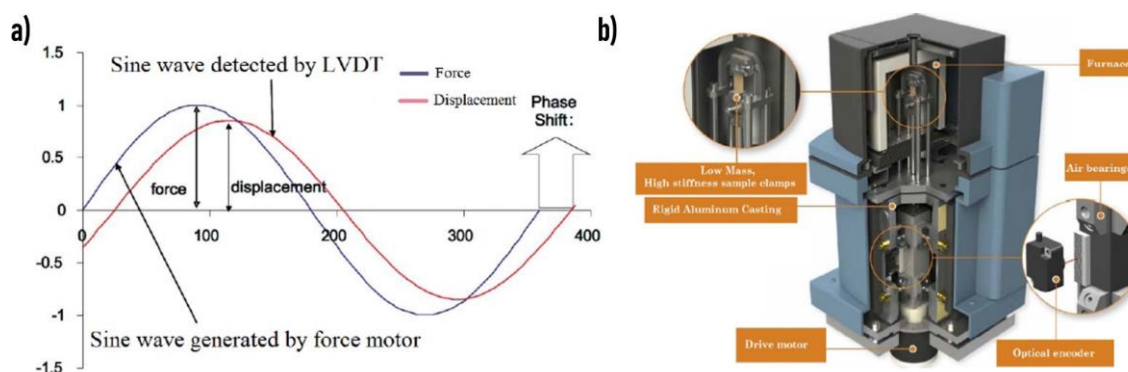


**Figure 2.23:** a) Schematical representation of the oscillatory (sinusoidal) force applied to a sample and the corresponding deformation response. b) Illustration of the most important part of TA Instrument DMA Q800.

### 2.4.4 Morphological characterisation

#### 2.4.4.1 Atomic force microscopy

One of the most suitable methods to investigate the morphology, electric, magnetic or other surface characteristics at the micro- and nano-scale is the Scanning Probe Microscopy (SPM). The instrument uses specially prepared tips in the form of needles as probes, with the working part (apex) usually of the size of ten nanometer or lower, mounted on a flexible supporting cantilever. One side of the cantilever is fixed to a support, while the other edge, where the tip is located, is free to move and is approached to the sample down to tip-surface distances of 0.1-10 nm, according to the technique used for the measurement. When the tip approaches the sample, several interactions between the tip and the substrate can be studied in order to get information on the sample surface features. Let the interaction be van der Waals forces between the two elements, as in the case of our morphology analysis, and the technique is thus referred as Atomic Force Microscopy (AFM); then, the tip will induce a deflection of the cantilever. A schematic of the experimental technique, its working principle and data-trace obtained, are represented in Figure 2.24.a-b. Since the dimension of the edge of the tip is close to the atomic dimension (nanometric size or even lower, as shown in Figure 2.24.c), the van der Waals energy of two atoms can be used to approximate the potential energy of the tip, as plotted in Figure 2.24.d, and approximated by the following:

## 2.4 Characterisation technique

---

$$U_{LD}(r) = U_0 \left\{ -2 \left( \frac{r_0}{r} \right)^6 + \left( \frac{r_0}{r} \right)^{12} \right\}$$

where  $r_0$  is the equilibrium distance between the atoms.

To detect the slight cantilever deflections, a laser beam, focused on its back and reflected, is acquired by a photodiode divided into four sectors: from the measurements of the relative intensity variations on the different sections, the amount of vertical and lateral deflection of the cantilever are extracted.

### 2.4.4.1.1 Surface morphology

In this thesis, imaging of morphological surfaces are carried out with Park NX10 AFM system, operating in a non-contact mode in air or PBS 1X, with the tip oscillating close to its resonance frequency,  $\omega_0$ . The height of the sample's surface is then described by the equation:

$$z(t) = z_0 + A_0 \cos(\omega t - \varphi)$$

where  $z_0$  is the mean height of the cantilever,  $A_0$  is the amplitude of the free oscillation,  $\omega$  is the oscillation frequency, and  $\varphi$  is the phase constant that is set to  $90^\circ$  for the free oscillating tip. The non-contact mode is obtained when the tip is far enough from the surface of the sample and stay in the attractive regime of the Lennard-Jones potential, thus where  $F = dU/dz > 0$  for the whole amplitude of the oscillation. When the tip is closer to the sample, the oscillation amplitude decreases to  $A(z)$ , with  $A(z) < A_0$ . This value is employed as a set-point to control the height of the tip, using a feedback system that gives the height of the sample surface.

For data analysis, the height-height correlation function (HHCF) is used in order to extract surface roughness and correlation length. For a randomly rough surface with a Gaussian correlation function (used in this work), the height-height correlation function can be written as:

$$HHCF = 2S^2 \left[ 1 - \exp\left(-\frac{d^2}{T^2}\right) \right]$$

where  $S$  is the surface roughness (root mean square deviation of the height),  $d$  the distance between height points, and  $T$  denotes the autocorrelation length.

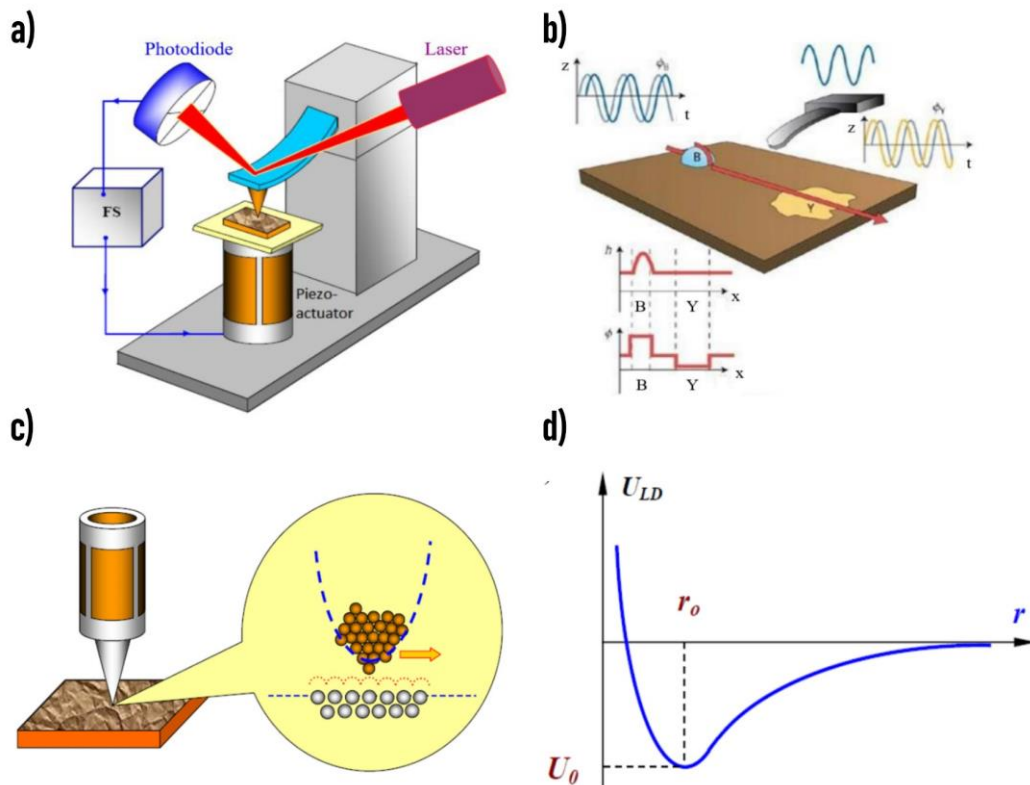


**Figure 2.24:** a) Schematic of an AFM. A laser shine on the cantilever head, and the reflected beam is collected by a photodiode, thus obtaining the bending of the cantilever due to atomic forces. The feedback mechanism (FS) is used to control the tip-surface distance, through the piezoelectric actuator under the sample holder, according to the deflection of the cantilever.<sup>400</sup> b) Scheme of the AFM operation, with the cantilever oscillation depending on the topography and its surface composition. The height and the phase images are registered, with phase-shift signal changing with dissipated energy variations on the sample surface. c) Atomic resolution with the AFM: the tip edge dimensions allow for an atom-atom interaction with the sample surface.<sup>400</sup> d) Qualitative form of the Lennard-Jones potential.<sup>400</sup>

#### 2.4.4.1.2 Surface conductivity

Conductive Atomic Force Microscopy (C-AFM) was invented in 1993 by M.P. Murrell and co-authors at the University of Cambridge, and it is an AFM technique able to record also the current flowing between the tip/sample nano-junction, simultaneously to the topography.

C-AFM structure is similar to standard AFM, save three main differences: i) the tip probe must be conductive; ii) since a potential needs to be applied between the tip and the sample, a voltage source is present; iii) a preamplifier is introduced with the aim to convert the analogical current signal into a digital voltage, read by the computer.<sup>401</sup> Moreover, in C-AFM experiments, the sample is often fixed to the holder with conductive tape or paste, in

## 2.4 Characterisation technique

---

order to have a net current flowing from tip to sample once the potential difference is imposed. Therefore, the local electrical properties of the sample surface can be studied with nanometric resolution. The current that is collected by C-AFM is the product of the current density  $J$  and the effective emission area through which electrons flow  $A_{eff}$  (effective area), i.e.  $I = J \cdot A_{eff}$ .  $J$  value depends on conductivities of the tip and sample and on the voltage applied between them, being affected by inhomogeneities in the sample, like local defects, thickness fluctuations and doping. The lateral resolution is defined by  $A_{eff}$ , which can range from tenths of square nanometres to thousands of square micrometres depending on the conductivity of the sample, the tip/sample contact force, the relative humidity of the atmosphere, the geometry of the tip and other experimental factors.

An important feature that has to be taken into account for C-AFM is that effective emission area,  $A_{eff}$ , does not always equal physical contact area,  $A_c$ , because in many tip/sample systems, the electrical field can propagate even laterally in the sample. This event happens for example, when the tip goes on a conductive metallic electrode (that is part of the sample), where  $A_{eff}$  is the entire area covered by the electrode due to the high lateral conductivity.<sup>402,403</sup> The effective area can indeed be defined as the sum of all infinitesimal spatial locations on the sample surface that are electrically connected to the C-AFM tip, thus having negligible potential differences.

### 2.4.4.2 Scanning electron microscopy

Scanning electron microscopy (SEM) is used to study the surface morphology of the samples under investigation. SEM is a microscopy technique that has the aim to provide a topographic image of the objects at a nanometric scale, rebuilding a signal produced by the interaction of an electron beam with the target. The SEM instrument used in this work, Cambridge Stereoscan 360, is thermionic-emission based since the beam has provided by the overheating of a filament (generally tungsten) through the use of an electric current. The electronic beam undergoes an acceleration to the target by a potential difference (approximately 40 kV), and is focused by a system of magnetic lenses. SEM permits to analyse of three kinds of signals: Back Scattered Electrons (BSE), Secondary Electrons (SE) and X-ray. Figure 2.25.a shows a section of interaction's volume between the electron beam and the object to analyse and the different zones of origin of the signals. BSEs are characterised by an energy range between 50 eV and the beam's energy. It is worth noting that those electrons are not emitted by the target, but they are always the original one that has been scattered (elastic scatter) with an angle of almost 180 degrees. BSE signal is proportional to the atomic number of the object to analyse, permitting to map the compositional information of the target. The high energy of electrons allows a penetration around 1  $\mu\text{m}$ , so it returns information about the internal structure but loses the external

## 2.4 Characterisation technique

one. SEs are the product of the interaction between beam and valence's electrons of external atoms; those are called secondary because they are the product of the interaction.

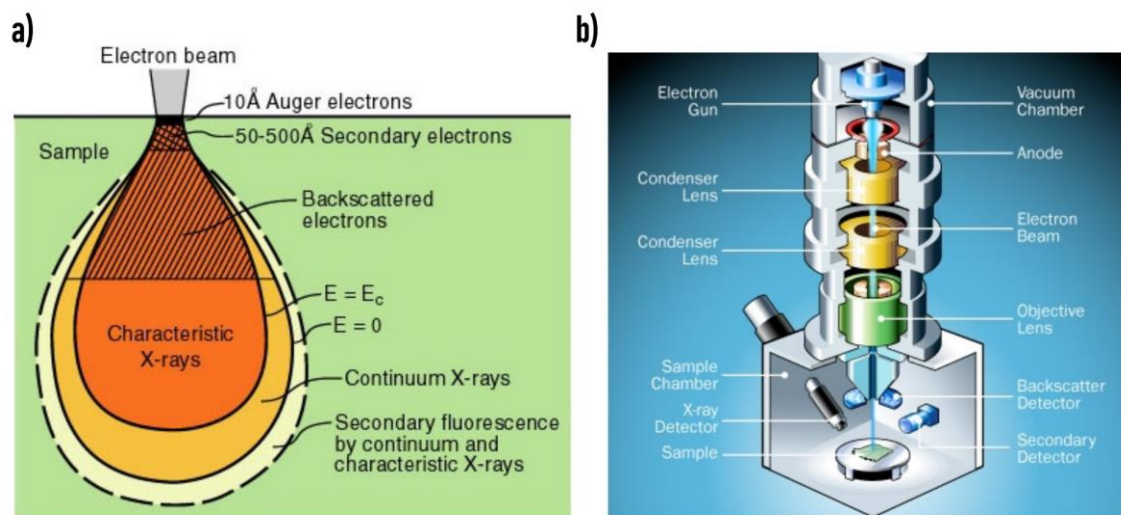


**Figure 2.25:** a) Section of interaction's volume between the electron beam and the sample. b) Internal pattern of a SEM.

It is possible to detect just the electrons that had been subjected to recombination processes, so that came from by the external surface (impossible more than 5 nm). Their energy, consequently, is lower compared with BSE. SEs give an external morphology with a higher resolution of the BSE. X-rays are produced by the loss of energy of atoms after the ionisation caused by the impact of the primary beam's electrons with the core atom's one. The ionised core electron creates a hole that is filled by an electron of a more external shell. This transition de-energised the atom that emits energy in X-ray form. Figure 2.25.b shows the cross-section of a SEM instrument.

### 2.4.4.3 FTIR

Fourier Transform Infrared (FTIR) Spectroscopy is a technique employed to obtain an infrared spectrum of absorption or emission of a solid, liquid or gas substance and is based on the idea of the interference of radiation between two beams (interferogram).<sup>404</sup> The interferogram is a signal produced by the change of path length of the two beams with the domains of distance and frequency being interconvertible using the following Fourier transformation analysis.

The basic setup of the FTIR spectrometer is shown in Figure 2.26.a: the radiation is emitted from a source and passes through an interferometer to the sample and then reaches the detector. After the amplification of the signal and the elimination of high-frequency contributions (filtered), the data are collected for a subsequent Fourier transformation:

$$I(\delta) = \int_0^{+\infty} B(\bar{\nu}) \cos(2\pi\bar{\nu}\delta) d\bar{\nu}$$

$$B(\bar{\nu}) = \int_0^{+\infty} I(\delta) \cos(2\pi\bar{\nu}\delta) d\delta$$

These equations relate the intensity falling on the detector as a function of the difference in path length,  $I(\delta)$ , to the spectral power density at a certain wavenumber,  $\bar{\nu}$ , given by  $B(\bar{\nu})$  and vice versa.

The basic experiment to obtain FTIR spectrum consists of an interferogram production with and without a sample on the beam, then transforming the interferogram into the spectra for the source with the sample absorption and another one for the source without sample absorptions. Then, the ratio of the former and the latter results in a double-beam dispersive spectrum.

Reflectance methods can be used for samples difficult to analyse using the conventional transmittance study. In particular, Attenuated Total Reflectance (ATR) spectroscopy is employed, which exploits the phenomenon of total internal reflection, as shown in Figure 2.26.b. A beam of radiation that enters a crystal is totally reflected when the incident angle at the interface between sample and crystal is higher than the critical angle. A fraction of the beam wavelength penetrated the reflecting surface, and the sample selectively absorbs radiation, thus making the beam lose energy. The depth of penetration in ATR spectroscopy for a non-absorbing medium can be calculated using the following:

$$d_p = \frac{\left(\frac{\lambda}{n_1}\right)}{\left[2\pi \sqrt{\sin^2\theta - \left(\frac{n_1}{n_2}\right)^2}\right]}$$

where  $\lambda$  is the wavelength,  $n_2$  is the refractive index of the crystal,  $\theta$  is the incident angle and  $n_1$  is the refractive index of the sample. The resulting attenuated radiation is collected and plotted over the wavelength using a spectrometer, giving the typical spectral characteristics of the investigated sample. Indeed, the interaction of infrared radiation with the matter is translated in variations of molecular dipoles due to vibrations (stretching and bending) and rotations. Since each compound and substance has its own bondings and is composed of determined molecules with their typical infrared absorption (vibrations and rotations), ATR-FTIR spectroscopy is used to study the precise composition of textile fabric and fibres. Brucker Alpha Platinum-Attenuated Total Reflectance (ATR) spectrophotometer equipped with ATR Diamond window (32 scans, 4  $\text{cm}^{-1}$  resolution) has been used to acquire the spectrums.

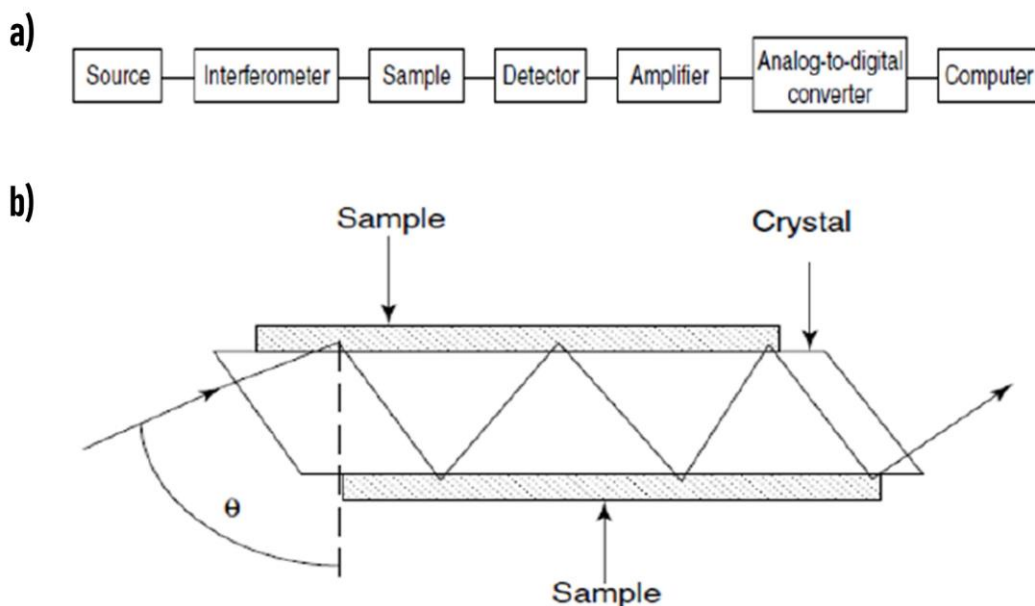


**Figure 2.26:** a) Block-schematic of the basic components in a FTIR spectrometer. b) Schematic of a typical ATR cell, with  $\theta$  being the incident angle of the beam.<sup>405</sup>

#### 2.4.4.4 DSC

Differential scanning calorimetry is a technique in which the difference in heat flow (power) to a sample and to reference is monitored against time or temperature while the T of the sample, in a specified atmosphere, is programmed. By means of this technique is possible to measure how much power is given to the sample and to the reference. The difference is calculated, and it gets the enthalpy of the transition happening into the crucible. Therefore, it is possible to calculate the enthalpies of reaction while on the x-axis there is temperature or time that is going to be changed. There are two types of DSC that have been recognised: power compensated and heat flux DSC. In the first one, sample and reference are heated separately by using individual heaters and the temperature difference is kept close to zero (Figure 2.27.a)<sup>406</sup>. The reference pan is normally empty, and when heat is supplied, its temperature increases gradually, while the sample pan will not increase at the same rate because there are materials in it. Since the system has to keep a difference in temperature equal to zero, it has to supply more power toward the sample pan while the difference in electrical power needed to maintain equal temperature is measured.

In the heat flux DSC, the same single source heats the sample and reference pan, and the temperature difference is constantly measured. This signal is converted to a power difference  $\Delta P$  using the calorimetric sensitivity (Figure 2.27.b).

## 2.4 Characterisation technique

DSC enables the measurements of melting temperature, glass transition temperature, the heat of fusion, latent heat of melting, reaction energy and temperature, crystalline phase transition temperature and energy, denaturalisation temperatures, precipitation energy and temperature, oxidation induction times and specific heat or heat capacity. Here, a TA Instruments DSC Q2000 is used to perform textile composition characterisation reported in chapter 5.

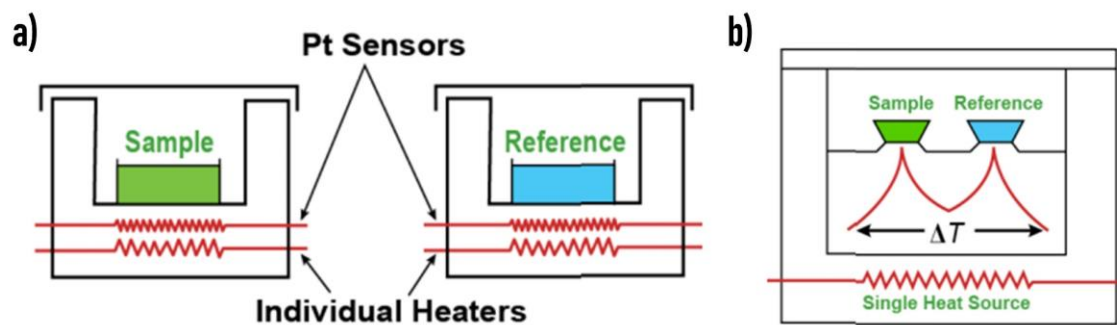


Figure 2.26: Measuring principle of a) power compensation and b) heat-flux DSC.<sup>406</sup>

# Chapter 3

## Textile sweat sensors

This chapter presents the experimental results regarding a fully textile platform to monitor pH and chlorine concentration in human sweat. Starting from general considerations about the operation of the organic electrochemical transistor (OECT), the relevant simplification of the sensors moving from three to two terminals will be presented. This simplification step is fundamental to realise biosensors using a textile single-thread exploiting only two terminals. Subsequently, it will be reported a complete description and characterisation of the reliability of the sensors first in universal buffer and then in artificial sweat, providing details about the morphology, electrical response, stability, reproducibility and possible interference. In addition, the feasibility and wearability of the Cl<sup>-</sup> textile sensors will be demonstrated using a portable wireless data-reader connected via Bluetooth with a smartphone. Finally, as a proof-of-concept and an applicative example in similar real-life conditions, the sensors are characterised when sewn into a T-shirt neck.

### 3.1 Sweat sensing

Wearable sensing technologies are attracting a rising academic and industrial interest thanks to the large prospective impact on real life and the driving force of market demand. Personalised healthcare and point-of-care medical assistance, together with fitness, represent the main fields of applications meeting the highest request for wearable biosensors. The category of wearable chemical sensors is at an early stage of development even if they represent a powerful tool to monitor human physiological parameters in a real-

### 3.1 Sweat sensing

---

time, non-invasive and accurate manner. Several new chemical sensors are proposed in the literature to detect electrolytes<sup>407–410</sup> and biochemical markers like dopamine,<sup>411</sup> adrenaline,<sup>40,412</sup> cortisol,<sup>51</sup> glucose,<sup>413</sup> lactate,<sup>414</sup> phenolic compounds<sup>415</sup> to provide new tools for monitoring human health, physical exertion, fatigue and mental accuracy. An interesting approach has been proposed by Gao et al. based on a fully integrated and mechanically flexible sensor array for multiplexed sweat analysis, which selectively and simultaneously measures perspiration electrolytes (sodium and potassium ions) and metabolites (glucose and lactate<sup>22</sup>).

Their widespread use of textiles, in addition to a well-established manufacture background, made them promising and cutting-edge materials for a new concept of smart sensors. It is possible to exploit their flexibility, portability, non-invasiveness, and light weight to continuously monitor the human body. The possibility to integrate into a fabric an array of multiple textile sensors able to selectively detect different analytes in human perspiration would allow the implementation of a powerful textile multi-sensor platform, a sort of lab-on-fabric device. In the last decade, chemical textile-based sensors were presented to measure various sweat parameters<sup>149</sup> simultaneously. Still, preliminary multi-sensing systems based on functionalised textiles have only been reported in the previous two years.<sup>153,154</sup>

The main biomarkers present in sweat move from the bloodstream to the skin surface. They can be exploited to gain information about human physiological status and health with a non-invasive sampling performed outside the body. In addition, iontophoresis can be used to stimulate sweating on-demand, allowing continuous monitoring without external contamination and before the analyte degrades. Chloride and pH are two common parameters used in wearable sensing applications because they are related to human biomarker monitoring. Their simultaneous detection allows for an overview of hydration status,<sup>416</sup> fatigue,<sup>417</sup> alkalosis,<sup>418</sup> metabolic reactions<sup>419</sup> and physiological conditions. It is worth noting that the  $\text{Cl}^-$  concentration in sweat (10–100 mM<sup>99</sup>) allows making significant progress in developing textile electrochemical sensors without requiring a sub-mM limit of detection. Moreover, typical pH values in human perspiration range from 4.7 to 6.6, but values up to pH 9 have been found in patients affected by cystic fibrosis.<sup>420</sup>

Table 3.1 reports the performance of new wearable chemical sensors able to monitor  $\text{Cl}^-$  concentration and pH of sweat in a linear range that is physiologically relevant. In particular, in 2019, Xu et al.,<sup>421</sup> reported electrochemically wearable  $\text{Cl}^-$  sensors that could be used in parallel with a  $\text{Ca}^{2+}$  sensor patch showing a sub-nerstian sensitivity. Kim et al. described<sup>422</sup> a two-terminal PEDOT:PSS thread that can be sewn into a fabric and non-selectively sense total cations concentration. Bujes-Garrido et al.<sup>423</sup> reported voltammetric screen-printed three-terminal  $\text{Cl}^-$  sensors with AgNPs deposited onto the working electrode, employing both PET and Gore-Tex as substrate. Despite the low limit of detection of 5  $\mu\text{M}$ , it exhibits a narrow operation range 5–60 mM, thus limiting its operation to

applications where small concentration variations are expected and in liquid where the  $[Cl^-]$  does not exceed 60 mM. All reported systems are based on an electrochemical transduction that can be amperometric, potentiometric or mediated by an organic electrochemical transistor and must be endowed with additional elements such as reference, counter or gate electrodes. Therefore, several threads must be inserted into the fabric and immersed in the same electrolyte solution during sensing. In the present chapter, a two-terminal sensor that keeps the robustness of the potentiometric-like transduction will be reported for the simultaneous and real-time detection of pH and  $Cl^-$  in human sweat.

**Table 3.1:** Main features of recent textile and wearable sensors for pH level and Chloride ions.

	Active Material	Textile Support	Transduction mechanics	Sensitivity	Characterisation solution	Linear range	Ref
pH	IrOx film	Nylon-based conducting fabric	Potentiometric	47.54 Mv/Ph	Buffer/real sweat	4-8	423
	Graphite-polyurethane composite	Cellulose polyester blend cloth	Potentiometric	4 mV/pH	Buffer	6-9	137
	PANI	Gold fibres woven into textile matrix	Potentiometric	60.6 mVpH	Buffer/Artificial Sweat	4-8	138
Cl <sup>-</sup>	Ag ink	PDMS	Potentiometric	-51.05 mV/dec	NaCl, artificial Sweat	10-160 mM	421
	PEDOT:PSS		OEET	150 10 <sup>-3</sup> dec <sup>-1</sup>	PBS, Artificial/human sweat	1 mM-1 M	422
	Ag NPs	PET/Gore-Tex	Voltammetric	292.2 $\mu$ AM <sup>-1</sup>	Synthetic sweat	5-60 mM	423

## 3.2 Organic electrochemical transistor

The first organic electrochemical transistor was developed by Wrighton et al. in the early 80s.<sup>424</sup> Currently, OEETs are gaining much interest due to the new and innovative opportunities related to printed electronics. Due to low-voltage operation, ease of fabrication (also on flexible substrates<sup>425</sup>) and the possibility of integration in biological environments, OEETs have been used for several applications, including analyte sensing (dopamine,<sup>296</sup> ascorbic acid,<sup>426</sup> ions,<sup>427</sup> adrenaline,<sup>412</sup> lactate<sup>428</sup>), tissue engineering biosensors,<sup>429</sup> neural activity sensing,<sup>430</sup> neuromorphic devices<sup>431</sup> and even in wearable platforms.<sup>32,40</sup>

OEETs are fabricated using an electrolyte solution to contact gate and semiconductor channel, as shown in Figure 3.1.a. A permeable conducting polymer is used as a semiconducting channel, such as PANI, PPy, polycarbazole, PEDOT:PSS, and other polythiophene derivatives. Due to the permeability of the polymer used, the whole material bulk interacts with the electrolyte solution and can be used for detection. Thus, reversible doping and de-doping of the polymer results in bulk changes in the channel conductivity, giving a very high transconductance (i.e. high amplification properties for low voltage application) dictated by the volumetric capacitance.<sup>432</sup> Transconductance is an important

## 3.2 Organic electrochemical transistor

---

figure of merit of the OECT, representing the efficiency of its transduction mechanism and is calculated as the first derivative of the transfer curve,  $g_m = \partial I_d / \partial V_g$ .<sup>433</sup>

The OECT working principle is based on capacitive processes, where ions pushed in the channel electrostatically compensate the presence of opposite charges<sup>434</sup> without exchanging charges with the semiconducting film, thus without electrochemical reactions between channel and electrolyte. They operate in two different regimes: Faradaic and non-Faradaic (capacitive).<sup>435</sup> In the Faradaic regime, irreversible reduction/oxidation reactions occur between electrode and electrolyte upon the application of a gate voltage, thus leading to a steady-state gate current, which lowers down the potential drop at the gate/electrolyte interface, increasing the gate effect operating on the channel. Though this regime owns the highest sensitivity, the irreversible oxidations or reductions taking place in the electrolyte affect device characteristics that will decay with time and will be sensitive to electrolyte nature. In a non-Faradaic regime, gate voltage application leads only to a capacitive current at the gate electrode,<sup>436</sup> because the gate electrochemical potential remains inside the stability window of the electrolyte, thus only reversible charging of ionic double layer at the gate or electrolyte interface occurs. Therefore, a significant potential drop is present at this interface, which reduces the effective gate voltage operating on the channel. Since both regimes depend on the quantity of active material and the capacitances at the interfaces, the geometry of the transistor matters and, in particular, the ratio between gate and active channel areas ( $A_g/A_{ch}$ ) have been explored and studied in many works.<sup>435,437,438</sup> More precisely, it has been proven that channel thickness also affects OECT behaviour and sensitivity,<sup>426,439</sup> thus highlighting that volumetric capacitance should be taken into account.<sup>440</sup>

OECTs exhibit intrinsic properties for portable applications given the simple readout electronics required, the low power supply, and the resulting low power consumption (typically applied voltages  $<1$  and power  $<100\mu W$ ). Additionally, the OECT configuration does not require freestanding reference electrodes used in traditional electrochemical setups and offers design freedom in terms of geometries, sizes, and substrates. In addition to their inherent versatility, robustness, and ease of integration, they can be fabricated and miniaturised with low-cost, large-scale technologies.

### 3.2.1 Working principle of OECT

OECTs can work either in accumulation or in depletion mode, the latter being the most commonly utilised in recent works. In this case, the polymer is in its pristine doped state and is switched to the un-doped state via gate bias. The OECTs presented in this work are based on a PEDOT:PSS channel of p-doped conductive polymers and working mainly in depletion mode. Thus, the application of a positive bias on the gate pushes cations from the electrolyte into the semiconducting channel, de-doping it and decreasing the source-

## 3.2 Organic electrochemical transistor

---

drain current,  $I_{ds}$  (Figure 3.1.b). OEET working principles are well-described using the Bernards-Malliaras model.<sup>441</sup> The device is divided into two circuits: ionic and electronic. The former takes ion flow into account in the gate-electrolyte-channel structure, while the latter describes the electronic transport in the semiconducting channel (Figure 3.1.c).

Ohm's law is employed to describe holes movement in the semiconducting channel of the electronic circuit:

$$J(x) = q \mu p(x) dV(x)/dx \quad (3.1)$$

where  $J$  is the current flux,  $q$  is the elementary charge,  $\mu$  is the hole mobility,  $p$  is the hole density, and  $dV/dx$  is the electric field. Under applying a positive  $V_g$ , each injected cation from the electrolyte to the channel compensates one acceptor. This process occurs in two steps in order to maintain electrical neutrality in the semiconductor at the steady-state. When a cation compensates an acceptor, applying a positive  $V_d$ , a hole is extracted from the source (lower potential) and not replaced at the drain.

Then, the expression for the effective dopant density inside the volume  $V$  is:

$$p = N_i - N_{inj} = p_0(1 - Q/qp_0V) \quad (3.2)$$

with  $p_0$  as the initial hole density in the organic semiconductor before de-doping process and  $Q$  is the total charge of injected cations. In order to simplify the equations and calculations, negative ions are assumed to have no effect on the organic semiconductor and charge densities are assumed to be uniform across the organic semiconductor film thickness, limiting the use of this model to thin films.

The ionic circuit can be described by a resistor ( $R_s$ ) and a capacitor ( $C_d$ ) in series,<sup>397</sup> the former taking into account the conductivity of the electrolyte (i.e. its ionic strength), with the latter representing the polarisation at the gate electrode/electrolyte and electrolyte/semiconducting channel interfaces. Since the high capacitance of semiconducting polymers (in primis PEDOT:PSS),<sup>442</sup> channel capacitance is expected to be higher than gate capacitance (per unit area). Thus, properties such as the response time and the gating effect will depend on gate capacitance, which is affected by the dimensions and material composition of the electrode. The current flowing at the gate electrode is a sum of the capacitive charging of an electrical double layer at the electrolyte/gate interface (non-Faradaic process)<sup>443</sup> and electrochemical reactions occurring at the gate electrode (Faradaic process) which are neglected.

The RC ionic circuit has a transient behaviour of a charging capacitor upon the gate bias application, described as:

$$Q(t) = Q_{ss}[1 - \exp(-t/\tau_i)] \quad (3.3)$$

### 3.2 Organic electrochemical transistor

---

Where  $Q_{SS} = C_d \Delta V$  represents the total charge passing through the circuit,  $\Delta V$  is the voltage applied across the electrolyte, and  $\tau_i = C_d R_s$  (RC constant) is the ionic transient time. As demonstrated by Rivany et al.<sup>439</sup>, on OECT formed by organic semiconductors, as PEDOT:PSS, which are permeable to ions, capacitance per unit volume (volumetric capacitance,  $C^*$ ) should be used in these calculations.

In order to model the OECT device behaviour, the effective dopant density (Eq 3.2) must be spatially known inside the semiconducting channel. Considering the Figure 3.1.d, the charge in the volume fraction  $WTdx$  at the steady-state for the differential slice,  $dx$ , in the position  $x$ , can be expressed as:

$$Q(x) = C^* (V_g - V(x)) WTdx \quad (3.4)$$

where  $V_g$  is the voltage applied on the gate,  $T$  and  $W$  are the thickness and the width of the slice, respectively, and  $V(x)$  is the spatial voltage profile in the semiconductor film. Through the combination of Eq. 3.1, 3.2 and 3.4, the general OECT equation at steady-state can be described with:

$$J(x) = q\mu p_0 \left(1 - \frac{Q(x)}{qp_0 v}\right) dV(x)/dx = q\mu p_0 (1 - (V_g - V(x))/V_p) dV(x)/dx \quad (3.5)$$

with  $V_p = qp_0/C^*$ , pinch-off voltage (also called threshold voltage), i.e. the voltage needed to accumulate a charge density equal to the intrinsic dopant density in the semiconductor. At the steady-state,  $J(x)$  must be spatially constant along the channel, thus for the ideal geometry, shown in Figure 3.1.d, it can be expressed as  $J(x)=J=I/WT$ . Thus,  $I_d$  can be obtained from Eq 3.5 for different regimes, keeping in mind that  $0 \leq |V(x)| \leq |V_d|$  and de-doping occurs only when  $V(x) < V_g$ . From the source-drain current, it is possible to calculate the transconductance  $g_m = \partial I_d / \partial V_g$  of the device, or the figure of merit that quantifies the efficiency of the transduction (OECT amplification).

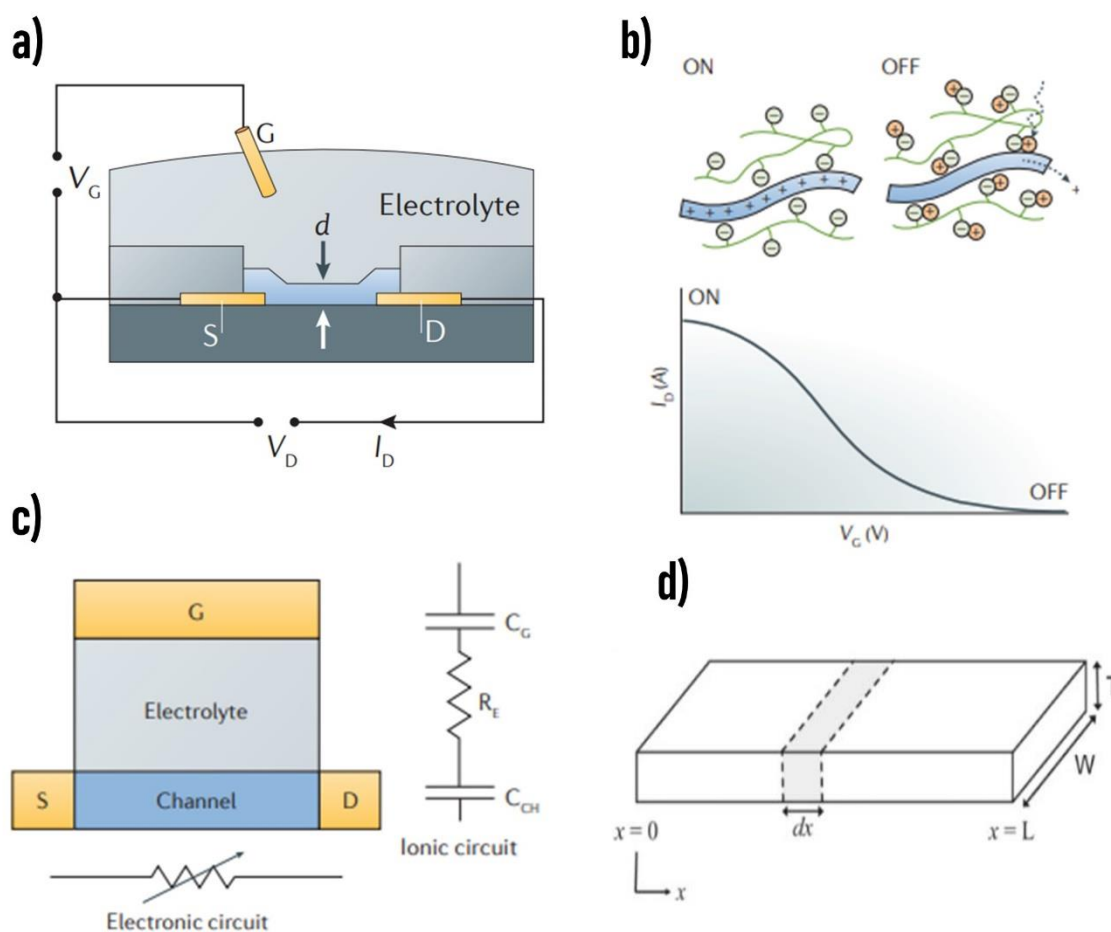


**Figure 3.1:** The typical structure of an organic electrochemical transistor (OEECT), showing the source (S), drain (D), electrolyte and gate (G). b) Transfer curve showing depletion-mode operation of an OEECT with a conducting polymer channel. At zero gate voltage, holes on the conducting polymer contribute to a high drain current and the transistor is ON. When a gate voltage is applied, the holes are replaced by cations and the transistor is OFF. c) Ionic and electronic circuits used to model OEECTs. The electronic circuit, shown below the device layout on the left, is modelled as a resistor with a resistance that varies upon gating. The ionic circuit, shown in the middle, consists of capacitors corresponding to the channel,  $C_{CH}$ , and gate,  $C_G$ , respectively, and a resistor corresponding to the electrolyte,  $R_E$ . d) Organic semiconductor film with the source is located at  $x = 0$  and the drain at  $x=L$ .

### 3.3 OEECT as chloride sensor

The monitoring of chloride ions in a liquid environment can be achieved in different ways exploiting various reactions according to the sensors' working principle. In order to take advantage of the OEECT amplification feature, a silver metal wire with AgCl coating is employed as gate electrode to have a selective response for  $Cl^-$  ions. Figure 3.2.a reports an example of an OEECT on glass substrate with a channel of PEDOT:PSS and the Ag/AgCl gate

### 3.3 OECT as chloride sensor

---

electrode immersed in an electrolyte solution with the schematic circuit. The fabrication procedure of the OECT device utilised has been previously reported by Gualandi et. al.<sup>41</sup> In this way, the gate electrode is involved in a spontaneous Faradaic reaction ( $\text{Cl}^- + \text{Ag} \leftrightarrow \text{AgCl} + e^-$ ) that produces an electrochemical potential  $E$  (usually measured with respect to a reference electrode) described by the Nerst equation:

$$E = E_0 - kT/e \cdot \ln[\text{Cl}^-] \quad (3.6)$$

where  $E_0$  is the standard potential of Ag/AgCl redox couple,  $k$  is the Boltzman constant,  $[\text{Cl}^-]$  represent the  $\text{Cl}^-$  ions concentration,  $e$  is the elementary charge, and  $T$  is the absolute temperature. From the equation, a variation in the  $\text{Cl}^-$  concentration is responsible for the offset of the analyte solution's electrochemical potential respective to the gate electrode. The variation of the potential  $E$  in such transistor geometry corresponds to an offset of the effective gate potential ( $\Delta V_g$ ).<sup>444</sup> Since the semiconducting channel is capacitively coupled with the gate electrode, a variation in carrier density and the source-drain current is observed. A positive potential offset is responsible for the injection from the solution to the channel of immobile cations that replace the mobile carriers, namely the hole charges. This response ( $\Delta I_d$ ) can be quantitatively estimated introducing the transconductance  $g_m$  as

$$\Delta I_d = g_m \cdot \Delta V_g. \quad (3.7)$$

The term  $g_m$  describes the amplification effect in an organic electrochemical transistor and is defined as  $g_m = \mu C^* t V_d W / L$  where  $\mu$  is the mobility of the charge carriers,  $C^*$  is the volumetric capacitance,  $T$  is the channel thickness,  $V_d$  is the drain-source potential, and  $W$  and  $L$  are the width and length of the channel, respectively.<sup>439</sup> In this case, the measured transconductance has a maximum value of  $9 \cdot 10^{-4} \text{ A V}^{-1}$  when the gate potential is around 0 V, suggesting that the device works best in the two-terminal configuration.<sup>445</sup> The combination of equation 3.6 and 3.7 lead to the quantitative formula:

$$\Delta I_d = -g_m \cdot \frac{kT}{e} \ln \frac{[\text{Cl}^-]_2}{[\text{Cl}^-]_1} \quad (3.8)$$

where  $[\text{Cl}^-]_1$  (starting) and  $[\text{Cl}^-]_2$  (final) are the chloride concentration that cause the variation in conductivity.

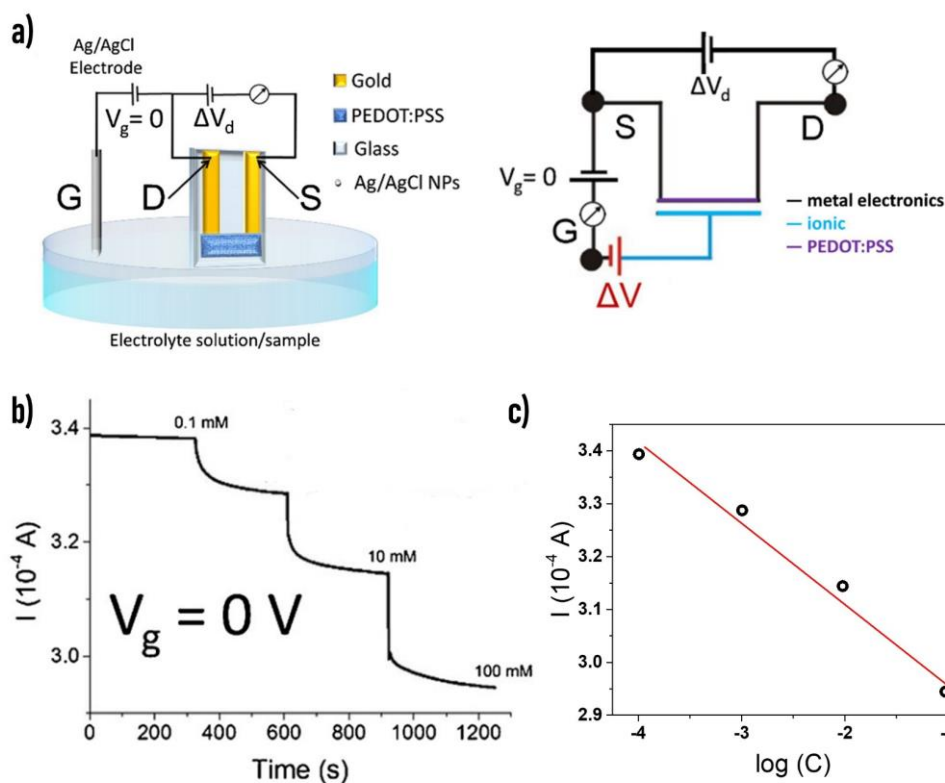


**Figure 3.2:** a) Schematic layout of an OEET composed by a PEDOT:PSS channel and an Ag/AgCl gate electrode with the schematic circuit. b) Source-Drain current vs time plot recorded while increasing the concentration of  $\text{Cl}^-$  in the 0.1M  $\text{KNO}_3$  solution ( $V_g = 0$  V;  $V_d = +0.05$  V). c) Linear dependency of the current with the logarithm of analyte concentration.

Figure 3.2.b reports the current variation over time when the  $\text{Cl}^-$  concentration in the electrolyte solution changes from 0.1 mM to 100 mM. Figure 3.2.c shows the current dependency with the analyte concentration highlighting the predictive linear trend between  $I_d$  and the logarithm of concentration. The efficient Faradaic efficiency and large transconductance appear when the applied gate voltage is zero as the PEDOT:PSS based channel behaves as a doped semiconductor working in a depletion mode and the spontaneous and reversible reaction of Ag/AgCl nanoparticles that reacts with  $\text{Cl}^-$  ions is able to change the charge flux in the external circuit proven by the small gate current (one order of magnitude smaller than the drain current). This reaction modulates the channel conductivity by the extraction on charge carrier without requiring a gate bias.

### 3.3.1 Two-terminal configuration

Taking into account this result, it is possible to design simpler devices with a semiconducting polymer channel endowing its surface directly with gating features

provided by nanoparticle compounds (Figure 3.3.a-b). The new concept of semiconducting polymer-nanoparticles (SP/NPs) interface relies on the NPs providing the electrochemical reactions at the surface channel maintaining the transistor amplification effect even without the presence of the gate electrode. The selectivity of the device to Cl<sup>-</sup> ions is achieved by growing silver/silver chloride NPs onto the channel surface that are responsible for the Faradaic reaction at the solution/SP interface providing the potential offset  $\Delta V$  which changes according to the analyte concentration. A model that describes the transduction mechanism highlighting the charge transfer process that takes place in the channel/ solution interface is shown in Figure 3.3.c. The increment in the Cl<sup>-</sup> concentration in the surrounding solution leads to the release of electrons following the redox equilibrium reaction involving Ag and AgCl. Since the NPs are in direct electrical contact with the semiconductor polymer, the released electrons are collected into the PEDOT:PSS channel and the consequent hole-electron recombination takes place. The direct effect is the decrease of the charge carriers concentration and the source-drain current. When low  $V_d$  bias is applied through the channel, the conductivity is linearly related to the mobility, electronic charge, and charge carrier density:

$$\sigma = \mu e n. \quad (3.9)$$

As reported by Malliaras et al.,<sup>434</sup> the amount of charge carrier injected into the polymer under the presence of a potential difference  $\Delta V$  can be expressed introducing the volumetric capacitance as:

$$\Delta n = \frac{C^*}{e} \Delta V. \quad (3.10)$$

As previously stated, the Nerst equation governs the redox reaction between Ag and AgCl which generates the potential difference  $\Delta V$  in the SP/NP material. Merging the equation 3.6, 3.9, and 3.10, the logarithmic relationship that correlates the conductivity variation  $\Delta\sigma$  with the Cl<sup>-</sup> concentration is found:

$$\Delta\sigma = -C^* \mu \left( \frac{kT}{e} \ln \frac{[Cl^-]_2}{[Cl^-]_1} \right) \quad (3.11)$$

Considering the applied potential  $V_d$  and the geometric factor of the channel, it is possible using the Ohm's law ( $V = I l / \sigma A$ ) to express the current variation:

$$\Delta I = - \frac{W T C^* \mu V_d}{l} \left( \frac{kT}{e} \ln \frac{[Cl^-]_2}{[Cl^-]_1} \right) \quad (3.12)$$

This formula is equal to one derived for the OECT endowed with a silver or silver chloride wire as the gate electrode. If the device structure presents only two terminals, the

### 3.3 OECT as chloride sensor

proportional constant  $c$  linking the current and  $E$  variations has the same meaning of the transconductance  $g_m$  of an OECT (see equation 3.8) and can be used to evaluate the amplification.

Figure 3.3.d shows the response of a two-terminal SP/NPs device realised on glass substrate under subsequent additions of  $\text{Cl}^-$  in the electrolyte solution. The semiconducting polymers is PEDOT:PSS, while the silver/silver chloride nanoparticles present on the channel surface endow the device with  $\text{Cl}^-$  sensing ability. Similar behaviour to the OECT device is also reported by the two-terminal structure with a decreasing linear correlation between the current and the logarithm of  $\text{Cl}^-$  concentration (Figure 3.3.e). Table in Figure 3.3.f reports a quantitative comparison between the two- and three-terminal devices. The sensitivity is expressed using the normalised current variation as  $\Delta(1 - I/I_{max})/\Delta(\log[\text{Cl}^-])$  while the response time is evaluated as the time required to reach 90% of the final response after an additional 100 mM of  $\text{Cl}^-$ . The close electric contact between the SP material and NPs minimise the electric resistance between the PEDOT:PSS channel and Ag/AgCl NPs, allowing a better charge transfer with a consequent improvement in the response time. Finally, the comparable sensitivity values show that the two-terminal device maintains the intrinsic amplification feature typical of an OECT.

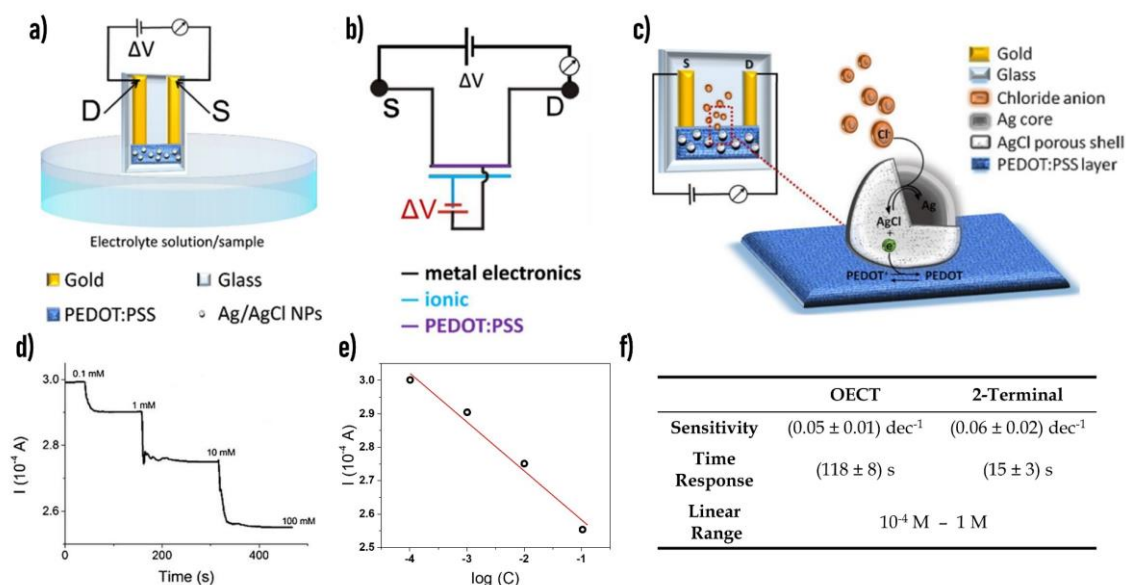


**Figure 3.3:** a) Schematic layout of the SP/NP-based two terminal sensor, composed by a PEDOT:PSS stripe modified with Ag/AgCl NPs, and b) schematic circuit; c) Operation mechanism of the  $\text{Cl}^-$  sensor composed by a PEDOT:PSS stripe modified with Ag/AgCl NPs. d) Source-Drain current vs time plot recorded while increasing the concentration of  $\text{Cl}^-$  in the electrolyte ( $V_d = + 0.05 \text{ V}$ ). e) Linear trend of the device current with the logarithm of concentration. f) quantitative comparison between the two- and three-terminal devices.

#### 3.3.2 Silver/silver chloride nanoparticles

The device simplification from three- to two- terminal is possible due to the presence of silver or silver chloride material, in the form of nanoparticles, onto the semiconducting channel. The fabrication procedure, as well as the physical and chemical properties of the nanostructured material utilised to produce the textile thread sensors are outlined below.

##### 3.3.2.1 Fabrication procedure

The conductive polymer PEDOT:PSS Clevios PH1000 is mixed with ethylene glycol, dodecylbenzenesulfonic acid, and 3-glycidylpropyltrimethoxysilane in the following volumetric ratio 78.95:20:0.05:1. The solution is then spin-coated onto a glass substrate patterned with chromium/gold contacts for the electric contacts to realise the conductive channel of the device. Ag/AgCl NPs are prepared by electrodeposition using a three-electrode cell (working electrode: PEDOT:PSS channel, reference electrode: saturated calomel electrode, counter electrode: Pt wire). The deposition procedure involves two consecutive steps as reported in Figure 3.4.a. In the first step, the Silver particles are deposited by applying a potential of -0.2V for 30 s while the sample is immersed in a 0.1 M AgNO<sub>3</sub> solution. After washing the electrode with distilled water, the second step takes place when immersing the channel in a solution of 1M KCl for 30 s applying a potential of +0.6V. This second step allows the formation of an external shell of AgCl onto the already present silver particles.

##### 3.3.2.2 Characterisation

A uniform coverage with particles with a diameter of  $(300 \pm 8)$  nm and a density of 7.5 particles  $\mu\text{m}^{-1}$  is obtained on the surface of the conductive channel of PEDOT:PSS. The SEM image in Figure 3.4.b shows the particles do not form a continuous layer that can effectively carry charge, thus the electrical properties of the composite material are mostly attributed to the conductive polymer layer. Additionally, a characterisation with Atomic Force Microscopy (AFM) in Scanning Kelvin-Probe Mode (SKPM) permits the electronic structure of the material to be shown. SKPM allows the measurement of the local surface potential. For all conducting materials, conductive polymer and, in this case, NPs, variations of surface potential are correlated with variations of the work function (WF). Using a gold substrate with a work function of 5.1 eV as a reference, Figure 3.4.c shows a WF map for a particle deposited on a PEDOT:PSS film with the corresponding AFM image (Figure 3.4.d). The surrounding conductive polymer has a work function of 5.05, in agreement with the values reported in the literature for PEDOT:PSS PH1000.<sup>446</sup>

### 3.4 OEECT as pH sensor

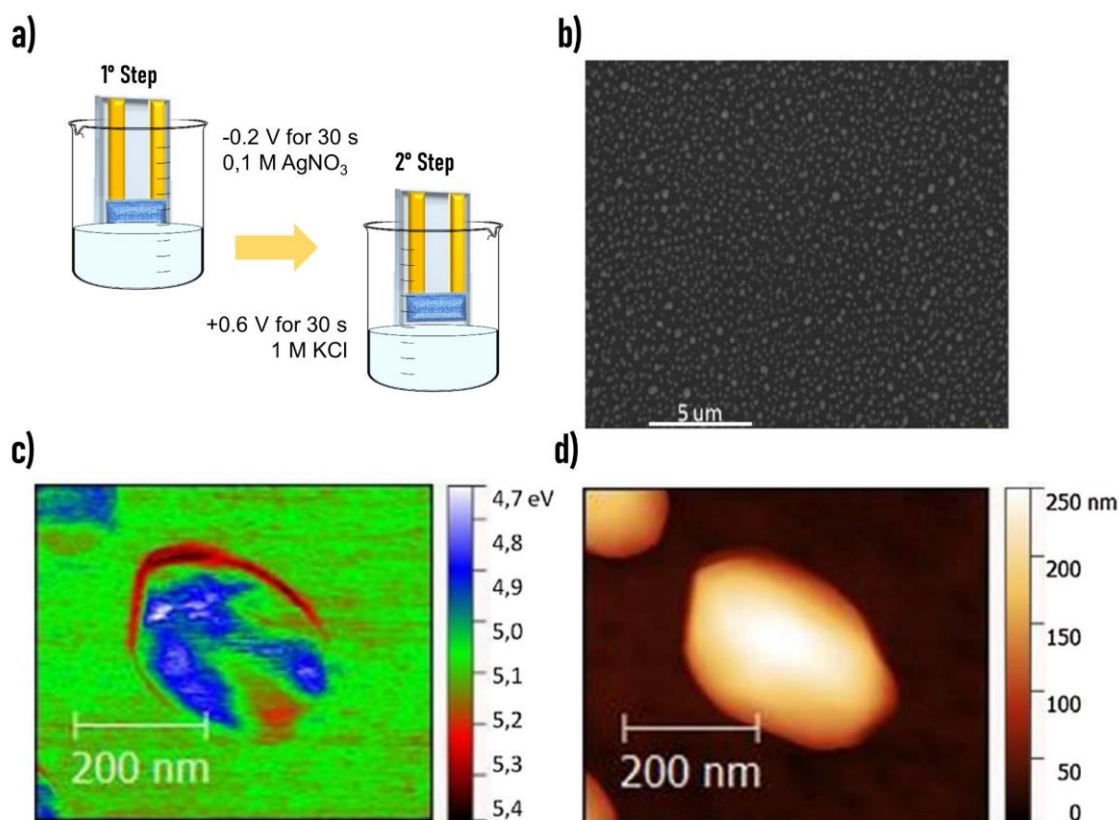


**Figure 3.4:** a) Two consecutive steps for the deposition of Silver/Silver Chloride nanoparticles. b) SEM image of PEDOT:PSS modified with Ag/AgCl NPs. c) KPFM and d) AFM image of a single Ag/AgCl NP.

Two main phases are observed on the NPs: one in the centre of the particle and one in the boundaries. The red colour on the edge of the particle indicates a WF of 5.5 eV, which is higher than that of PEDOT:PSS, and is associated with the presence of AgCl.<sup>447</sup> Inside the particle, however, the blue and white colouring indicates that the WF reaches values below the level of PEDOT:PSS ascribed to the presence of metallic silver in the centre. It is responsible for the electrostatic attraction with the tip of the AFM; the obtained values between 4.7 eV and 4.8 eV are characteristic of elementary silver.<sup>448</sup> It is concluded that the electrodeposited NPs are formed by a central silver zone and a porous outer layer of AgCl. However, the different constituents of the composite material (e.g., conductive polymer and particles) are in direct electrical contact and on single Fermi level for the whole material to be considered.

### 3.4 OEECT as pH sensor

The non-invasive and real-time measurement of the pH of biofluids, such as human sweat, is attracting much interest<sup>449,450</sup> given its close connection with physiological conditions, such as dehydration or alkalosis.<sup>125,451</sup> Many sensitive wearable platforms able

to measure pH have been reported, but most are based on colorimetric determination by pH indicators<sup>452</sup> or potentiometric transduction by electropolymerized polyaniline (PANi).<sup>453</sup> The biggest limitation of these optical systems is related to the complex and bulky readout electronics required while the potentiometric-based systems have a sensitivity limited to the ideal Nernst value of 59 mV pH<sup>-1</sup>, as well as needing a reference electrode. In this scenario, OECTs represent a three-terminal device that shows favorable characteristics to overcome the above limitations. Typically, the gate contact is metallic and the channel is made of a thin layer of conductive polymer, especially PEDOT:PSS. Due to the ability of PEDOT:PSS to transduce ions into electrons, OECTs operate in aqueous environments and are able to convert biochemical to electronic signals with particularly high sensitivity. In this thesis, it is reported that the working principle and the performance of a flexible pH sensors for human sweat based on a PEDOT:dye composite is able to transduce the pH solution in an electronic signal. Before this new technology is applied in textile sensors, the electrochemical performance of the dye-based pH sensitive material and the high sensitivity in an organic electrochemical transistor configuration will be described.

#### 3.4.1 OECT with PEDOT:BTB-modified gate

The pH sensitive material here used is based on an idea proposed by Balamurugan et al.,<sup>346</sup> and exploits the dye Bromothymol Blue as a PEDOT counterions, bonded via electrosynthesis.

##### 3.4.1.1 Electrochemical characterisation of PEDOT:BTB as pH sensing material

Using a polymerisation solution made of 10 mM EDOT monomers, 1 mM BTB, and 1 mM PBS in 0.1 KNO<sub>3</sub> aqueous solution, reported by Gualandi et al.,<sup>347</sup> a glassy carbon electrode (GCE) is covered by a blue iridescent film of PEDOT:BTB by a three-electrode electrodeposition. The material response to pH was studied performing voltammograms (scanning velocity of 10 mV s<sup>-1</sup>) of GCE electrode covered with PEDOT:BTB in buffer solution with different pH. Figure 3.5.a shows the couples of well-defined reversible peaks in a large pH range, with a shift of the peak potential ( $E_p$ ) toward less anodic values when the pH of the electrolyte solution increases. The electrochemical characteristics of the pH-sensitive film were evaluated by taking the values of the peaks ( $E_p$ ) in the forward and reverse cycles, and plotting these values as a function of the pH of the electrolyte solution, thus obtaining a linear relationship. The direct sensitivity for the PEDOT:BTB film on GCE is  $(48 \pm 2)$  mV pH<sup>-1</sup> and the inverse sensitivity is  $(62 \pm 2)$  mV pH<sup>-1</sup>. With this result, the PEDOT:dye compound can convert a chemical signal such as pH into an electrical signal due to the formation of pH-dependent electron states within the conductive polymer when the BTB is used as a counterion (See paragraph 2.2.3 - Material and Methods).

### 3.4 OECT as pH sensor

#### 3.4.1.2 OECT pH-sensor: working principle

Exploiting this feature, an OECT with an output signal dependent on the solution's pH level is reported for the first time. The device operates without requiring a reference electrode, and utilises a metal gate electrode coated with PEDOT:BTB and a conductive channel of PEDOT:PSS (Figure 3.5.b). Figure 3.5.c shows the electrochemical process underlying the device's operation as a pH sensor.  $M^+$  represents cations from the electrolyte solution generated by the gating effect. The acid-base balance of the BTB directly influences the doping level of the PEDOT at the gate electrode. Consequently, balance takes part in the doping/dedoping process that occurs at the PEDOT:PSS channel when cations are injected/extracted from the electrolyte under the gate action. Specifically, the protonation/deprotonation of the BTB counterion impacts the electrochemical potential, and thus the PEDOT capacitance at the gate resulting in the pH-dependent modulation of the current ( $I_d$ ) in the channel. The ion circuit in Figure 3.5.d outlines the electrolyte solution resistance ( $R_s$ ), the channel resistance ( $R_{ch}$ ) and capacitance ( $C_{ch}$ ), and the gate capacitance ( $C_g$ ).

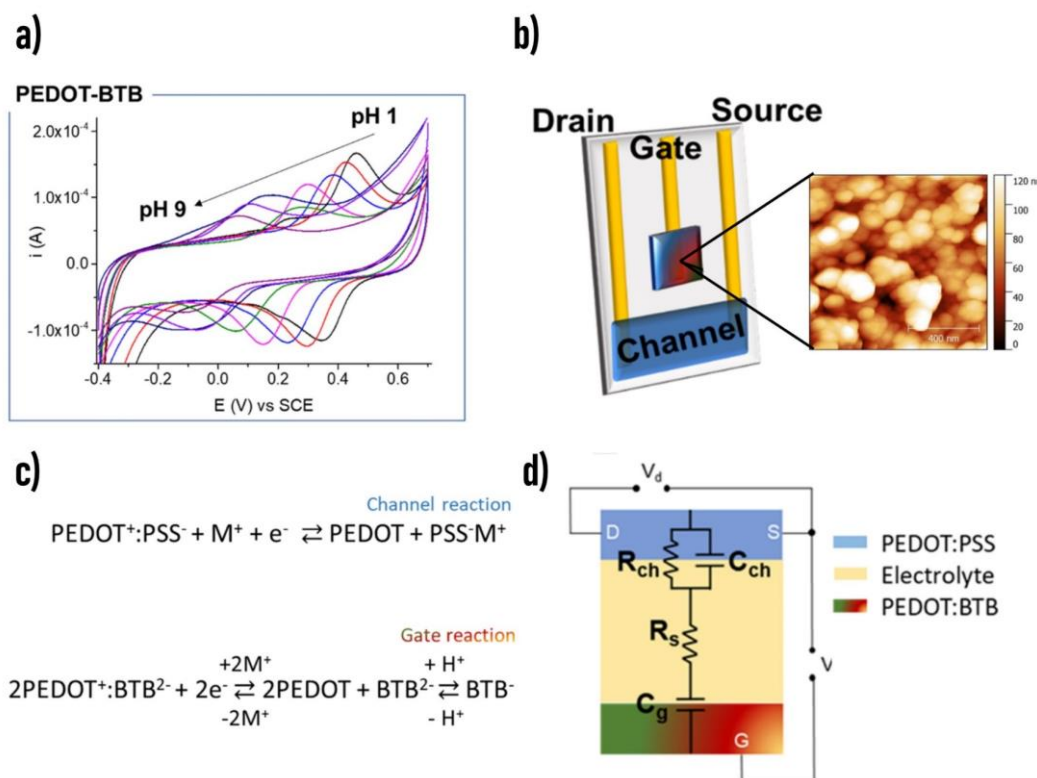


**Figure 3.5:** a) pH response of the synthesized materials. CV of PEDOT:BTB film on GCEs recorded at 10 mV s<sup>-1</sup> in different pH buffers. b) Cartoon of the resulting device after gate functionalization with the pH sensitive materials. Drain, source, and gate gold contacts are opportunely insulated with PDMS to define the active areas. The inset shows the topography maps obtained by AFM imaging for gate electrodes modified with 10 deposition cycles PEDOT:BTB films. c) Electrochemical processes that rule the OECT working as pH sensor. d) Equivalent circuit of the OECT.

### 3.4 OECT as pH sensor

#### 3.4.1.3 OECT pH-sensor: fabrication

The OECTs fabricated present planar U-patterned channels, with the gate electrode in the middle. The electrical contacts are made with thin strips of thermal-evaporated chromium/gold (50 nm). The channel (800 nm thickness) is made by spin-coating a PEDOT:PSS based solution with EG as second dopant, (3-glycidyloxypropyl)trimethoxysilane (GOPS) as cross linker and dodecylbenzenesulfonic (DBSA) as surfactant. The electrochemical transduction in the OECT is achieved by coating the gold gate electrode with PEDOT:BTB film by potentiodynamic electrodeposition varying the potential between 0 V and 1 V for 10 deposition cycles. The inset in Figure 3.5.b shows the AFM image of the PEDOT:BTB layer on the gate electrode. The presence of discrete particles with large, uniform distributed domains, and the well-defined globular grains are common features for electrodeposited PEDOT.<sup>454</sup>

#### 3.4.1.4 OECT pH-sensor: characterisation and results

The OECT can operate with a two-fold transduction process that is potentiodynamic and potentiostatic; both showing super-Nernstian sensitivity and robustness. The potentiodynamic approach involves the application of a constant drain potential of -0.3 V while the gate potential is varied from -0.5 to +0.6 V. Figure 3.6.a shows the concept of a potentiodynamic measurement.  $I_g$ - $V_g$  curves are acquired by immersing the device in buffer solutions with different pH.

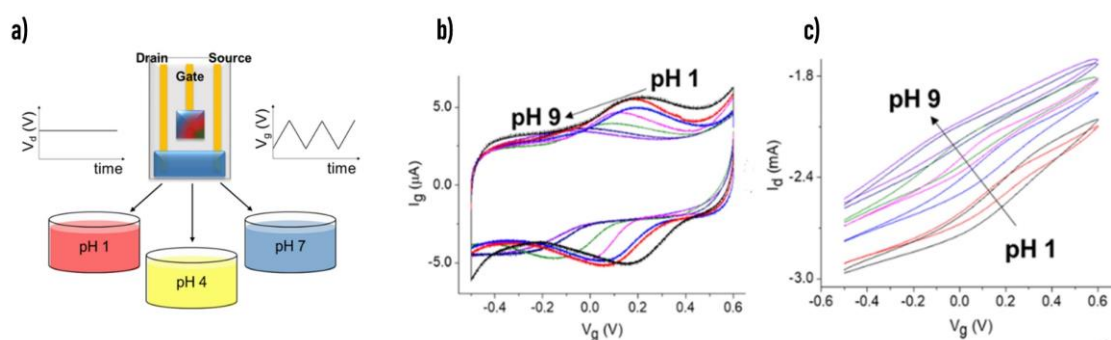


**Figure 3.6:** a) Scheme of the potentiodynamic approach. b)  $I_g$ - $V_g$  and c) transfer curves in different pH buffers.  $V_g$  scanned from -0.5 to +0.6 V at  $10 \text{ mV s}^{-1}$ ;  $V_d = -0.3 \text{ V}$ .

The curves in Figure 3.6.b show well-defined and reversible peaks, similar to the  $E_p$  peaks in cyclic voltammetry, which follow a linear trend as the pH changes. In this case, the signal peaks, expressed by  $V_{g,r}$ , shift toward cathodic values as the pH value of the buffer solution increases, from pH 1 to 9. Simultaneously, the negatively biased channel current is modulated by the action of the gate, which is sensitive to the pH of the buffer solution.

### 3.4 OECT as pH sensor

Depending on the pH value, increasing from acidic to basic, an upward shift in the transfer curves occurs, showing inflection points that gradually move toward smaller values of  $V_g$  (see Figure 3.6.c). Due to the definition of the transconductance  $g_m (= \delta I_d / \delta V_g)$ , these inflection points have the same abscissa of the maximum values in the plot  $g_m$  versus  $V_g$ . The  $g_m$  maximum peak potential is chosen as the analytical signal.

The positions of the transconductance curves' peaks are therefore expressed by the corresponding potential values  $V_g$ , and linearly depend on the pH solution (Figure 3.7.a). The peaks shift toward cathodic values as the acidity of the solution increases. A sensitivity equal to  $(93 \pm 8) \text{ mV pH}^{-1}$  is extracted from three different OECT pH sensors, each randomly immersed in different buffer solutions. The super-Nernstian behaviour is shown in Figure 3.7.b (highlighted in red) and is compared with the grey shadow representing the ideal slope of  $59 \text{ mV pH}^{-1}$ .

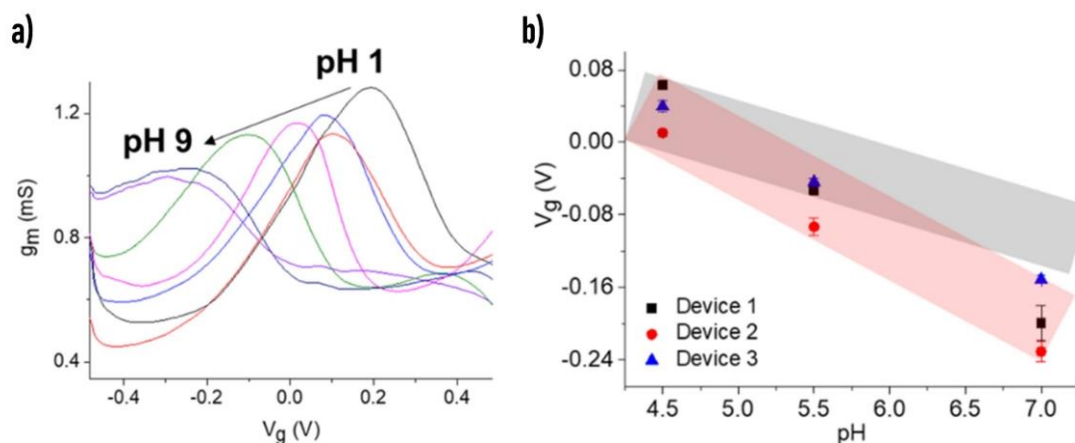


**Figure 3.7:** a) Transconductance calculated from the backward scan of Figure 3.6.b versus  $V_g$ . b) Transconductance peak potential versus pH for three devices tested three times. Error bars indicate the standard deviation. The dark shadow represents the Nernstian slope  $-59 \text{ mV pH}^{-1}$  for comparison.

With the aim of monitoring pH changes in real time, the OECT is tested potentiostatically by changing the pH value of the solution in which it is immersed. Constant potentials of  $-0.2 \text{ V}$  and  $-0.1 \text{ V}$  are applied to the channel and gate, respectively, according to the scheme shown in Figure 3.8.a. The gate and channel currents as a function of time are shown in Figure 3.8.b. Increasing the pH of the solution leads the device to a new steady-state current situation in which the  $I_g$ , increasing its value, causes modulation of the step-like current in the channel.

### 3.4 OECT as pH sensor

The normalised current ( $1-I/I_{\max}$ ), which aids in the comparison of different devices, is linearly correlated to the pH solution where the average sensitivity is  $(14.8 \pm 0.5) \text{ pH}^{-1}$  (Figure 3.8.c). To compare this result with that obtained in the potentiodynamic mode, the  $V_{g \text{ offset}}$  value is used as the analytical signal. This parameter, introduced for the first time by Bernardis et al.,<sup>444</sup> appears in the general expression of effective gate potential,  $V_{g \text{ Eff}} = V_g + V_{g \text{ offset}}$ .

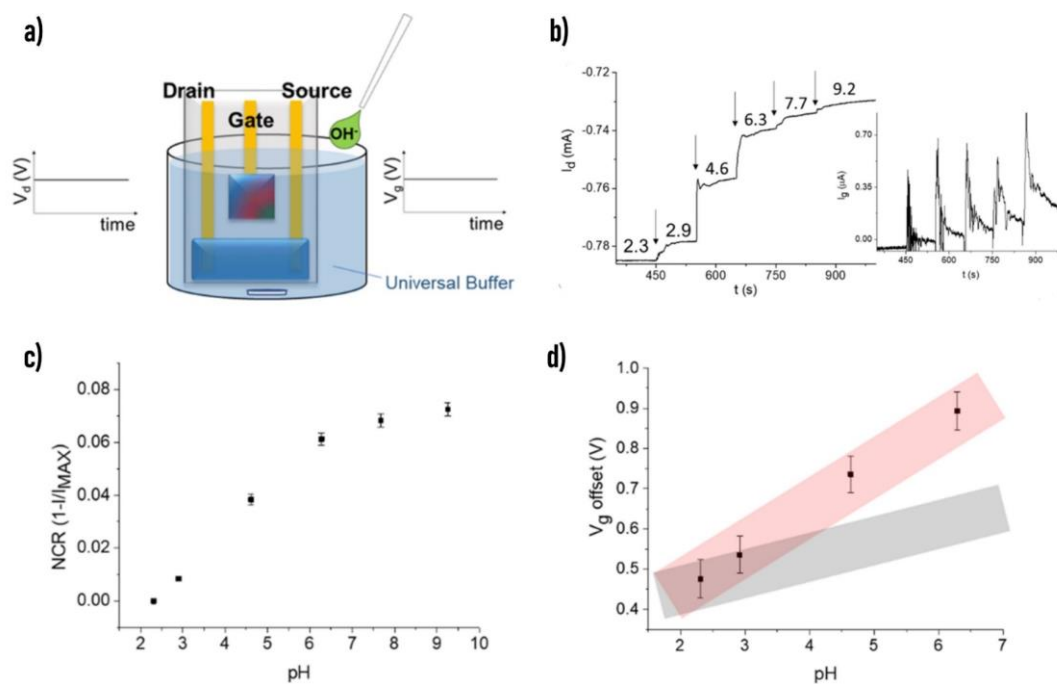


**Figure 3.8:** a) Scheme of the potentiostatic approach. b)  $I_d-t$  and  $I_g-t$  (inset) curves recorded for equimolar additions of KOH to universal buffer under stirring.  $V_d = -0.2 \text{ V}$ ,  $V_g = -0.1 \text{ V}$ . c) Normalized current response versus pH. d) Offset gate potential of the transistor versus pH in the linearity range. The dark shadow represents the Nernstian slope  $-59 \text{ mV pH unit}^{-1}$  for comparison.

The  $V_{g \text{ offset}}$  represents the gate voltage that is effectively acting on the transistor channel when charge-transfer reactions driven by the presence of a redox-active species alter the chemical potential equilibrium between the gate electrode and the electrolyte solution. This potential shift  $V_{g \text{ offset}}$  is strictly linked to the electrochemical potential expressed by the Nernst equation. Based on this, it is linearly correlated to the logarithm of analyte concentration and used as the analytical signal (Figure 3.8.d). Expressing the OECT response by the  $V_{g \text{ offset}}$  dependency to pH, the devices show a super-Nernstian sensitivity of  $(1.1 \pm 0.3) 10^3 \text{ mVpH}^{-1}$ .

### 3.4.2 From three- to two-terminal configuration

The OECT with the modified and electrochemically active PEDOT:BTB electrode is an excellent example of a portable pH sensor in an aqueous environment, such as body fluids. This configuration allows the avoidance of a reference electrode and the exploitation of the amplification effect of a transistor configuration achieving a super-Nernstian sensitivity. The further conceptual step presented in this paragraph opens the way to develop a cost-effective and highly sensitive wearable pH sensor with a simple two-terminal configuration. An electrochemically gated pH sensor is presented with a simple, two-terminal configuration, comprising a charge transport layer of PEDOT:PSS and a pH-sensitive layer based on the Nernstian transducer PEDOT:BTB. The simple geometry of this device will allow the fabrication of pH sensors on a textile single-thread for wearable application and monitoring of human biofluids.

The potentiometric response of the electrodeposited PEDOT:BTB layer on GCE electrode highlights that the transduction mechanism originating the pH sensitivity of PEDOT:BTB relies on spontaneous redox events. The inset of Figure 3.9.a shows the schematic of the potentiometric measure. This is a fundamental feature for the chemically-sensitive layer of an electrochemically gated device. The step-like trend of the open circuit potential in Figure 3.9.a (measured with respect to a reference electrode) indicates an electromotive force's generation at the solid/liquid interface, which endows the PEDOT:BTB with pH transduction capability. A pH value between 2 and 7 leads to a sensitivity of  $(8.3 \pm 0.2) \cdot 10^{-3} \text{ pH}^{-1}$ , which can be expressed in terms of potential as  $62 \text{ mV pH}^{-1}$  based on the previous result (section 3.4.1.4).

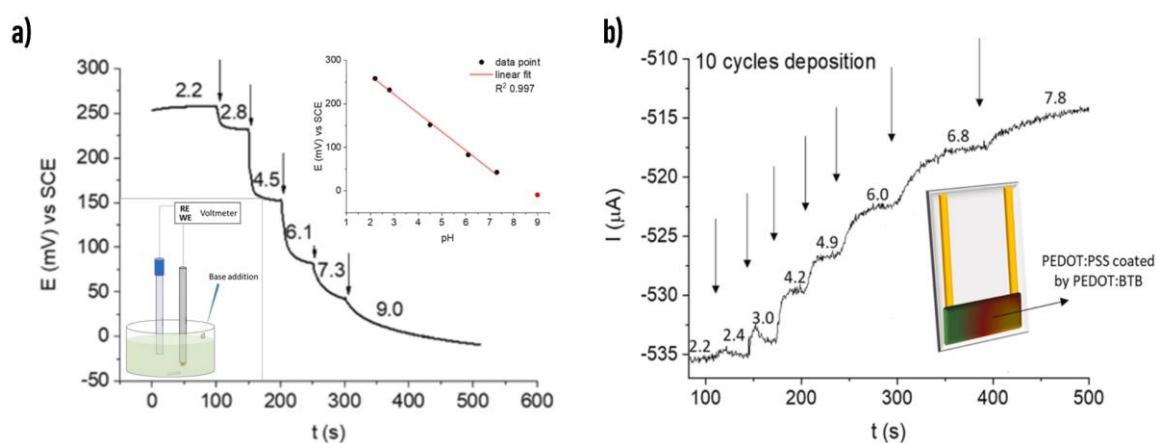


**Figure 3.9:** a) Potentiometric experimental setup used to record the electrochemical potential vs time of PEDOT:BTB/GCE during the addition of 1 M KOH to a Universal Buffer solution and calibration plot obtained from the potentiometric response ( $R^2$  0.997). b) Schematic illustrations of the two-terminal sensor. Current vs. time response to pH variations in U.B. following base additions recorded with a sensor obtained by 10 cycles of deposition of PEDOT:BTB.  $V_{\text{app}} = -200 \text{ mV}$ .

### 3.4 OECT as pH sensor

The electrochemical potential is linearly correlated with the pH solution (inset Figure 3.9.a). With this feature, the pH-susceptible electromotive force generated at the PEDOT:BTB/electrolyte interface acts as a spontaneous electrochemical gating on a semiconducting channel. In order to remove the gate electrode, significantly simplifying the architecture, the PEDOT:BTB is electrochemically deposited directly on top of a spin-coated PEDOT:PSS film achieving a two-terminal configuration (inset Figure 3.9.b). The device response upon KOH additions, which increases the pH value, is reported in Figure 3.9.b, showing the stepwise decrease of the current until a steady-state value is reached.

In order to investigate and understand the mechanism responsible for the two-terminal sensor response, a third electrode is evaporated onto the PEDOT:BTB, achieving a geometrical configuration similar to one proposed by Wringtonh et al.,<sup>424,455,456</sup> for the first OECT example, in which the gate electrode directly touched the channel (Figure 3.10.a). The third electrode is exploited both as an indicator electrode to measure the electrochemical potential of the pH-sensing film (PEDOT:BTB) and as a gate electrode that modulates the conductivity of the organic film in a transistor-like device. Both uses describe the transduction mechanism responsible for the transduction of the two-terminal devices. In the first case, the channel is connected to a source meter to apply a fixed potential and measure the current  $I$ , while the third top-electrode is connected to a voltmeter to measure the electrochemical potential  $E$  with respect to a SCE reference. The simultaneously measured values of  $I$  and  $E$  upon reversible variation of the electrolyte pH are reported in Figure 3.10.b. Following the previous results on the electrochemical potential and the current sensors, both  $E$  and  $|I|$  decrease as the pH value increases.

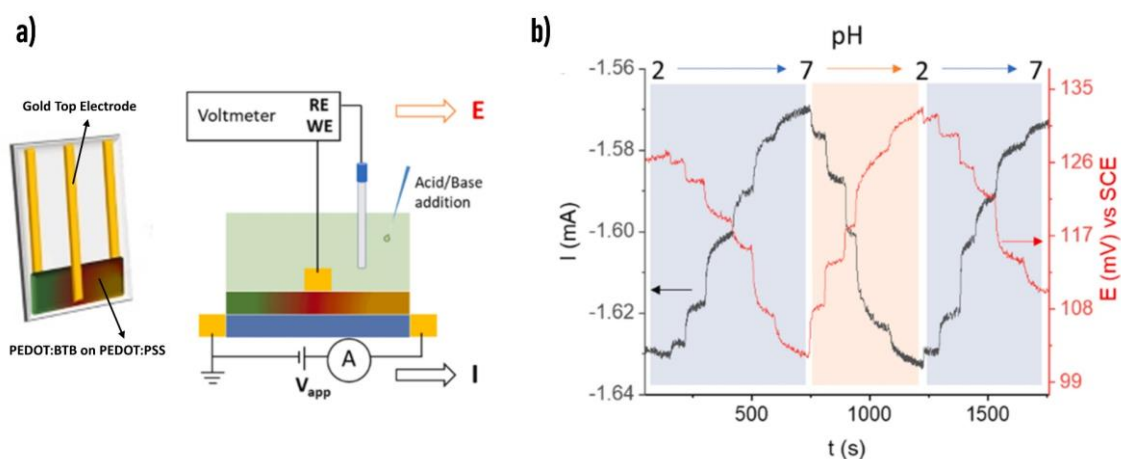


**Figure 3.10:** a) Schematic illustrations of the sensor with an additional gold track making contact with the sensing layer and the experimental setup used to study the sensing mechanism. b) Simultaneous recording of electrochemical potential and current upon variations in the pH of the electrolyte solution.  $V_{app} = -200$  mV.

### 3.4 OECT as pH sensor

It is possible to explain this mutual effect taking into account the scheme in Figure 3.11.a, which shows the interface between the pH-sensing layer and the carrier transport layer. Due to their electrical contact, the two organic layers reach an equilibrium state where their Fermi levels are aligned. The Nernstian dependency of the electrochemical potential at the PEDOT:BTB/electrolyte with the pH can be acquired with respect to the reference electrode, which presents a stable and defined potential of the vacuum level. Therefore, when the pH value of the electrolyte solution is changes, a potential difference is generated at the PEDOT:BTB/PEDOT:PSS interface acting as an electromotive force. Thus, to recover the equilibrium state at the interface between the organic films, the Fermi level of PEDOT:PSS film must shift (Figure 3.11.b). In summary, the spontaneous electrochemically-driven gating effect can regulate the concentration of charge carriers state in the PEDOT:PSS, and thus is directly related to the current dependence on the pH value in the two-terminal sensor.

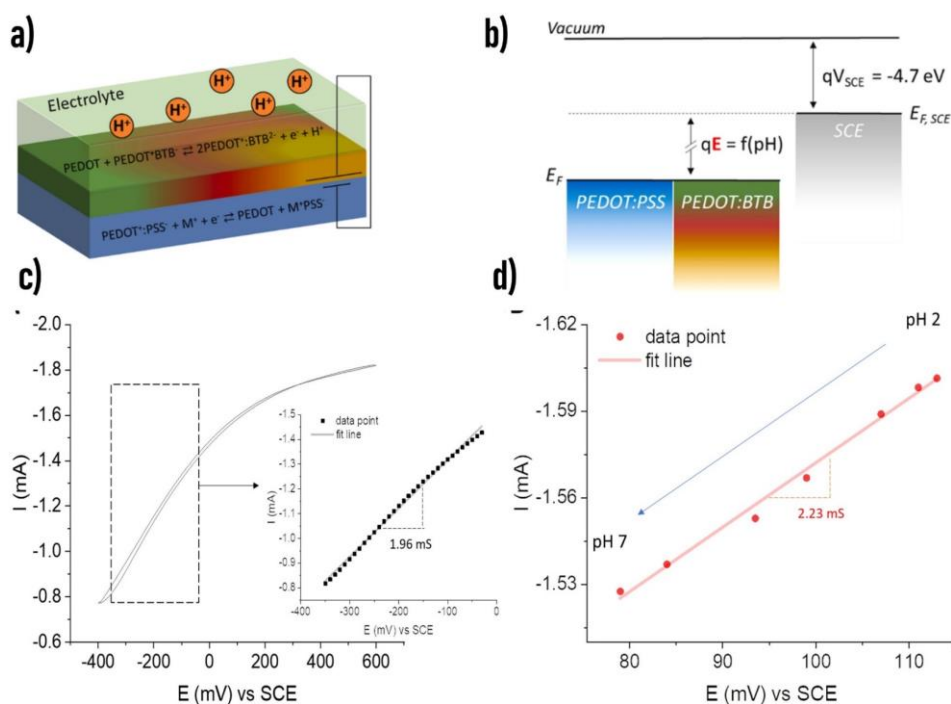


**Figure 3.11:** a) Schematic illustration of the proposed sensing mechanism. b) Qualitative energy diagram illustrating the Fermi level shift due to pH variations.  $E_F$  = Fermi level of PEDOT in the polymeric films;  $E_{F,SCE}$  = Fermi level of the reference electrode;  $q$  = electron charge;  $qV_{SCE}$  = reference electrode energy level;  $E$  = potential difference measured between the reference electrode and the PEDOT:BTB layer, which is a function of the electrolyte pH. c) Modulation of the current flowing in a two-terminal device upon application of a triangular potential waveform to the additional gold track evaporated on top of the PEDOT:BTB layer. U. B. pH 2; scan rate  $10 \text{ mV s}^{-1}$ .  $V_{app} = -200 \text{ mV}$ . Inset: magnification of the linear region of the transfer characteristics ( $R^2 = 0.997$ ). d) Modulation of the current flowing in a two-terminal device upon spontaneous electrochemical gating generated by pH changes in U. B. due to 1 M KOH additions.  $V_{app} = -200 \text{ mV}$ . ( $R^2 = 0.992$ ).

In the second case, the third gold electrode can be directly connected to a potentiostat in order to characterise the transistor-like device. Figure 3.11.c reports the modulation of the current flowing in the two-terminal device ( $V_{\text{app}} = -0.2$  V) upon the application of a triangular potential waveform (scan rate  $10$  mV s<sup>-1</sup>) to the third gold track, where the  $E$  value acts as a gate potential. The electrolyte is an universal buffer solution with pH 2.

The transfer characteristic reported in Figure 3.11.c highlights the typical transistor behaviour of devices with the same geometry.<sup>455,457</sup> To evaluate the current induced by the external source of potential, the transconductance  $g_m = \partial I / \partial E$  is calculated and reports a value of  $(1.96 \pm 0.02)$  mS. A similar value for  $g_m$  ( $= 2.23 \pm 0.09$  mS) is also obtained for the two-terminal sensor extracted from the graph in Figure 3.11.d. When a constant potential of  $-0.2$  V is applied, the flowing current and the electrochemical potential are acquired upon variation of the pH solution. These similar results prove that the PEDOT:BTB layer is the source of a natural electrochemical gating able to modulate the conductivity of the PEDOT:PSS layer in response to an electrochemical reaction involving pH, in analogy with the gate element in an OECT.

## 3.5 Textile single-thread sensors

The innovative sensors reported in the previous paragraphs are based on the biocompatible, soft, and flexible semiconducting polymer PEDOT:PSS (poly(3,4-wthylenedioxythiophene):poly(styrene sulfonate)) endowed with specific sensing features provided by the functionalisation of silver/silver chloride (Ag/AgCl) nanoparticles and bromothymol blue (BTB) dye for Cl<sup>-</sup> concentration and pH detection, respectively. This is a progression in the conceptualisation of two-terminal devices for wearable applications utilising textile single-thread sensors to monitor human sweat parameters. The textile nature of the substrate allows the sensors to be directly integrated with sewing procedures in cloths, garments, or accessories. Three different types of textile threads—cotton, polyester, and silk—are considered to further evaluate possible influences by the material substrated in the sensors' performance. Based on current industry knowledge, the Cl<sup>-</sup> thread sensor reported here is the first example of a selective and fully-textile thread device operating without a reference electrode to monitor Cl<sup>-</sup> concentration. In addition, the two-terminal pH and Cl<sup>-</sup> sensors are integrated into an array of multiple textile sensors able to simultaneously operate in real-time, exploiting sensing capability in a sweat environment.

### 3.5.1 Fabrication of textile single-thread sensors

#### 3.5.1.1 Chemicals

CLEVIOS PH 1000 suspension (PEDOT:PSS) is purchased from Heraeus. (3-glycidyloxypropyl)trimethoxysilane (GOPS), silver nitrate ( $\text{AgNO}_3$ ), potassium nitrate ( $\text{KNO}_3$ ), phosphate buffered saline (PBS), potassium hydroxide (KOH), boric acid ( $\text{H}_3\text{BO}_3$ ), acetic acid ( $\text{CH}_3\text{COOH}$ ), 85% phosphoric acid ( $\text{H}_3\text{PO}_4$ ), sodium dihydrogen phosphate ( $\text{NaH}_2\text{PO}_4$ ), sodium chloride (NaCl), L-histidine, potassium chloride (KCl), 3,4-ethylenedioxythiophene (EDOT) and bromothymol blue (BTB) are purchased from Sigma-Aldrich. Ethylene glycol (EG) and polyethylene glycol (PEG) are obtained from Carlo Erba. All chemicals were of reagent grade. The Universal Buffer solution is prepared with 0.01 M  $\text{H}_3\text{BO}_3$ , 0.01 M  $\text{H}_3\text{PO}_4$ , and 0.01 M  $\text{CH}_3\text{COOH}$  in 0.1 M  $\text{KNO}_3$ . The artificial sweat formulation (ISO pH 5.5) is made up of 0.05% w/v L-histidine, 0.22% w/v  $\text{NaH}_2\text{PO}_4$ , and 0.5% w/v NaCl in distilled water.

#### 3.5.1.2 From pristine yarns to sensing textile threads

This paragraph reports the procedure to turn ordinary textile yarns into a two-terminal sensor. The first step is to convert the yarns into conductive textile threads. A conductive solution is prepared mixing CLEVIOS PH1000 suspension, ethylene glycol (secondary dopant) 3-glycidyloxypropyltrimethoxysilane (cross linker) and polyethylene glycol in the volumetric ratio 77.1:13.8:0.9:8.2. After mixing in a sonicator the CLEVIOS PH1000 suspension, ethylene glycol (secondary dopant) and 3-glycidyloxypropyltrimethoxysilane (cross linker) for 10 min, solid polyethylene glycol is inserted in the solution and stirred vigorously for 20 minutes until completely dissolved. The resulting conductive ink is warmed in an oven at 70° C aiming to increase the solution viscosity. Three different types of threads, both natural (cotton: COT, silk: SILK) and synthetic (polyester: POL), are employed as substrates. In order to deposit the polymeric mixture, the yarns are first washed with distilled water and neutral soap. They are then immersed in the viscous solution and rolled around a stick with a constant velocity until the thread surface is evenly blue in color (characteristic color of PEDOT:PSS). The modified thread electrodes are dried completely in an oven before proceeding with the subsequent fabrication steps. The total amount of conductive polymer deposited on 2 cm long thread is approximately  $(0.5 \pm 0.2)$  mg, varying slightly depending on the fibre.

The second functionalisation process is aimed to create conductive textile threads that are highly sensitive and selective towards the target bio-compound. Exploiting the transduction features reported in the previous paragraphs of this chapter, the chloride ion thread sensor is realised by electrochemically depositing Ag/AgCl nanoparticles using a

### 3.5 Textile single-thread sensors

three-electrode cell unit (RE: SCE, and CE: Pt) and Metrohm Lab Potentiostat. Two consecutive phases compose the procedure: the Ag NPs is deposited dipping the conductive thread (2 cm long) in 0.1 M AgNO<sub>3</sub> solution and applying a potential of - 0.2 V for 60 s. The device is rinsed in distilled water, dried, and then immersed in 1 M KCl where the Ag/AgCl composite particle is formed by applying a bias of +0.6 V for 60 s.

The polymerisation solution (PS) used to deposit PEDOT:BTB on conductive threads is prepared mixing 10 mM EDOT, 1 mM PBS with pH 7.0, and 1 mM of BTB in 0.1 M KNO<sub>3</sub> aqueous solution and stirring for 20 minutes. The thread is immersed in 25 ml of PS, and cyclic voltammetry is carried out, sweeping the potential from 0 to 1 V applied vs SCE with a scan rate of 0.1 Vs<sup>-1</sup> for ten cycles. The samples/threads are then rinsed in DI water. This easy and low-cost fabrication process offers high handling features, conductive behaviour and sensing capability. Figure 3.12.a shows a schematic sketch of the fabrication and functionalisation procedure of the chloride ions and pH thread sensors.

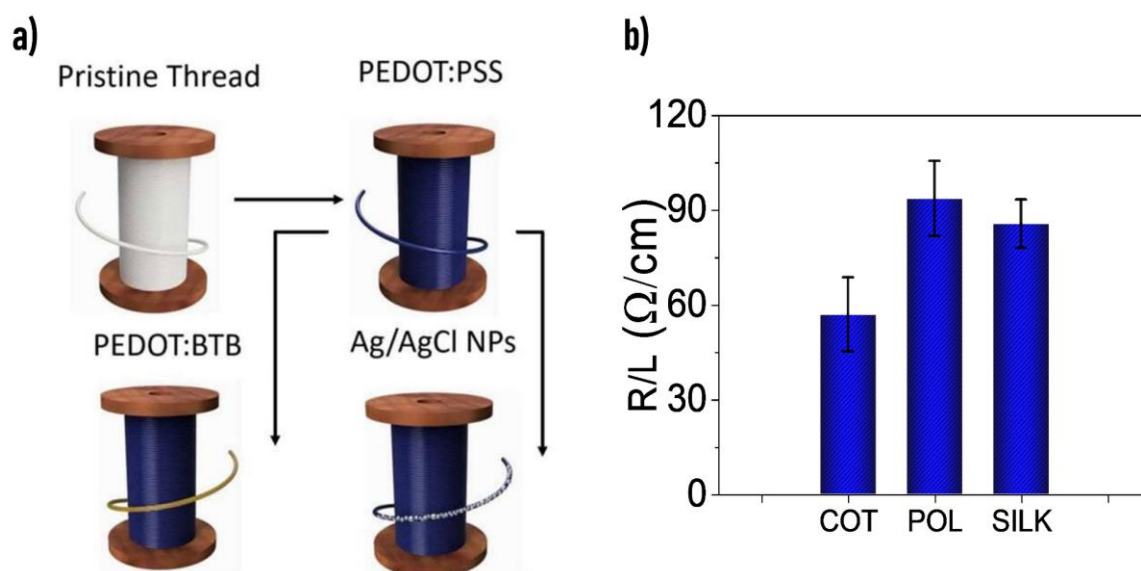


**Figure 3.12:** a) Schematic representation of the conductive thread before (top) and after (bottom) the electrochemical functionalisation. b) Average resistance value of the four different PEDOT:PSS coated yarns measured with a four probes set-up.

#### 3.5.2 Morphological and electrical characterisation

The threads are purchased in a local market and due to their intrinsic textile nature can be sewed into a fabric with a standard sewing machine or an industrial textile system. Two bundles twisted together compose all of the threads. The electrical resistance of the conductive threads coated with the semiconducting solution based on PEDOT:PSS are measured for all the different fibres. The four-point probes are placed one centimetre apart from each other and are connected to a SMU Keithely 2400. COT (pure cotton), POL

### 3.5 Textile single-thread sensors

(polyester) and SILK (pure silk) threads have resistance values of  $(56 \pm 9) \Omega \text{cm}^{-1}$ ,  $(90 \pm 10) \Omega \text{cm}^{-1}$  and,  $(85 \pm 7) \Omega \text{cm}^{-1}$ , respectively (see Figure 3.12.b).

Scanning Electron Microscopy (SEM) images of the three yarns coated with the polymeric solution, before and after the electrochemical deposition step, have been acquired to study the material distribution. Figure 3.13 exhibits SEM images and Energy-Dispersive X-ray Spectroscopy (EDX) for the COT sample, while Figure 3.14 exhibits the SEM images for POL and SILK. The four coated yarns do not present substantial differences, and the semiconducting polymer PEDOT:PSS mainly covers the outside of the thread with an average thickness of  $(12 \pm 2) \mu\text{m}$ , as highlighted from the cross-section images. This is further confirmed by EDX on cotton yarn that displays the presence of sulphur (distinctive mark for PEDOT:PSS) only in the outer shell of the thread (yellow), while carbon is present everywhere in the sample.

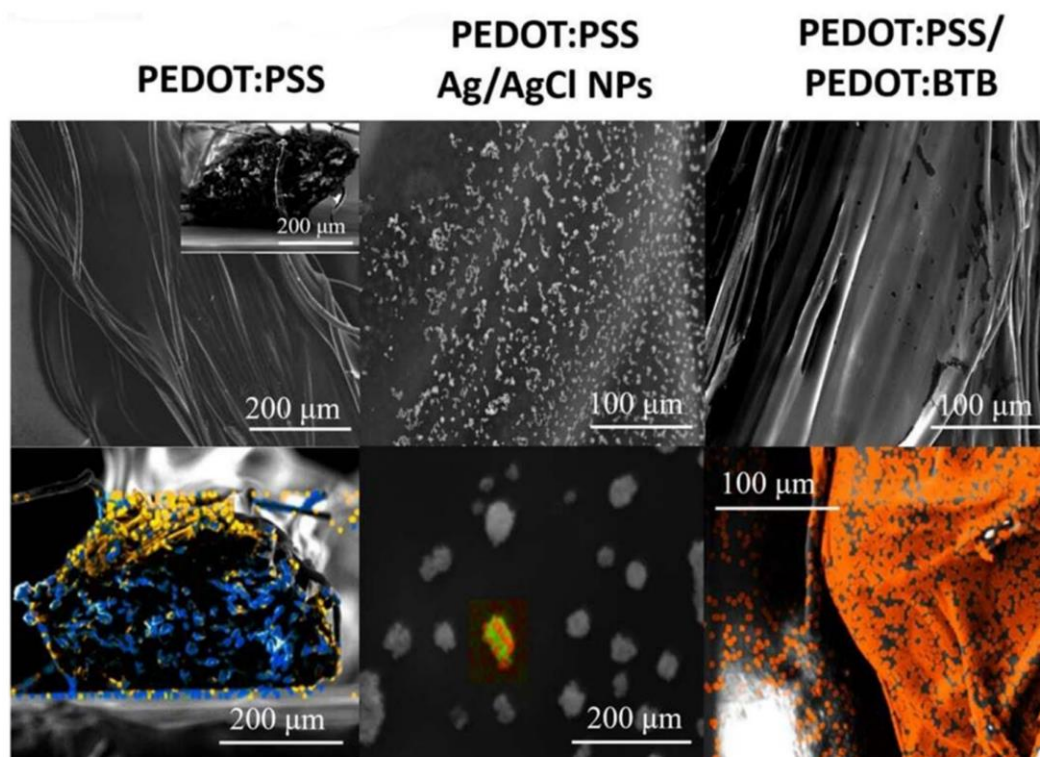


**Figure 3.13:** SEM-EDX images of cotton thread (COT) covered with PEDOT:PSS (left: yellow = sulphur group; blue = carbon), Ag/AgCl NPs (middle: red = chloride; green = silver) and PEDOT:BTB (right: orange = bromide). The images on bottom show the corresponding EDX analysis.

The distribution of Ag/AgCl NPs is uniform onto the surface of the polymer-coated threads and presents various sizes ranging from 30  $\mu\text{m}$  to 300 nm. EDX shows that Ag (green) and Cl (red) are present in the outer shell of the NPs, suggesting the AgCl aggregation. The PEDOT:BTB electrodeposition is not affected by the different nature of the yarn and only slightly changes the fibers' surface, which appears rougher than before the

### 3.5 Textile single-thread sensors

electrodeposition. The EDX map shows that bromine (typical for BTB:  $C_{27}H_{28}Br_2O_5S$ ) is uniformly present on the surface (orange), suggesting that PEDOT:PSS is covered by an almost continuous layer of PEDOT:BTB.

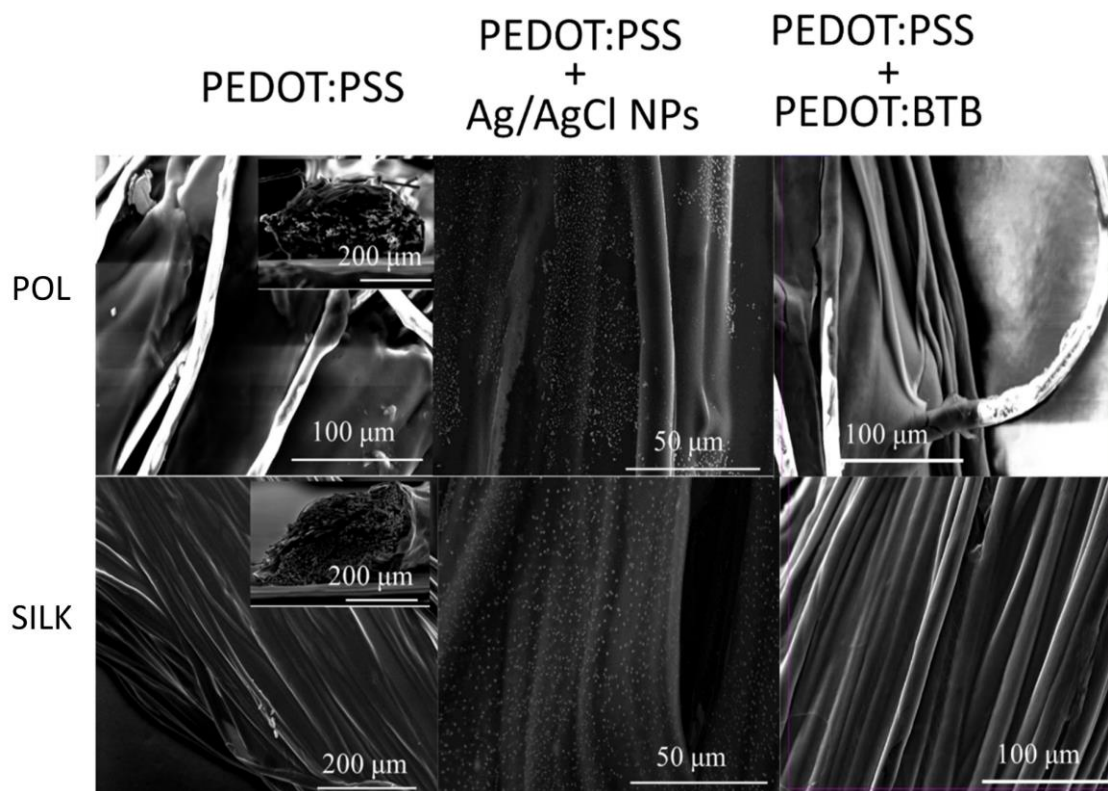


**Figure 3.14:** SEM images of the sensorized threads. Thread coated with PEDOT:PSS (left column), with electrodeposited Ag/AgCl NPs (middle column) and with PEDOT:BTB (right column). Each row corresponds to a different kind of yarn: Polyester (first) and Silk (second).

#### 3.5.3 Liquid sampling volume independency

As a first example to prove the sensing ability of a two-terminal textile thread as a sensor, a long-term measure is carried out, dipping the threads covered with Ag/AgCl NPs in 10 mL of 0.1 M  $KNO_3$  under a gentle stirring. Figure 3.15.a shows the normalised current for the three different yarns. The  $[Cl^-]$  changes upon adding an appropriate amount of 2 M KCl whereas the conductive threads are connected to the SMU that supply a constant potential of +0.1 V and measure the flowing current. All fibres are individually tested in a  $Cl^-$  concentration range from 0.1 mM to 120 mM to match the  $Cl^-$  content in human sweat (10–120 mM)<sup>99,458</sup>. In all cases, a linear correlation between the normalised current variation ( $\Delta I/I_0$ ) and the logarithm of  $[Cl^-]$  is found in the physiologically relevant range (Figure

### 3.5 Textile single-thread sensors

3.15.b). All of the calibration plots are linear ( $R^2 > 0.97$ ) in agreement with a potentiometric-like transduction described by the Nernst equation. The current value recorded at the lowest concentration of 0.1 mM  $[\text{Cl}^-]$  represents the  $I_0$ . The points are reported without vertical error bars since the relative error is less than 1%. Figure 3.15.c shows the sensitivity values calculated with the least square methods with the associated statistical error. This first characterisation proves the robustness and the reliability of the two-terminal sensors over a wide concentration range and, simultaneously, the reliability of the characterisation method.

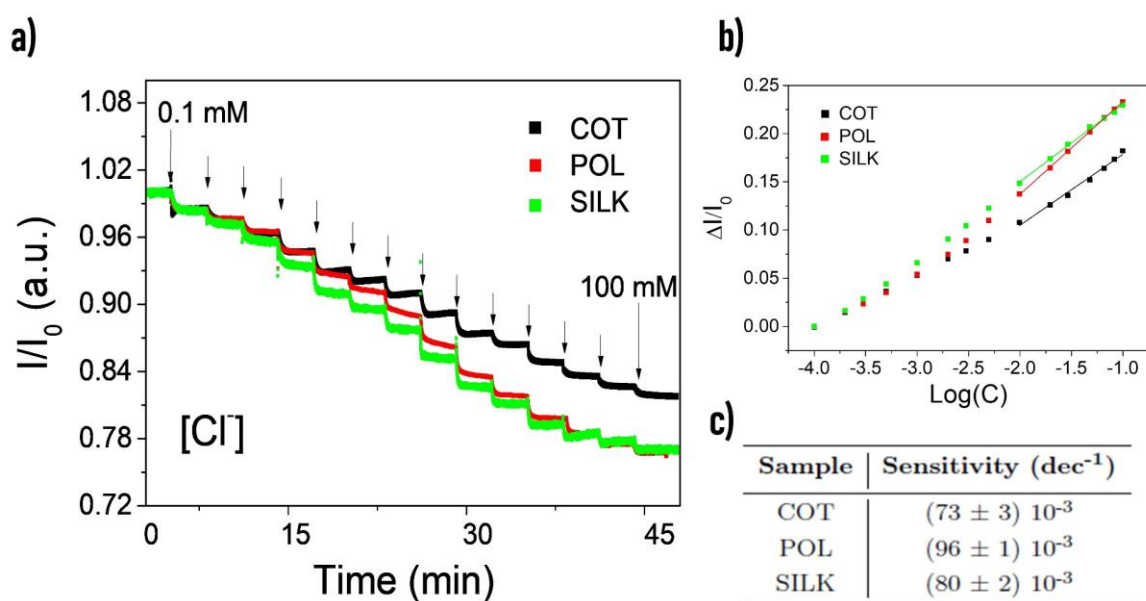


**Figure 3.15:** Current signal acquired with a source meter for the different yarns immersed in 10 mL of 0.1 M  $\text{KNO}_3$ : (a)  $I/I_0(t)$  and (b) normalized current  $(I_0 - I)/I_0$  vs the logarithm of  $\text{Cl}^-$  concentration from 0.1 mM to 100 mM of chloride concentration range. The potential applied to the two-terminal textile device is 0.1 V. The linear fit is performed in the physiological relevant concentration range for human sweat, that is between 10 and 100 mM. The sensitivities reported in table (c) are calculated in the same operational range.

The reliability and repeatability of the textile sensor in a different volume is assessed by characterising the  $\text{Cl}^-$  ions sensors when dipped in a different amount of 0.1 M  $\text{KNO}_3$ . Figure 3.16.a shows the response of COT thread after successive increments of  $[\text{Cl}^-]$  and reports a perfect superposition of the normalised currents, even increasing the total volume of the solution. Figures 3.16.b-c report the complete agreement of the sensitivities, the robustness, and the high repeatability of the measure.

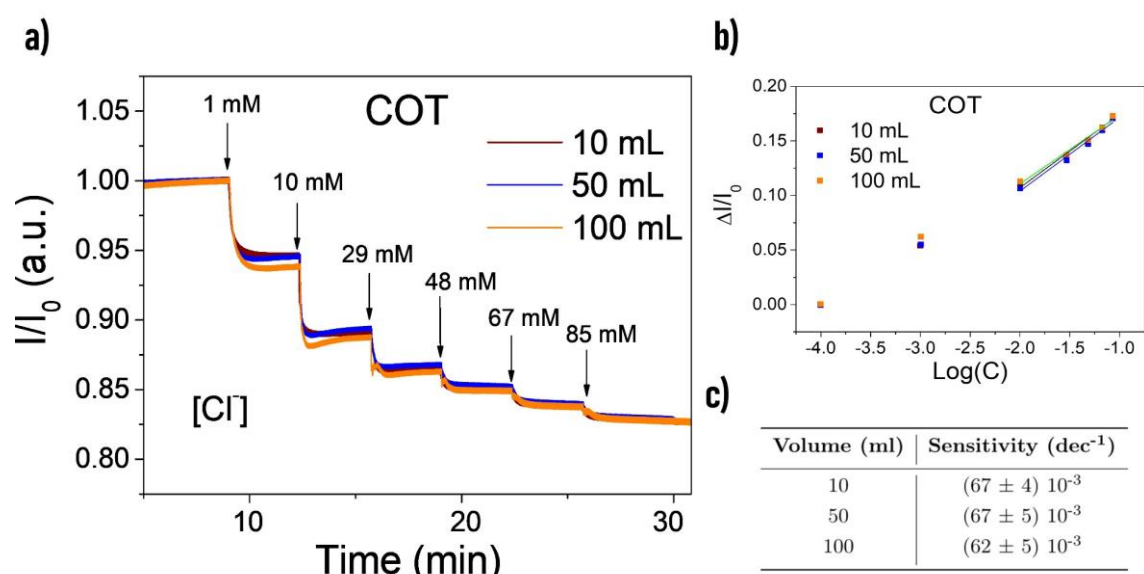


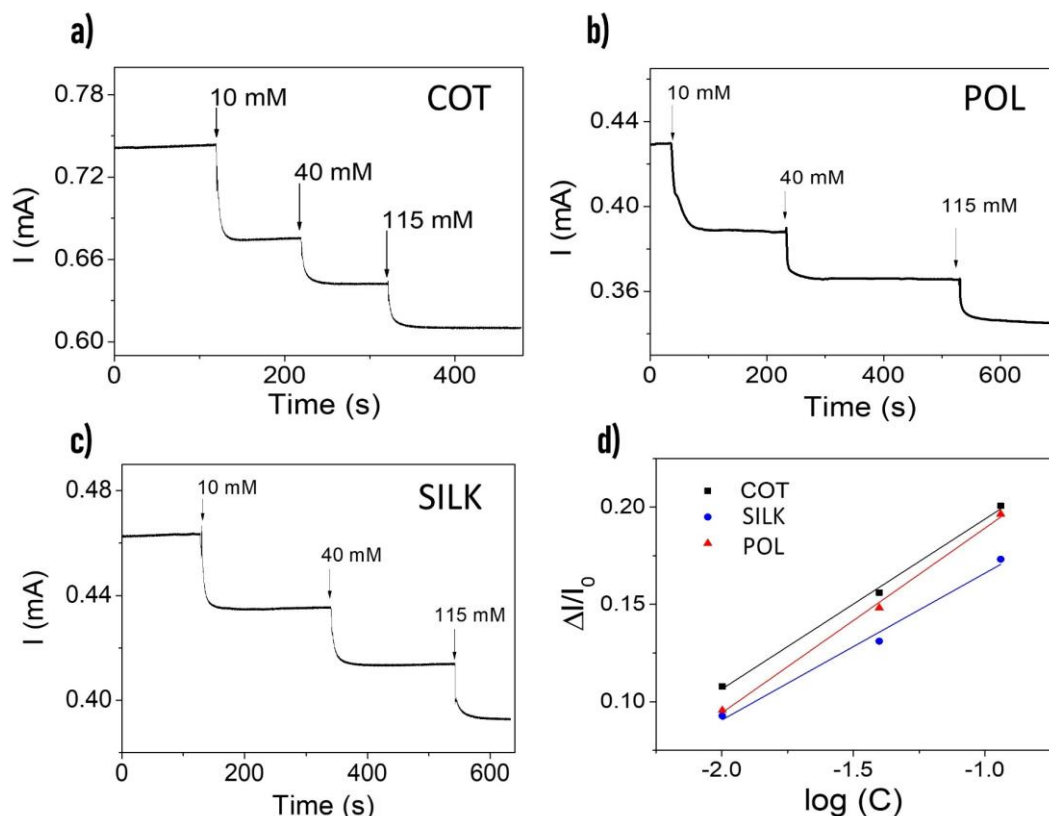
**Figure 3.16:** Effect of the volume in the sensor response for COT thread. a)  $I/I_0(t)$  and b) normalized current  $(I_0 - I)/I_0$  vs the logarithm of  $\text{Cl}^-$  concentration from 1 to 115 mM of chloride concentration range. Three different solution volumes are presented: 10 mL, 50 mL and 100 mL. The linear fit is performed in the physiologically relevant concentration range for human sweat. The sensitivities at different volumes of a COT yarn sensor are shown in table c).

### 3.5.4 Single thread detection in universal buffer

In order to quantitatively assess and compare the performance of single thread sensors in the detection of  $\text{Cl}^-$  concentration and pH, the two textile sensors are separately evaluated in 10 mL of Universal Buffer (UB). The UB solution allows stabilisation of the pH values to obtain a well-controlled variation upon the addition of an acid or base. The potential values used for the characterisation of the sensors in UB will be used overall in the following work presented.

#### 3.5.4.1 Textile $\text{Cl}^-$ sensors

The two-terminal  $\text{Cl}^-$  sensor operates with a bias of +0.1 V, while the chloride ion concentration is varied in the physiologically relevant range of human sweat using 2 M KCl solution. The UB has been prepared with an initial  $[\text{Cl}^-]$  of 0.1 mM. The current acquired in this condition ( $I_0$ ) is used as a normalising value for the current signal. Figures 3.17.a,b, and c show the current flowing through cotton, polyester, and silk thread functionalised with Ag/AgCl NPs, respectively, as a function of time. The arrows highlight the increasing variation of  $\text{Cl}^-$  concentration.



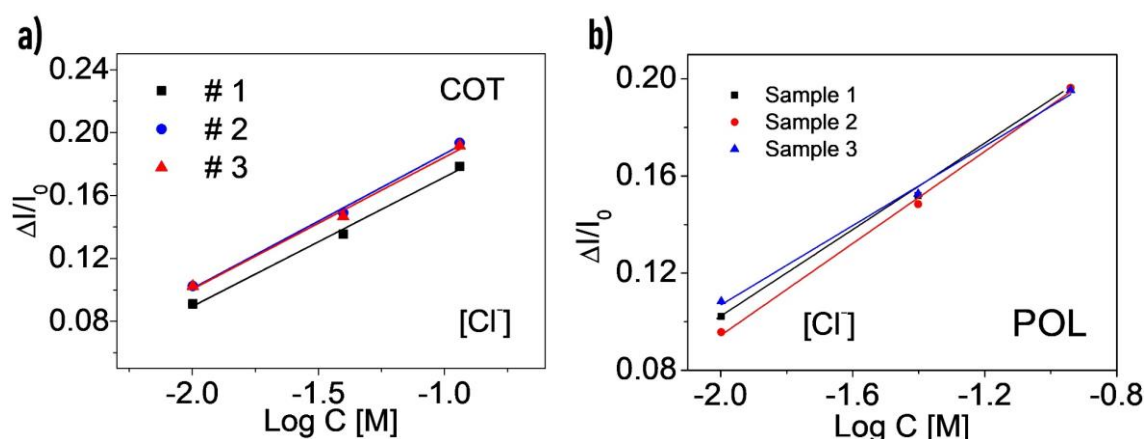
**Figure 3.17:** Current vs time plots recorded in 10 mL of Universal buffer for Cl<sup>-</sup> sensor based on a) COT, b) POL and c) SILK. The applied potential is 0.1 V. d) Linear response of the normalized current variation versus the (c) logarithm of chloride ion concentration. Each thread is characterized separately. The error bars are omitted since the relative error is less than 1%.

Figure 3.17.d shows the normalised calibration curve that follows a linear trend with the logarithm of Cl<sup>-</sup> concentration in the 10 mM -115 mM range. The sensitivity values are represented by the slope of the linear fitting curve and assume the value of  $(82 \pm 5) 10^{-3} \text{ dec}^{-1}$ ,  $(94 \pm 5) 10^{-3} \text{ dec}^{-1}$  and  $(86 \pm 5) 10^{-3} \text{ dec}^{-1}$  for COT, POL and SILK, respectively. This highlights the accuracy and the comparable behaviour of the sensors despite the thread type. The average response time (assessed as the time required to reach 90% of the final signal) is equal to  $(19 \pm 6)$  s for a 115 mM chloride addition. Moreover, POL and COT based sensors show the highest and lowest sensitivities, respectively. Repeatability and reproducibility are fundamental features for reliable sensors and are evaluated in chloride detection, using COT and POL threads as examples. Figure 3.18.a shows the repeatability study carried out using one cotton thread to measure [Cl<sup>-</sup>]. In this study, the same thread is used to perform three consecutive experiments, giving almost superimposable responses with the same sensitivities. As far as the reproducibility, Figure 3.18.b shows the results of experiments conducted over three different POL threads for [Cl<sup>-</sup>] detection. The reproducibility is very high, as pointed out by the same trend presented by three different sensors. The calibration

### 3.5 Textile single-thread sensors

plot confirms the reliability of the fabrication technique and the possibility to realise textile thread sensors with comparable responses.

It is worth noting that Ag/AgCl is a well-known and widespread material approved for use on skin in various medical applications, such as ECG<sup>459</sup> and EEG<sup>460</sup> electrodes, and can be considered non-toxic<sup>461</sup> in the framework of the final application of these sensors. Furthermore, according to the solubility equilibrium of silver chloride in a water-based solution, the eventually released nanoparticles would not influence the Cl<sup>-</sup> sensor signal.



**Figure 3.18:** a) Repeatability of COT fibre using the same Ag/AgCl NPs-functionalized device tested three consecutive times. b) Reproducibility of three different POL threads samples functionalized with Ag/AgCl NPs. All measurements are carried out in 10 mL of Universal buffer.

#### 3.5.4.2 Textile pH sensors

The two-terminal textile pH sensors operate at a bias of  $-0.2$  V, while the current value recorded at the initial pH 4.2 is used to normalise the signal. The pH level is studied in the physiologically relevant range from 4 to 7, adding 1 M KOH to the buffered solution. Figures 3.19.a, b, and c show the current flowing through the PEDOT:BTB functionalised cotton, polyester, and silk threads, respectively. The arrows indicate the variation, upon KOH additions, of pH level of the UB solution. The sensitivity values are represented by the slope of the linear fitting curve and assume the value of  $(82 \pm 5) 10^{-3} \text{ dec}^{-1}$ ,  $(94 \pm 5) 10^{-3} \text{ dec}^{-1}$  and  $(86 \pm 5) 10^{-3} \text{ dec}^{-1}$  for COT, POL and SILK, respectively. The calculated sensitivities of  $(7.8 \pm 0.4) 10^{-3} \text{ pH}^{-1}$ ,  $(21 \pm 1) 10^{-3} \text{ dec}^{-1}$  and  $(14 \pm 1) 10^{-3} \text{ dec}^{-1}$  for COT, POL and SILK, respectively, vary with the fibre substrate and are likely affected by the commercial yarns' chemical nature and surface treatment.

### 3.5 Textile single-thread sensors

COT and POL sensing threads report the lowest and highest sensitivity, respectively, and are used as an example to prove the repeatability and reproducibility of the pH sensors. Figure 3.20.a shows the repeatability study carried out using one cotton thread to measure pH level. The same cotton thread is characterised in three consecutive experiments, giving almost superimposable response with the same sensitivities. Regarding reproducibility, Figure 3.20.b shows the results of the experiments involving three different POL threads for pH detection. The perfect overlapping of the calibration curves points out the extreme reproducibility of the fabrication technique and the sensors' response.

Finally, no chemical contamination between the functionalised textile-thread sensors and the overall solution that can affect the sensing of the target analytes has been observed. In order to avoid any possible contamination of the sample solution, the sensors are always thoroughly rinsed with distilled water after the electrodeposition step. For the BTB-functionalised thread sensor, no colouration of the solution is observed after several measuring hours, thus confirming that the release of BTB dye is negligible, if present at all.

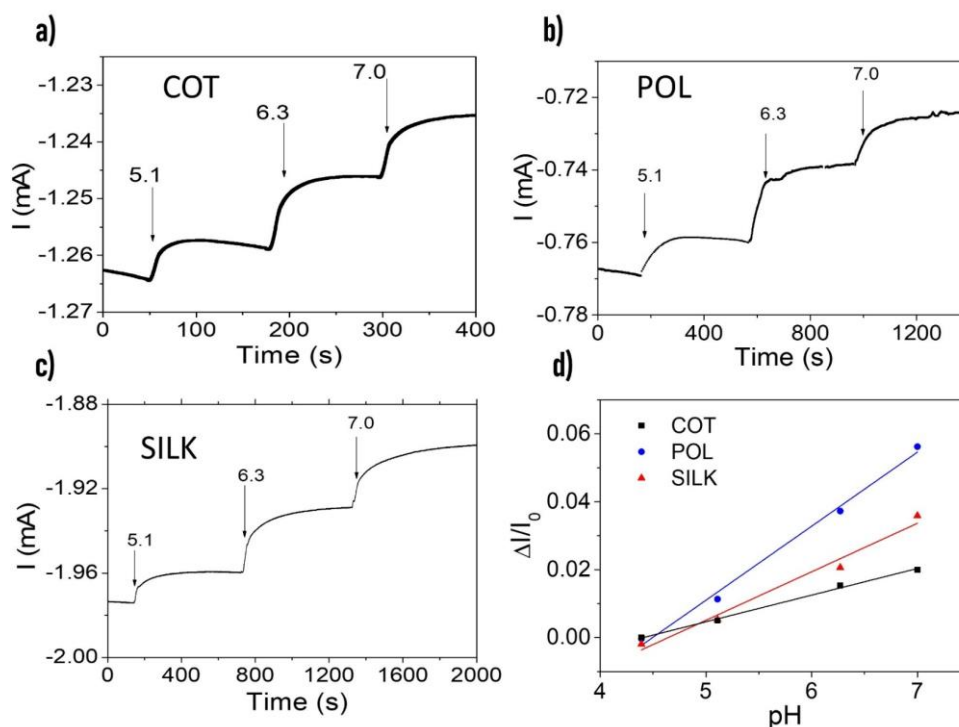


**Figure 3.19:** Current vs time plots recorded in 10 mL of Universal buffer for pH sensor based on a) COT, b) POL and c) SILK. The sensor response is evaluated in the pH relevant range for human sweat between 4.5 and 7 pH level. The applied potential is -0.2 V. Linear response of the normalized current variation versus the pH value.

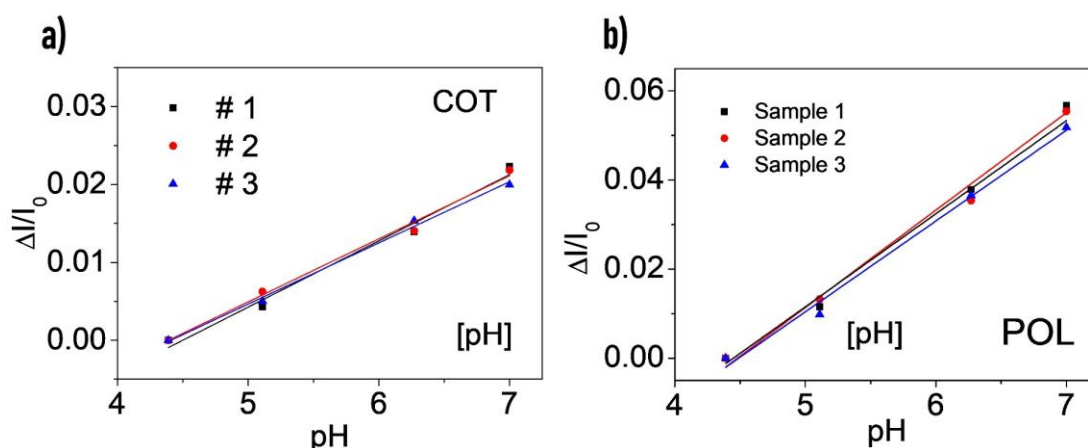


**Figure 3.20:** a) Repeatability of COT fibre using the same pH thread sensor tested three consecutive times. b) Reproducibility of three different POL threads samples functionalized with PEDOT:BTB. All measurements are carried out in 10 mL of Universal Buffer.

### 3.5.4.3 Comparison between cotton thread sensors

In order to evaluate the possible effects of different thread structures and fibre arrangement of the same material, a second cotton yarn, named COT2, has been investigated. It results in a tighter thread with a Metric Count of 2/30 instead of 2/50. The Metric Cotton Count represents an indirect measure of the linear density, with the first number referring to the number of strands plied together and the second number indicating how many hanks of 1000 metre lengths of a single ply of the yarn it would take to weigh one kilogram. The different cotton threads have a different number of fibres that compose the yarns. Even if the sensitivity to chloride is comparable for both COT and COT2 based sensors, COT shows a considerably lower sensitivity to pH than COT2. The reason may be found in the different way that PEDOT:PSS is adsorbed by the threads and fills the inter-fibres' spaces. COT thread presents higher conductivity ( $G = 1/\text{Resistance}$ ), while COT2 exhibits a pH sensor, the higher sensitivity ( $S$ ). It is hypothesised that this behaviour is related to the different linear densities of the two threads. The reported Metric Count, a standard parameter to express the size of cotton yarns, can be expressed as a linear density with values of  $\rho_L=33$  g/km and  $\rho_L=20$  g/km for COT2 and COT, respectively. Assuming the same cross-section for every fibre and the same volumetric density for both yarns (both are made of the same material), COT presents fewer fibres than COT2. Figure 3.21.a reports the schematic and simplified representation. For this reason, a higher quantity of semiconducting polymer coats the COT thread without wetting the bulk of the yarn. Accordingly, a lower resistance is reported for COT than COT2, where a less amount of PEDOT:PSS is present only on the external surface. Ag/AgCl NPs (Figure 3.21.b) and PEDOT:BTB (Figure 3.21.c) functionalised the PEDOT:PSS-coated threads differently. Ag/AgCl Nanoparticles, owing to the small diameter, are deposited onto almost all

### 3.5 Textile single-thread sensors

PEDOT:PSS layer whereas the PEDOT:BTB, acting as a surface coverage,<sup>83</sup> is not present on the polymeric material between the fibres, which remains in its pristine state. To summarise, the Ag/AgCl NPs functionalise all of the PEDOT:PSS present onto the yarns and the [Cl<sup>-</sup>] sensors report closer sensitivities for the two kinds of cotton. The unfunctionalised PEDOT:PSS presents in the spaces among the separated fibres of COT thread, leading to halved sensitivities compared to the one reported by COT2 where all of the polymeric layer is modified with PEDOT:BTB.

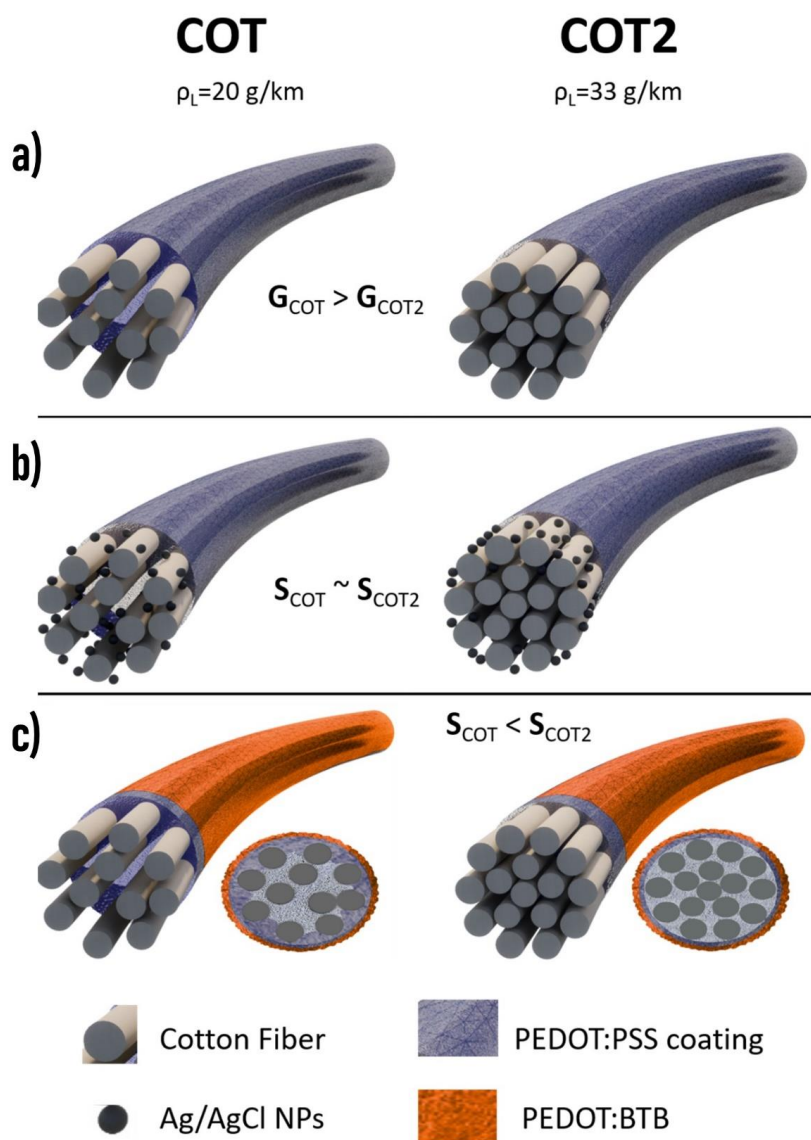


**Figure 3.21:** Schematic view of the proposed COT and COT2 polymeric coating (a), Ag/AgCl nanoparticles (b), and PEDOT:BTB functionalization (c), with the consequent relative comparison of conductivity and sensitivity. G and S represent the conductivity and the sensitivity, respectively.

### 3.5.5 Multi-thread detection in universal buffer

A further step in order to produce a textile platform with multiple sensors is to assess the ability of the two-terminal  $[\text{Cl}^-]$  and pH sensors to work in parallel for simultaneous and selective data collection from the same analysed solution. Figure 3.22.a reports a schematic representation of the two textile-thread sensors sewn into a woven fabric to integrate them directly into garments or accessories. Firstly, long-term stability has been assessed by recording the current response after  $[\text{Cl}^-]$  and pH variation in UB for 30 minutes. The signal acquired for sensors realised with COT yarn is reported in Figure 3.22.b. Both textile sensors show a minimal drift in the current signal, highlighting the reliable long-term monitoring capability of  $[\text{Cl}^-]$  and pH. The selectivity, chemical interference, and eventual cross-talk effect are crucial properties for wearable sensors that have to process the simultaneous variation of different analytes or metabolites in the same medium.

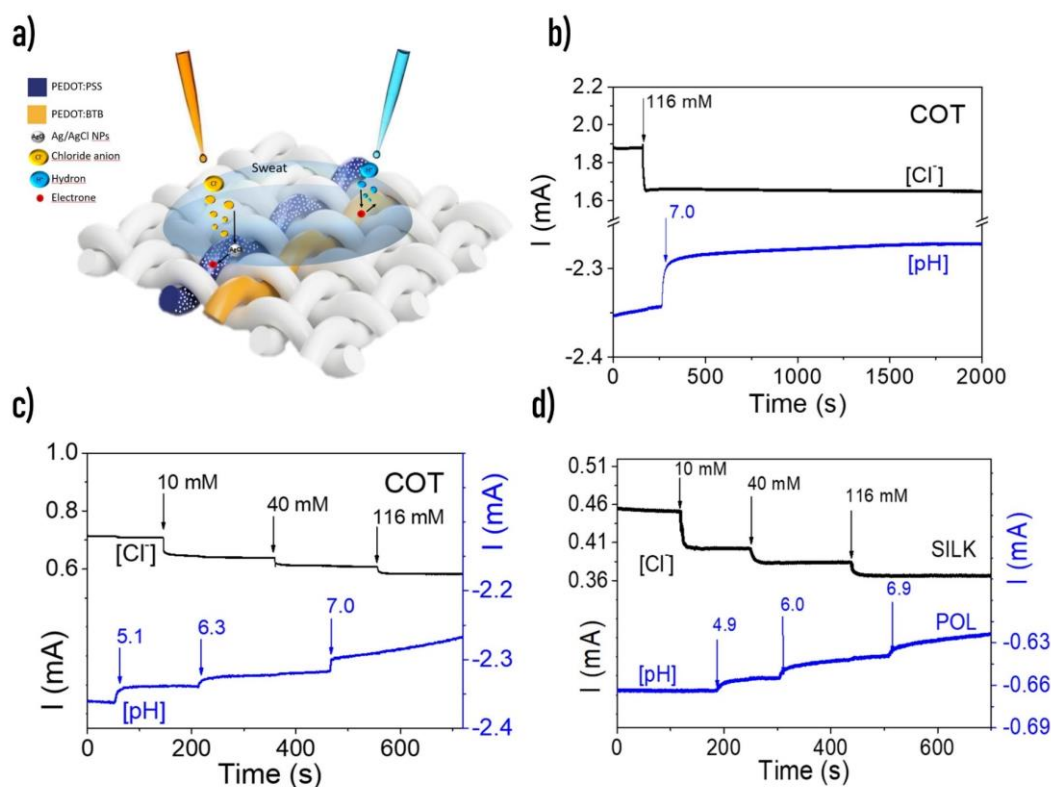


**Figure 3.22:** a) Schematic representation of working principle of thread sensors able to simultaneously detect, without interferences,  $\text{Cl}^-$  and pH level in sweat. b) Long-term stability of COT thread sensors for  $\text{Cl}^-$  (black line) and pH level (blue line). Selectivity tests: c) response after subsequent additions for two single COT thread sensors, and d) response of silk and polyester thread sensors. The  $\text{Cl}^-$  sensors are reported in black, while the pH ones in blue. In the two measurements, the order of the additions is exchanged to properly assess the lack of interference effects. Both chloride concentration and pH value range are chosen in the physiologically relevant range of human sweat ( $\text{Cl}^-$ : 10 mM to 115 mM; pH from 5 to 7)

### 3.5 Textile single-thread sensors

To investigate the potential interference of the multi-textile thread platform, the current responses of the two textile sensors are measured simultaneously (Figure 3.22.c-d). Both 1 M KOH and 2 M KCl are alternately added to 10 mL of UB. Figure 3.22.c shows the response of two sensors realised with the same fiber (COT), while Figure 3.22.d proves the effectiveness of employing sensors based upon different yarns (i.e. POL and SILK for the pH and [Cl<sup>-</sup>], respectively). As reported in Figure 3.22, when the single-thread sensors work in parallel and in the same UB solution, they perform the same in terms of stability, selectivity, and sensitivity, compared to when they are characterised separately. No cross-talking or interference effects appear. Table 3.2 resumes the sensitivity values of the thread sensors operating simultaneously. Therefore, quantitative and multiplexed detection of the two analytes can be carried out simultaneously and with no need to perform correction or ad-hoc processing in the output signal. These results assess the opportunity to integrate the sensors directly into fabrics, choosing the yarn substrate according to the needed specifications in terms of material compatibility and sensitivity. Both natural and synthetic fibers, after a proper functionalisation procedure, can be exploited to produce a complete textile platform able to monitor chloride ion concentration and pH level.

**Table 3.2:** Sensitivity values of the thread sensors during simultaneous operation.

Graph	Thread	Sensitivity	
a	COT	[Cl <sup>-</sup> ] (dec <sup>-1</sup> )	(75 ± 2) 10 <sup>-3</sup>
		[pH] (pH <sup>-1</sup> )	(12 ± 2) 10 <sup>-3</sup>
b	SILK	[Cl <sup>-</sup> ] (dec <sup>-1</sup> )	(76 ± 6) 10 <sup>-3</sup>
	POL	[pH] (pH <sup>-1</sup> )	(22.7 ± 1.4) 10 <sup>-3</sup>

### 3.5.6 Textile platform for sensing in artificial sweat

To achieve a specific use in monitoring the health or performance of athletes during endurance sports, it is essential to demonstrate the operation and reliability of textile sensors in conditions as similar as possible to those in real life. The first step is to use an artificial sweat solution that mimics the composition of sweat produced by the human body. The ISO pH 5.5 formulation is used in laboratory experiments. Applying the previously reported voltages, +0.1 V for [Cl<sup>-</sup>] and -0.2 V for pH, the graphs in Figure 3.23 exhibit the response of individual sensors when immersed in 10 mL of artificial sweat under [Cl<sup>-</sup>] (a-c) and pH (d-f) changes. Even using artificial sweat instead of UB, a linear response of the normalised current with the logarithm of [Cl<sup>-</sup>] and pH can be achieved. Current values measured at 40 mM Cl concentration and pH 5.5 are used as the value of I<sub>0</sub> to extract the sensitivities shown in the graphs in Figure 3.23. Comparable sensitivities values are obtained with the exception

### 3.5 Textile single-thread sensors

of silk fibre which reports twice the sensitivity of cotton and polyester fibres in chloride monitoring.

In order to work in a complex medium as sweat, the sensors must be able to detect the desired species selectively. Figure 3.24.a reports the results of a selective test conducted on a COT sensor for  $[\text{Cl}^-]$ . Using AS as the testing solution, urea, ethanol, and lactate are added to reach the typical concentration in human sweat.<sup>103,105,458,462</sup> A cotton thread sensor for  $[\text{Cl}^-]$  has been tested as an example. After adding all of the different compounds, no difference in the recorded current is detected when the sensor is supplied with +0.1V, except for the KCl addition, which increases the  $\text{Cl}^-$  amount. This measure proves that no interference by other analytes can occur during the determination of  $\text{Cl}^-$  concentration.

To ensure the reliability of the sensors in real-life and unpredictable conditions, a  $[\text{Cl}^-]$  COT thread sensor is randomly dipped in five different artificial sweat solutions, each of them with a different chloride content. The sensor response is shown in Figure 3.24.b where the coloured regions indicate when the sensor is immersed in the solution. The current dramatically rises when the cotton thread is removed from the AS solution and left in air, returning to its initial value. After each immersion, the current value decreases and rapidly stabilises according to the specific  $\text{Cl}^-$  concentration. Figure 3.24.c reports the calibration plot, with the extracted sensitivity comparable to the one obtained with the standard characterisation method. This test allows to neglect hysteresis and memory-like effects in the sensors.

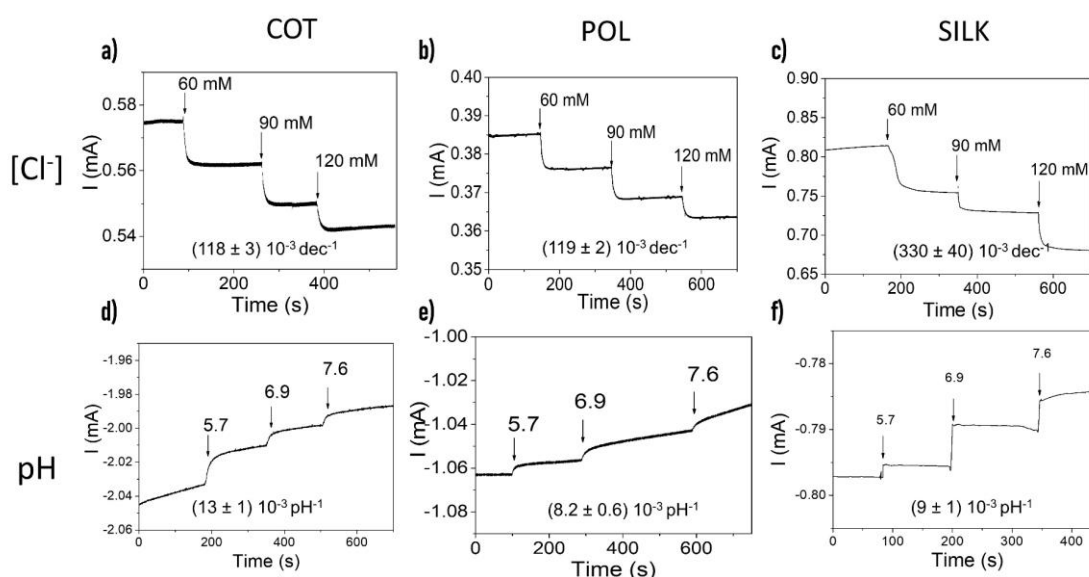


**Figure 3.23:** Electrical response of the different thread sensors in 10 mL of Artificial Sweat. The first row reports the  $\text{Cl}^-$  thread sensors response after the increments of chloride concentration, while the second row reports the response of pH thread sensors after the addition of KOH, which change the pH value.

### 3.5 Textile single-thread sensors

The wearability of the  $[\text{Cl}^-]$  thread sensor is further demonstrated using a custom portable wireless data-reader connected via Bluetooth with a smartphone. Figure 3.24.d shows the characterisation of the COT-based  $[\text{Cl}^-]$  sensors when immersed in the solution, and connected to the portable reader together with the custom application for the smartphone. The setup allows monitoring and recording the current signal in real-time with the results displayed on a smartphone screen.

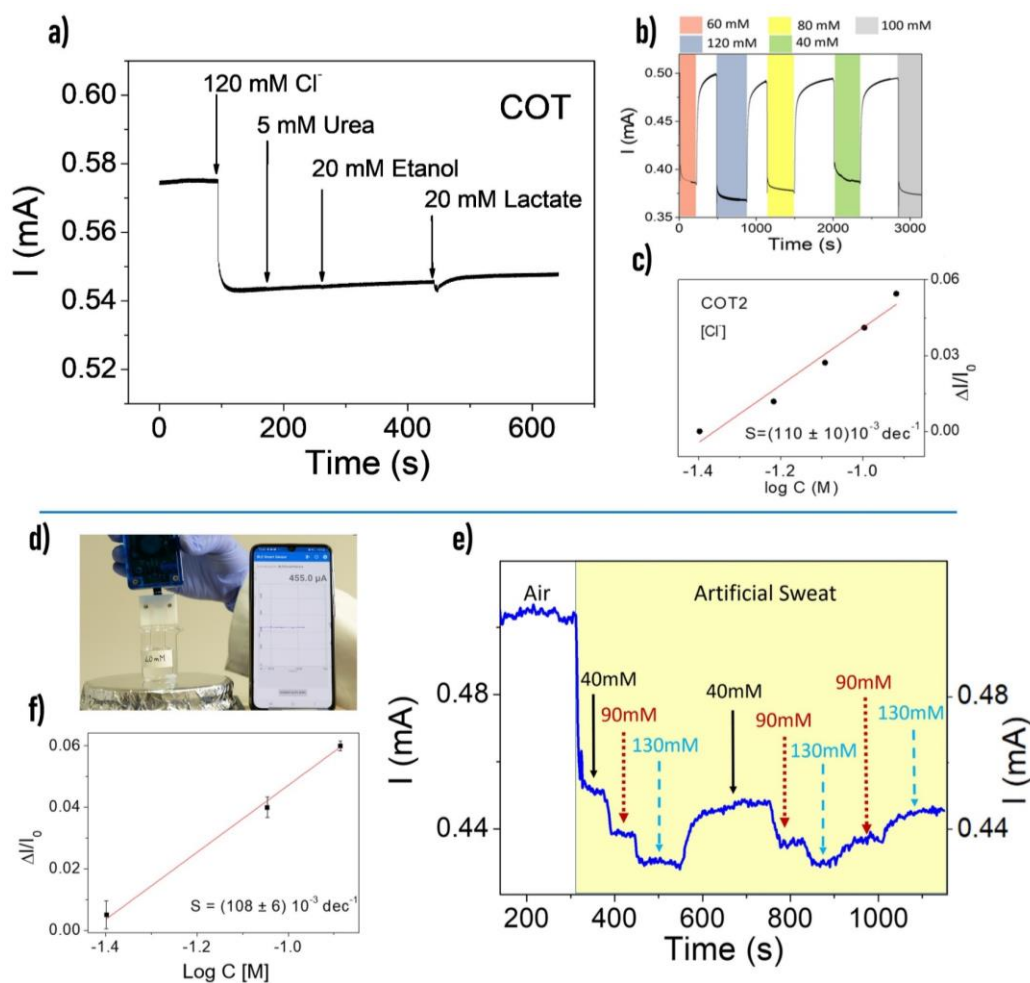


**Figure 3.24:** a) Selectivity test at typical concentration in artificial sweat. b) Random immersion of the COT  $\text{Cl}^-$  sensor in solutions. The white and colored regions indicate thread sensor in air or immersed in the solution. c) Calibration plot of the COT thread. d) Test of  $\text{Cl}^-$  concentration in artificial sweat with a custom wireless data-reader. e) Plot of the signal shown on a smartphone. f) Calibration plot of the sensors randomly dipped in the three solutions.

After a first calibration procedure, the thread sensor can be used to record the effective chloride concentration variations in solution as artificial sweat. Figure 3.24.e reports the current acquired over time with the portable device when the  $[\text{Cl}^-]$  of the AS solution is reversibly modified by the addition of 2M KCl. The characterisation plot of the

### 3.5 Textile single-thread sensors

cotton-based sensor in Figure 3.24.f shows the recovery ability and reliability of the response after  $[\text{Cl}^-]$  variation, mimicking a real-life condition.

#### 3.5.6.1 Multi-sensing in artificial sweat

Human perspiration is a complex mix of several compounds, thus the ability to discriminate diverse stimuli is a fundamental feature to define the performance of a sensor. Figure 3.25.a shows the interference test results using two different COT thread sensors to simultaneously detect  $[\text{Cl}^-]$  and pH in the same AS solution. Here, the sensitivities of the  $[\text{Cl}^-]$  and pH sensors are still comparable with that obtained in the single thread characterisation as KCl or KOH additions barely affect the pH and  $[\text{Cl}^-]$  sensors behaviour. Their values in artificial sweat are  $(141 \pm 8) \cdot 10^{-3} \text{ dec}^{-1}$  and  $(18 \pm 2) \cdot 10^{-3} \text{ pH unit}^{-1}$  for  $\text{Cl}^-$  and pH sensors, respectively (table in Figure 3.25.c). Figure 3.25.b-d reports the calibration curves of different sensorized threads obtained from two separate interference tests. In both situations, no interference is observed with the perfect agreement of the sensors' sensitivities highlighting the device reproducibility. The multi-sensor textile platform composed of the two functionalised threads sensors maintained high selectivity in artificial sweat as the sensors' response is only affected by the target species.

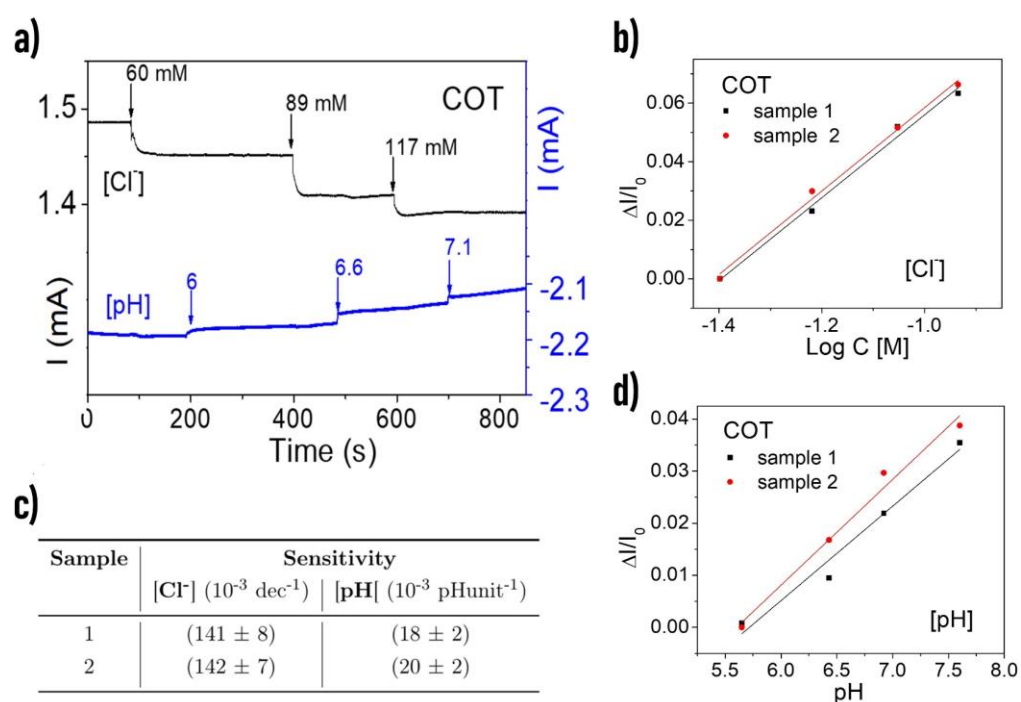


**Figure 3.25:** a) Interference test in 10 mL of Artificial Sweat to simulate real-life condition using COT threads. b - d) Calibration curves of different sensors based on cotton threads obtained from two separate interference tests, and c) the respective sensitivity.

## 3.6 Conclusions

Finally, sewing the two types of sensing threads into the neck of a T-shirt proves the ability to perform in-situ sweat analysis to monitor  $[\text{Cl}^-]$  and pH levels. Figure 3.26.b shows a representative picture of the threads sensors sewn into a fabric to monitor analytes concentration in real-time. As the sensors' response does not depend on volume, the sensors platform can work with a very low amount of human perspiration. In this case, the COT threads are soaked in 1 mL of artificial sweat, and independently, an addition of 1 M KOH changes the pH from 5.5 to 7.7 while 3 M KCl varies the chloride concentration from 30 to 100 mM. As a first proof, using a hydrophobic T-shirt allows the absence of a microfluidic system, which is required for further development.

Figures 3.26.a-c report the acquired signal, the calibration plot, and the sensitivities values of the pH and  $[\text{Cl}^-]$  sensors, respectively. Even in circumstances similar to real-life, the sensors report good performances that are comparable to that obtained in laboratory conditions with a sensitivity of  $(19 \pm 1) 10^{-3} \text{ pH}^{-1}$  and  $(78 \pm 5) 10^{-3} \text{ dec}^{-1}$ , for the  $[\text{Cl}^-]$  and pH sensor, respectively.

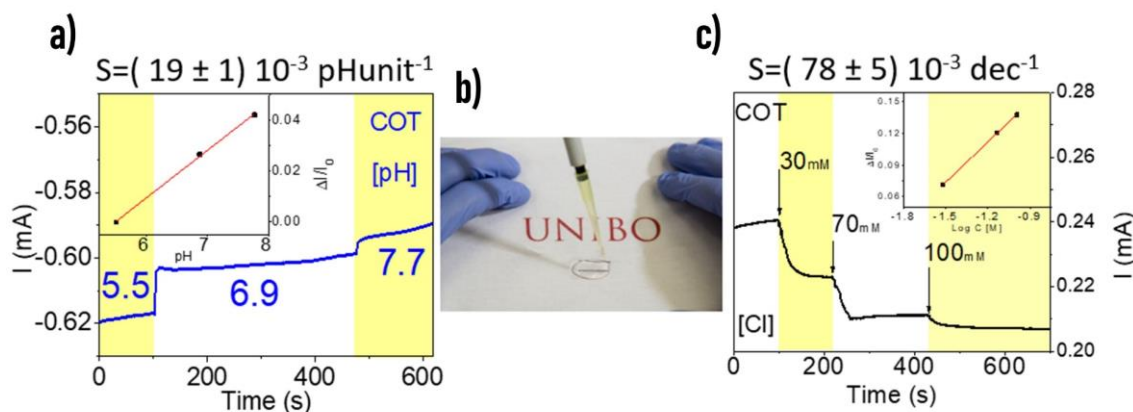


**Figure 3.26:** Current signal, calibration plot and sensitivity for a) pH sensor and c)  $\text{Cl}^-$  sensor. The threads are immersed in 1 mL of artificial sweat. b) Example of a sensorized T-shirt for hydration and pH monitoring used to characterize the textile thread sensors in real life-like conditions.

## 3.6 Conclusions

This chapter reports the major results regarding the realisation and characterisation of a textile platform based on conductive and functionalised textile thread capable of measuring chloride ions' concentration and pH in human sweat. The results are also summarized in ref.<sup>463</sup> The mechanism of operation of this new category of two-terminal sensors is based on the electrochemical gating by Ag/AgCl Nanoparticles, or PEDOT:BTB, directly on the conductive channel of PEDOT:PSS.

The first paragraph, starting with a detailed description of organic electrochemical transistors, reports the transduction mechanisms used by the textile sensors and was

### 3.6 Conclusions

---

recently proposed by the Semiconductor Physics Group of the University of Bologna. After demonstrating the possibility to realise three-terminal OECTs able to monitor  $[\text{Cl}^-]$  and pH level, the integration of the gate terminal directly on the channel of the device, exploiting an electrochemical gating effect that allows the obtainment of two-terminal potentiometric-like devices still benefitting from the typical OECTs' amplification, is possible.

Exploiting this new concept of electrochemical transduction, textile threads with the ability to detect pH level and chloride in human sweat are extensively present. Each sensor consists of a two-terminal device based on a textile single-yarn (cotton, polyester, or silk) capable of working in an aqueous solution without the need for a reference or gate electrode, leading to a significant simplification in the final device architecture compared to the amperometric, potentiometric, or transistor configurations. The sensitive yarns are fabricated using commercial textile fibres, both natural and synthetic, coated with the semiconducting polymer PEDOT:PSS and functionalised to selectively detect  $[\text{Cl}^-]$  and pH levels in sweat. The reliability of the sensors is demonstrated first in Universal Buffer, and then in artificial sweat to simulate a real-life environment. The sensors show stability, reproducibility, and repeatability, with no significant differences between the various fibres in terms of the overall performances, highlighting the possibility to use the appropriate yarns depending on the final textile product. Their ability to work in parallel, without interfering, changing sensitivity, or requiring cross-talk shielding, paves the way for simultaneous, real-time monitoring of  $[\text{Cl}^-]$  and pH level in body fluids, such as sweat. These results provide the technical basis for the fabrication of single-thread sensing elements and describe their assembly into a multi-platform biosensor system. However, in order to be used for real applications, further improvements are needed. A reliable sampling system should be employed to regenerate sweat on the surface of the sensors to ensure continuous monitoring, and new functionalisation procedures should be designed to expand the numbers of biocompounds that can be detected using this new electrochemical approach.

# Chapter 4

## Textile wound sensors

This chapter presents the latest result on textile wound sensors to continuously monitor a chronic wound's pH and moisture level. These two fundamental parameters allow tracking the healing process, helping the physicians to non-invasively monitor the progressive state of the wound healing. A new Metal Oxide-based pH sensor is introduced thanks to its higher sensitivity and linearity behaviour in the range of interest for wound healing monitoring than PEDOT:dye. After an exhaustive explanation of the working principle of the new two-terminal pH sensor, a comparison between rigid and flexible devices made on glass and textile, respectively, will be reported. The textile-based sensor's excellent behaviour under real-life conditions makes it a perfect candidate for use in real applications.

In the second part of the chapter, another example of a textile-based device used as wound dressing for moisture level monitoring is reported. The textile sensor is composed of conductive polymer PEDOT:PSS screen printed on the sensing gauze. It has been characterized in active and passive mode, reporting a novel example for a fully passive and wireless textile moisture sensor for wound care. The reported sensors represent an effective example of biocompatible, low-cost, disposable and low power consumption devices that can work in intimate contact with chronic wounds for continuous monitoring.

### 4.1 Introduction to wound care

The rising Internet of Medical Things (IoMT) is taking wearable devices and allowing technologies to revolutionize healthcare with a dedicated patient-centric vision, inspiring innovative management and design of clinical trials. One of the medical fields that could benefit from the IoMT approach is the treating of nonhealing wounds. The wound healing course is a complex cascade of physiological events, which are exposed to both body status and external factors, and whose dysregulation leads to compromised healing or chronicity. The standard chronic wound care involves labour-intensive work, a lot of time, frequent and painful removal of wound dressings. Chronic wounds typically exceeding a 3-month healing process are recognized as a major source of mortality in bed-ridden and diabetic patients and imply high treatment costs.<sup>464-466</sup> Moreover, the number of chronic wound patients is constantly increasing as a result of many factors, including the old age population, which brings considerable economic costs.<sup>467</sup> Part of the current medical care requires constant removal of the dressing in order to observe the healing stage, clean the wound, detect any bacteria or infection and apply therapy if required. In addition, the wound status is typically assessed by visual inspection and dressing change is often done needlessly, with persistent risk of causing a further injury or disturbing the wound healing process.<sup>198,468</sup> The clinical assessment of the healing progression remains challenging due to its complexity and dynamism<sup>160</sup>, as well as the lack of quantitative and firmly established tools for wound monitoring over time.

Nowadays, the medical field demands diagnostic tools and monitoring systems that would provide much better comfort, simplicity and non-invasiveness to tissues. The design of new IoMT devices and smart dressings able to non-invasively monitor the wound site can have a strong effect on the results of wound management and healthcare costs.

#### 4.1.1 Wound healing process

The wound repair mechanism depends on the immune response of the body and is affected by various factors, including age, nutrition, mechanical action, diseases like diabetes, and many biochemical or physiological parameters.<sup>469</sup> Understanding the complex tissue repair mechanism is the most important step towards the development of a wound dressing. Wound tissue repair is classified into 3 stages: hemostasis and inflammation, proliferation, and remodelling.<sup>163</sup>

Hemostasis is the initial wound healing phase characterized by a coagulated blood clot formation. The function of the initial stage is to attract various bioactive agents and white blood cells at the wound site. Soon, a protective inflammatory response becomes responsible for pathogens prevention and tissue repair initiation. After 2-3 days, the white cells reach the wound and produce nitric oxide, with important repair and antimicrobial

## 4.1 Introduction to wound care

---

functions. Neutrophils and macrophages release chemokines and cytokines that stimulate tissue repair by organizing the cells for the next wound healing phase. Neither too short nor chronic inflammation is desired. Chronic wounds have a prolonged inflammatory phase which disturbs the healing progression. Therefore, inhibition of the inflammatory response by reducing the number of white blood cells coming at the wound site is beneficial in this case. It is crucial to differentiate inflammation from infection: infection is microbial driven, which stimulates the inflammatory response. The healing course of a wound depends on several factors such as temperature, moisture, pH, uric acid, glucose and lactate level. The parameters of temperature and pH value at the wound site at this phase are higher than normal tissues, so cooling down and reducing the pH can contribute to the healing. The slightly basic pH value found in chronic wounds is to be between 7.15 - 8.9, which supports tissue degradation, as more oxygen can be consumed in this environment or there are alkaline byproducts of microorganisms.

Proliferation is the stage of tissue rebuilding which usually starts 2-10 days after the injury. The necessary cells, including fibroblasts, are well organized to build an extracellular matrix that will provide a new skin barrier and new blood vessels and capillaries crucial for water and nutrient supplies.

Remodelling takes place 2-3 weeks after the injury and can last a year or more, while immune response is gradually stopped.<sup>163</sup> Healthy skin tissue is slightly acidic, pH 4-7, while wounded tissues have pH values shifted to more basic values due to abnormal cell functions, enzyme degradation, infections or bacteria. In order to accelerate the healing rate, a normal pH range has to be achieved at the wound site.

At the same time, the moisture level of a wound takes a relevant role in the healing process: a low moisture level can desiccate the wound and slow down the recovery, while a high value can lead to wound maceration.<sup>470</sup> Optimal moisture level in the wound bed is vital for proper tissue regeneration. These represent the main reasons why pH and moisture level are used as important parameters for wound treatment.<sup>184,464,465,469,471</sup>

### 4.1.2 Wound dressings

According to their functional properties, there are different categories of wound dressings: passive, interactive, advanced, and bioactive. Their suitability for treatment depends on the wound condition. For instance, higher hydrophilicity, swelling and low adhesive substrate properties are not suited for deep wounds as they can easily separate from the wound bed. On the other hand, these properties are favoured for easier and pain-free removal of dry wounds.

Passive dressings have a passive role in wound coverage and include textile gauzes. However, they are painful for removal and do not possess sufficient barrier properties. Interactive wound dressings produced by polymeric films, foams and hydrogels provide a

hydrophilic, flexible surface with a moisturizing effect and painless removal. The swelling behaviour of hydrogels can balance the moisture level and wound hydration, cool down the wound temperature and provide an ideal environment for dry wounds. An additional regenerative function characterizes advanced dressings compared to the previous systems. For example, calcium ions from the alginate wound dressing have a healing function towards deep wounds by forming a gel. Bioactive dressings offer an environment of biological scaffolds. Drug delivery, cell culture, active regeneration, accelerated healing and personalized treatment are their main attributes. Chemical signals like growth factors and cell adhesion molecules can be cultured in the scaffolds to significantly improve tissue regeneration or rebuild burns.<sup>163</sup> All these dressing systems can be integrated directly with specific sensing ability to extract crucial information about the underlying wound.

### 4.1.3 Wound sensing

Nowadays, miniaturized wearable readers and sensors have been developed, and various body fluids such as tear,<sup>472</sup> saliva<sup>473</sup> or sweat,<sup>474</sup> are exploited to monitor relevant biomarkers for healthcare applications. However, the wound environment is still scarcely investigated. On the one hand, significant limitations related to the development of wearable devices employed in contact with human skin are conformability and safety, which become even more strict when the sampling site is an injury under healing. The sensing device should neither cause discomfort or pain nor contaminate the injured tissues or interfere with the healing progression. On the other hand, technical challenges concern its complex composition and the small sample volumes and the necessity to evaluate spatial distributions rather than carrying out numerous time-consuming punctual measurements at specific locations.<sup>167</sup> If all these requirements for wound treatment are satisfied by a smart wound dressing, the treatment would be much more simplified, effective, cheaper and comfortable. This can be achieved by constructing an advanced wound dressing with wound coverage, parameters monitoring and regenerative functions. The substrate structure has to be produced by nontoxic, biocompatible materials and to provide the best possible environment for wound healing. Flexibility, similarity to skin tissue, high comfort, easy adsorption and painless removal without any damage are some of the crucial structural requirements. The barrier properties need to allow gas exchange and prevent infections and bacteria. Recent examples of smart bandages have been proposed for the detection of pH,<sup>468,475</sup> uric acid, moisture,<sup>197</sup> and bacteria infection.<sup>174,476</sup>

## 4.1 Introduction to wound care

---

### 4.1.3.1 pH monitoring

Real-time monitoring of wound bed pH is a likely candidate for remote wound healing monitoring. In fact, the wound pH varies according to the wound healing phases<sup>477</sup> and, for this reason, noninvasive wound pH valuation can be useful to define the wound state and the effectiveness of the therapeutic strategy. While a slightly acidic pH provides optimum healing conditions to control collagen formation, increase fibroblasts activity, and hamper bacteria proliferation, more alkaline pH values (7–9) are typical of hard-to-heal wounds.<sup>478,479</sup> Conventional clinical methods of pH monitoring rely on chronoamperometry or optical transitions of test strips and pH meters but require frequent removal of wound dressings which damages the skin, the healing process and increases the risk for infections. For this reason, it is interesting to incorporate a pH sensory function in the dressing to display what is going on in the wound bed without the need for frequent removal.

Although pH sensing is standard analytical practice and several potentiometric probes are available in the market, commercial sensors might be barely adapted to wound healing monitoring. An alternative to the bulky and fragile glass membrane electrodes, solid-state pH sensors based on transition-metal oxides (MOx) have been subjected to a rapid expansion thanks to their biocompatibility, electrical and electrochemical properties, and inherent stability to harsh experimental conditions. However, the MOx based textile pH sensors have not been considered in the area of wound treating yet. In its place, the conjugated polymer polyaniline (PANI) represents the gold standard in the fabrication of textile potentiometric probes for quantitative pH detection. PANI-based wearable pH sensors have been developed using polyester<sup>480</sup> and cotton<sup>193–195</sup> threads, mainly exploiting the potentiometric transduction requiring the fabrication of flexible and reliable reference electrodes, which is still a crucial aspect.

### 4.1.3.2 Moisture monitoring

Concerning wound moisture monitoring, a possible strategy to detect the moisture level is to integrate a relative humidity (RH) sensor and correlate the increment up to the 100% value to the liquid saturation of the wound dressing.<sup>481</sup> In the field of wearables, textile humidity sensors have attracted significant interest due to the intrinsic hydrophilicity properties of fibre/fabric materials that help humidity sampling. Regarding the sensing configuration and mechanism, various working principles have been reported: resistive, capacitive, and impedance-based. For example, employing carbon nanotubes (CNTs) in a polymer matrix such as polylactide (PLA)<sup>482</sup> or poly(vinyl alcohol) (PVA)<sup>52</sup> it's possible, exploiting the hygroscopic property of the polymers, to change the CNT conductivity by water swelling. On the contrary, covering a dielectric material as polyamide fibres with copper thread, a reversible variation of RH can alter the whole capacitance of the yarn.<sup>483</sup> In

## 4.2 pH Wound monitoring

---

addition, two adjacent electrodes covered with a humidity-sensitive film can work as impedance-based RH sensors performing AC measures.<sup>484</sup> PEDOT:PSS have also been proposed as a humidity sensing layer due to its hygroscopic behavior<sup>485-487</sup>, but in every case, they are used for breath monitoring or measuring RH in the air without application in a wound environment. Moreover, an actual correlation between bandage saturation and RH has not been studied yet. To fulfil this gap, the straightforward solution is to directly focus on moisture sensors in order to quantify the volume of exudate in the bandage.

The first example of a smart bandage with a moisture sensor was presented in 2007 by McColl et al.<sup>197</sup> They proposed two Ag/AgCl electrodes insulated with silicon, inserted in a commercial dressing and, exploiting the ionic nature of exudate and measuring the impedance variation ( $\Delta Z$ ), they obtained a correlation between the  $Z$  and moisture loss. After this first example, in 2016 a commercial moisture sensor for wound care called "Wound Sense" was released.<sup>198</sup> Even in this case, the plastic-based sensor consists of Ag/AgCl electrodes connected to a bulky reader and is able to give quality moisture reading using a visual five drop-scale (dry, moist to dry, moist, wet to moist, wet). Therefore, driven by the absence of noninvasive and wearable systems for moisture monitoring in wounds, a two-terminal impedance sensor based on PEDOT:PSS integrated into commercial dressing will be reported in the following paragraphs. The considerable impedance variation recorded was used to interface the sensor with an RFID reader, thus providing a fully passive wound monitoring.

## 4.2 pH Wound monitoring

As already mentioned, the pH of the wound bed is a fundamental parameter to monitor the healing process of chronic wounds, and in the following paragraphs, two examples of a smart wound dressing able to measure the pH level are reported. The modest sensitivity in the relevant wound pH range of the PEDOT:dye-based textile sensor made it necessary to develop a new and more performing system using Metal-Oxide compounds capable of covering the range of interest with higher sensitivity values.

### 4.2.1 Textile sensors based on PEDOT:dye compound

As already reported for the pH detection in the human sweat environment, the same working principle has been applied to monitor the pH value in exudate liquid. Due to the nature of the sampling site, the sensitive element based on the coupling of a conductive channel of PEDOT:PSS and a film of PEDOT:BTB, is directly deposited on a wound dressing instead of using a textile thread. Bromothymol blue, BTB, acts as PEDOT counterion able to stabilize the gaps in the conducting polymer (see section 2.2.3). In an aqueous environment,

BTB is spontaneously involved in acid-base processes that modify its protonation state and, consequently, its ability to stabilize charge carriers in the PEDOT. Due to this phenomenon, PEDOT:BTB exerts an electrochemical gating effect and reversibly modulate the conductivity of the PEDOT:PSS channel depending on the pH of the analyzed solution.

### 4.2.1.1 Fabrication of smart dressing pH sensor

The structure of a generic smart dressing is designed as shown in Figure 4.1.a. In particular, it provides three different layers held together by a heat-sealing web glue. Layer 1 is the protective or separation layer in direct contact with the wound and is aimed at protecting the latter from any possible migration of material coming from the next layer on which the sensor has been printed. Layer 2 is the sensorized layer, i.e. in which the sensing element is printed and/or deposited and responsible for transduction. This layer must be compatible with the screen printing process used to print the PEDOT-based ink. Layer 3 is the absorbent layer, which allows for the accumulation of the sampled fluid. Finally, an adhesive layer allows the dressing to stick onto the skin and to be firmly in touch with the wound.

Layers 1 and 2 do not require high absorption or retention capacities but must ensure the passage of exuded fluid to subsequent layers avoiding preferential paths. Conversely, high fluid retention and absorption values are desired for layer 3, so as to achieve a capillary gradient when combined with previous layers to generate a vertically directed exudate flow. All layers should disfavour stagnation and remixing of sampled fluid (back mixing), thus ensuring a continuous supply of fresh exudate to layer 2. The fabrics used here to make the intelligent dressing have been supplied by the company Plastod S.p.a. and are covered by an industrial patent.

The sensing capability to the smart dressing is ensured by screen-printing a layer of PEDOT:PSS-based ink onto the second layer. PEDOT:PSS-based inks (Clevious PH1000 as commercial formulation) containing the secondary dopant ethylene glycol (EG), the cross-linking agent 3-Glycidoxypropyltrimethoxysilane (GOPS), and the plasticizer polyethylene glycol (PEG) is used to deposit the conductive sensing element. The screen printing process imprints the ink onto layer 2 in a uniform manner. Using a mask, the desired print geometry for the printed electrodes is defined, while the printing resolution depends on the ink composition and the characteristics of the textile material. In the present case, the conductive polymer track has a rectangular shape of  $2 \times 0.5 \text{ cm}^2$ . Once the electrode is printed, the sensorized layer 2 is dried in an oven at  $60^\circ\text{C}$ . After the screen-printing process, the electrodes printed on layer 2 are provided with textile connections that allow extraction of the electrical signal. Specifically, commercial conductive threads are sewn to the ends of the electrodes, and the junction points were protected locally with the minimum amount of silicone insulator (polydimethylsiloxane, PDMS), which was subsequently cross-linked at

## 4.2 pH Wound monitoring

150°C for 1 minute on a hot plate. The inset in Figure 4.1.b reports a picture of the smart dressing.

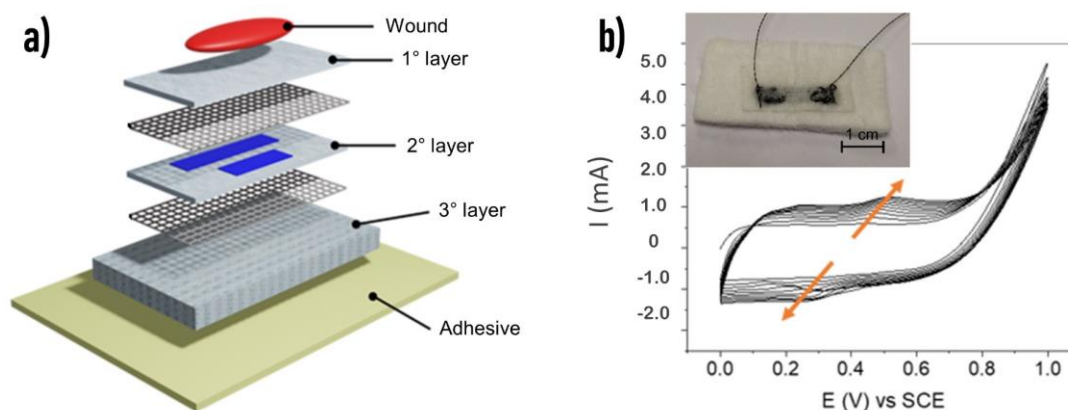


**Figure 4.1:** a) Generic structure of a wound dressing bandage with the three different composition layers. b) Cyclic voltammogram ( $0 < E < 1$  vs SCE) recorded during the deposition of PEDOT:BTB onto the conductive surface. The inset reports a picture of the smart dressing.

The screen-printed tracks present resistance of  $(50 \pm 5) \Omega$ , and this allows the electrochemical deposition of the PEDOT:BTB layer onto the conductive film. The gauze modified with PEDOT:PSS is placed in an electrochemical cell and immersed in the polymerization solution, containing the EDOT monomer and the BTB counterion in concentrations of 10 and 1 mM, respectively. Electrodeposition is performed using the gauze as the working electrode, a saturated calomel electrode (SCE) as the reference electrode, and a platinum wire as the counter electrode. A potential scan is applied to the working electrode in the range  $0 < E < 1$  V vs SCE for ten successive cycles at a scan rate of  $0.1 \text{ V s}^{-1}$ . The voltammogram recorded during electrodeposition of PEDOT:BTB is shown in Figure 4.1.b. In particular, the increase in current recorded cycle after cycle demonstrates the progressive deposition of PEDOT:BTB on the screen-printed PEDOT:PSS. After this fabrication step, the three layers are then hot glued together, using a Web Glue film, to form the final stacked structure.

### 4.2.1.2 Performance evaluation

With the aim to achieve a smart bandage capable of measuring the pH level in a wound, in-flow testing is employed to characterize the textile and stacked pH wound sensors. This condition can simulate the actual behaviour of a real wound and the diffusion of the exudate liquid through the dressing. The flow system is constructed with an HPLC pump capable of delivering a constant flow between  $0.01$  and  $9.99 \text{ mL min}^{-1}$  over the surface

## 4.2 pH Wound monitoring

of the dressing. This flow system allows a volume of liquid similar to that generated by a wound to be continuously delivered to the surface of the dressing. Specifically, a constant voltage is applied to the ends of the two-terminal sensor, recording its current over time during the delivery of a continuous flow of pH-varying buffer solution (Universal Buffer) to the sensed layer 2.

The application of a potential of  $-0.2$  V does not allow the acquisition of a stable signal, as the recorded current presents a continuous drift regardless of the pH of the solution delivered by the pump. This is the first difference between the textile thread sensors for pH in sweat and the here reported pH wound sensors. To overcome this problem, a lower potential of  $20$  mV is applied to the two-terminal sensor. The current vs time curve is shown in Figure 4.2.a, and a variable current signal is evident in correspondence with changes in pH of the fluid delivered by the pump. The steady-state current as a function of pH is shown in Figure 4.2.b, suggesting a parabolic trend over the pH range from 4 to 9.

The characterization reported here demonstrate the possibility of realizing a smart dressing capable of detecting real-time pH changes in a small volume of moving fluid. Coupling the sensorized layer with an absorbent gauze (layer 3) allows creating a sampling system capable of directing small volumes of fluid through the sensing element in the desired verse and without apparent problems of mixing or stagnation. However, the PEDOT:PSS film and PEDOT:BTB layer deposited on a textile wound gauze allows to realize a wound pH sensor that presents an undesired current drifting and a parabolic trend over a wide pH range. Narrowing the studied pH range in order to have an approximately linear response would result in a low sensitivity ( $9 \pm 2$ )  $\text{pH}^{-1}$  in a region not relevant for wound pH monitoring.

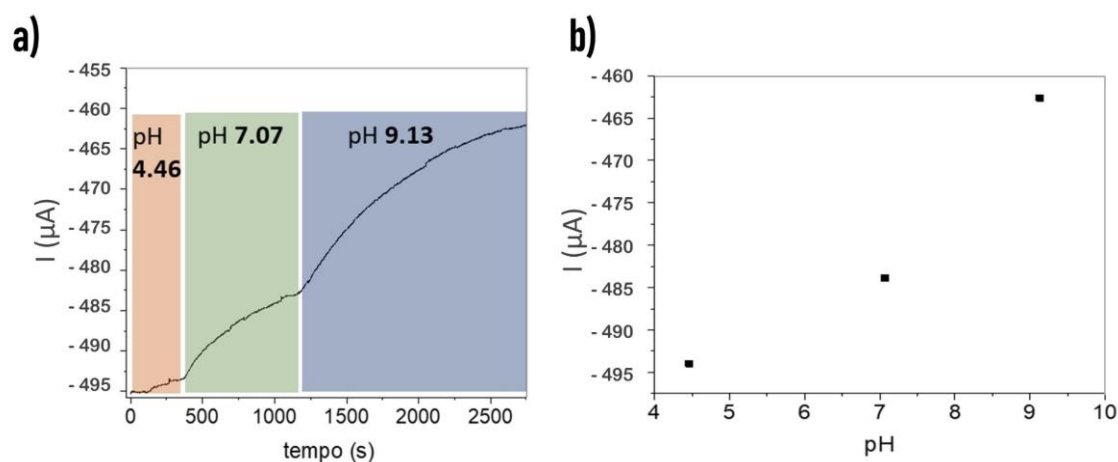


**Figure 4.2:** a) Current recorded in the smart bandage when the pH of the in-flow solution gradually increases from 4.46 to 9.13. b) Plot of the steady-state current as a function of pH value.

Overall, these results underline again the feasibility of pH transduction by the PEDOT:BTB compound deposited on textile but do not make it a valid solution for the purpose of creating a commercial product for wound monitoring. For this scope, a new transduction method based on Metal-Oxides has been introduced and extensively studied. This allows the fabrication of a two-terminal pH sensor able to work reversibly and linearly in the medically relevant pH range for wound monitoring thanks to its excellent sensitivity and without being subject to interference by the most common chemical agents present in the exudate.

### 4.2.2 Non-textile pH sensors based on metal-oxide compound

The solid-state pH sensors based on transitional-metal oxides (MOx) have represented an alternative to the fragile and bulky glass membrane electrodes for the monitoring of pH in a liquid environment. The unique electrical and electrochemical features, biocompatibility and stability, allowed the implementation of MOx compounds for pH measurements. Among them, IrOx is recognized as one of the most promising materials for pH sensing with superior sensitivity, wide detection range, and long-term stability.<sup>488-491</sup>

IrOx films have been utilized for the in vitro monitoring of cells and tissues pH,<sup>492-496</sup> the fabrication of transistor-based pH sensors<sup>497,498</sup> and, more recently, the development of wearable pH sensors for sweat monitoring on plastic substrates<sup>499-502</sup> and conductive fabrics.<sup>137</sup> However, IrOx-based textile pH sensors have not entered the area of wound management yet.

The main example of realizing textile sensors for pH monitoring relies on the conjugated polymer polyaniline (PANI). Using this material, Guinovart et al.<sup>192</sup> reported wearable pH sensors using cotton and polyester thread employing potentiometric probes. However, despite the remarkable successes in the design and manufacturing of potentiometric-based sensors, the major limitation consists in the realization of reliable reference electrodes by printing or coating methods, which is still at the embryonic level. To overcome this issue here is reported a new material-based approach for the development of electrochemical sensors leading to the benefits of the potentiometric transduction but using a referenceless two-terminal configuration.

As previously presented, the sensor architecture relies on a mechanism named electrochemical gating, and is easily adapted to unconventional substrates as fabric, textile threads or wound dressing. The novel two-terminal sensor for pH monitoring is based on chemically synthesized IrOx particles (IrOx Ps) embedded in a PEDOT:PSS thin film. The conductivity of this hybrid material reversibly changes with pH variations thanks to spontaneous redox reactions involving the IrOx Ps, leading to remarkable sensing performances in terms of reproducibility, accuracy and stability. The simple two-terminal

configuration allows to directly deposit the sensing compound in a wound dressing structure in order to perform real-time pH monitoring.

The following paragraphs report the fabrication method, the electrochemical characterization and the working principle of PEDOT:PSS/IrOx Ps-based pH sensor realized on a rigid substrate before depositing it onto a wound dressing to realize a smart bandage for pH monitoring.

### 4.2.2.1 Fabrication of PEDOT:PSS/IrOx film

The pH-sensitive semiconductor PEDOT:PSS/IrOx Ps is prepared using a double-step procedure consisting of: (a) IrOx · nH<sub>2</sub>O Particles synthesis, and (b) electrodeposition of particles on a PEDOT:PSS thin film (Figure 4.3.a). A deep-blue aqueous suspension of IrOx nH<sub>2</sub>O Ps is chemically synthesized starting from a 2 mM IrCl<sub>4</sub> aqueous solution and following the procedure reported by Zhao et al.<sup>503</sup> NaOH (10 wt %) is added dropwise to the brownish solution under stirring until the pH turned basic, giving a light yellow colour. The solution is heated at 90 °C for 1 h under stirring until a homogeneous light blue colour appeared. Therefore, it is rapidly cooled down, and 3 M HNO<sub>3</sub> is added dropwise in order to achieve an acidic pH solution. Finally, the solution is kept under stirring for 80 min at room temperature and then the dark-blue suspension containing IrOx Ps is stored at 4 °C, protected from light sources.

The IrOx Ps suspension as such is employed as the electrolyte solution to carry out the electrodeposition of the particles onto a PEDOT:PSS film. The conductive film is achieved by spin-coating the PEDOT:PSS solution (Clevios PH1000, EG, DBSA, GOPS in the following volumetric ratio 93.75:5:0.25:1) at 500 rpm, for 3 s with an acceleration of 500 rpm/s. The electric contact is realized with Cr/Au (10/40 nm) tracks deposited on the glass via thermal evaporation. A standard electrochemical cell is used where the polymer film is the WE, and a Pt wire and an SCE are the CE and RE, respectively (Figure 4.3.b). The potential of the WE is scanned between 0 < E < 1 V vs SCE for 100 cycles at a rate of 100 mV s<sup>-1</sup>, achieving a functionalized PEDOT:PSS surface (Figure 4.3.c).

Figure 4.3.d shows a typical deposition voltammogram, and the current increase suggests that a growing number of particles are embedded upon cycling into the semiconductor film. Three faradic peaks, labelled as a-a<sup>1</sup>, b-b<sup>1</sup>, and c-c<sup>1</sup> can be identified taking also into account the strongly acidic pH of the electrolyte solution. The peaks b-b<sup>1</sup> and c-c<sup>1</sup> are ascribable to the Ir<sup>III</sup>/Ir<sup>IV</sup> and Ir<sup>IV</sup>/Ir<sup>V</sup> redox couples, respectively.<sup>504,505</sup> Differently, the peaks a-a<sup>1</sup> is associated with the altered electrostatic interaction between PEDOT and its sulfonate counterion due to the pH of the electrodeposition solution. Figure 4.3.e confirms this hypothesis in which bare PEDOT:PSS film is cycling in pH buffers below and above the pK<sub>a</sub> of PSS (e.g., 1.50),<sup>506</sup> showing that a faradic feature appeared at low pH when the counterion is protonated.

## 4.2 pH Wound monitoring

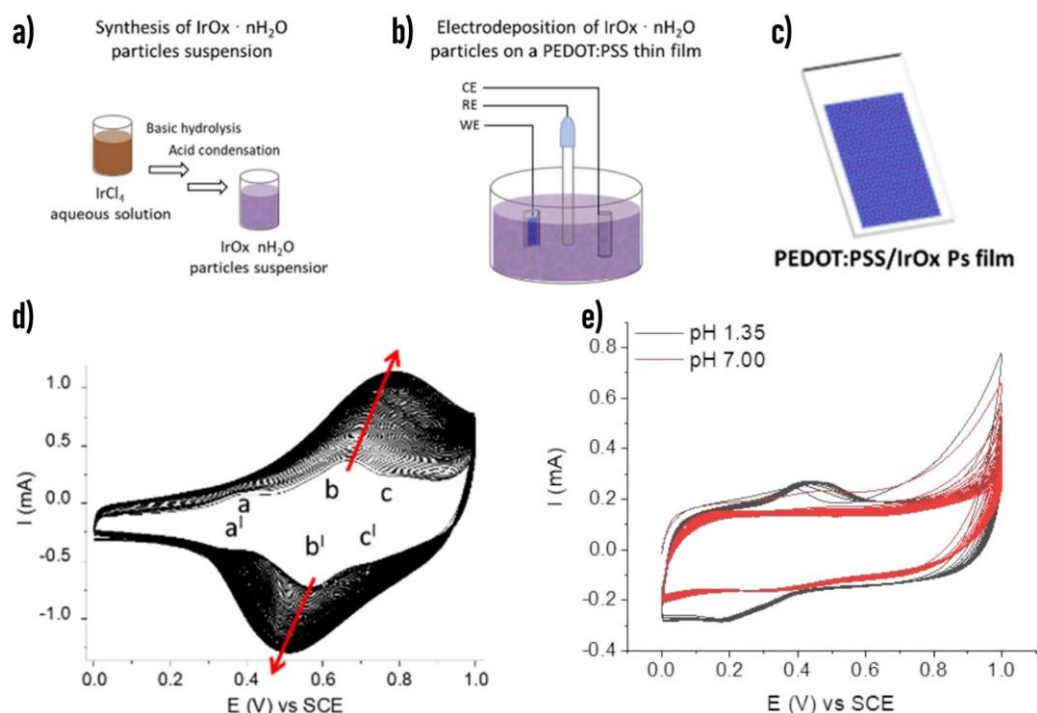


**Figure 4.3:** Preparation of the composite film on a glass substrate with the a) synthesis IrOx particles, b) electrodeposition setup for IrOx Ps on a PEDOT:PSS film and c) the final PEDOT:PSS/IrOx Ps. d) Electrochemical deposition of IrOx Ps on the PEDOT:PSS film. Scan rate = 100 mV s<sup>-1</sup>. e) Cyclic voltammograms of a PEDOT:PSS film in U.B. recorded in acidic and neutral pH conditions. Scan rate: 20 mV s<sup>-1</sup>.

### 4.2.2.2 Morphology structure

The morphology of the resulting PEDOT:PSS/IrOx Ps film is investigated by AFM (Figure 4.4.a-b). Discrete globular structures are shown in the height profile, and this highlights the difference from the flattened surface typical for spin-coated PEDOT:PSS films<sup>454</sup> (Figure 4.4.a). The RMS roughness increases from (0.6 ± 0.1) nm for the pristine PEDOT:PSS film to (1.0 ± 0.1) nm after the electrodeposition of the particles. However, the thickness of PEDOT:PSS before and after the deposition of IrOx Ps showed no statistically relevant variations, from (6.1 ± 0.9) × 10<sup>2</sup> nm to (6.3 ± 0.9) × 10<sup>2</sup> nm. KPFM map reported in Figure 4.4.b shows the presence of particles of about 300 nm diameter. Emerging from the PEDOT:PSS background of 5 eV,<sup>41</sup> a work function (WF) of 4.7/4.8 eV is calculated from the KPFM potential for IrOx Ps, and it is consistent with the WF ranges reported for amorphous and crystalline iridium oxides.<sup>507,508</sup> A sample area showing a protruding particle is also analyzed by SEM-EDS (Figure 4.4.c-d). By tilting the sample surface, the EDS map of the site, including the particle, is acquired obtaining a background signal due to the Sulfur atoms in the polymer backbone (representative for PEDOT:PSS), and a peak for Ir in correspondence of the particle location. Based on these results, it is reasonable to hypothesize that the particles are partially embedded within the PEDOT:PSS film, rather

than only confined onto the polymer surface. This is consistent with the three-dimensional swelling properties of PEDOT:PSS thin films in an aqueous environment during electrochemical deposition.

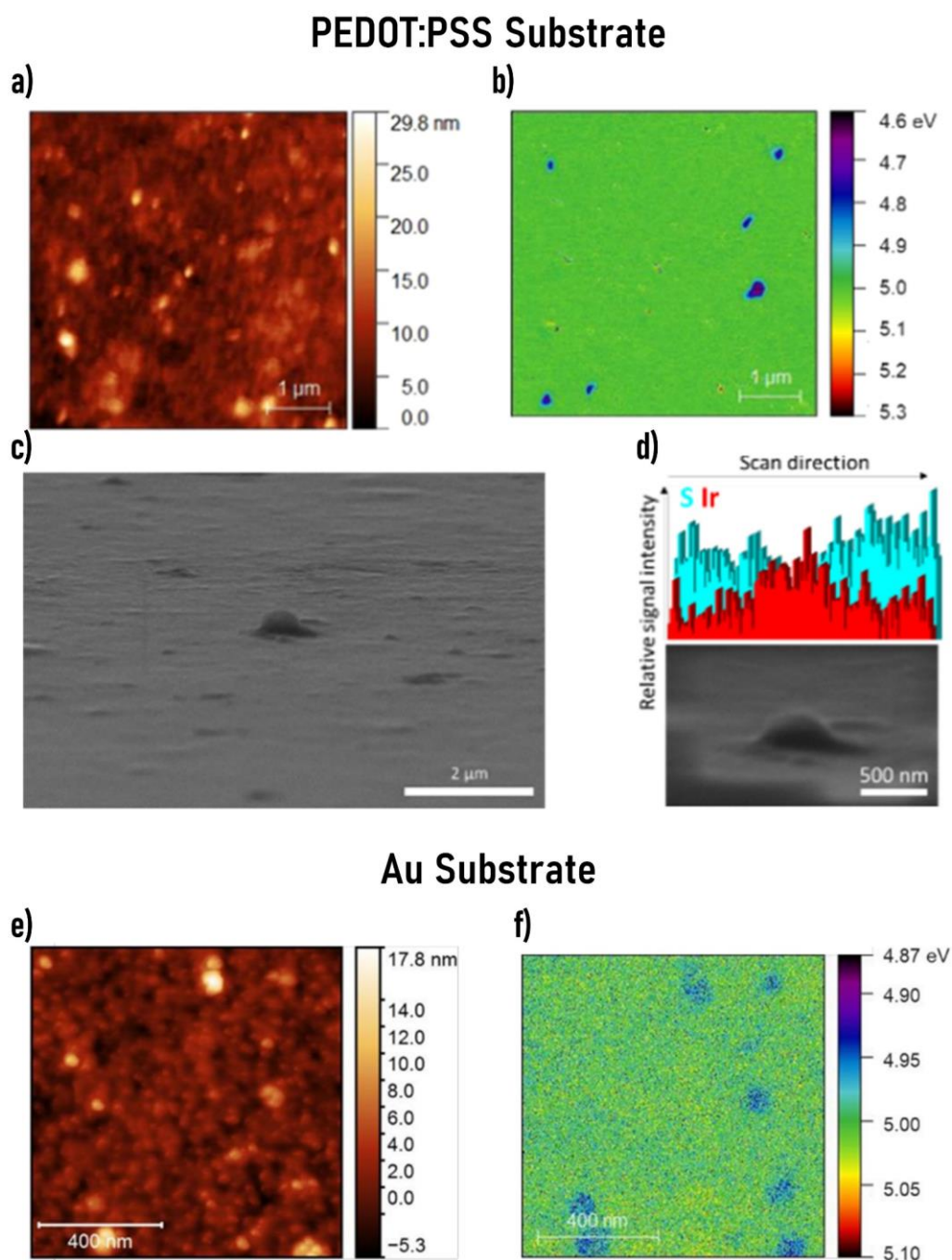


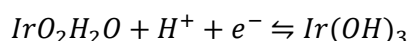
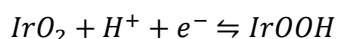
**Figure 4.4:** Morphology of the PEDOT:PSS/IrOx Ps film. a) AFM height, and b) KPFM map of the composite film. c) SEM imaging of the tilted sample surface and d) EDS profile of the portion localized around a protruding particle. e) AFM height, and f) KPFM image of an Au film after IrOx Ps electrodeposition. The reduced KPFM resolution is due to the use of an Au AFM probe.

Finally, it is worth noting that these particles are not clearly visible from the AFM height profile map reported in Figure 4.4.a but are only evident by electrically biasing the AFM tip (via KPFM). To better investigate the effect of the substrate on the particle deposition, the electrodeposition is performed on a thin film of gold as WE using the same experimental conditions. Au cannot swell in an aqueous environment and presents big differences from the three-dimensional PEDOT:PSS structure. Thanks to this feature, AFM-KPFM characterization reported in Figure 4.4.e-f show good matching between the sample topography (Figure 4.4.e), and the KPFM profile (Figure 4.4.f) that highlight the presence of smaller IrOx particles of around 100 nm diameter onto the gold surface.

### 4.2.2.3 Electrochemical characterization

Before exploiting the new IrOx Ps-based compound in a two-terminal smart sensor, the electrochemical behaviour of the PEDOT:PSS/IrOx Ps film has been investigated in response to pH variations of the electrolyte solution. Potentiometric measurements are performed in Universal Buffer (U.B.) by recording the zero-current electrochemical potential (open-circuit potential, OCP) of the thin film during base additions (Figure 4.5.a). The E vs pH plot in Figure 4.5.b shows a linear relationship in the wide pH range 3–11 with a slope of  $(-81 \pm 2)$  mV pH<sup>-1</sup>. It is worth noting, as reported in Figure 4.5.c, that the functionalization with IrOx Ps is essential to endow the organic semiconductor with pH sensing properties. The red curve shows that the slight response of PEDOT:PSS thin film to pH variation is one order of magnitude less than the functionalized sample.

The electrochemical response of PEDOT:PSS/IrOx Ps is also studied by cyclic voltammetry (CV) employing different pH buffers (with the same ionic strength) as electrolyte solutions. The voltammograms reported in Figure 4.5.d are characterized by a couple of quasi-reversible redox peaks, whose peak potential ( $E_p$ ) shifts toward more anodic values as the pH decreases. The peak position at acidic pH (black line) suggests that it refers to the main redox wave (system b-b<sup>1</sup>) found during the potentiodynamic deposition of the particles (Figure 4.5.d). This indicates that the Ir<sup>III</sup>/Ir<sup>IV</sup> redox couple is responsible for pH transduction, probably due to one of the following reactions:<sup>509,510</sup>



which can be described by the Nernst equation:

$$E = E^0 + RT/F \ln[H^+]$$

## 4.2 pH Wound monitoring

where  $E^0$  is the standard reduction potential of the redox couple,  $T$  is the absolute temperature,  $R$  is the gas constant, and  $F$  is the Faraday constant. This can explain the OCP decrease in Figure 4.5.a, and the shift of the peak potential toward more cathodic values in Figure 4.5.d as pH increases.

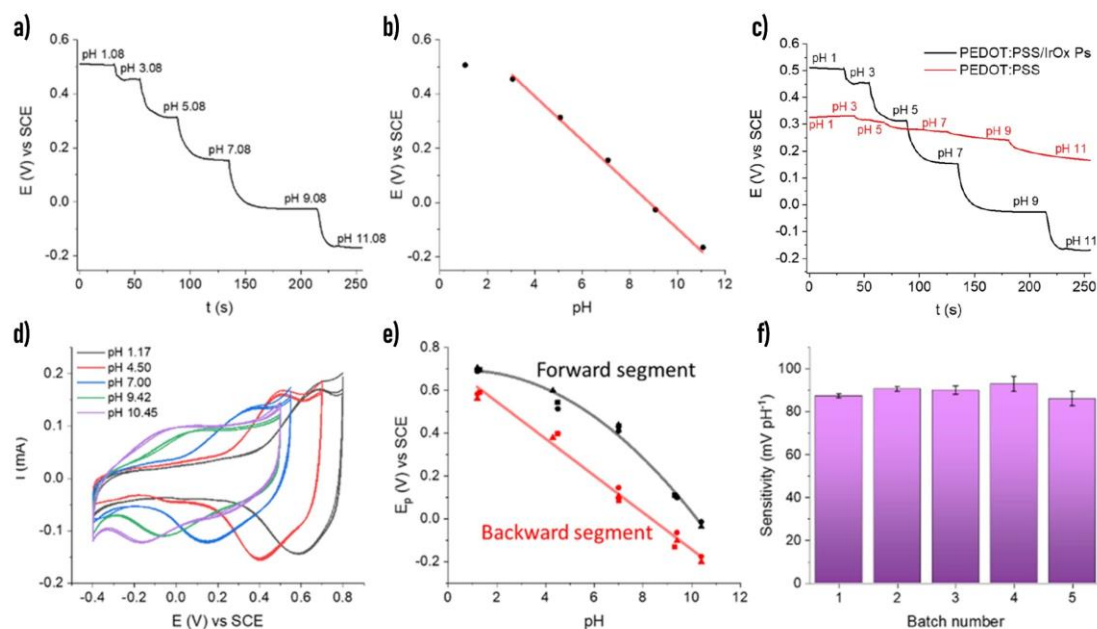


**Figure 4.5:** Electrochemical characterisation of the PEDOT:PSS/IrOx Ps film. a) Open-circuit potential response of a PEDOT:PSS/IrOx Ps film during 1 M KOH additions in U. B. b) and corresponding calibration plot ( $R^2 = 0.998$ ). c) OCP responses obtained from a PEDOT:PSS film functionalised with IrOx Ps and the pristine PEDOT:PSS film. d) Cyclic voltammograms of the same film in buffers at different pH values. Scan rate = 20 mV s<sup>-1</sup>. e) Peak potentials vs pH plots of the forward (black) and backward (red) segments from CV characterisations of three different PEDOT:PSS films after functionalisation with IrOx Ps coming from the same synthesis batch. f) Reproducibility of the backward peak potential sensitivity among different IrOx Ps synthesis batches.

The values of the peak potential  $E_p$  for the backward and forward segments are plotted vs pH in Figure 4.5.e, showing linear and non-linear correlations, respectively. In this case, a backward slope of  $(-86 \pm 3)$  mV pH<sup>-1</sup> is calculated in the pH range 1–10. This parameter is also used to compare the PEDOT:PSS/IrOx Ps films prepared from five different IrOx Ps synthesis batches to prove the reliability of particle synthesis and deposition (Figure 4.5.f). With an average slope of  $(-89 \pm 3)$  mV pH<sup>-1</sup> and a relative standard deviation (%RSD) equal to 3%, it can be concluded that the overall procedure for the preparation of PEDOT:PSS/IrOx Ps films shows good reproducibility.

### 4.2.2.4 Two-terminal pH sensors

The electrochemical characterization underlines that the compound material presented here is a pH transducer and that it can change its redox state in response to pH variations spontaneously. This feature makes the PEDOT:PSS/IrO<sub>x</sub> Ps composition a suitable platform to develop an electrochemical pH sensor. In view of wearable applications, a solid-state configuration without complex readout electronics and brittle components is highly desired. For this reason, the PEDOT:PSS/IrO<sub>x</sub> Ps film is then patterned between two evaporated gold electrodes, realizing the two-terminal architecture illustrated in Figure 4.6.a.

#### 4.2.2.4.1 Device characterization

The two-terminal sensor is connected to a source-measure unit to perform pH monitoring. A slight potential difference ( $V_{app} = -200$  mV to optimize the signal-to-noise ratio and reversibility) is applied between the two conductive electrodes. The generated current flowing across the semiconducting film is acquired versus time the two-terminal sensor is immersed in 0.1 M KNO<sub>3</sub> U. B. The pH of U. B. solution is varied upon controlled additions of 1 M KOH or 1 M HNO<sub>3</sub>, and stepwise decrements or increments of the measured current are observed, respectively (Figure 4.6.b). The exact pH value of the U.B. solution after each addition is measured in a *blank experiment* using the glass electrode.

Figure 4.6.c reports a scheme of the proposed sensing mechanism. A basic environment stimulates the oxidation of Ir<sup>III</sup> sites to Ir<sup>IV</sup>, causing the related injection of electrons into the PEDOT:PSS film. Therefore, the semiconductor is reduced (gains electrons), leading to a decrease of the charge carriers concentration and of the current flowing through the PEDOT:PSS film. Conversely, a current increase is observed upon acid additions, as the charge transfer reaction between Ir species and PEDOT:PSS causes the injections of holes in the semiconductor and increases its conductivity.

## 4.2 pH Wound monitoring

The particularity of the two-terminal sensor is that a non-linear response in the pH range 2–11 is obtained when the steady-state current (extracted from curves similar to the one in Figure 4.6.b) is plotted vs pH (Figure 4.6.d).

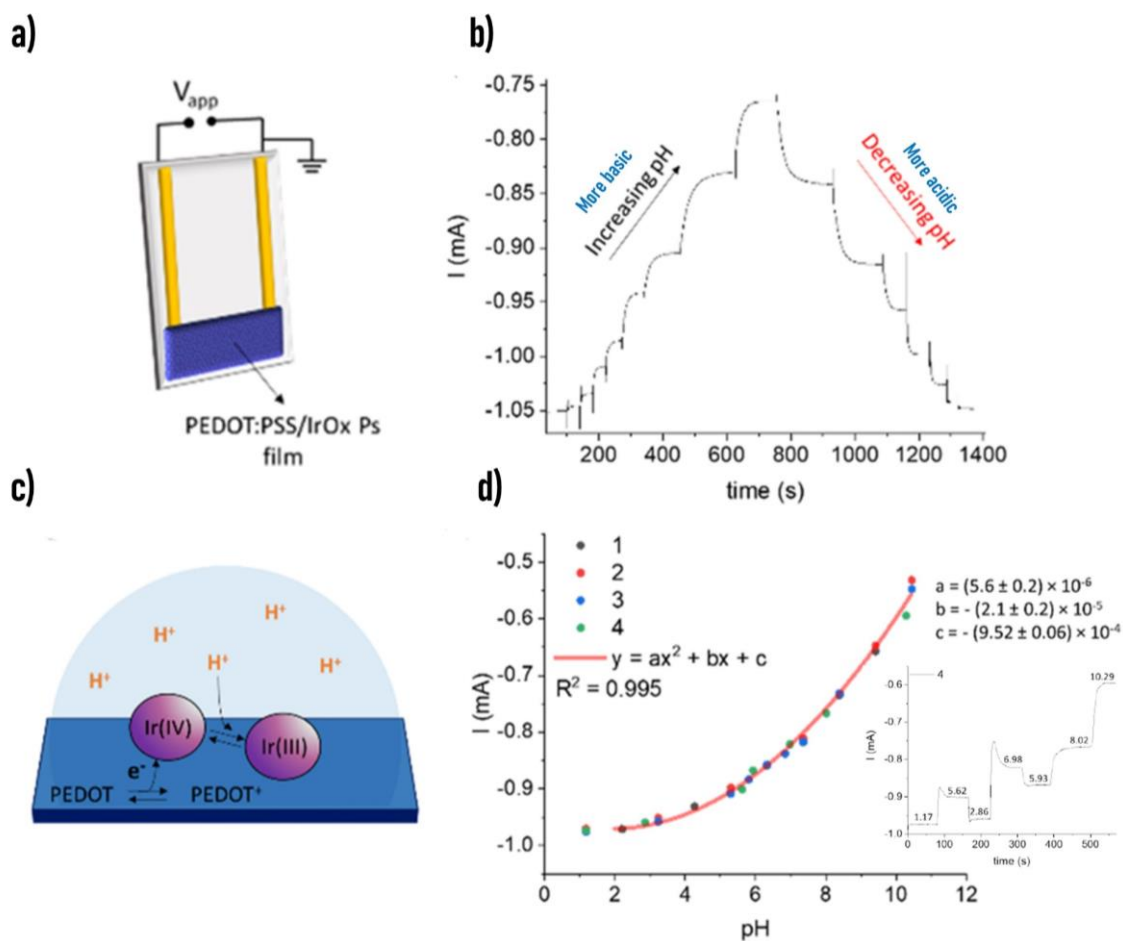


**Figure 4.6:** a) Scheme of the two-terminal sensor. b) Sensor response recorded in U.B. during 1 M KOH and 1 M HNO<sub>3</sub> additions.  $V_{app} = -200$  mV. c) Proposed sensing mechanism in the two-terminal pH sensor. d) Polynomial curve describing the sensor response obtained from the four independent I/t measurements.

The graph collects the data of four different devices and a second-order polynomial curve with the equation  $y = ax^2 + bx + c$  is the best fitting curve. Although a similar response can be unusual, the robustness of the quadratic regression is demonstrated characterizing the devices by randomized additions of acid and base to U.B., as reported in the inset of Figure 4.6.d. The sensor's response time (time to reach the 90% of the steady-state current) varies according to the pH range. In the acidic, intermediate, and basic pH intervals, it is 7, 19, and 70 s, respectively. This dependence in the response time is likely due to the different interactions of OH<sup>-</sup> and H<sup>+</sup> with the metal oxide IrOx Ps, and the faster diffusion speed of H<sup>+</sup> species, which are major in the acidic solutions.<sup>511,512</sup>

## 4.2 pH Wound monitoring

### 4.2.2.4.2 Film composition

The effect of film composition on the two-terminal pH sensors performance device is investigated, and the main results are reported in Figure 4.7. The relative amount of IrOx Ps within the semiconductor film is changed by varying the number of deposition cycles during the electrochemical functionalization. In particular, Figure 4.7.a reports the last deposition cycle of four different devices when 10, 50, 100, and 200 cycles are performed. Figure 4.7.b shows the four PEDOT:PSS/IrOx Ps two-terminal devices tested for pH detection in U.B. Figure 4.7.c shows the four PEDOT:PSS/IrOx Ps two-terminal devices tested for pH detection in U.B.

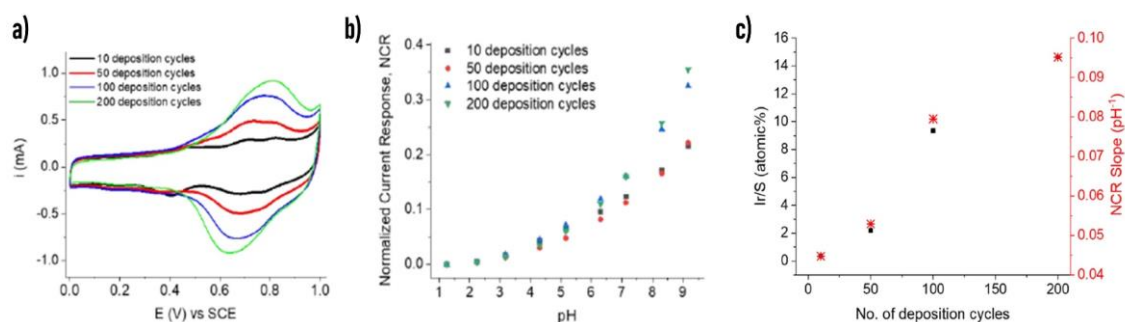


**Figure 4.7:** a) Last cycle of the voltammograms recorded during electrochemical depositions using different numbers of cycles. b) Comparison among the normalised current responses (NCR) obtained from four sensors during pH detection in U.B.  $V_{app} = -200$  mV. c) Plot of Ir/S atomic ratio, calculated from EDS analysis, and NCR sensitivity in the pH range 6.4 – 9.3 as function of the number of deposition cycles.

The resulting films are further analyzed by SEM-EDS to estimate the Iridium/Sulfur atomic ratio. In addition, as evident from SEM-EDS analysis, Figure 4.7.c shows that the relative amount of Ir atoms (Ir/S) increases with the number of deposition cycles, and it also well correlates with the NCR sensitivity values in the basic pH range (6 - 10). This suggests that a more significant amount of IrOx Ps within the polymer film would improve the sensing ability in the basic pH range requiring, however, a double fabrication time.

### 4.2.2.4.3 Reproducibility and linear range

The reproducibility is investigated by repeatedly testing ( $N > 3$ ) three different sensors, as reported in the calibration plot of Figure 4.8.a. The current response highlights a 5% variability in the baseline current that is attributed to geometrical differences, while the normalized current response ( $NCR = 1 - I/I_0$ ) curves eliminate the geometry factors and allow the comparison with different devices (Figure 4.8.b). In this case, the resulting values of the coefficients  $a$ ,  $b$ , and  $c$  in the non-linear regression are  $(5.7 \pm 0.5) \cdot 10^{-3}$ ,  $(2.3 \pm 0.6) \cdot 10^{-2}$ , and  $(3 \pm 1) \cdot 10^{-2}$ , respectively.

Considering the non-linear trend of the pH sensor, it is possible to analyse the response in smaller pH intervals in which two segments of the polynomial curve are reliably

## 4.2 pH Wound monitoring

interpolated by a straight line. The linear responses within limited pH ranges allow to analytically express the sensor's performance by means the pH sensitivity.

The new calibration plots in the pH ranges 2.5–5.2 (Figure 4.8.c) and 6.4–9.3 (Figure 4.8.d) point out the linear I/pH correlation in the narrower ranges. The calculated sensitivities are  $(20 \pm 1) \mu\text{A pH}^{-1}$ , and  $(59 \pm 4) \mu\text{A pH}^{-1}$ , respectively. Interestingly, the highest sensitivity is reported in the pH interval equivalent to the range of interest for wound healing monitoring.

### 4.2.2.4.4 Interfering agents

Focusing on the target of wound healing monitoring, the effects of interfering species and temperature are evaluated. Controlled amounts of the main chemical species that are typically present in wound exudate, i.e.,  $\text{K}^+$  and  $\text{Na}^+$  ions, glucose (glu), urea, lactate and uric acid (UA), are added at their typical concentrations<sup>172</sup> to a U. B. solution at pH 7.00 (Figure 4.9.a). The addition of lactate generates the predictable variation of the measured current due to its acid-base properties (circled in red), while the addition of 0.1

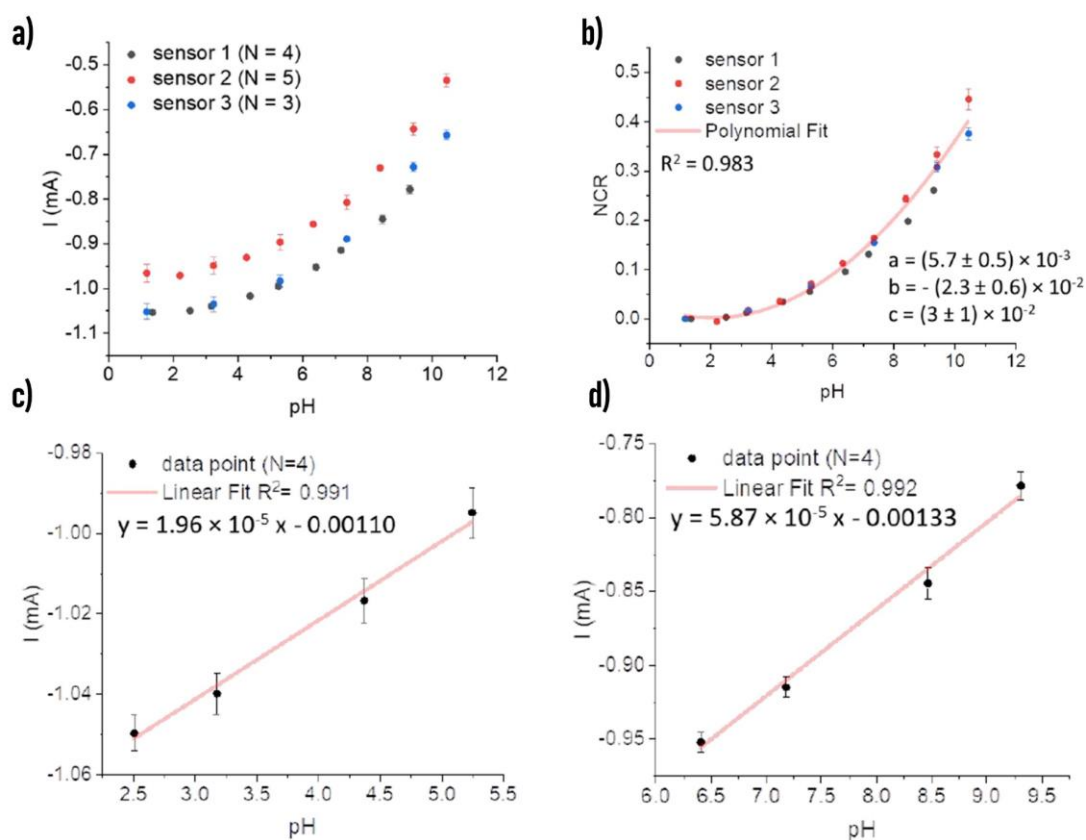


**Figure 4.8:** Reproducibility of the two-terminal sensors. a) current/pH calibration plots, and b) normalised current response (NCR)/pH calibration plots.  $V_{\text{app}} = -200$  mV. Approximation of the polynomial response with linear responses in c) acidic and d) basic environments.

## 4.2 pH Wound monitoring

M Na<sup>+</sup> leads to a 0.05% current decrease that can be associated to the pronounced increase of the ionic strength of the solution and, thus, of the pH solution due to the modification of the activity coefficients.

The sensor stability is studied during daily and long-term use. The result reported in Figure 4.9.b demonstrates that a drift of the measured signal with a relative standard deviation (%RSD) below 2% is achieved under both basic and acidic pH conditions over a five hours experiment. In addition, even after 40 days of storing the devices in the air under ambient conditions, the sensors retain their performance and only a baseline shift is observed that, however, could be corrected by normalizing the recorded current (Figure 4.9.c).

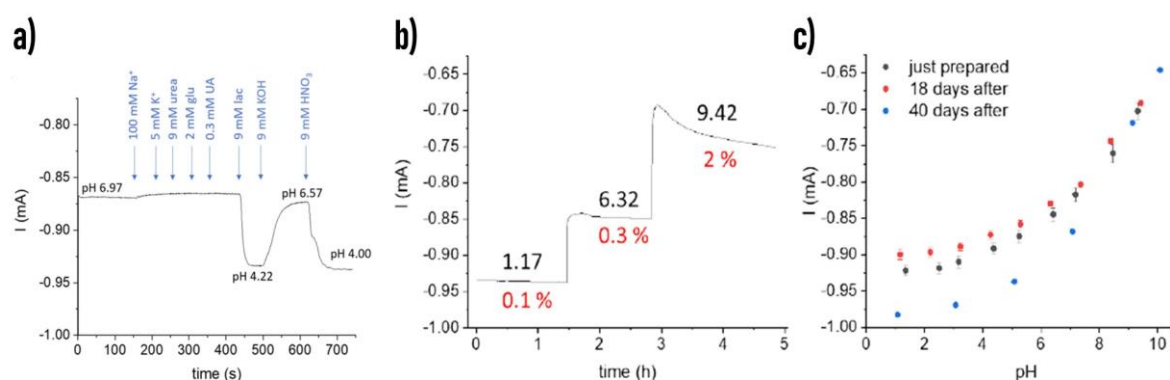


**Figure 4.9:** a) Interference study in U.B. adjusted to pH 7.00 by adding controlled amounts of chemical species that are typically found in wound exudate (Na<sup>+</sup>, K<sup>+</sup>, glucose, uric acid, urea, and lactate). b) Two-terminal sensor stability during daily use and c) over a long-term period.  $V_{app} = -200$  mV.

### 4.2.2.5 Working principle

The study of the sensing mechanism of the two-terminal pH sensor is performed, paying particular attention to the electrochemical interaction between IrOx Ps and the PEDOT:PSS film. Considering the intimate contact between the charge transport layer (PEDOT:PSS) and the potentiometric transducer (IrOx Ps), a spontaneous electrochemical gating generated at the interface between the two elements is responsible for the sensor response. In fact, IrOx Ps can be seen as a collection of miniaturized gate electrodes incorporated within the semiconducting channel of a transistor, whose conductivity is switched on/off upon a reversible gating. In this case, as for the Ag/AgCl NPs, the gate action appears from the spontaneous redox reactions occurring at the IrOx Ps/pH buffer solution interface that does not need an external source bias to take place. This has two major effects: i) in the two-terminal device, the different pH of the solution modulates the current, and it can be quantitatively used as the analytical signal for pH sensing, and whose

reliability and robustness are supported by the potentiometric transduction, and ii) the physically separated gate electrode is eliminated, as the sensing features come through spontaneous redox reactions involving IrOx particles placed in electrical contact within the polymer film.

The experimental setup in Figure 4.10.a is employed to understand the origin of the non-linear response of the two-terminal sensor. A measurement of the electrochemical potential of the grounded terminal (source) with respect to a reference electrode is simultaneously done meanwhile the two-terminal sensor detects the pH solution. Figure 4.10.b shows two different curves for E (electrochemical potential), and I (current) recorded over time upon base additions (top), and the corresponding calibration plots (bottom). As already mentioned, the pH-dependent current trend results from charge transfer reactions implicated in the electrochemical gating mechanism, which is driven by the potentiometric pH transducer IrOx and, E and I show complementary trends.

In addition, the I vs E curve of the PEDOT:PSS/IrOx Ps film is recorded by sweeping the potential of the grounded terminal between  $-0.2$  and  $+0.8$  V vs SCE and shown linear and saturation regions of conductivity, which are typical of the organic semiconductor film<sup>457</sup> (Figure 4.10.c). If the data in Figure 4.10.b are plotted in the same figure, it turns that the sensor response is superimposed to a portion of the I/E curve that perfectly lies between the two distinct regions. Therefore, it can be determined that the polynomial response of the PEDOT:PSS/IrOx Ps two-terminal sensor originates from the non-linear variation of charge carrier mobility in the semiconductor (represented by the current I) within the electrochemical potential window of interest ( $0 - 0.4$  V vs SCE).

### 4.2.3 Smart textile dressing for pH monitoring

After assessing and studying the response of the two-terminal PEDOT:PSS/IrOx Ps pH sensor, the optimized fabrication procedure developed for glass substrate is implemented onto a textile substrate to design a wearable smart dressing for wound healing monitoring. The following paragraphs report the fabrication procedure and the characterization for a new concept of smart textile wound dressing able to sense the pH variation during dynamic flow testing.

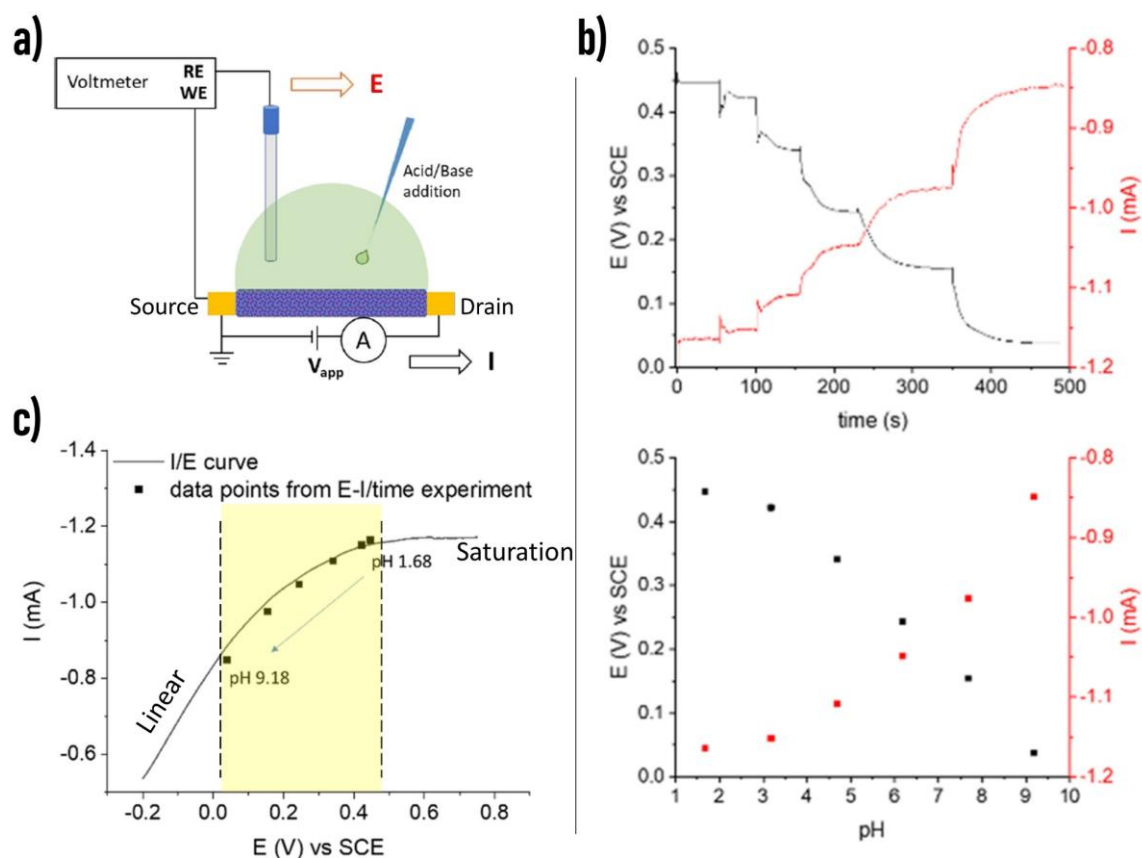


**Figure 4.10:** a) Experimental setup used for the simultaneous recording of the electrochemical potential and current during variations in the pH of the electrolyte solution. b) Simultaneous measurement of the electrochemical potential of the grounded terminal and the current flowing across the semiconductor during pH detection, and the corresponding calibration plots.  $V_{app} = -200$  mV. c) Superimposition of the data collected from b) and an  $I/E$  curve recorded by sweeping the electrochemical potential of the grounded terminal in U. B. Scan rate =  $10$  mV  $s^{-1}$ .

#### 4.2.3.1 Fabrication

The sensing layer is realized by screen-print a conducting ink formed by 78% v/v PH1000, 20% v/v EG, and 2% v/v GOPS onto the sterile textile dressing. Warming up the solution in an oven at  $60$   $^{\circ}C$ , the liquid evaporation allows losing about 40% of the initial weight in order to obtain a more viscous compound suitable for the deposition. A physical mask is employed to impress the conductive pattern ( $2 \times 0.5$  cm<sup>2</sup> stripe) onto the textile until a uniform layer is achieved. Subsequently, the device is placed on a hotplate at  $150$   $^{\circ}C$  for 10 min to allow the partial reticulation of PEDOT:PSS chains by GOPS. Two commercial stain steel threads are sewn at the edges of the sensor area and sealed with a small amount of conductive silver paste to reduce the contact resistance between the conducting threads and the conductive polymer. A mixture of PDMS-curing agents (9:1 w/w) is applied over

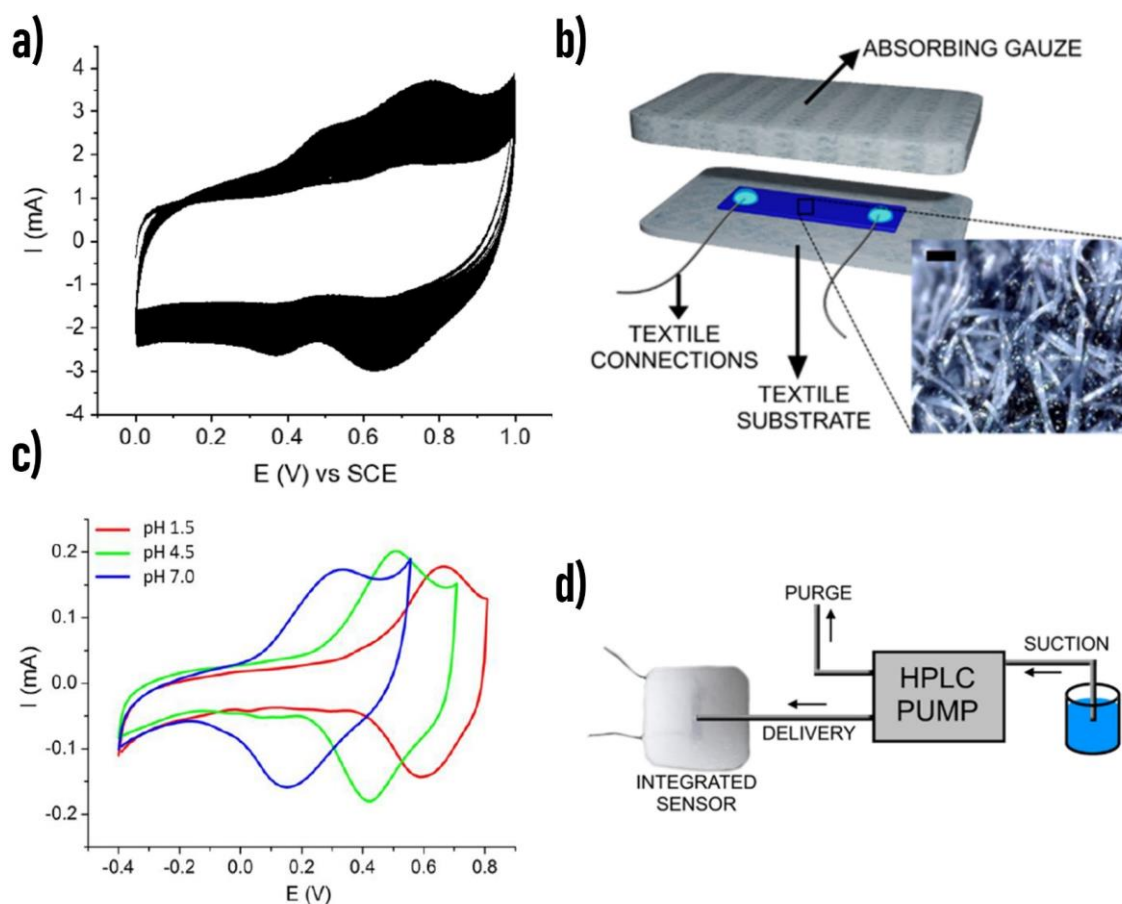
the silver paste to obtain electrical insulation. The textile two-terminal configuration here described is similar to the one fabricated on a glass substrate.

After the deposition of the conductive PEDOT:PSS film onto the textile wound dressing, the IrOx Ps are electrochemically deposited following the same procedure described above, and an example of the voltammogram is reported in Figure 4.11.a. After that, the smart pH sensing bandage is assembled in a sandwich-like manner coupling the sensing layer with an absorbing material (thickness of around 2 mm) for wound dressings acting as a fluid reservoir and as a passive pump for the sample fluid. The resulting smart pad is schematically represented in Figure 4.11.b.

### 4.2.3.2 Characterization and comparison

The electrochemical characterization by cyclic voltammetry performed in U.B. at various pH levels demonstrates the textile substrate's successful functionalization. Figure 4.11.c shows the typical E peak shift towards a more cathodic value as the pH increases. To best simulate the dynamic wound environment, the performance of the pH sensing dressing is validated in flow analysis using an HPLC with the setup reported in Figure 4.11.d. The pump continuously delivers precise volumes of the pH-variable solutions to the surface of the textile sensor. The solution moves across the sensing gauze thanks to the adsorption gradient generated by coupling together the different materials. The pump flow is set to  $0.05 \text{ mL min}^{-1}$  to simulate the exuding rate of a real wound bed.<sup>513</sup> The smart dressing ability to monitor real-time pH variations within the whole sensor response is assessed by injecting U.B. aliquots at different pH values to the pumping system.

The result, with the expected polynomial response, is reported in Figure 4.12.a. Considering the normalized current response (NCR) data, a good match is found among the coefficients of the interpolating curve obtained under flow analysis conditions using the textile sensor (Figure 4.12.b), and those obtained for the sensor fabricated on glass (Figure 4.8.b). Furthermore, the smart dressing response is studied under flow analysis conditions using simulated wound exudate (SWE) aliquots in the pH range of interest for wound healing monitoring. SWE is prepared by mixing 0.142 M NaCl, and 0.0025 M  $\text{CaCl}_2 \cdot 2\text{H}_2\text{O}$  while using 0.025 M TRIS (tris(hydroxymethyl)aminomethane), and 0.005 M Histidine HCl  $\cdot \text{H}_2\text{O}$  as a pH buffer. The pH is adjusted through the addition of known volumes of 1 M KOH and HCl using a glass electrode. Figure 4.12.c report in flow characterization in a limited pH interval, in which the sensor current variation with pH is approximately linear ( $R^2 = 0.970$ ), and the resulting sensitivity is  $(54 \pm 5) \mu\text{A pH}^{-1}$ , i.e., statistically comparable with the one obtained with the glass substrate.



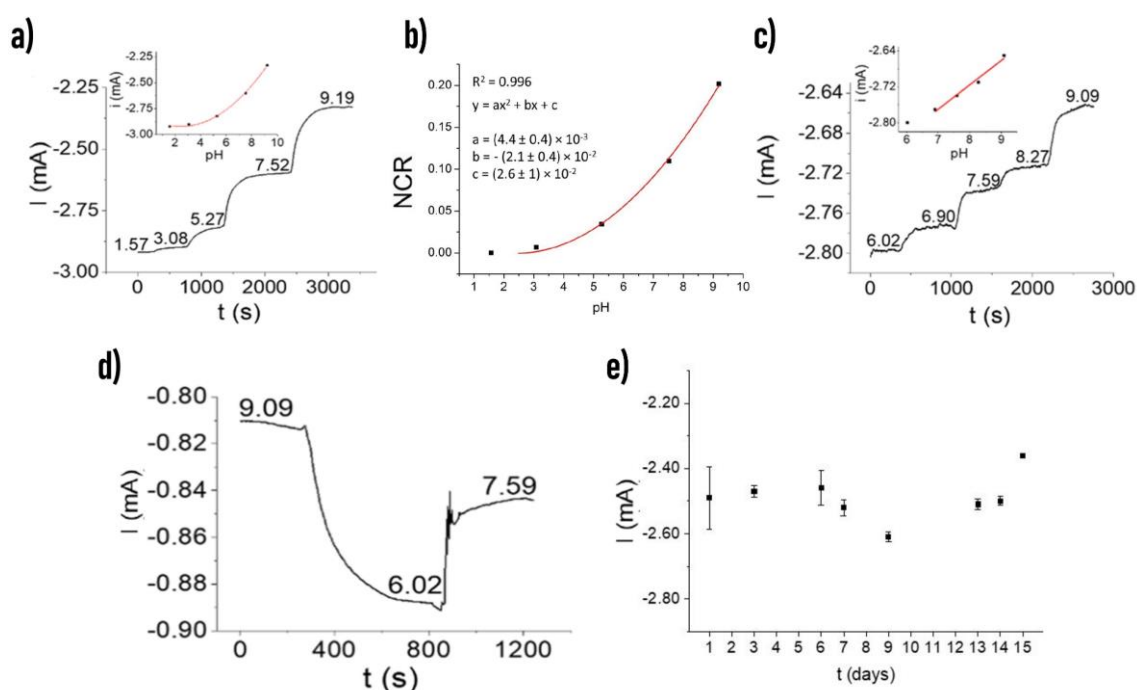
**Figure 4.11:** a) IrOx Ps electrodeposition on a textile PEDOT:PSS printed electrode. b) Scheme of the smart dressing for wound healing monitoring, comprising the PEDOT:PSS/IrOx Ps two-terminal sensor printed on a textile substrate and the absorbing gauze. Inset: picture of the textile PEDOT:PSS/IrOx Ps two-terminal sensor (scale bar = 100  $\mu\text{m}$ ). c) Cyclic voltammograms recorded from the resulting PEDOT:PSS/IrOx Ps textile electrode in buffers at different pH (right, scan rate 20  $\text{mV s}^{-1}$ ). d) Experimental setup used for flow experiments with the smart pad.

Figure 4.12.d reports the reversible current response, which demonstrates the capability of the textile sensor to detect random pH variations in SWE. Under flow conditions, the response time ( $t_{90}$ ) of the textile device is calculated as the time required to achieve the 90% of the steady-state current following each pH variation in the artificial wound exudate. An average  $t_{90}$  of  $(1.6 \pm 0.3) \times 10^2$  s is obtained.

The operational stability of the fully assembled textile sensor is studied by keeping it immersed in SWE (pH 7.50) for 15 consecutive days. The current generated upon application of  $V_{\text{app}} = -200$  mV is recorded daily for 1 h. Figure 4.12.e presents the current data and allows for tracking both drift and stability during the 2-week-long experiment, which reliably simulates a typical use of the smart dressing for monitoring chronic wounds. An average current drift of almost 1% is calculated during each daily measurement, while the % RSD of the mean current recorded throughout the 15 days is equal to 3%. Overall,

### 4.3 Textile moisture sensors

these results confirm the robustness of the smart dressing structure and textiles components. However, further improvements are required to apply the smart dressing to a medically relevant environment effectively. Nevertheless, to the best of our knowledge, this is the first time that the long-term stability of a textile sensor is tested during prolonged contact with the sample solution, and therefore, no comparison with other literature reports can be made. Considering the early stage of development, the results here represent a step forward among the state-of-the-art for wearable technologies and suggest that the identification of standardized protocols for assessing their analytical performances would benefit the whole research field.



**Figure 4.12:** a) Real-time, in-flow response of the wearable sensor in U.B. at different pH values; inset: calibration plot ( $R^2 = 0.996$ ). b) NCR calibration plot obtained from the in-flow, real-time pH measurement with the smart dressing. c) Real-time, in-flow response of the wearable sensor in SWE within the medically relevant pH range; inset: calibration plot ( $R^2 = 0.970$ ). d) Signal reversibility in SWE;  $V_{app} = -200$  mV. e) Long-term stability data collects during a two-week experiment in which the smart dressing is kept immersed in SWE (pH 7.50). Data points represent the average current value records for 1 hour. Error bars represent standard deviations.

### 4.3 Textile moisture sensors

In this section, the latest result about a moisture sensor based on PEDOT:PSS layer embedded into a commercial bandage for wound healing monitoring is proposed. The performance of the moisture sensors is studied using different geometries to extract two

parameters: (i) the threshold exudate volume  $V_T$  to discriminate between a dry and wet wound status, and (ii) saturation exudate volume  $V_S$ . Different patch configurations based on materials with opposite hydrophilicity features are here compared. The moisture sensors operate in real-time, and their impedance varies over four orders of magnitude between the dry and the wet conditions. The drastic change in the sensor impedance is further exploited to interface the smart dressing with RFID technology, leading to a wireless and fully passive wound management. Presenting different combinations of bandage layers, the final device structure can be adapted according to the different types of wounds or the actual healing stage, which can require a specific moisture condition.

#### 4.3.1 Textile single-layer structure

As already mentioned, the textile wound dressing materials used to fabricate smart sensors are divided into three types: the protective layer in contact with the skin, the active layer containing the sensitive pattern, and the reservoir fabric that stores the exudate. As the first example, a simple architecture based on just one single layer is here presented. In this case, in order to develop a moisture wound sensor, two textile substrates that differ from material composition and thickness are investigated and compared as the primary support for the active layer. The first gauze is named “Gauze PET” and is consists of an open mesh fabric formed by 100% polyethylene terephthalate (Figure 4.13.a). The second one is “Gauze Rayon” and is composed of 30% polyethylene terephthalate (PET), 70% rayon, and a thin anti-adherent film of polyethylene (PE) (see Figure 4.13.b).

Since fluid absorption by the wound dressing has a key role in the chronic-wounds treatment, the absorption feature of the two textile substrates is measured following the international procedure UNI EN ISO 9073-6; 2004. Shortly, the weight of a  $(25 \times 25)$  mm<sup>2</sup> gauze is measured before ( $m_i$ ) and after ( $m_f$ ) immersion in artificial exudate, and the liquid absorption is calculated as  $(m_f - m_i) / m_i \cdot 100$ . The difference in the weaving structure and composition influences the dispersion of liquid throughout the textile gauze, as reported in Figure 4.13.c and Figure 4.13.d for gauze PET and Rayon, respectively. Puring the same amount of an orangey-colour solution in the centre of  $(25 \times 25)$  mm<sup>2</sup> gauze, the liquid widely spreads over a large area for the gauze PET, while it remains confined in the middle in case of the gauze Rayon.

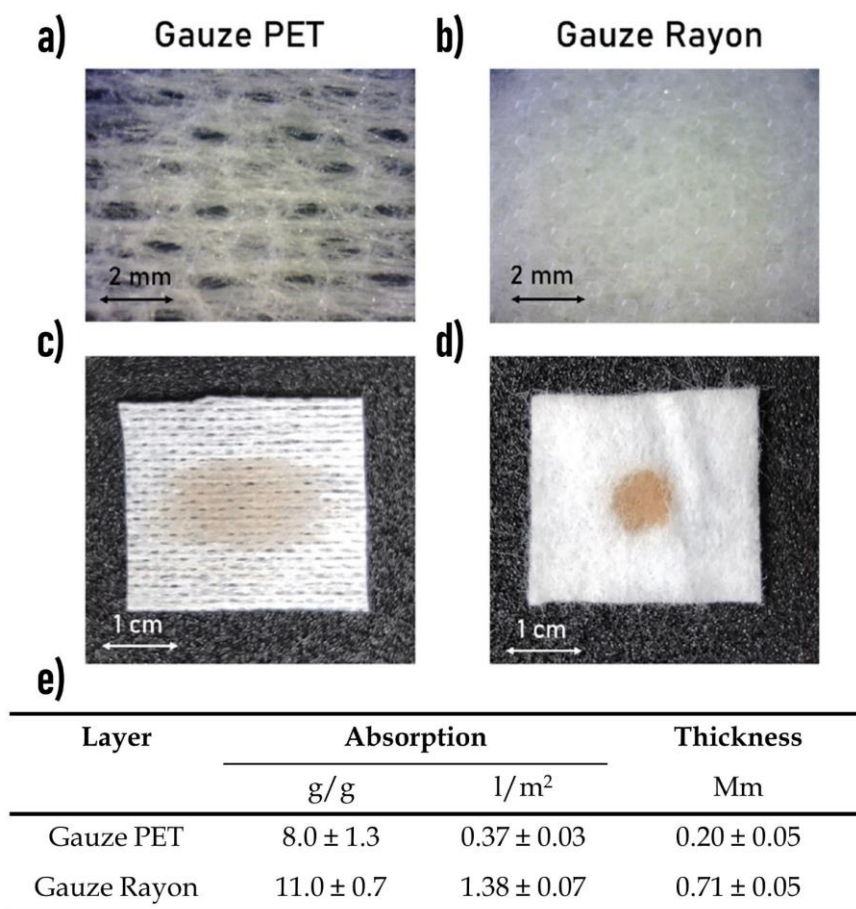


**Figure 4.13:** a -b) Enlarged top view and c-d) top view photos of the active substrates showing the different spreading of a coloured liquid through the textile surface of PET and Rayon gauzes. e) Physical properties of the first layers. The absorption is reported in g/g and in l/m<sup>2</sup> to indicate the percentage amount of volume absorbable by the textile material compared to its initial weight or planar dimensions, respectively.

#### 4.3.1.1 Fabrication procedure

These two types of gauzes have been used as the active substrate to fabricate a simple moisture sensor configuration based on PEDOT:PSS by screen printing technique. The conductive ink is prepared by mixing PEDOT:PSS and ethylene glycol (EG) in the ratio 0.95:0.05. The viscous ink is used for the screen printing procedure after losing 60% of its initial weight by heating it up in an oven at 70°C. The deposition procedure is the same reported above for the pH wound sensor, with the difference that the serigraphy frame has a mask to deposit two straight non-consecutive PEDOT: PSS-based strips. After the deposition, the conductive ink is dried at 70°C for 30 min. The procedure is repeated two times to obtain a homogeneous and highly conductive layer. It is estimated that an amount of (93 ± 7) mg of the conductive solution is deposited onto the gauze. Using this method, the geometry can be changed by modifying the pattern of the mask according to the specific

request. Two stainless-steel conductive threads are still employed to realize the electrical connection with the conductive layers.

#### 4.3.1.2 Results

The gauze Rayon and PET are used as the substrate to realize the single-layer moisture sensors, and two configurations that differ from the distance between the conductive strips, 2 mm and 5 mm, are evaluated (see Figure 4.14.a).

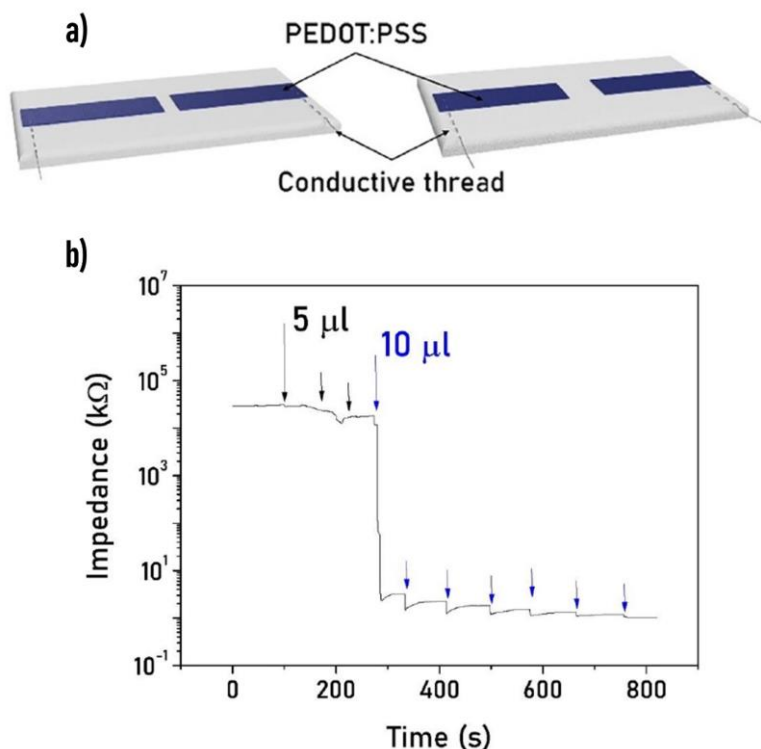


**Figure 4.14:** a) Representation of smart dressing with different distance between the conductive strips. b) Example of the textile moisture sensor's impedance response after subsequent addition of artificial exudate. The black and blue arrows indicate additions of 5  $\mu\text{L}$  and 10  $\mu\text{L}$ , respectively. The configuration is Gauze PET - 5mm distance between electrodes.

The moisture sensor characterization is performed by monitoring the change in the device impedance after successive additions of artificial exudate. The simulated exudate is prepared according to the standard recipe (Solution A<sup>197</sup>) by mixing 2.5 mM CaCl<sub>2</sub>, and 0.142M NaCl in distilled water. The artificial solution presents a viscosity equivalent to water. AC signal with a peak voltage of 100 mV is applied and the resulting current measured by the MFLI Lock-in Amplifier. The frequency of 1 kHz is chosen after an impedance spectroscopy investigation. Figure 4.14.b shows the typical impedance variation over time due to the additions of artificial exudate for gauze PET in the 5 mm configuration.

### 4.3 Textile moisture sensors

From these experimental plots, it is possible to extract the trend of the impedance versus the exudate volume present onto the gauze.

Figure 4.15 shows the performance of the sensors fabricated with gauzes PET and Rayon for both configurations: 2 mm (Figures 4.15.a-c) and 5 mm (Figures 4.15.b-d).

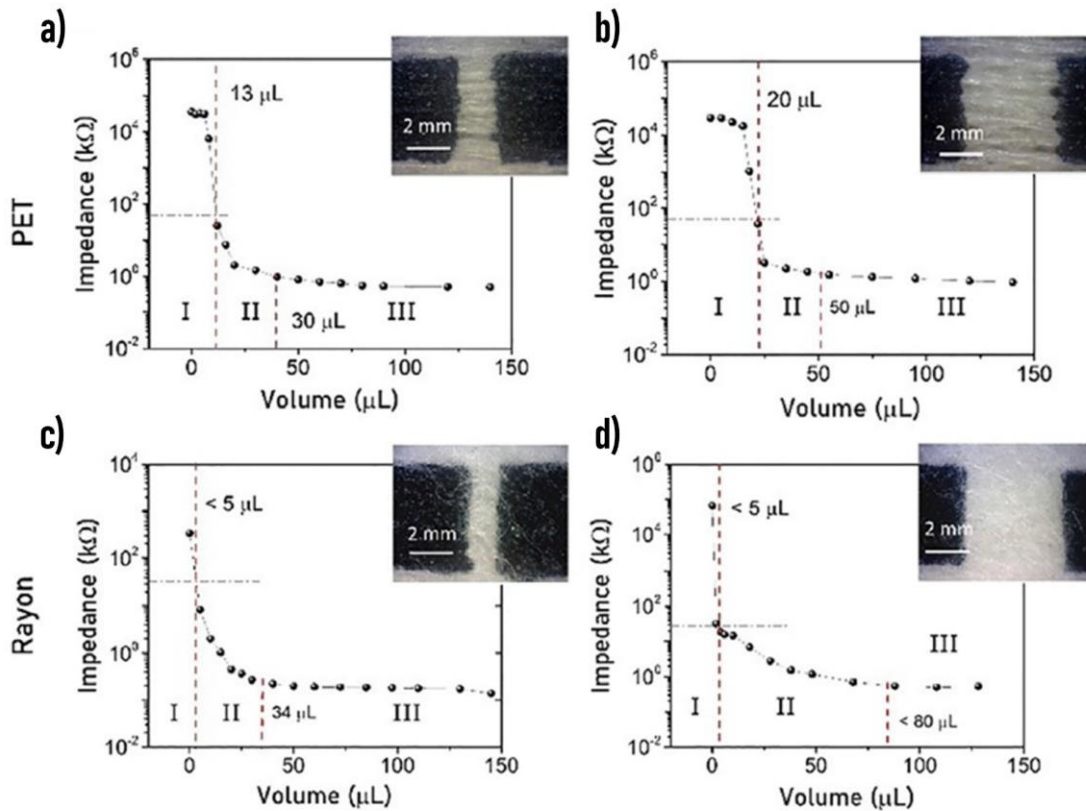


**Figure 4.15:** Impedance versus exudate volume response for moisture sensors fabricated on the gauze PET (a-b) and the gauze Rayon (c-d).

The main parameters used to characterize the wound moisture sensors are the threshold volume ( $V_T$ ), which is the amount of exudate needed to drop the sensors' impedance under a target value of 50 k $\Omega$ , and the saturation volume ( $V_S$ ), which represents the maximum quantity of liquid that can induce a detectable and significant impedance variation. These values are extracted by plotting the impedance versus volume data on a log-log scale. Two linear regimes are identified in these plots and allow the calculation of  $V_T$  and  $V_S$ . As reported in Figure 4.16.a, the first one is computed by the intersection of the linear fitting curve with the horizontal line at 50 k $\Omega$ , while the second one is extracted from the intersection point between the two linear fitting lines. The errors associated to these values are extracted with the standard error propagation methods. Using these parameters, it is possible to identify three distinguished regimes in the impedance versus volume plot. Considering the gauze PET (Figure 4.15.a-c), the first dry regime (I) has a high impedance (>10 MOhm), and small additions of exudate (<  $V_T$ ) do not affect the sensor response. When

### 4.3 Textile moisture sensors

the volume of exudate exceeds the threshold volume, the sensor goes into the second regime (II). The ions-rich formulation of the simulated exudate enables the electrical contact between the electrodes, and, exploiting the ionic-electronics conduction properties of PEDOT: PSS, the total impedance starts to decrease. When the amount of exudate present onto the dressing is high enough, the impedance reaches a stable value leading the system to the third regime (III), the saturation. The threshold impedance value of 50 k $\Omega$  to separate the first dry regime to the second intermediate regime is based on the final target to realize an entirely passive wound moisture sensor employing an RFID tag.

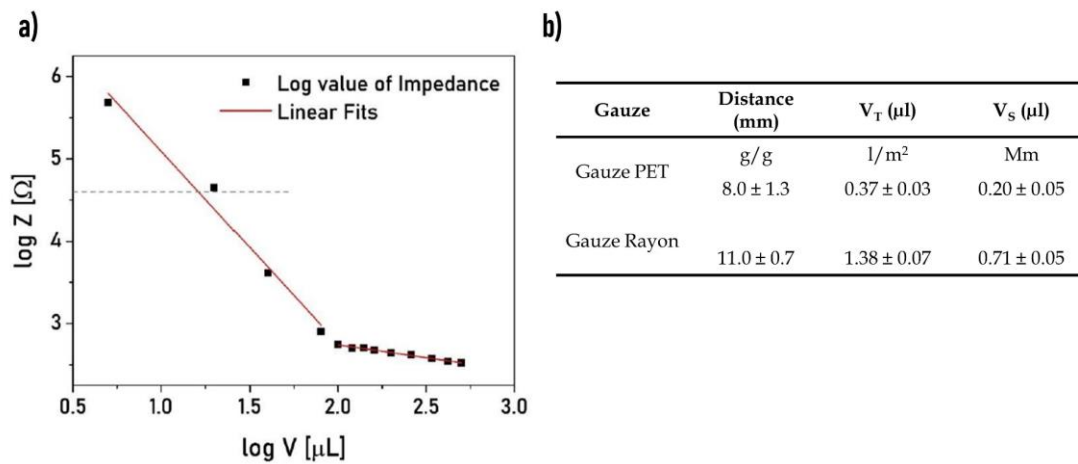


**Figure 4.16:** a) Calculation method to extract the threshold and saturation volume of the textile moisture sensor. The dashed line represents the impedance of 50 k $\Omega$ , and the intersection with the fitting curve identifies the threshold volume. Instead, the saturation volume is given by the intersection point between the linear fit of the two different linear regimes. b) Moisture sensor parameters in single-layer architecture.

Similar trends have also been obtained exploiting the gauze Rayon, as shown in Figures 4.15.b-d. In this case, however, the first dry regime is negligible since, after the addition of few microliters of simulated exudate (less than 5  $\mu$ l), the impedance value drops immediately into the second intermediate regime. Threshold and saturation volumes are reported in Figure 4.16.b for both sensors' configurations. Comparing the results, it is evident that the sensor's performance is affected by gauze composition/properties and configuration. On the one hand, how the solution disperses into the gauzes directly impact the V<sub>T</sub> estimation. More exudate is needed to decrease the impedance value of the sensor fabricated on gauze PET under the target of 50 k $\Omega$  since it can widely spread over the surface (Figure 4.15.c). In the case of the gauze Rayon, the drop stays in the middle of the two electrodes (Figure 4.15.d) and leads to a sudden impedance decrease. This is the predominant effect that allows to control and tune the sensors' threshold volume, while the distance between the two electrodes exerts a weaker influence. On the other hand, the

saturation volume is mainly affected by the distance between the electrodes, and with a larger sensing area, more exudate is needed to saturate the sensor's response.

#### 4.3.2 Integrated bandage sensor

The moisture sensor fabrication is a two-step procedure composed of the deposition of the active material and then the assembly of three different textile-based layers to obtain a smart and sensitive wound dressing. The final configuration is realized by heat-sealing together three textile layers: protective, active, and reservoir in a stacked configuration.

Figure 4.17.b shows a top view of the final sensor architecture, while the schematic structure is shown in Figure 4.17.c. The first layer is a thin gauze, directly in contact with the wound and guarantees biocompatibility and sterility, while the second layer is the active gauze (PET or Rayon) containing the moisture sensor. Figure 4.17.a shows the cross-section highlighting the different diffusive behaviour of liquids through these gauzes. Finally, the bandage is completed with the absorbing layer (Figure 4.17.d) that has several tasks: guide the exudate flux through the sensing area avoiding stagnation, collect the total amount of exudate, and protect the wound from external impact.

In order to study the impact of a different absorption behaviour on the sensor's response, two different textile-based reservoirs are used as the third layer. The main scope of this layer is to continuously drive the wound exudate across the sensing part and store it. The first one, called Abs Layer PE, is a thick layer of non-woven cotton, while the second one, called Abs Layer C, is a polyurethane foam attached under a cellulose-based mesh fabric. The thickness of the two different substrates is comparable but Abs layer C has an absorption coefficient that almost doubles the other (Figure 4.17.e). The difference in the absorbing layer structure influences the exudate distribution. Figure 4.17.d shows the top view and cross-section photographs of the absorbing layers while a drop of a coloured solution is dropped onto the surface. Abs Layer PE spreads the liquid in the horizontal direction, while Abs Layer C tends to transport the liquid downwards, where the C-foam absorbs it by swelling.

Since the previous paragraph reported that the influence of the distance between the PEDOT:PSS electrodes has a weak impact on the sensor performance, the final bandage architecture is tested in the 2 mm configuration. The results obtained by the four substrates combinations (gauze PET and gauze Rayon, Abs Layer C and Abs Layer PE) are reported in Figure 4.18.a-d. The behaviour of the stacked sensor is slightly different from that of the single-layer sensor. In this case, the first dry regime does not show a plateau or stable impedance value but decreases right after a small addition of artificial exudate. Threshold volumes are identified when the impedance reaches the target value of 50 kOhm, and they are reported in the table of Figure 4.18.e together with the saturation volumes. As in the

### 4.3 Textile moisture sensors

single-layer configuration, the threshold volume is mostly influenced by the gauze type (Figure 4.16.b).

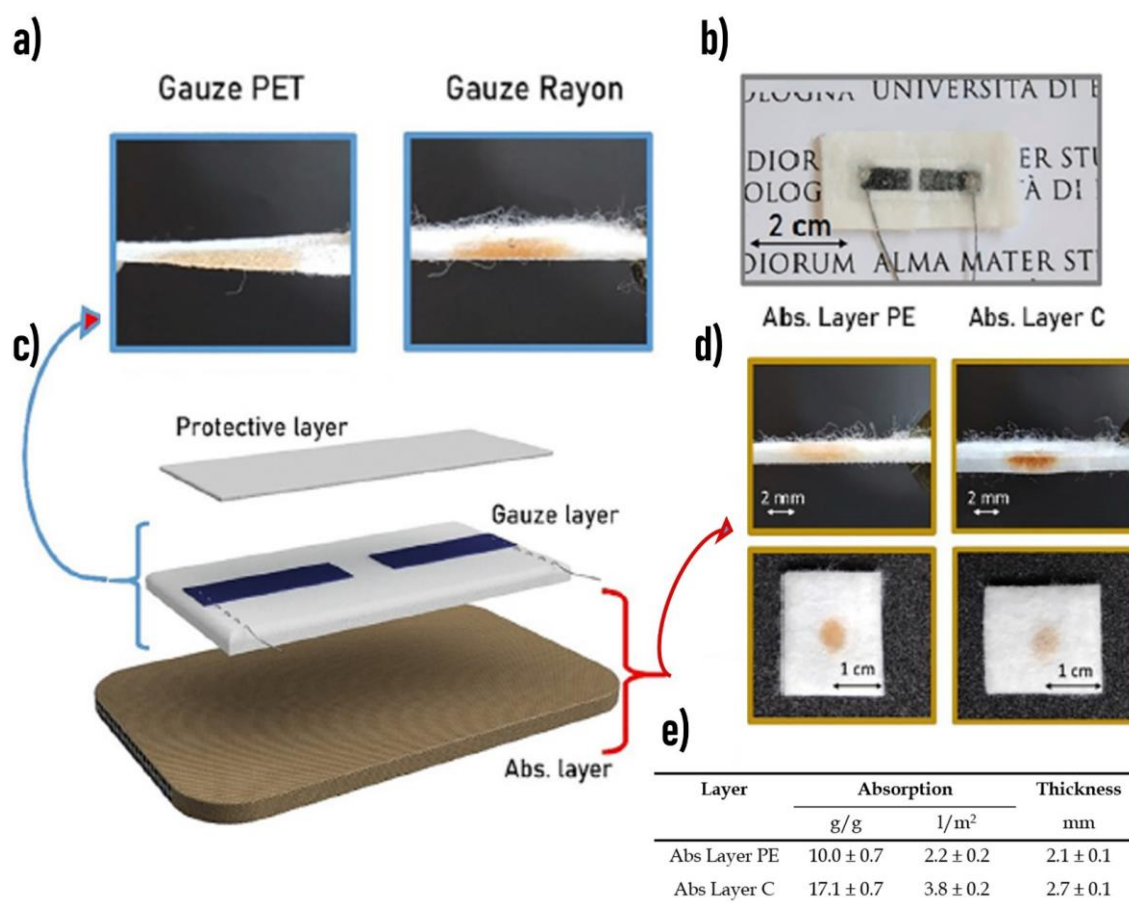


**Figure 4.17:** a) Cross section of the Gauzes PET and Rayon with the diffusion profile of a coloured drop. b) Optical image of the final textile moisture sensor prototype. c) Structure of the bandage sensor showing the three different composition layers. d) Cross section and top views of the two absorbing layers used as reservoir substrate highlighting their different wettability. e) Physical properties of PE and C layers. The absorption is reported in g/g and in l/m<sup>2</sup> to indicate the amount of volume absorbable by the textile material compared to its initial weight or planar dimensions, respectively.

On the other hand, the absorbance layer predominantly affects the saturation volume. Remarkably, even if the Abs Layer PE has a low absorption capability when it is used as a reservoir in a bandage, it leads to a right-shifting of the saturation regime with respect to the bandage fabricated using Abs Layer C. This is related to the different liquid dispersion ability of the absorption layers. Abs Layer C can absorb a high total volume of exudate, which is accumulated under the sensor, while the Abs Layer PE can spread the liquid towards a larger surface area, implying that a higher liquid quantity is needed to saturate the moisture sensor.

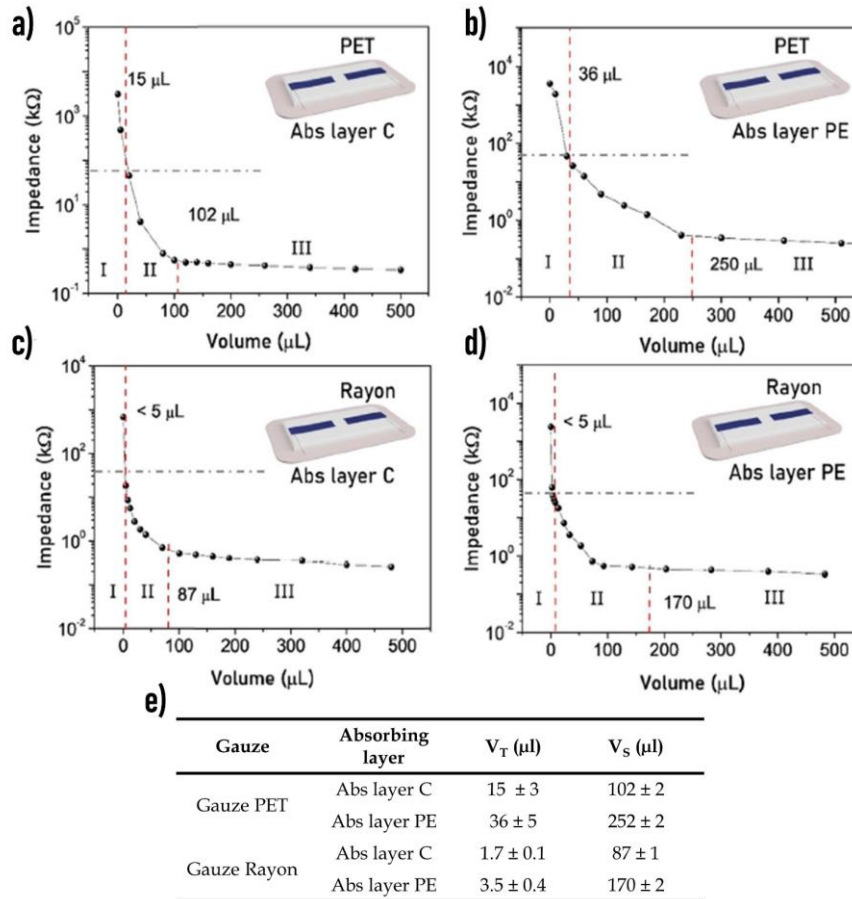


**Figure 4.18:** Bandage sensor response to the addition of synthetic exudate using the configuration with a 2 mm distance between the electrodes. The dashed lines identify the threshold and the saturation volumes and demarcate the three regimes. The sensors based on gauze PET (a-b) show a higher threshold volume than those based on gauze Rayon (c-d). e) Moisture sensor parameters in different bandage configurations. The spacing between the two electrodes is fixed to 2 mm.

### 4.3.3 Wireless wound dressing remote readout

The studies on the sensor's performance due to the material features allow for further development of the moisture sensor in a wireless and smart bandage. The main feature that affects the behaviour and the response of the sensor is the composition of the textile substrate. On the one hand, the characterization with artificial exudate assessed that the threshold volume at which the impedance drops under the value of 50 kΩ is related to the gauze used as substrate. On the other hand, the saturation volume depends on the specific features of the absorption layer. Moreover, the absorption coefficient is not the only value that affects the sensor's behaviour, but the horizontal exudate distribution through the textile also has a strong impact. Other factors, such as the distance between the two conductive electrodes, have a lower influence on the moisture sensor performance.

Considering that the sensor records a significant impedance variation when it passes from the dry to the wet state, this allows to directly integrate a passive RFID chip into it, achieving a low cost and passive moisture sensor tag. The representation of the final and a fully passive smart bandage is reported in Figure 4.19.a. The integrated “smart” moisture sensor exploits the RFID’s tamper function, similarly to the one proposed by Cramer et al.,<sup>514</sup> in which the “tamper bit” changes state (0-1) when impedance varies above and below a threshold. Upon wireless interrogation, the integrated RFID tag is able to report a qualitative measure of the moisture sensor’s impedance, reporting back the “tamper bit” status, with dry (impedance > thousand k $\Omega$ ) or wet (impedance < hundred k $\Omega$ ) conditions. In the same vein, the recovery and reversibility features of the smart moisture sensors are investigated by performing forward and backwards switching cycles from wet to dry conditions. The wet state is achieved by pouring 5  $\mu$ l of artificial exudate onto the sensor, while the dry state is reached speeding up the evaporation process with a hot-plate set at 50°C. The sensor impedance is monitored while the bandage switches from the dry to the wet status several times. Figure 4.19.b shows that the impedance variation lies in the same range for each cycle, confirming the reversibility and reliability of the sensor. A suitable combination of gauze and absorption layer can be used to obtain a passive smart bandage able to give an RFID tamper alarm when the wound switches from dry to wet and vice-versa. In addition, the moisture sensor has been equipped with a more advanced RFID-NFC tag (NHS3152) to perform a quantitative measurement.

Upon wireless interrogation by a reader (an Android-based smartphone in this case), the tag harnesses the RF power signal, and measures the sensor output. Figure 4.19.c shows the moisture bandage attached to a NFC prototype able to perform a DC resistance measure without requiring a solid-state power source. The measured value is then transmitted and read with a smartphone equipped with an NFC reader. Figure 4.19.d report the data acquired with the smartphone upon variation of the wettability level for a bandage composed by Gauze PET and Abs Layer C.

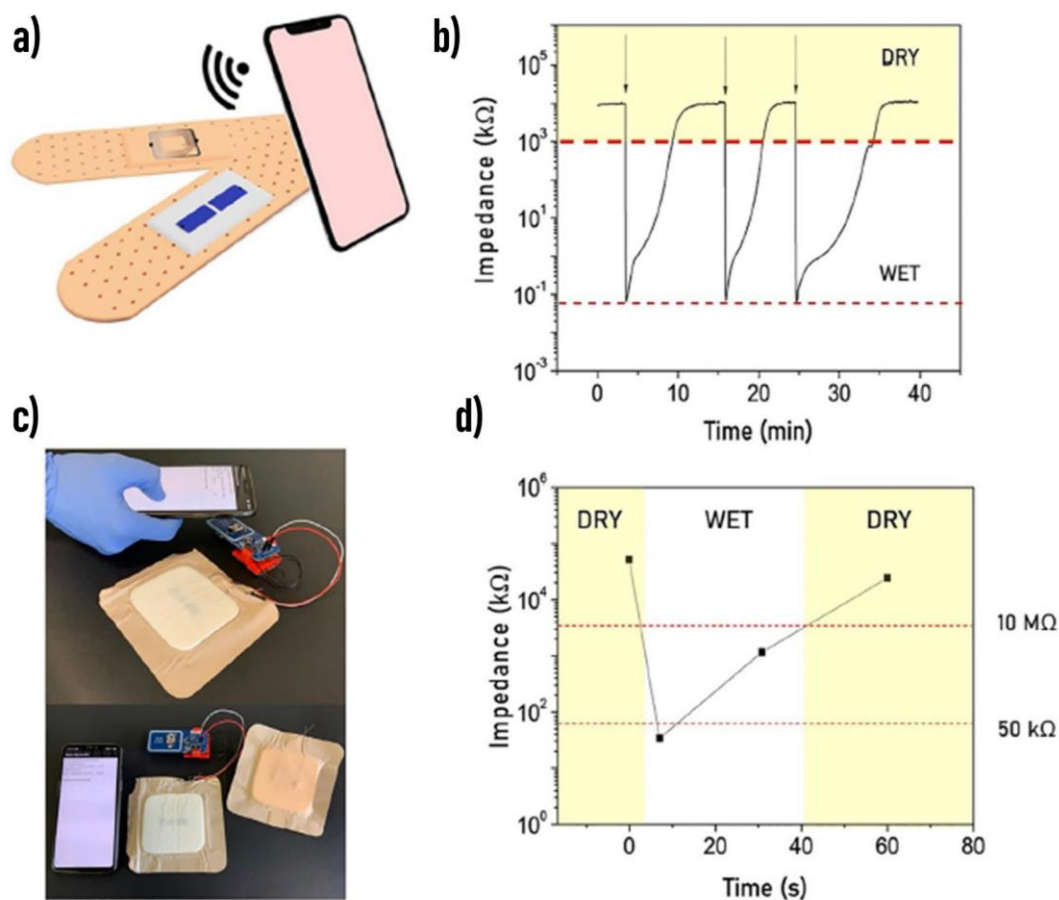


**Figure 4.19:** a) Illustration of the smart moisture bandage with the electrodes in the internal parts of the patch and the RFID tamper alarm on the external side to realize a fully passive device. b) Real-time monitoring of the sensor's impedance when the status switches between wet, and dry showing a reversible behaviour. c) Moisture sensor embedded in a real wound dressing and attached to an NFC interface. d) The wireless communication with a NFC reader (a smartphone) allows to perform a quantitative measurement to investigate the wound condition in real-time.

## 4.4 Conclusions

This chapter reports the latest results regarding the development of smart plasters capable of monitoring pH and moisture levels in wounds. Commercial sterile fabrics actually used for the production of dressings have been treated with the conductive polymer PEDOT:PSS, which is the common feature of the devices presented here. By employing appropriate functionalizations and various geometries, it is possible to make patches that can provide important information about the progress of wound healing.

The first example consists of a smart patch able to monitor the pH of artificial exudate using the same operation principle reported in the previous paragraph to monitor the pH

## 4.4 Conclusions

---

in sweat. A two-terminal device composed of a layer of PEDOT: PSS/ PEDOT: BTB deposited on textile allows to record a pH variation with two main advantages. First, it allows the realization of a two-terminal device that benefits from the robustness of a potentiometric transduction regardless of its practical chemoresistor-like structure. Secondly, this configuration makes a solid-state probe compatible with textile substrates and for flow analysis when equipped with a sampling system suitable for the noninvasive collection of biofluids. However, a low sensitivity in the area of interest for wound monitoring has been achieved for this textile device. With the aim of improving these performances in order to create patches that can really be used in medical applications, the second paragraph describes the combination of a soft organic semiconductor with a potentiometric metal oxide transducer to design a novel pH sensing material that shows promising characteristics for wearable device design. The intimate interaction between PEDOT:PSS and IrOx Ps originates a pH sensing mechanism based on electrochemical gating. When a real-world application is simulated through the implementation of an intelligent wound dressing operating with a small and continuous flow of synthetic exudate, the textile sensor showed no statistically different analytical performance in the pH range relevant to wound healing, i.e., 6-9, compared with the device fabricated on glass, with metal connections, and tested in solutions buffer. In addition, important advances have been achieved with respect to state of the art in textile pH sensors, mostly based on PANi-based working electrodes in a conventional potentiometric configuration, and concern both the elimination of the reference electrode and the adaptability to flexible and textile substrates without affecting reliability. The normalized sensitivity of the two-terminal sensor presented here is almost 1 order of magnitude higher in the physiologically relevant pH range for wound monitoring compared with the only example of an electrochemically gated pH sensor reported to date<sup>83</sup> and based on doped PEDOT.

Finally, the further idea reported for the realization of smart textile moisture sensors allows combining different commercial textile substrates, which are regularly used in wound care, to implement and design an advanced smart dressing that can continuously and in real-time monitor the wound moisture level. Adjustable characteristics and performance can be achieved based on the wound type. After an extensive study of various gauzes, and fabric combinations, the best dressing configuration can be designed according to actual clinical needs. In addition, the ability to connect the smart bandage to RFID or NFC interface leads to a fully passive smart bandage for fast, low-cost, and real-time monitoring of wound moisture.

Both the examples reported in this chapter on the monitoring of fundamental parameters for optimal wound healing open the way for the development of further noninvasive textile applications that can be truly used for next-generation IoMT devices for wound management.

# Chapter 5

## Textile Physical Sensors

Previous chapters introduced textile sensors capable of converting changes in the chemical composition of biofluids such as sweat and exudate into measurable electrical signals. Due to their specific application and translation methods based on chemical phenomena, such as the electrochemical gating effect, they have been affixed with the name of textile chemical sensors.

In the present chapter instead, two examples of textile sensors capable of monitoring the physical contact pressure, and the dose of incident ionizing radiation are presented. The first feature allows the realization of wearable devices able to monitor the pressure exerted on the wearer as a result of a relevant action being performed. These 2D sensors are extremely thin, flexible, light and non-invasive, and represent an ideal solution for safety applications in the workplace, such as monitoring of repetitive wearing actions, monitoring of sports performance of athletes such as cyclists, runners, weightlifters etc, up to the automotive and aerospace industries. Similarly, from a completely different nature but driven by the same ambition to improve safety at work without sacrificing the convenience, practicality and integrability of textile sensors, are presented for the first time a completely textile sensor capable of detecting the presence of x-rays. Besides taking into account the possibility of integrating both sensor functionalities in a single textile platform particularly suitable to improve the safety monitoring of workers usually exposed to the risk of contact with ionizing radiation or/and subjected to high physical stress, several applications of the single sensors make this new research topic particularly attractive for both the academic and the industrial world.

### 5.1 Textile pressure sensors

In recent years, the area of wearable technology has been attracting significant attention, and different types of sensors have been developed in several fields such as medical<sup>515</sup>, healthcare<sup>516,517</sup>, wellness<sup>518</sup>, entertainment,<sup>519,520</sup> and safety<sup>521</sup>. The most requested applications regard wearable activity trackers that offer detailed and powerful self-monitoring as well as an opportunity to control personal behaviours and habits. Such devices represent a valid tool for monitoring and the early diagnosis of diseases.

In the first part of this chapter, a detailed overview of the scopes, fabrication, characterization, and last results of textile pressure sensors are presented to show the potential applications of this new wearable device category. Special attention is dedicated to comparing the static response of sensors realized by different conductive formulations and the dynamic behaviour using various fabric types as substrates. Changing the appropriate parameters allows the realization of textile pressure sensors with the highest sensitivity in the desired pressure range.

#### 5.1.1 Applications

Recently, many efforts have been devoted to developing sports garments and accessories to reduce injuries<sup>207</sup>, increase the athlete's performance<sup>209</sup>, comfort, or improve safety in the workplaces. In this last field, there is a current request to develop a procedure and a system able to monitor the activity of workers in order to prevent serious injuries during work. Analogously, athletes that perform repetitive movements, for example, with hands (e.g. tennis players), may benefit from a technology able to non-invasively record hand motion in real-time in order to improve their performance and to prevent accidents. Indeed, uncomfortable positions, prolonged movement repetitions, high force stress or a combination of these elements represent risk factors for the musculoskeletal system. Nowadays, the methods typically used to determine acceptable stress demands and to identify activities at risk of injuries are mainly based on empirical observations, supported by subjective evaluation (Borg scale) or through video analyses.

However, video analysis, even if performed frame-by-frame, has some difficulties in force estimation, especially when the movements are fast, and it is time consuming<sup>515</sup>. According to the current method, the force produced by adults during power hand gripping is measured by a JAMAR-dynamometer and by a Martin-Vigorimeter<sup>522</sup> or, more recently, by a Grip-ball dynamometer<sup>517</sup>. These studies have shown a high correlation between the strength measured with different instrumentations<sup>523</sup>, and enable to defined the pressure range for hand movements from a few Pa up to 140 kPa.

It is convenient to divide the broad pressure range into four smaller sub-ranges related to different activities. A tactile sensibility response belongs to the ultralow pressure

## 5.1 Textile pressure sensors

---

range (1 Pa–1 kPa). This range is crucial for the development of ultra-sensitive electronic-skin for robot applications<sup>524</sup> or input devices for virtual reality interfaces and rehabilitation<sup>525</sup>. Pressures experienced by gentle manipulation of items belong to the low-pressure range (1 kPa–10 kPa)<sup>526</sup>. It is noteworthy that repetitive movements can cause injuries, even if low pressures are applied, as is the case for manual workers that use their hands daily to repeatedly manipulate objects<sup>527</sup>. The third range comprises medium pressures (10 kPa–100 kPa), while the high-pressure range deals with pressures over 100 kPa. Examples of everyday pressures in these last two ranges are the pressure produced by the foot due to body weight, the force exerted by athletes using tools (i.e. tennis racket, baseball bat), and the activity of heavy-duty manual workmen (i.e. using a jackhammer or weightlifting) where force peaks can easily be > 100 kPa.<sup>517</sup>

Today, the standard access methods to estimate applied forces are obtained in experimental conditions mimicking manual tasks, but they do not allow for real-time and real-condition measurement and monitoring. The recent developments in stretchable and wearable sensors open the way to implementing innovative alternatives.

Wearable pressure sensors recently developed for electronic skin in robot applications are comfortable and very sensitive<sup>528,529</sup>, but they typically operate only in the low and ultra-low pressure range and are usually very expensive. Flexible and stretchable pressure sensors currently available with high sensitivity in the medium to the high-pressure range are mainly implemented for foot plantar monitoring devices<sup>530</sup>. Often, these sensors cannot be easily integrated into a garment, such as gloves or shoes, without hindering the natural motion. Alternatively, Peratech quantum tunnelling composite sensors<sup>531</sup> were used to improve touch-based interaction thanks to their ability to detect a wide variety of tactile inputs. Thanks to the resistive force-sensitive elements, they can quantify the amount of force applied to the touch sensing panel. They offer a high sensitivity, but their operative pressure range does not fit with the required gripping and pinching force range recorded in adult working populations. More recently, flexible grip and pressure sensors have been implemented in gloves<sup>532,533</sup>, allowing measurements in a wider range of tools, objects and surfaces. However, they are bulky, hinder the hand's movements and alter the frictional conditions between the skin and the contact area. Other limitations include high costs due to significant damage during use and the need for balancing and calibration.

Employing textiles substrate to directly fabricate pressure sensors allow to realize thin, flexible and non-invasive tools to fulfil the necessary requirements for a monitoring platform applicable in workplaces and during sports activities.

### 5.1.2 Fabrication procedure

In the pressure sensors developed in this thesis, the active element is a conductive polymer deposited on a 100% woven cotton fabric. Poly(3,4-ethylenedioxythiophene):poly(4-styrenesulfonate) (PEDOT:PSS) in the Clevios P formulation is the main component of the conductive solution drop-casted on the fabric (Figure 5.1.a). Additives, like second dopant ethylene glycol (EG), can be added to the main solution in order to properly tune the conductivity of the solution and the corresponding device response. After deposition, the samples are dried in an oven for 30 min at 70 °C. Then, a commercial two-ply stainless steel conductive thread (resistivity of  $500 \Omega\text{m}^{-1}$ ) is sewn using a lockstitch by an Elna eXa 320 sewing machine in the final pressure sensor configuration (Figure 5.1.b). Two conductive stitches are perpendicularly sewn on both sides of the cotton fabric and are electrically isolated. Since each stitching line is made by two threads (needle and bobbin threads), top conductive paths are obtained when using the stainless-steel yarn as the needle thread and non-conductive (100% cotton) yarns as the bobbin threads. Conversely, bottom conductive paths are obtained by flipping the sewing face of the fabric.

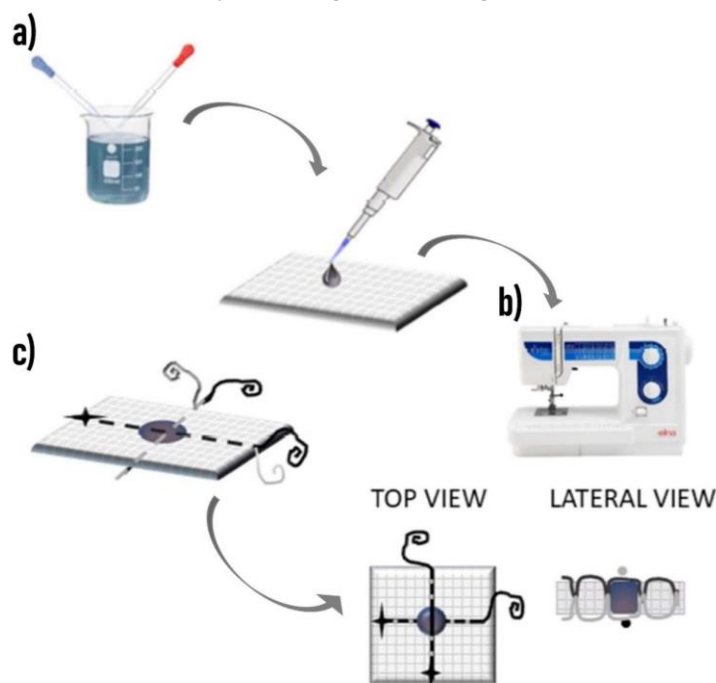


**Figure 5.1:** a) Fabrication procedure of the textile pressure sensors with a sketch of solution preparation and drop-casting deposition. b) Sewing machine used to realize the electrical contacts. c) Schematic representation of the sensing pixel on cotton fabric.

Figure 5.1.c shows the final structure of a single textile pressure sensor pixel on cotton. This easy and low-cost fabrication process can be simply scalable for large-scale production and to realize a large matrix to fine monitor the pressure distribution. However, even if the pressure sensor itself is simple on its own, the interaction of conductive polymers

with the textile substrate yields a complex and new system. The resulting pressure sensor area is  $A = (0.20 \pm 0.07) \text{ cm}^2$ . The thickness of the cotton fibre at rest is  $(0.35 \pm 0.05) \text{ mm}$ , while the final pressure sensor had a total thickness, at rest, of  $0.55 \text{ mm}$ . In addition, to analyse the influence of the fabric on the textile device, a comparison of the electrical properties with a thin film is performed. The same conductive formulation is deposited by spin-coating onto a glass substrate with an area of  $2.0 \times 2.0 \text{ cm}^2$ . The electrical contacts are placed in the four corners by a silver paste coating.

### 5.1.3 Effect of different formulations

In this paragraph, it is analyzed the effects of the addition of EG on the electrical properties and on the morphology of PEDOT:PSS directly deposited on cotton fabric. The conductive polymer is soluble and dispersed in water. It can be used as an ink and can be easily deposited on different substrates, even on fabric, by low cost, highly scalable solution-based fabrication processes. Furthermore, recent investigations into its piezoresistive properties<sup>534</sup> enabled its application as the active layer of pressure sensors. The features of PEDOT:PSS depend on the PEDOT and PSS ratio, on the solvent, and also on the presence of other so-called secondary dopants in the solution<sup>535</sup>. For example, the addition of a low amount of dimethyl-sulfoxide<sup>536</sup>, ethylene glycol<sup>537</sup> (EG) or sorbitol<sup>342</sup> has strong effects on the properties of PEDOT:PSS thin films, for example, enhancing the electrical conductivity up to three orders of magnitude with respect to the pristine formulation. Even if these phenomena are well known for thin films, the effects of such additives on the piezoresistive properties of inks, and thus on the performance of textile pressure sensors based on PEDOT:PSS, are here presented for the first time.

#### 5.1.3.1 Electrical and morphological properties

In order to evaluate how the addition of EG affects the electrical properties of the conductive polymer, three different formulations of PEDOT:PSS (P, 5% EG, 10% EG) in a thin film configuration deposited on a glass substrate and on cotton fabric are studied and compared.

The thin films' thickness is extracted by AFM images, and the values are reported in Figure 5.2.c. All the thickness values are comparable within the error, so the presence of EG does not significantly affect the processability of the three formulations. The thin-film electrical resistance is measured with the four-probe method (Figure 5.2.a). The results reported in Figure 5.2.c are averaged over four samples and clearly indicate that the EG acts as a secondary dopant as the resistance decreases from  $(160 \pm 10) \text{ k}\Omega$  for the pristine formulation down to  $(190 \pm 10) \Omega$  for the 10% EG content formulation. The observed variation in the resistance of three orders of magnitude is in good agreement with the results

## 5.1 Textile pressure sensors

reported in the literature for thin films<sup>535</sup>. In order to evaluate the influence of EG in the electrical properties of PEDOT:PSS on cotton fabric, the in-plane and out-of-plane resistance (Figure 5.2.a) of textile samples are characterized. The in-plane configuration enables the four-probe resistance mode and gives a direct comparison with the thin film resistance, while the out-of-plane resistance is strictly related to the pressure sensor working principle. The results in Figure 5.2.b confirm that EG acts as a secondary dopant, also enhancing the samples' conductivity in the textile samples: the samples coated with 10% EG content ink show an in-plane resistance one order of magnitude lower than the ones coated with the pristine formulation. The effect is less evident when compared to thin films on glass because the cotton fabric is a complex substrate, where the conductive paths are not continuous and strictly depend on the weaving pattern. However, in the out-of-plane configuration, the effect of the presence of EG is still present, and the resistivity of the 10% EG formulation is three times lower than the pristine case.

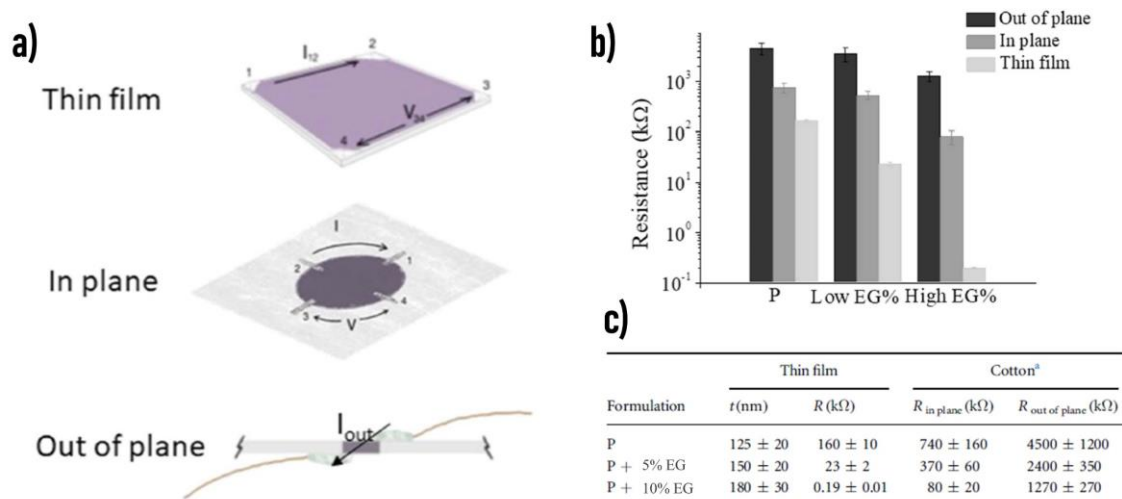


**Figure 5.2:** a) Experimental configuration for the resistance measurements. b) Comparison of the resistance obtained with the three formulations: pristine (P) (dark grey), 5% EG (grey) and 10% EG (light grey). c) Resume of the thickness and resistance values for thin film, in-plane and out-of-plane configuration.

Figure 5.3 shows SEM images of cotton fabric both in pristine form and coated with the conductive polymer solution. The top views (Figure 5.3.b-c) emphasize the homogeneous deposition of the solution and thus the origin of the conductivity of the in-plane configuration. The Energy Dispersive X-ray Spectroscopy (EDX) image of a section of cotton fabric coated with the conductive polymer shows the uniform distribution of sulfur (S - red) along with the whole thickness of the fabric, thus making it possible to measure an out-of-plane resistance. As S atoms are present only in PEDOT:PSS, mapping the presence of the S in the fabric samples allows evaluating the PEDOT:PSS distribution on the cotton

## 5.1 Textile pressure sensors

fibres. It is evident that the conductive ink is homogeneously distributed all over the fibres. There is no significant variation among the different SEM images, and it is possible to conclude that the presence of EG does not affect the coating on a microscopic level. The difference in the electrical properties might be related to the nanoscale interactions between PEDOT:PSS domains and interfaces as proposed for thin films on glass substrate<sup>340,537</sup>. This result is in agreement with a recent study on polyester fabric coated with PEDOT:PSS and immersed in EG solution<sup>538</sup>.

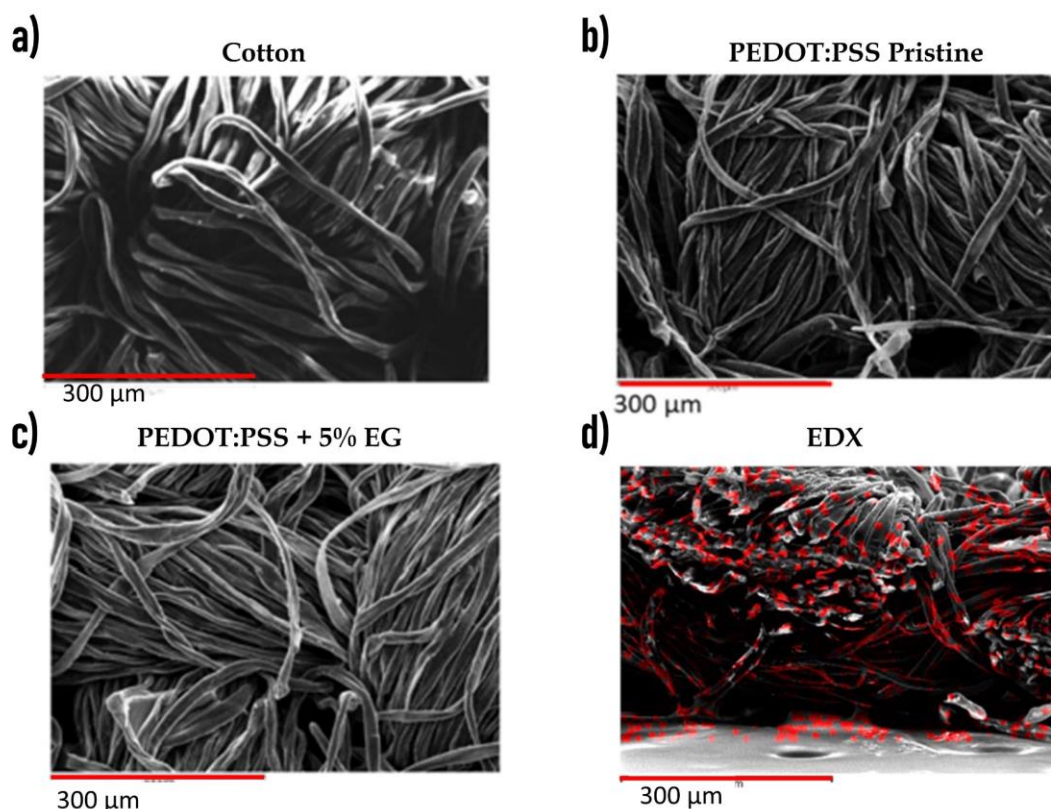


**Figure 5.3:** SEM images: Top view of a) untreated cotton and cotton treated with PEDOT:PSS, b) pristine, and c) 5% EG. d) SEM-EDX image of cotton fabric covered with PEDOT:PSS + 10% EG where the red spots highlight the presence of Sulfur atoms.

### 5.1.3.2 Textile Pressure sensors characterisation

The performance of textile pressure sensors is evaluated by combining Dynamic Mechanical Analysis and resistance measurements by a source meter. DMA Q800 by TA Instrument applies pressure in a range from 10 kPa to 100 kPa onto the sensing element. The electrical response of the textile pressure sensors based on the three conductive ink formulations is expressed by the resistance and reported in Figure 5.4.a. The measures are acquired by applying a constant current of 1  $\mu$ A on the sample and measuring the voltage variation. The same graph (blue line, right, y-axis) reports the sensor thickness during compression, measured with the DMA. The sensors' response reflects the behaviour

## 5.1 Textile pressure sensors

observed in the electrical characterization: by increasing the amount of the EG content in the conductive ink formulation, the overall resistance decreases.

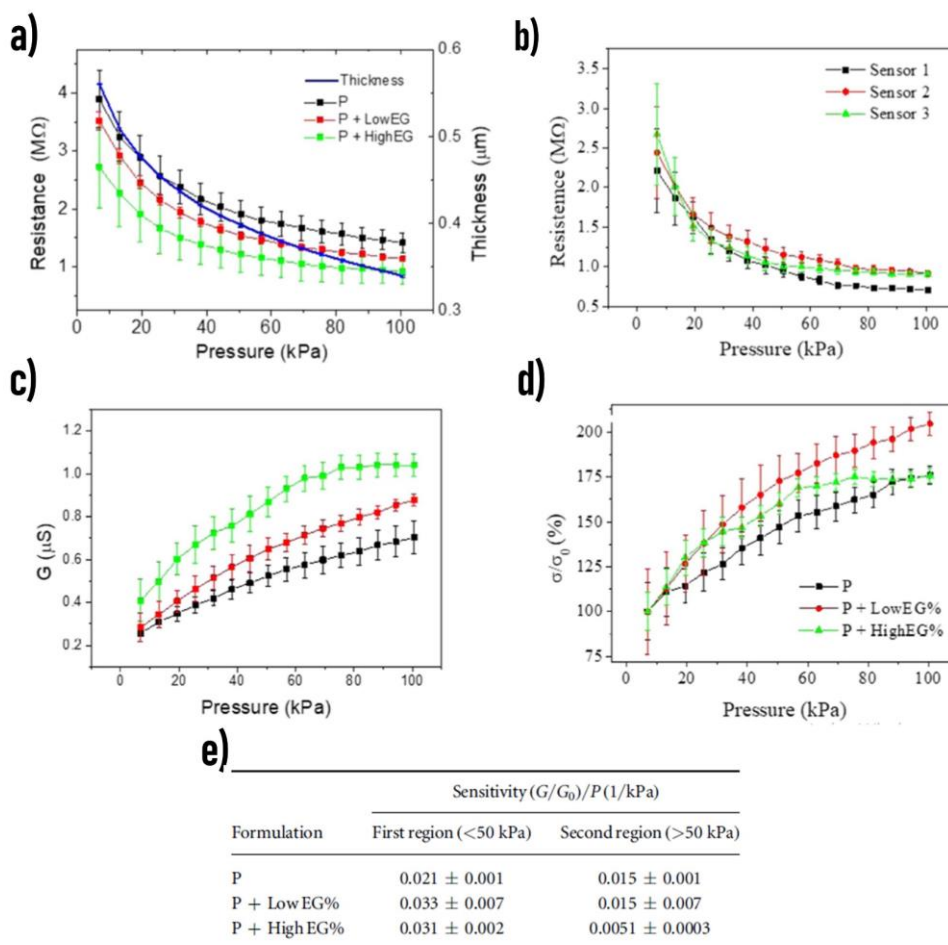


**Figure 5.4:** a) Resistance response of textile pressure sensors based on different formulations: pristine (black), with a low concentration of EG (red), with a high concentration of EG (green). In blue, the thickness variation during compression (y-axis, right). b) Reproducibility refers to the formulation with 10% EG. c) Conductance response, and d) normalized conductivity. e) Table with the sensitivity for both the pressure ranges.

It is noteworthy that sensors fabricated in different batches have the same resistance trend, demonstrating the high reproducibility of the fabrication technique. Figure 5.4.b shows the results for three samples based on the most conductive formulation. The electrical response of the textile pressure sensor respects the Pouillet's law  $R = \rho \cdot t/A$ , where  $\rho$  is the resistivity,  $t$  the total thickness and  $A$  the sensor area. Since the sensors area and the thickness variation are the same for all the sensors, the resistance is strictly related to the resistivity variation. In a first approximation, the resistance  $R$  is inversely dependent on the applied pressure  $P$ <sup>207</sup>, while the conductance  $G$  is linearly dependent on  $P$  (Figure 5.4.c). This graph highlights the different behaviours of the textile pressure sensors based on the three formulations. Two regions depending on the pressure range can be divided in the graph:

below 50 kPa and above 50 kPa. The sensitivity, the most important parameter in a sensor, is the slope of the linear fit of the normalized conductance versus the applied pressure (Figure 5.4.e). A comparison of the results shows that in the first region (<50 kPa), the sensitivity of the P formulation is lower than that with 10% EG. In contrast, in the second region (>50 kPa), the 10% EG content formulation shows a sensitivity one order of magnitude lower than the pristine one. Since the same configuration is used for all the samples, and the thickness  $t$  is evaluated in real-time during the compression, it is possible to calculate the variation of conductivity  $\sigma$  upon compression. Figure 5.4.d reports the normalized conductivity variation of textile pressure sensors fabricated with the three formulations.

### 5.1.3.3 Working principle

In order to explain the global performance of the textile pressure sensor, three different contributions are observed from macroscopic to the nanoscale level. At a macroscopic level, when the applied pressure increases, the total thickness  $t$  of the textile sensor decreases because the two conductive wires move closer, and the total resistance decreases for geometrical reasons following Pouillet's law (Figure 5.5.a). This contribution is equal for all devices fabricated with different formulations and can be eliminated by normalizing the result with a thickness measured with DMA during the compression phase (Figure 5.4.a).

The second contribution is active at the microscopic level. SEM images show that the presence of EG does not affect the coating on fibres and that each cotton thread is composed of several fibres with an average diameter of 10  $\mu\text{m}$ . As the conductive ink coats the surface of the fibre, when the applied pressure increases, the fibres of the cotton thread are compressed, and, by coming closer, the number of contact points increases, thus contributing to the decrease of the overall resistance in agreement with the result previously reported in the literature<sup>539</sup> (Figure 5.5.b). This second contribution, on the one hand, is similar for all three pressure sensors; as we observed in the SEM images, the presence of EG does not affect the fibre distribution in the space. On the other hand, it depends on the ink formulation in terms of the overall resistance because the cotton fibres coated with the different PEDOT:PSS solutions have different conductivity. However, this contribution cannot be the only microscopic phenomenon responsible for the observed macroscopic behaviour as it does not justify the saturation of the sensor response in the high-pressure range observed for 10% EG sensors.

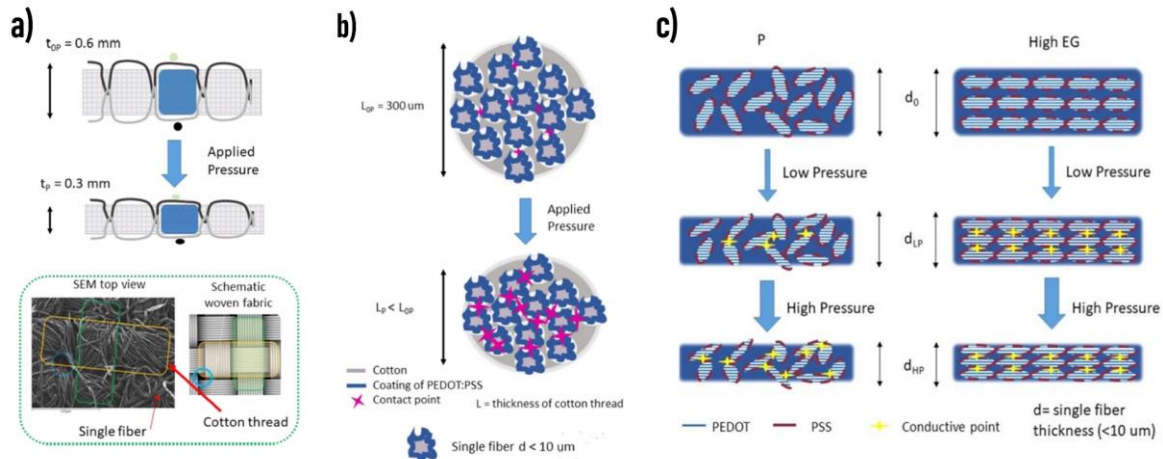


**Figure 5.5:** a) Scheme of the first contribution at a macroscopic level. Inset: a SEM image of  $900 \times 1200$   $\mu$ m of the woven cotton fabric. b) The second contribution at microscopic scale with the better adhesion of the fibres under pressure. c) Model of the third contribution at the nanoscale level to highlight the effect of the EG in the conductive solution.

A third contribution, related to the piezoresistivity of the PEDOT:PSS in then introduced. At the nanoscale level, it has been observed that in thin films of PEDOT:PSS, the presence of EG induces a reorganization of the domains of PEDOT and PSS, leading to a higher conductivity (Figure 5.5.c)<sup>340,537</sup>. Under applied pressure, the fibres are compressed, and the domains become closer, increasing the number of contact points between the fibres and thus enhancing the overall conductivity<sup>534</sup>. The presence of EG typically induced a domain-ordered structure with a high number of contact points, even when the cotton fibres are at rest (at zero applied pressure). By increasing the applied pressure, the number of contact points reaches saturation. On the other hand, in disordered domains (i.e. in pristine PEDOT), higher pressures are needed to reach the saturation region. Further investigations are needed to confirm the reported explanation and to identify other possible phenomena occurring at the nanoscale level.

### 5.1.4 Effect of different fabrics

However, even if the high sensitivity and the linear response range are the two main aspects that describe a pressure sensor performance, when it involves a real-life application, it is fundamental to consider its reaction related to a dynamic pressure change. The literature reports scarce details on standard characterization procedures that would allow a comparison of different sensors' performances. Few examples of wearable pressure sensors can be found showing high sensitivity, but most of the results are obtained in a single step pressure measurements, or in a very slow dynamic mode that is far from the real-life applications. For example, polyethylene combined with a carbon sheet is applied to a glove

and show sensitive responses in the range between 1 kPa and 70 kPa. In this case, the sensor performance is evaluated with a delay from 30 s to 180 s to reach the rest conditions after each measure<sup>540</sup>. He et al. reports a modified graphite polyurethane piezoresistive sensor that shows a slow dynamic range of almost 10 kPa/min<sup>541</sup>. On the contrary, Tian et al. obtained a graphene-based resistive pressure sensor with a high sensibility of 0.96 kPa<sup>-1</sup>, a large response range (0–50 kPa), and a dynamic response demonstrated in a fast mode of 75 kPa/min.

As already stated, the pressure sensors based on the 10% EG formulation shows higher sensitivity and a wider linear operation range but with lower reliability compared to those realized using the pristine solution. These results demonstrate the complexity of the textile pressure sensor system due to the active role of multiple parameters (i.e., the structure and fabric composition, the targeted pressure range, the polymer formulation, etc.) and suggest a protocol to optimize and tune textile pressure sensors according to the final application.

In this paragraph, the influences of the type of fabric and the weaving structure on the pressure sensors performance in dynamic operation mode are presented. Four types of fabrics that differ in thickness, material composition, sewing method and layered structure are characterized and used as the substrate for the textile pressure sensors. The mechanical tests (creep-recovery and stress-strain) of fabrics, and the electrical characterization in dynamic mode operation of textile pressure sensors fabricated with the four types of textile, allow evaluating how the mechanical features of the fabrics affect the operation regime. The sensors have the same geometry and structure with two different solutions used to fabricate the conductive and sensing element. Careful data analysis allows finding the best linear operation range for each type of sensor that allows their usage according to the final application.

### 5.1.4.1 Characterisation of fabrics

Four fabrics with different material compositions, weave arrangements, layered structure, and thickness are taken into account, considering both knitted and woven structures (Figure 5.6). All the fabrics are commercially available, and the woven structure is made by crossing in a regular order two sets of threads so that they cross each other orthogonally. On the contrary, the knitted fabrics are made by interlocking a series of loops composed of one or more yarns, with every single row of loops locked into the previous row. Fabric A consists of three layers with the internal non-woven part embedded between two layers of knitted fabric. Fabric B is composed of two layers, one knitted and one non-woven, distinguished by the colour of the different threads. Fabric C, instead, is based on

## 5.1 Textile pressure sensors

woven fabric. Finally, we also consider an elastic knitted textile, fabric D, whereby the special lengthwise stretchability is given by the particular knitting way of the yarns.

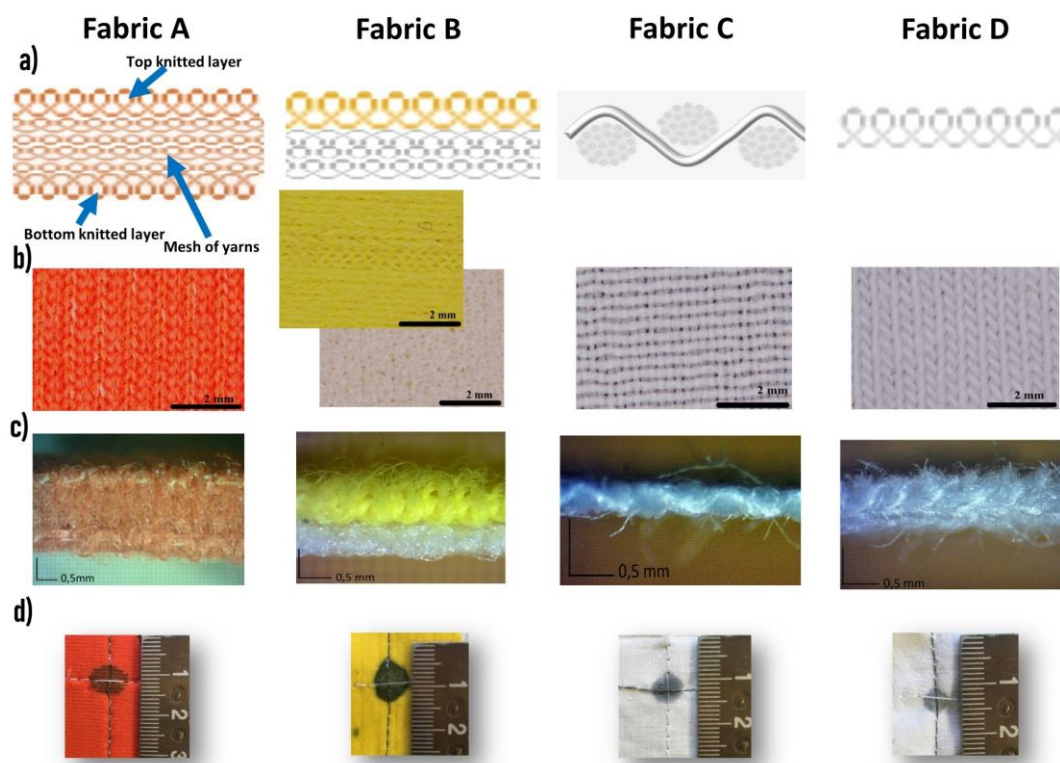


**Figure 5.6:** a) Schematic representation of the fabric weaving structure. Optical images of top b) and lateral c) view. d) Appearance of one pressure sensor element.

### 5.1.4.1.1 Composition investigation

The fabric composition is studied by acquiring Fourier transform-infrared (FT-IR) spectra by Bruker Alpha Platinum-Attenuated Total Reflectance (ATR) spectrophotometer equipped with ATR Diamond window (32 scans, 4  $\text{cm}^{-1}$  resolution). In addition, Differential Scanning Calorimetry (DSC) measurements are carried out with a TA Instruments DSC Q2000 apparatus equipped with Refrigerated Cooling System RCS90, heating twice 3–5 mg samples in aluminium pans from  $-50\text{ }^{\circ}\text{C}$  to  $30\text{ }^{\circ}\text{C}$  at  $10\text{ }^{\circ}\text{C}/\text{min}$ , with intermediate cooling run carried out at  $-10\text{ }^{\circ}\text{C}/\text{min}$ .

Fabric A is a soft orange material that displays an FT-IR pattern typical of nylon fibres (Figure 5.7.a), a synthetic material widely used for technical textiles<sup>542</sup>. The ATR mode allows identifying the nature of the textile material, in this case, polyamide (i.e.,

## 5.1 Textile pressure sensors

nylon), thanks to the peaks at  $3293\text{ cm}^{-1}$  absorption ascribed to free N-H stretching in a solid-state,  $1630\text{ cm}^{-1}$  band (typical of carbonyl stretching - amide I band), and  $1532\text{ cm}^{-1}$  signal ascribed to NH bending vibration (amide II band).<sup>348</sup> However, infrared spectroscopy is not helpful in identifying the exact composition of the polymer. Hence the thermal behaviour of the fabric is analyzed in DSC, and the resulting thermogram in the second heating scan (Figure 5.7.a) displays two main events, both endothermic: the highest temperature signal centred at  $252\text{ }^{\circ}\text{C}$  is the typical melting point of the Nylon 6,6 crystal phase. The low-temperature peak is attributed to the melting of some waxy elements applied as sizing coating to the fibres during the weaving processing.

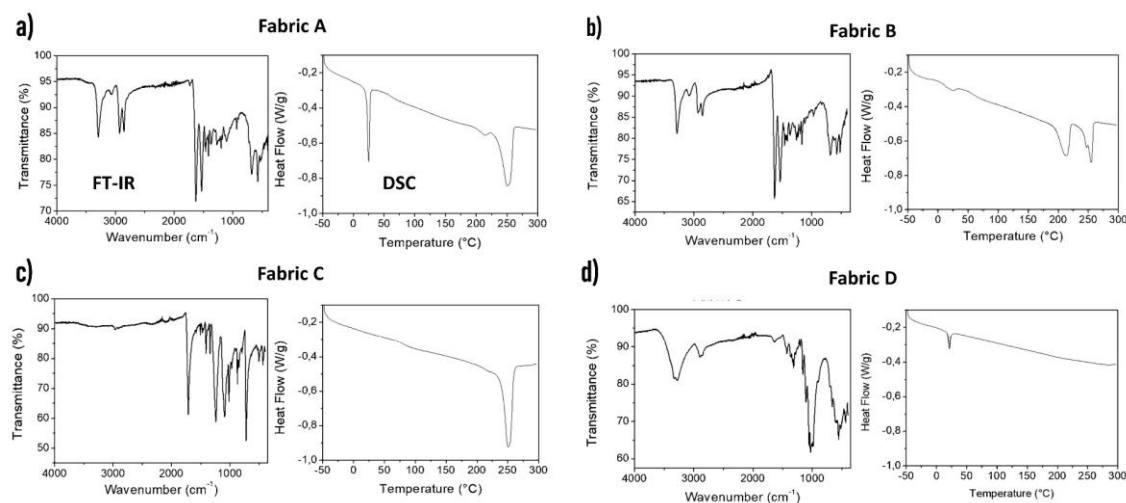


**Figure 5.7:** Fourier transform-infrared (FT-IR) and Differential Scanning Calorimetry (DSC) thermogram pattern for the four fabrics.

Even if fabric B presents evident differences with Fabric A (at least the colour), when analyzed with the ATR-IR technique, it displays exactly the same spectrum from both layers. Figure 5.7.b shows the spectrum of the yellow face, and the absorption pattern strongly resembles the previously discussed spectrum of fabric A, which is attributed to a polyamide fibre, identified as mainly Nylon 6,6. DSC analysis of fabric B, however, reveals a slightly different thermal behaviour than fabric A (Figure 5.7.b), with the presence of two high-T endothermic peaks: one in the same position and attributed to the melting of Nylon 6,6, while a new endothermic event, positioned at a slightly lower T, associated to the polyamide Nylon 6.

Fabric C presents an ATR-IR spectrum significantly different from the previously discussed ones (Figure 5.7.c), with features ascribed to a polyester filament. Indeed, the spectrum displays the major peaks associated with the structure of polyethylene terephthalate (PET) with the terephthalic acid ester carbonyl stretching at  $1712\text{ cm}^{-1}$ , the asymmetric C-C-O and the O-C-C stretching at  $1240$  and  $1091\text{ cm}^{-1}$ , respectively, and the

## 5.1 Textile pressure sensors

---

C-H wagging vibrations from the aromatic structures at  $722\text{ cm}^{-1}$ .<sup>543</sup> The DSC thermogram confirms this hypothesis displaying a single endothermic event centred at  $252\text{ }^{\circ}\text{C}$  (Figure 5.7.c), that can be associated with the melting of PET crystal phase. Such a polyester is once again well renowned for its use in textiles and garments.

Finally, Fabric D shows an infrared absorption that is different from all the previously analyzed fibres (Figure 5.7.d), with the lack of any C = O feature, some prominent broad OH stretching band in the region  $3500\text{--}3000\text{ cm}^{-1}$  and C-O-C signals in the  $1150\text{--}1075\text{ cm}^{-1}$  region that are reminiscent of a cellulosic structure. Cellulosic fibres are the most relevant natural fibres used in textiles, both as cotton and flax fibres, suggesting that fabric D is cotton fabric. Cotton is not expected to provide any significant thermal signal in DSC analysis since cellulosic fibres thermally degrade before being able to undergo any thermal transition. In fact, DSC second heating scan displays only a low-T signal (Figure 5.7.d), in a position similar to that previously detected in Fabric A and B, suggesting the presence of a common wax product to functionalize the fabric surface.

### 5.1.4.1.2 Mechanical properties

After determining the exact nature of the four different textiles, the studies of the mechanical properties allow to compare and correlate the response of the pressure sensors with each fabrics' own mechanical behaviour. The vertical direction is the most interesting since the textile pressure sensors are compressed along the vertical axis.

The first characterization is a creep-recovery test where the selected highest pressure used in this study ( $100\text{ kPa}$ ) is continuously applied for 1 min. After that, the recovery curve is recorded for 3 min. This test provides information about the vertical elastic properties of each fabric. Figure 5.8, in the left column, shows the creep-recovery trends, and the relevant parameters are summarized in Table 5.1. The thickness of fabrics A and B is considerably different compared to the thickness of fabrics C and D. Strain is, therefore, the most appropriate quantity to be used in order to compare the creep-recovery test results. The maximum strain value reached by every fabric under the  $100\text{ kPa}$  pressure was quite the same ( $\sim 45\%$ ). Observing the residual deformation, fabric A and fabric B have good elastic properties recovery up to  $5.3\%$  and  $8.5\%$ , respectively.

On the other hand, Fabric C and D result less elastic, and their residual deformation is  $20\%$ . These results underline the fact that the elastic consistency of fabric D (the elastic one) mainly concern horizontal stretching and does not affect the vertical mechanical properties. Even though the creep recovery test gives relevant information about the fabric elastic properties, it does not represent their actual behaviour in the textile pressure sensors during a dynamic operation mode. Further information is achieved by performing cycles of compression and decompression in a stress-strain test.

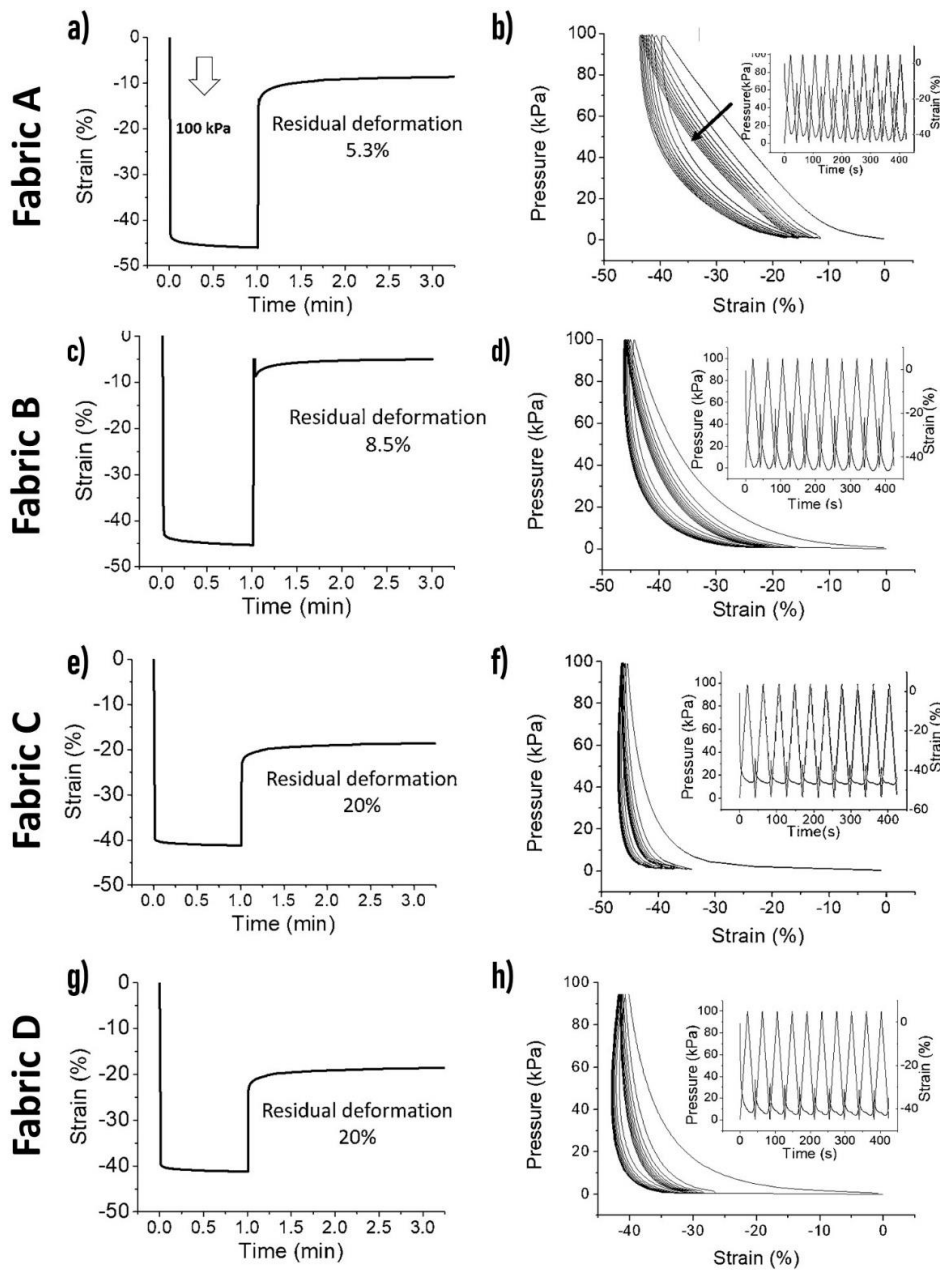


**Figure 5.8:** a-c-e-g) Mechanical characterization of the four different tested fabrics under creep recovery test: the arrow indicates the applied pressure (100 kPa for 1 min). The recovery time is 3 min. b-d-f-h) Stress-strain curve of fabrics: the arrow indicates the curve shift direction from the first to the tenth cycle. Inset: pressure (black line) and strain (red line) as a function of time for each fabric.

Figure 5.8 in the right column reports the stress-strain curves where the stress value represents the applied pressure. The fabrics show a substantial variation in the stress-strain curve after the first cycle. This is in agreement with the previous results, in which a complete recovery has not been observed for any fabric. The stress-strain test confirms that Fabric A

has good elastic properties, indicated by the linearity of the compression curve for each cycle. However, it does not have enough time to complete the recovery, and after each cycle, the strain curve does not overlap with the previous one.

On the other hand, Fabric B does not show proper elastic properties, and the compression curve is not linear. However, apart for the first one, the strain curves are increasingly overlapping in subsequent cycles.

Fabrics C and D do not show a linear compression curve. After the first cycle, both fabrics remain compressed, but each strain curve almost overlaps one of the previous cycles. To better evaluate this aspect, the insets of Figure 5.8 show the strain against time (right axis) while cycled pressure is applied (left axis). In this representation, it is possible to observe the dynamic strain range (the difference between the maximum and the minimum strain value in a cycle) and the symmetries of the strain curve during compression and decompression. Ruling out the first cycle, in Fabric A, the strain value ranges from -10% to -40% for the second cycle and from -13% to -43% for the tenth cycle, resulting in a large dynamic strain range of ~30%. As observed before, Fabric B seems to be less elastic than fabric A, but the strain values are more reproducible and range from -15% to -40% with a dynamic strain range of ~25%. Since the symmetry between compression and decompression curves, both fabrics are provided with reasonable elastic features. The thinner fabrics behave differently, underlining the fact that the structure/geometry characteristics of textile can influence the response. They show a greater thickness variation after the first cycle and a lasting compression during the others. They have a lower dynamic strain range of about 10%. The strain values range from -35% to -45% for fabric C and from -30% to -40% for fabric D. Moreover, the compression and decompression regions of the strain curve are not symmetric, and the smallest thickness does not correspond with the highest stress. All the mechanical features are presented in Table 5.1.

### 5.1.4.2 Textile pressure sensors performance

The textile sensors are fabricated with the four different fabrics and consist of a circle pixel of PEDOT:PSS deposited on it and by two conductive stainless steel threads that are in contact with each other through the coated fabric. Increasing the applied pressure, the thickness of the fabric decreases and the piezoresistivity of conductive polymer changes while the whole pressure sensor resistance decreases (conductance increase)<sup>25,207</sup>. For clarity, sensors made from Fabric A will be called sensors A and so on. Due to the differences in thickness, it is important to adjust the volume of the conductive polymer in the drop-casting deposition in order to achieve a proper and comparable vertical coating also in thicker fabrics. For this reason, sensors A and B have a sensitive area  $A = (51.6 \pm 0.7) \text{ mm}^2$ ;  $B = (48.5 \pm 0.6) \text{ mm}^2$ ) larger than the area of pressure sensors C and D ( $C = (33.2 \pm 0.5) \text{ mm}^2$ ;  $D = (18.5 \pm 0.4) \text{ mm}^2$ ).

## 5.1 Textile pressure sensors

**Table 5.1:** Summary of main parameters extracted from mechanical analyses. The DMA Q800 measures the thickness of the sample, and the standard deviation associated with the average value corresponds to a percentage error less than 1%.

Fabric	Creep Recovery			Stress-Strain Test	
	Initial Thickness (mm)	Thickness @100 kPa (mm)	Thickness after Release (mm)	Residual Deformation	Dynamic Strain Range
A	2.49 *	1.34	2.36	5.3%	30%
B	1.54	0.74	1.40	8.5%	20%
C	0.36	0.19	0.29	20%	10%
D	0.71	0.37	0.57	20%	10%

### 5.1.4.2.1 Cyclic response

The main sensors results in dynamic mode are reported in Figure 5.9, where the upper graph of each section shows the resistance response (black, on the left) during the application of 10 pressure cycles (red, on the right). The performance of the textile pressure sensor is evaluated by cycling the applied pressure onto the sensors ten consecutive times. The resistance response is inversely proportional to the applied pressure because, when the pressure increases, the device resistance decreases. Direct and linear response of the electrical properties with the applied external pressure is more suitable for an easier data correlation and interpretation. Thus, it is more useful to evaluate the conductance as an alternative of the resistance. Plotting the conductance, a linear trend in some sub pressure range can be achieved. Figure 5.9.c-d-g-h show the conductance graph under compression for every pressure cycle. Sensors A and C, though the fabrics are considerably different, have a stable and reproducible responses. Sensor C shows a strong variation after the first pressure cycle because the woven polyester fabric necessities a first compression cycle to stabilize the vertical structure of its fibres. This behaviour is also confirmed by the stress-strain test. The conductance response for sensor B presents a small spread through 10 cycles that increases in the high-pressure range. With a single layer of knitted cotton fabric, sensor D is the least stable because an increase in the resistance is obtained every cycle.

As already indicated in the previous paragraph, the change of the conductive polymer formulations affects both its electrical and its piezoresistive properties. Changing the basic conductive formulation have consequences in the textile pressure sensors in terms of performance and pressure operating range. Apart from the pristine solution, 10% v/v of ethylene glycol (EG) is used to enhance the conductivity of the organic compounds<sup>339</sup>.

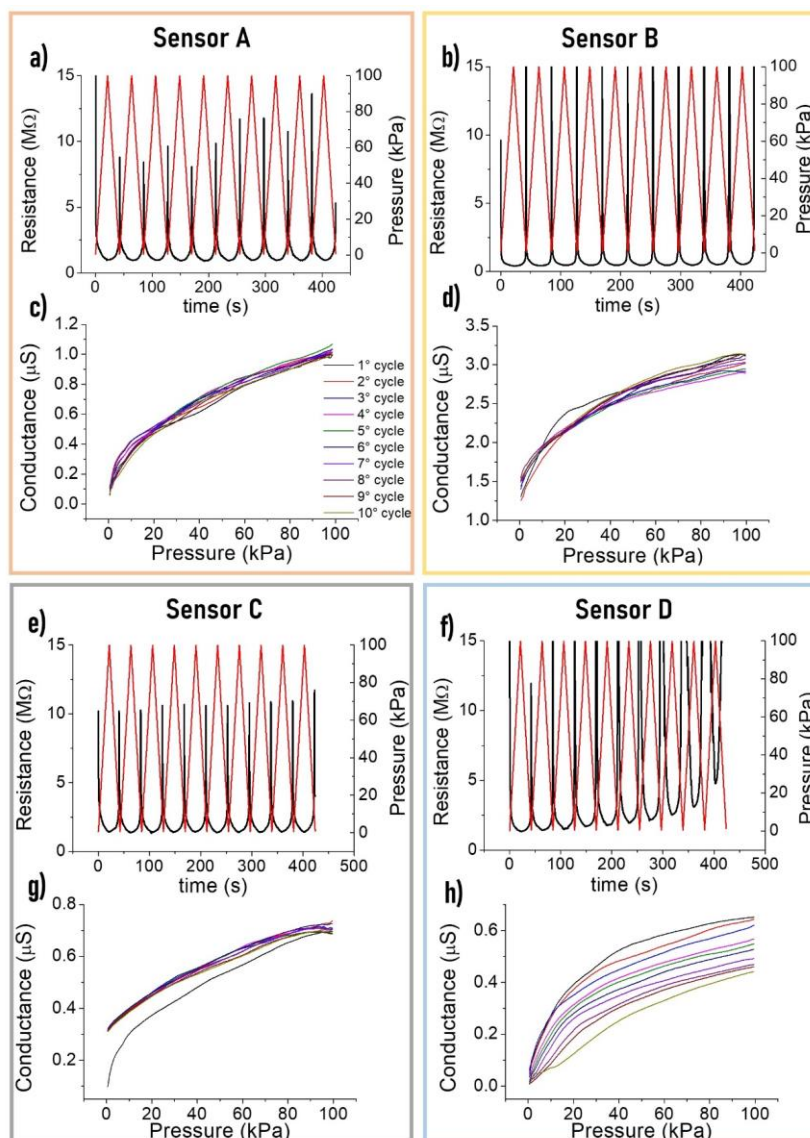


**Figure 5.9:** Comparison of the four fabrics. a-b-e-f) Resistance response in dynamic mode during 10 cycles with applied pressure from 0 to 100 kPa with a frequency of 5 kPa/s. c-d-g-h) Conductance trend during compression phase for every single cycle.

#### 5.1.4.2.2 Linearity study

Figure 5.10 shows the average trends of conductivity at every cycle with and without the presence of EG for textile-pressure sensors fabricated exploiting the four different fabrics. The linear working-range, reliability and sensitivity are indeed affected by the conductivity enhancement agent, EG. The sensors based on more conductive formulation have a greater sensitivity and a wider linear working range regardless of the fabric. However, the sensors with EG present a less reliable behaviour, as highlighted by larger

## 5.1 Textile pressure sensors

standard deviation values. In these dynamic tests, there is no saturation in the conductance as a function of pressure up to values of more than 70 kPa.

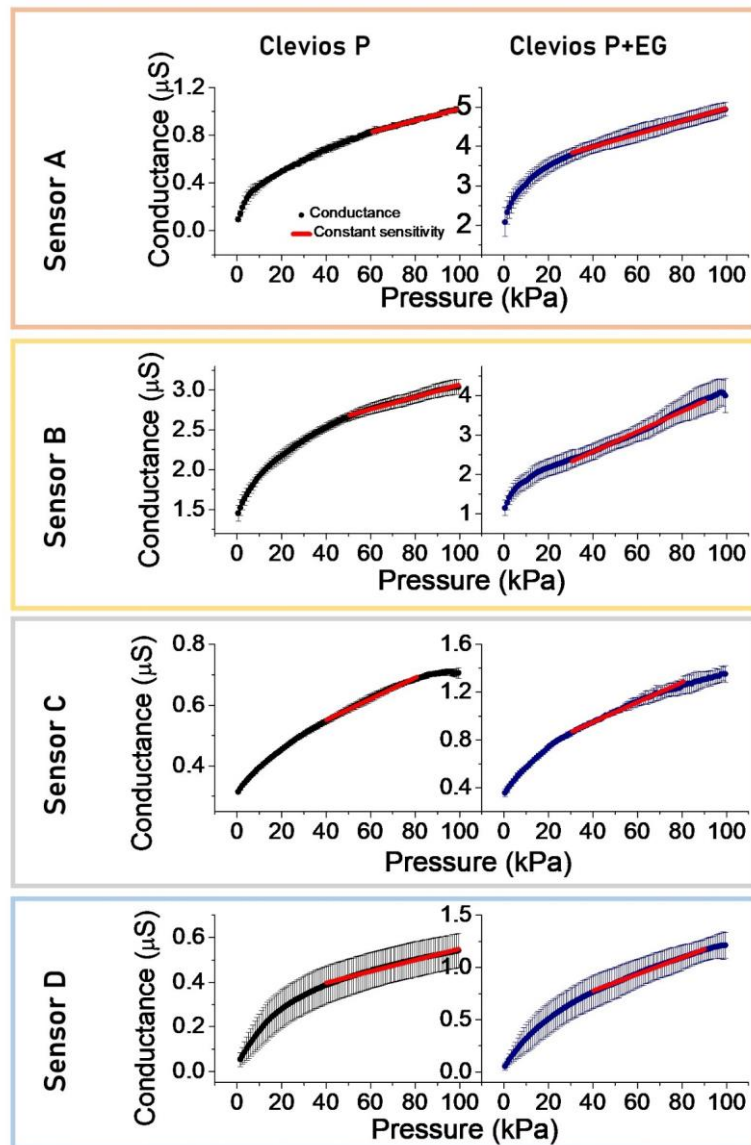


**Figure 5.10:** Average trend over ten cycles of the conductance response during compression-stress for both formulations.

The linear conductance ( $G$ ) response is modelled as  $G = S \cdot P + G_{off}$ , with  $S$  the sensitivity expressed in nS/kPa.  $G_{off}$  is the intercept value that is not zero because a preload force of 0.05 N is applied. Since the conductance trend is not linear over the entire range of pressures studied, to extract the region where the sensor shows a linear behaviour, the derivative of the curve of the conductance/pressure is calculated. According to the mathematical definition, the derivative represents the point sensitivity values and the region where it follows a constant trend, identifying the sensors linear operation range.

## 5.1 Textile pressure sensors

Figure 5.11.a shows an example of the derivative curve for sensor A with 10% EG formulation. For a better estimation of the working range, the linear correlation coefficient  $R^2$  is calculated for all the possible pressure ranges (with a minimum wide of 40 kPa), and the region with the highest value is chosen. The most relevant parameters for the textile pressure sensors are summarized in Table 5.2, where the conductance  $G_0$  is the one at the lowest applied pressure of 0.5 kPa, and the conductance  $G_{100}$  is the one at a pressure of 100 kPa. The weighted least mean squares method returns the sensitivity values reported in the table.

**Table 5.2:** Main parameters of textile pressure sensors realized with both formulations.

Sensor	Clevios P		Clevios P + EG	
	$G_0$ ( $\mu\text{S}$ )	$G_{100}$ ( $\mu\text{S}$ )	$G_0$ ( $\mu\text{S}$ )	$G_{100}$ ( $\mu\text{S}$ )
A	$0.09 \pm 0.02$	$1.01 \pm 0.02$	$2.1 \pm 0.4$	$4.4 \pm 0.2$
B	$1.4 \pm 0.1$	$3.03 \pm 0.09$	$1.1 \pm 0.2$	$4.0 \pm 0.4$
C	$0.314 \pm 0.003$	$0.70 \pm 0.01$	$0.35 \pm 0.03$	$1.35 \pm 0.07$
D	$0.05 \pm 0.03$	$0.54 \pm 0.07$	$0.05 \pm 0.03$	$1.2 \pm 0.1$
	$S_{\text{FIT}}$ (nS/kPa)	Linear Range	$S_{\text{FIT}}$ (nS/kPa)	Linear Range
A	$4.90 \pm 0.04$	60–100 kPa	$16.2 \pm 0.1$	30–100 kPa
B	$7.70 \pm 0.07$	50–100 kPa	$25.6 \pm 0.2$	30–90 kPa
C	$3.47 \pm 0.03$	40–80 kPa	$8.3 \pm 0.1$	30–80 kPa
D	$2.54 \pm 0.03$	40–100 kPa	$7.9 \pm 0.1$	40–90 kPa

The sensor's sensitivity is an essential parameter that defines how the estimated output varies when there is a variation in the input value. In this case, the output variable is the conductance that assumes a different value according to the pressure variation (the input parameter). The sensitivity coefficient allows knowing the effects on the measured output conductance due to a pressure variation. The relation between the measured quantity and the independent variable is used as a calibration curve for developing the optimized sensor.

The presence of uncertainty in the conductance value during the dynamic mode operation gives information about the sensor reliability. Elastic properties, material structure and conductive formulation, affect the sensor response after several working cycles. For example, the three-polyamide layers (Fabric A) and woven polyester fabric (Fabric C) are those that show the more stable response. Sensor D (knitted-cotton based fabric) is very unstable through the cycles and, though its sensitivity value calculated analitically is comparable with that of polyester-based sensors, it shows an excessive instability. In order to highlight the best textile and formulations for a real-life application of textile pressure sensors in a non-static framework, it is worth introducing another parameter, the pressure uncertainty value  $\delta P_i$  in each single applied pressure. It is defined by the formula,

$$\delta P_i = \frac{\delta G_i}{\left[\frac{\delta G}{\delta P}\right]_{P=P_i}}$$

where  $\delta G/\delta P_i$  is the single point sensitivity calculated differentiating the curves in Figure 5.10, and the conductance uncertainty values  $\delta G_i$ . This equation allows to extract information about the pressure uncertainty even if the sensitivity coefficient is not constant over all the studied pressure ranges. Figure 11.5.b reports the  $\delta P$  values for each sensor using the pristine conductive formulation. The instability in the dynamic operation mode with a subsequent huge uncertainty in the pressure estimation leads to rejecting Fabric D as a candidate for real pressure sensors. A possible explanation could be that cotton fibres coated with the conducting polymer increase their stiffness, and this can cause delamination or cracks during the compression and de-compression cycles, resulting in a variable and unstable trend. Similar results are reported in literature for similar mechanical stress levels<sup>37</sup>. Based on the analyses performed even on the sensors realized with the 10% EG formulation (Figure 5.11.c), it is possible to assert that the presence of EG decreases the reliability of the different sensors even if it contributes to increasing the sensitivity value and the dynamic range. Finally, sensors A and C with the pristine solution are the most stable and reliable examples and represent the best candidates to realize pressure sensors able to monitor and record a dynamic pressure variation.

### 5.1.5 Real-life applications

The main advantage of the textile pressure sensors here described is their simple implementation directly into the garment. To demonstrate this aspect in real-life conditions, the pressure sensors are directly fabricated into a cotton glove. A similar approach can be used to fabricate other wearable devices, such as socks or trousers. The reported fully textile sensorized gloves are comfortable and do not hinder the normal motion of the hand (Figure 5.11.a). For instance, Figure 5.11.b, reports cycled measurements when different forces are applied on the index. A wireless portable electronic reader is placed in the wrist as a common watch. The reader can record and transmit the sensor response in real-time. In the case shown, several sensors connected in series are placed among each finger and on the palm, resulting in five primary textile hand sensors. This solution reduces the number of wire connections and simplifies the electronic reader. The textile configuration's ease of design and fabrication enables multiple and varied geometries for the sensors that can significantly increase in number by optimizing the wiring scheme. The related electronic reader would only need a multiplexer system, easily miniaturized in view of a final commercial product. In a real-life application, at rest, the sensor response in terms of resistance is two orders of magnitude higher than at under pressure (few kPa), therefore it

## 5.1 Textile pressure sensors

is expected that the sensor would not be sensitive to movements or artefacts. However, as for any standard pressure sensors, a calibration procedure will be performed before any measuring sessions.

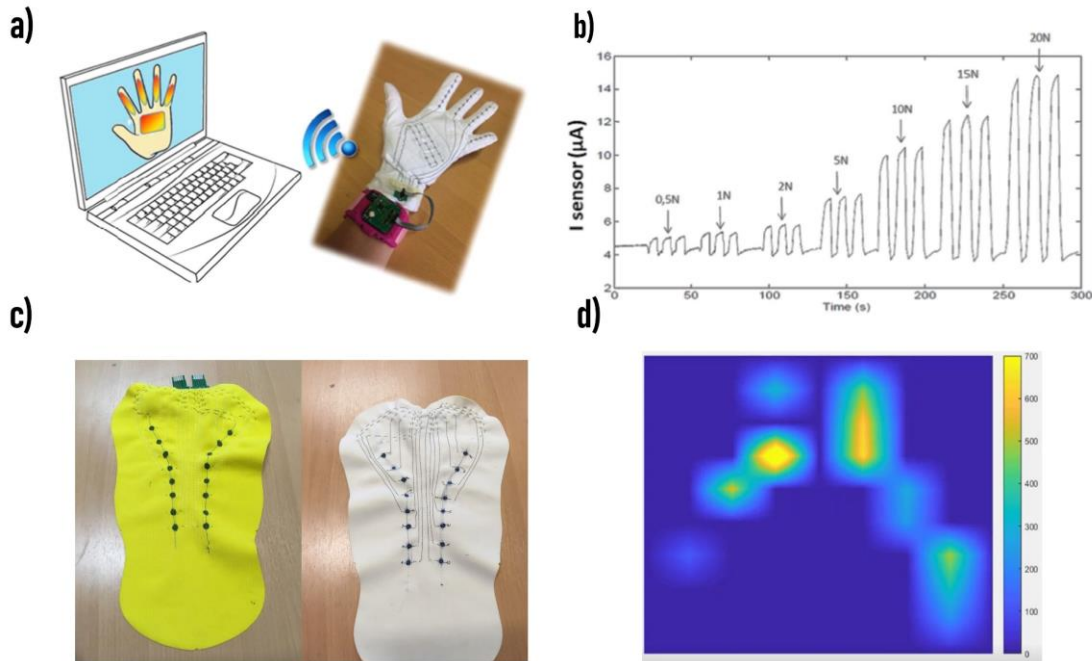


**Figure 5.12:** a) Cotton glove endowed with textile sensors and the portable reader to wirelessly interact with a personal computer. b) Example of the data acquired from the pointer finger at increasing pressure value. c) Pressure sensors integrated into a piece of textile used to realize cycling short (front and rear) and d) an example of data acquisition when the wearer is unbalanced on the right.

In addition, the thin configuration of the textile pressure sensors is suitable for all the applications where the accessible space is limited. In this context, they are placed in the internal part of padded cycling shorts to provide a personalized and dedicated pressure distribution monitoring on the saddle during biking (Figure 5.12.c). This application is particularly useful for knowing the weight distribution, the stresses exerted on the saddle surface and evaluating the biker's pedalling style. This important information allows to improve comfort and prevent genital or postural injuries.<sup>544</sup>

Moreover, as it is well known, exposure to liquids (for example, sweat) affects PEDOT:PSS's electrical properties, with potential consequences on its piezoresistivity. For this reason, when the sensors are tested in real-life trials, as reported in Figure 5.11.d, they are encapsulated with a thin film of hydrophobic plastic.

## 5.2 Textile ionizing radiation sensors

As already stated, the flexible, comfortable and breathable nature of fabrics makes these substrates ideal candidates for developing large-area physical wearable devices in direct contact with the human body. Despite the high number of different textile sensors realized so far, textile ionizing radiation detectors have not been proposed yet, mostly due to the incompatibility between conventional materials for radiation sensing and fabric substrates. The development of innovative functional materials and low-cost technologies for the detection of ionizing radiations has become an urgent need in the last years due to the relevant increase in the use of ionizing radiation in many parts of modern society, from medical applications to civil security. In particular, flexible and wearable innovative dosimeters are highly requested in hazardous environments, e.g. for personnel and patients in medical therapy and for space missions' crew.

Commercially available personal dosimeters and diagnostic detectors, based on inorganic materials (e.g. silicon-based solid-state devices for dosimeters, a-Si, a-Se, or poly-CZT for large-area flat panels) are heavy, bulky, rigid and uncomfortable to be worn. Furthermore, they are difficult to implement in large, pixelated matrices by means of low-cost and low-tech fabrication techniques. Recently, a new generation of X-ray detectors has been explored, based on organic semiconductors<sup>545-547</sup> and perovskites<sup>548-550</sup>, two classes of materials that allow for liquid phase deposition methods, enabling an easy device scaling-up to large areas and the implementation on unconventional flexible substrates, such as thin plastic foils<sup>551,552</sup> and even fabrics<sup>553,554</sup>.

Lead-halide perovskites are an emerging and promising class of materials for X-ray detection, thanks to their utmost electric transport properties, (i.e. high charge carrier mobilities and long carrier lifetime), excellent optical properties, together with high ionizing radiation stopping power due to the presence of heavy atoms (Br, Pb, I) in their molecular structure. The combination of all these features has led to the impressive performance of lead-halide perovskite devices in the direct detection of X- and gamma- rays, both in films<sup>555</sup> and single-crystal forms<sup>556-558</sup>. However, despite their excellent performance, single crystals retain a mechanical stiffness preventing the implementation of bendable devices. On the other hand, the growth of thick film-based perovskite detectors requires high-temperature processing (e.g. melting techniques), not compatible with flexible substrates. Flexible perovskite-based X-ray detectors have been less explored but, in the last years, the number of reports on their feasibility has been rapidly growing<sup>559-561</sup>. The possibility of conforming ionizing radiation detectors and dosimeters onto a non-flat object is one of the primary desired features needed, for example, when detectors have to be integrated inside specific probes during radiation therapy<sup>562</sup>, or in easy-wearable objects (bracelets, belt) and for potential vignetting limitation. Recently, Zhao et al.<sup>563</sup> proposed a highly sensitive and flexible direct X-ray detector based on a porous nylon membrane with metal halide

perovskite loaded by infiltration method. Such a perovskite-filled membrane has good stability and high sensitivity to X-rays, comparable to those of single perovskite crystals. Despite the remarkable detection performances, this flexible device, together with others in recent literature,<sup>564,565</sup> envisage complex multi-layered architectures and fabrication techniques requiring several steps and often an oxygen-free environment.

To overcome this limitation, it is reported for the first time the new concept of textile X-ray detectors (TX-RD) based on cotton conductive electrodes and perovskite single-crystal embedded into a silk-satin fabric. The fabrication procedure, morphological characterization, performance and potential application are reported in the next paragraphs.

### 5.2.1 Fabrication of TX-RD

The realization of the TX-RD consists of three different and straightforward steps carried out at room temperature and in ambient conditions: i) fabrication of textile electrodes, ii) growth from a solution of perovskite crystals into textile substrates, iii) sew and assembly of the fabrics in the final and desired geometry.

#### 5.2.1.1 Conductive electrodes

PEDOT:PSS textile electrodes are fabricated by using conventional serigraphy screen-printing technique (see 2.3.1.4) applying custom masks onto the frame in order to impress the cotton fabric with the desired geometry. The final electrode dimension depends on the prototype desired, and an ad-hoc serigraphic frame is realized to match the specifications (Figure 5.13.a). Textile conductive electrodes are realized by a conductive polymer ink, poly(3,4-ethylenedioxythiophene) polystyrene sulfonate (PEDOT:PSS), made by Clevis PH1000 and EG in 95:5 volume ratio, and 10% w/w of PEG. The solution is stirred for 20 minutes to disperse the PEG completely. A more viscose conductive ink is realized by drying the liquid solution in an oven at 70°C for 1 hour. The final conductive paste is placed onto the serigraphy frame and squeezed manually onto the cotton. To ensure electrical contact with the read-out set-up, a stainless steel conductive thread is sewn onto the electrode and along the fabric using an Elna Xplore 340 sewing machine. The resistance variation over a period of 5 months of the so fabricated textile electrode is shown in Figure 5.13.b, highlighting the fact that after an initial increment of the resistance, it remains constant over a period of 5 months. The optical images of the cotton substrate and the conductive cotton fabric constituting the electrodes with the typical bluish colour PEDOT:PSS is reported in the inset of Figure 5.13.b. Such screen-printed conductive electrodes represent a flexible, durable and deformable alternative to a standard metallic contacts in wearable applications.

### 5.2.1.2 X-ray sensing fabric

The sensing layer of the detector consists of a silk satin fabric functionalized with perovskite crystals (Figure 5.13.c). The precursor perovskite 1M solution is realized by adding the lead (II) bromide ( $\text{PbBr}_2$ ) and methylammonium bromide (MABr) powder in a stoichiometric ratio of 1:1 in N,N-Dimethylformamide (DMF) solvent. They are vigorously mixed for 4 hours and then filtered with a Teflon filter ( $0.45\ \mu\text{m}$  size) to remove colloids eventually present. A volume of 100 mL every  $\text{cm}^2$  of synthesized precursor solution is drop-cast onto a piece of  $20 \div 30\ \text{mm}^2$  fabric and let dry at  $80^\circ\text{C}$  to uniformly grow perovskite crystals as reported in section 2.3.2 (Figure 5.13.c-d).

Figure 5.13.c shows a picture of the silk-satin fabric before and after the perovskite crystals' growth, showing the typical orange colour of  $\text{MAPbBr}_3$  crystals. The deposition process is repeated three times in order to increase the crystals' density and achieve a layer with a thickness of about  $50\ \mu\text{m}$ . To the best of our knowledge, this is the first example of a fast, low-cost and uniform perovskite crystal growing procedure onto a fabric substrate. Thanks to typical satin weaving features, i. e. wrinkle-resistant, slipper, and tight stitches, the crystals cover the fabric uniformly and with a high density.

The as-prepared perovskite functionalized fabric is used to realize a stacked textile X-ray detector, placing it between two conductive cotton fabrics and sewing all the textile layers together by a sewing machine to obtain an intimate and stable electric contact (Figure 5.13.e-f). The sensor dimension depends on the areas of the conductive electrodes and of the functionalized silk-satin fabric. The TX-RD sensors have different areas from  $0.06\ \text{cm}^2$  up to  $1\ \text{cm}^2$ .

## 5.2.2 Morphological analysis

Figure 5.14.a shows the optical image of the surface of the silk-satin fabric after the first step of functionalization with  $\text{MAPbBr}_3$  crystals with a zoomed picture. SEM images (Figure 5.14.b-c) show the tight binding and the intimate contact between perovskite crystals and the fabric, a crucial feature to envisage wearable applications for TX-RD devices directly integrated on garments and able to withstand wearing stresses. The EDX image in Figure 5.14.d reports the distribution of crystals on the fabric after the first deposition step and their composition: the Br and Pb atoms, highlighted in green and red respectively, are significantly present only in crystals, leaving the surrounding textile fibres lead- and bromine-free.

## 5.2 Textile ionizing radiation sensors

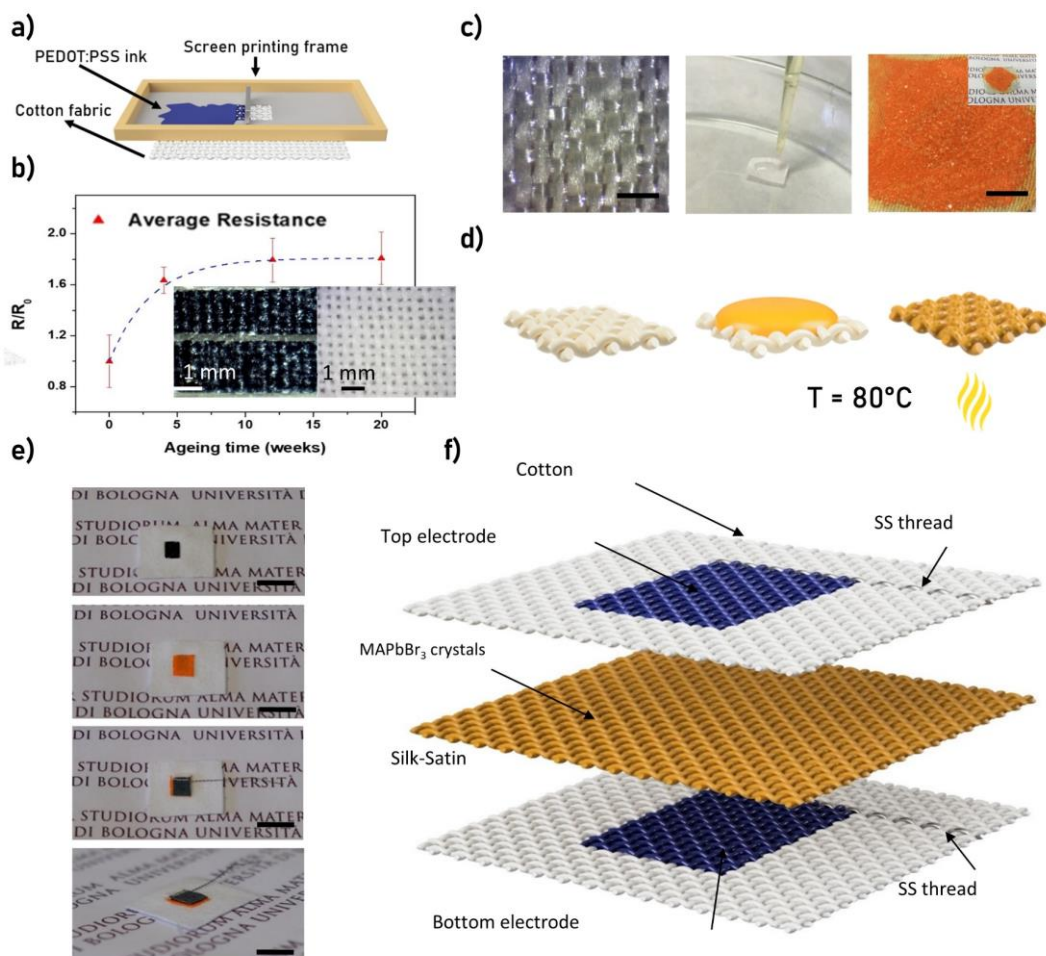


**Figure 5.13:** a) Schematic representation of the screen printing procedure. b) Ageing of ( $3 \times 3.5$ )  $\text{cm}^2$  cotton fabric coated with PEDOT:PSS under ambient conditions. The plot reports relative resistance variation, and the top view of pristine and functionalized cotton fabric with PEDOT:PSS. c) Optical picture of the top-side of the silk-satin fabric, drop-cast deposition of  $\text{MAPbBr}_3$  precursor solution on textile, and the optical image of the silk-satin fabric fully covered with the embedded polycrystalline absorption layer. d) Sketch of the crystal deposition procedure on the textile. e) Fabrication step of the TX-RD stacked devices. The three layers are sewn together. Black scale bar is 1 cm. f) Schematics of the stacked TX-RD, highlighting the presence of stainless steel (SS) conductive thread.

Figure 5.14.e shows the X-ray diffraction spectrum that highlights the crystallinity of perovskite crystals embedded into the final functionalized silk-satin fabric. The diffraction peaks position at  $15.1^\circ$ ,  $30.2^\circ$ , and  $46.02^\circ$  are converted into interplanar spacing, which correspond to (001), (002) and (003) crystal planes, respectively<sup>566</sup>. The high peaks intensity clearly indicates the high crystallinity nature of the sample with a constant orientation of (001) crystal planes parallel to the surface.

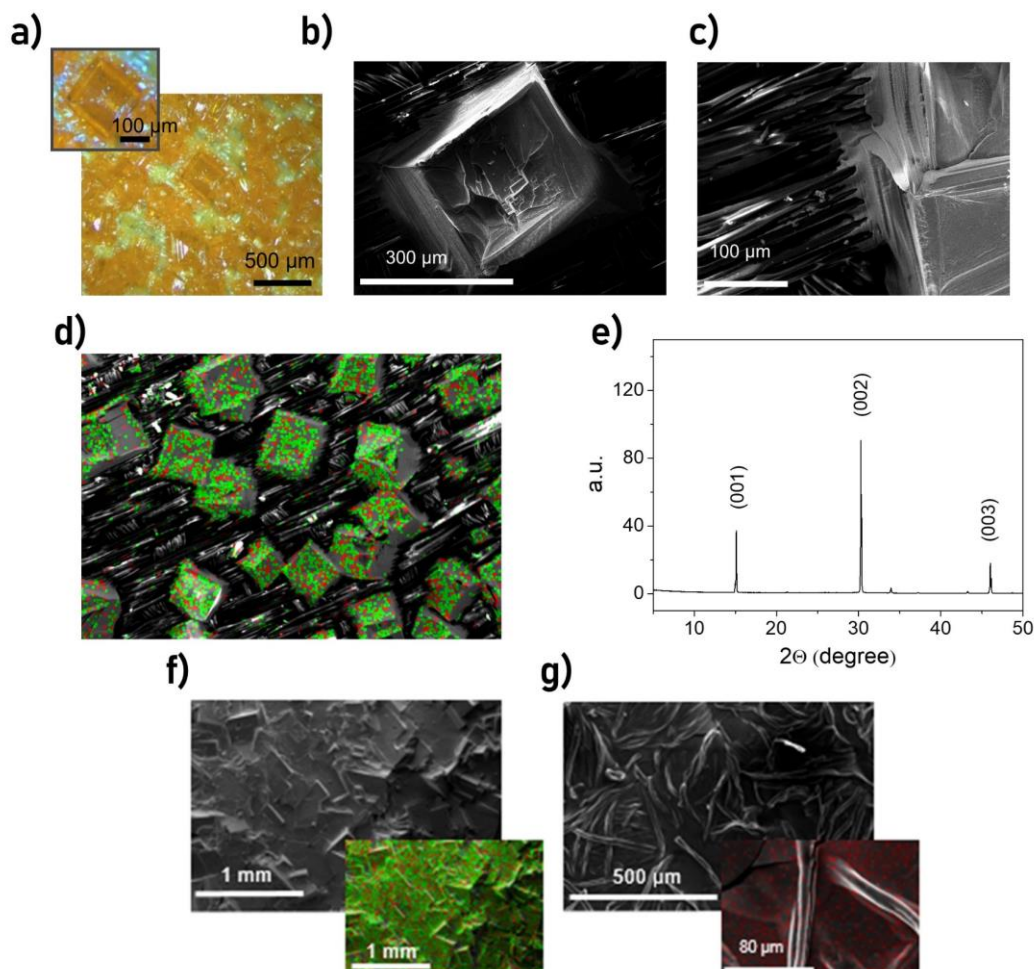


**Figure 5.14:** a) Optical image of MAPbBr<sub>3</sub> crystals. b) Top view SEM image of one MAPbBr<sub>3</sub> single crystal. c) SEM image of a MAPbBr<sub>3</sub> crystal embedded in the silk-satin fabric. d) Top-view SEM image of the silk-satin fabric after the first deposition step, showing the distribution of crystals embedded into the fabric. Red and green dots highlight the presence of lead and bromine, respectively. e) XRD spectrum of MAPbBr<sub>3</sub> crystals embedded into the silk-satin fabric. The peaks correspond to the (001), (002) and (003) crystal planes. f) SEM and EDX (inset) of the MAPbBr<sub>3</sub> absorption layer after three subsequent drop-cast depositions. g) SEM image showing the uniformity of the screen-printed PEDOT:PSS layer on cotton. The top view EDX image (inset) shows Sulphur's homogeneous distribution (red dots), the identifying element of PEDOT:PSS.

In order to achieve a TX-RD able to efficiently collect the charges induced by the interaction of the active layer with the X-rays, three consecutive drop-cast steps are needed to enhance the distribution of the crystal. After each deposition, the numbers and the crystals' arrangement change from single and isolated crystals to a continuous surface coverage after each deposition. The crystals' tight and dense arrangement transforms the silk-satin substrate into an effective photo-active textile (Figure 5.14.f) and creates a continuous, thick (300 μm on the average) and a uniform path that can efficiently transport charge carriers. The inset in Figure 5.14.f shows the Br (green) and Pb (red) uniform

dispersion through the entire crystalline layer. In the same vein, Figure 5.14.g shows a SEM image of the uniform and dense PEDOT:PSS coating of the cotton fabric, while the inset underlines through EDX analysis the homogeneous distribution of Sulphur (red), which characterizes the PEDOT:PSS presence.

### 5.2.3 Results of single TX-RD

The absorbing power of hard X-rays (40-150 kVp) by the cotton fabrics with the electrical contacts is far less than the one of silk layer covered with perovskite crystals. This is due to the low atomic number of the organic material on the conductive electrodes. The perovskite functionalized silk-satin fabric absorbs  $\approx 100\%$  X-ray photons at 40 kVp (15 keV mean energy), and the negligible absorption of the cotton fabric and PEDOT:PSS allows to fully exploit the absorption of the perovskite loaded textile layer without having to take into account shielding effects due to the top layers of the device in the stacked architecture.

Typical Current-Voltage (I-V) characteristics in the dark of a stacked TX-RD device show a limited hysteresis as well as good ohmic behaviour for an applied voltage from -5 V to +5 V (Figure 5.15.a). The average dark bulk resistance is  $(1.8 \pm 0.9)$  G $\Omega$  measured over eight samples. The bulk resistance is calculated considering the value extracted from the linear fit of the I-V curves, both increasing and decreasing the bias sweep.

The textile devices' performance as X-rays detector is tested in air without encapsulation. Figure 5.15.b shows the TX-RD photocurrent real-time response under irradiation with high-energy photons delivered at 150 kVp. The four different dose rates (from 1.5 mGy s<sup>-1</sup> to 6.4 mGy s<sup>-1</sup>) are delivered by changing the anodic current in the range (100 - 500)  $\mu$ A. The plot is realized by subtracting the average dark current to each measured current value ( $I_i - \bar{I}_{dark}$ ). The X-ray beam intermittently reaches the tested sample alternating 5 s of irradiation and 5 s of dark by a mechanical lead shutter. Multiple subsequent on/off cycles at the same dose rate are acquired to estimate the average photocurrent generated, defined as the difference between the average current value under X-rays and the average dark current before switching the X-ray beam on. To meet the low-power consumption request of wearable devices, the sample is biased at 5 V during the measurements (electric field of about 0.017 V  $\mu$ m<sup>-1</sup>s. Figure 5.15.c shows the TX-RD stability after 15 subsequent irradiation cycles at a high dose rate of 8.0 mGy s<sup>-1</sup>. The response is fast, sharp, and repeatable over multiple cycles with a relative variation of the photocurrent lower than 3%.

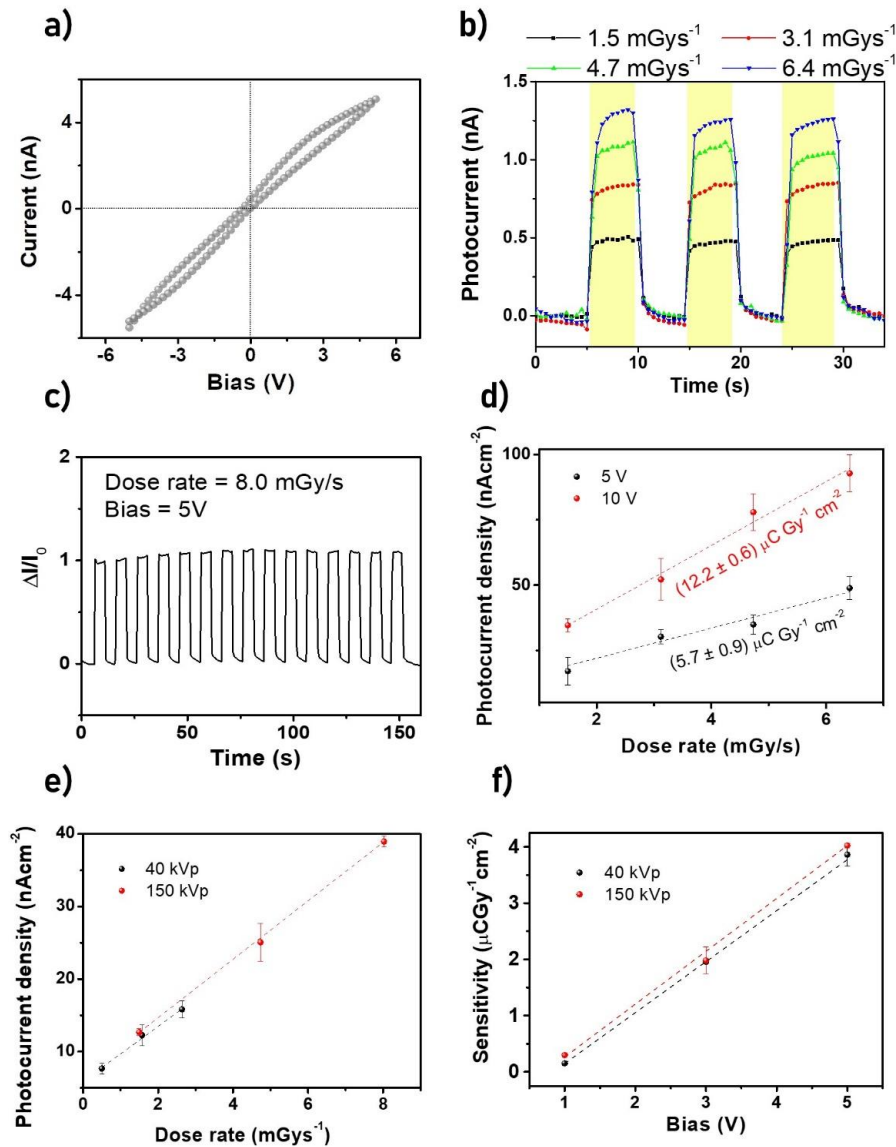


**Figure 5.15:** a) Typical Current-Voltage characteristics of the device in dark condition. b) Dynamic detector response of a stacked TX-RD biased at 5 V, under X-ray beam (150 kVp – 47.4 keV mean energy of the spectrum) at different incident dose rates. The yellow boxes indicate the time window when the X-ray beam is turned on (5 s ON and 5 s OFF). c) Reproducibility of photocurrent dynamic response, normalized by its initial value, over 15 X-rays irradiation cycles (5 s ON and 5 s OFF each) at 8 mGy s<sup>-1</sup>. The bias is 5 V. d) X-ray induced photocurrent as a function of the incident radiation dose rate for two different biases: 5 V and 10 V (e), and different accelerating voltages of the X-ray tube: 40kVp and 150kVp. f) Linear scaling with the bias of the sensitivity to X-rays recorded under 40 kVp and 150 kVp X-ray beam irradiation.

The detector's X-ray photocurrent density (normalized by the device area) exhibits a linear trend with the incident dose with a bias of 5 V and of 10 V applied to the sample. The

slope of the X-ray photocurrent density versus the dose rate curve is defined as the sensitivity per unit area of the sample, and it is one of the most important figures of merit of the X-ray detectors (Figure 5.15.d). The sensitivity at 5V in the stacked configuration reaches the value of  $(5.7 \pm 0.9) \mu\text{C Gy}^{-1} \text{cm}^{-2}$  at 150 kVp, and a top value of  $(12.2 \pm 0.6) \mu\text{C Gy}^{-1} \text{cm}^{-2}$  applying a bias of 10 V, corresponding to an applied electric field of  $0.034 \text{ V } \mu\text{m}^{-1}$ . The top sensitivity recorded well compares with one of the state-of-the-art inorganic materials currently used to fabricate large-area detectors (amorphous selenium has typical values of  $25 \mu\text{C Gy}^{-1} \text{cm}^{-2}$  at  $10 \text{ V } \mu\text{m}^{-1}$  for 200  $\mu\text{m}$  thick active layer typically)<sup>567</sup>. Figure 5.15.e reports the TX-RD response recorded under X-rays of 40 kVp and 150 kVp at different dose rates for a constant bias of 5 V (mean value and standard deviation over three subsequent irradiation cycles). The linear response with increasing dose rate is assessed both at 150 kVp and at 40 kVp, demonstrating the capability of the TX-RD to be used as real-time direct dosimeters under a wide range of X-ray energies and dose rates, from  $500 \mu\text{Gy s}^{-1}$  up to  $8.0 \text{ mGy s}^{-1}$ . The sensitivity value linearly increases with the increasing of the applied bias (from 1 V to 5 V in Figure 5.15.f) and, interestingly enough, it shows a scant dependence on the X-ray beam energy, opening to the potential application for energy-independent dosimetry.

### 5.2.3.1 Additional performance of TX-RD

The device performance under 150 kVp and 40 kVp X-ray beam irradiation with an applied potential of 5 V has been monitored for 40 days (Figure 5.16.a). During the first 20 days, the device sensitivity loses less than 10% of its initial value, while after more than one month, the sensitivity value decreased more than 50%. Furthermore, we performed a crumpling test to better assess the good connection ensured by deposition and sewing procedure. It consists in wrinkling the fabric (Figure 5.16.b) multiple times and measuring the sensors photocurrent before and after 20 repeated wrinklings. Figure 5.16.c shows the response when the sample is irradiated with 40 kVp and 150 kVp X-ray beam. Since the measured photocurrent decreases less than 30%, it indicates that the application of severe stress can just slightly decrease the response without making the device unusable.

In addition, we performed bending tests comparing the signals of a flat sample and in a bending position. Bending the sample down to a radius of 18mm, compatible with most of the wearable applications, both the photocurrent and the sensitivity increase (Figure 5.16.d-e). The photocurrent increases about three times. Accordingly, the sensitivity increases from  $(1.2 \pm 0.1) \mu\text{C Gy}^{-1} \text{cm}^{-2}$  to  $(3.4 \pm 0.1) \mu\text{C Gy}^{-1} \text{cm}^{-2}$ . This phenomenon can be correlated to a tighter contact between the textile layers, allowing a more efficient charge collection. Another important figure of merit to characterize the detector's performance is the minimum detectable dose, namely the limit of detection (LoD), defined as the minimum intensity of X-rays which provides a signal-to-noise ratio (SNR) equal to 3 (IUPAC standard

## 5.2 Textile ionizing radiation sensors

definition<sup>568</sup>). Figure 5.16.f reports the SNR over three orders of magnitude of dose rates for the sensors biased by 5V. The graphically-extracted LoD is  $3 \mu\text{Gy s}^{-1}$  when the X-rays accelerating voltage is 150 kVp. This value is well compatible with the typical radiation doses used in most medical diagnostic and dosimetry applications.<sup>569</sup>

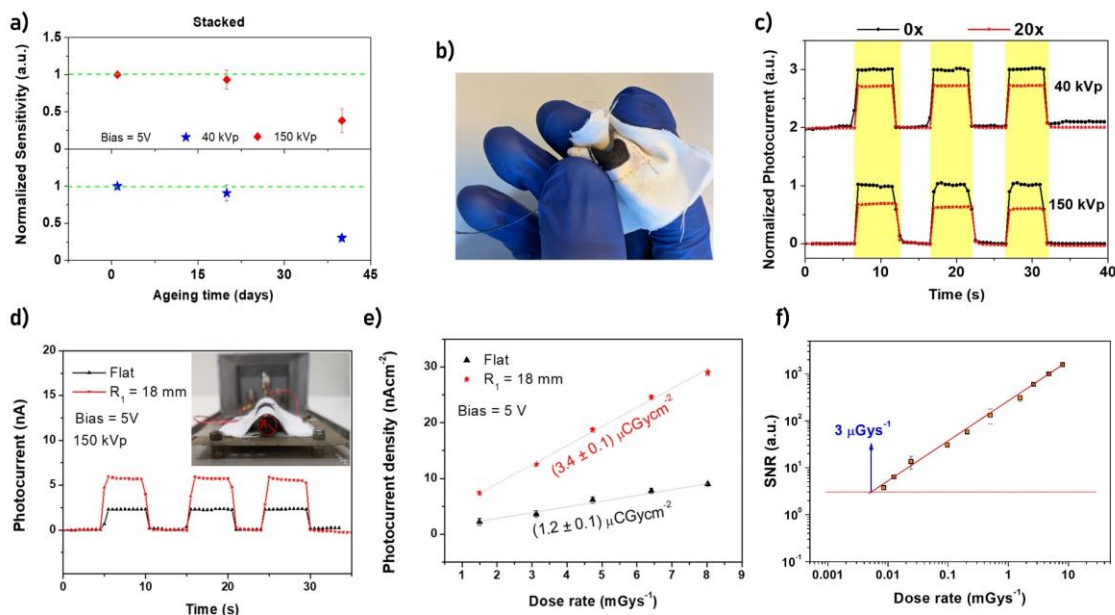


**Figure 5.16:** a) Ageing test of the textile X-ray detector performed over 40 days. b) Crumpling test and c) plot of normalized photocurrent, acquired both with 40 kVp (shifted in y-axis for clarity) and 150 kVp X-ray beam, before (black points) and after (red points) 20 wrinklings. d) Photocurrent response versus time of a device in the flat and bent configuration under a dose rate of  $8 \text{ mGy s}^{-1}$ . The inset shows the bending set-up. e) Photocurrent density versus the dose rate for the stacked sample in flat and bending position. Both measures have been taken with an X-ray beam energy of 150 kVp and applying a bias of 5 V. f) Graphical extraction of the Limit of Detection (LoD). The applied bias is 5V with an X-ray accelerating voltage of 150 kVp.

### 5.2.4 TX-RD matrix

As further proof of the potential application of such a new textile X-ray sensor, two cotton fabrics, each with three parallel conductive strips, are employed as top and bottom electrodes to realize a large-area X-ray matrix detector. This is feasible thanks to the possibility of easily screen printing different electrode patterns with a sub-millimetre resolution.

The sensor matrix consists of nine independent pixels, defined by the intersection of three electrodes printed both on the top and bottom fabric, as shown in the schematic of Figure 5.17.a. The photo-active textile, functionalized with perovskite crystals, is

## 5.2 Textile ionizing radiation sensors

---

sandwiched between them. Figure 5.17.b-c report the normalized dark current and photocurrent for each of the 9 pixels, respectively. The recorded variability of 13% for the dark current and of 20% for the acquired photocurrent signal highlights the overall homogeneity of sensors' response. To better stress this aspect, Figure 5.17.d reports each pixel's sensitivity per unit area at 5 V under an impinging X-ray beam at 150 kVp. The average sensitivity per unit area is  $(1.9 \pm 0.3) \mu\text{C Gy}^{-1} \text{cm}^{-2}$ . The TX-RD reproducibility in a matrix configuration is assessed by realising two matrices and recording their dark current and the X-ray photocurrent response. Figure 5.17.e reports their statistic distribution in a box chart plot, also showing their linear increase with increasing applied voltage. The high tested dose rate of  $8.0 \text{ mGys}^{-1}$ , assesses the reliability of the sensor matrix operation under strong irradiation conditions.

## 5.3 Conclusions

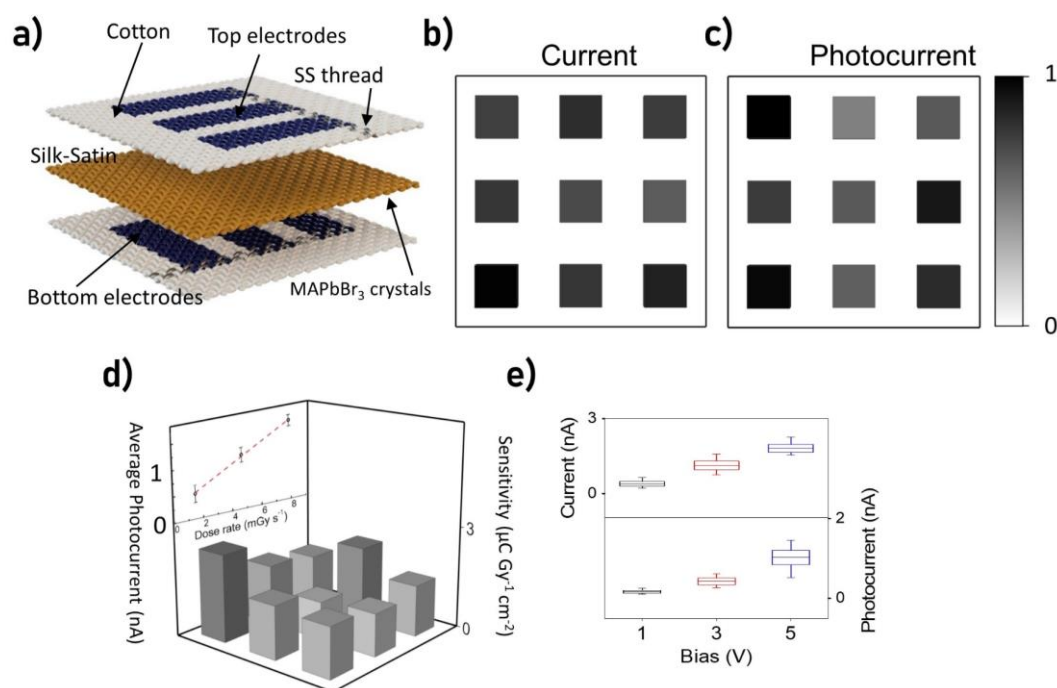


**Figure 5.17:** a) Schematic of the assembly of the textile matrix sensor. Distribution of the normalized dark current b) and X-ray induced photocurrent (bias 5V – dose rate 8.0 mGy s<sup>-1</sup>) c) for each of the 9 pixels. d) Sensitivity per unit area of all the pixels when 5V is applied with an impinging X-ray beam at 150 kVp. The plot of the average X-rays photocurrent of the sensor matrix in function of the dose rate is reported in the inset. e) Statistical distribution over 2 Matrix TX-RD samples of the dark current and photocurrent response for three different biases at a dose rate of 8 mGy s<sup>-1</sup>.

## 5.3 Conclusions

This chapter reported two examples of physical textile sensors developed to create a wearable platform that monitors workers' activities to improve safety standards, sports athletes, rehabilitation patients etc. Specifically, the performance of textile pressure sensors is investigated by changing both the different piezoresistive formulations responsible for the electrical response to external pressure and the mechanical or elastic properties of the textile substrate to adapt sensitivity and working range according to the desired application. Their versatility, flexibility, low thickness, ease of integration and scalability pave the way for various applications in contexts like sports, rehabilitation medicine and occupational safety.

### 5.3 Conclusions

---

Similar applications are envisaged for the new class of textile ionizing radiation sensors reported for the first time in this thesis. By combining an organic conductive polymer for the electrical contacts and perovskite crystals directly grown among the fabric fibres, a stacked configuration enables the fabrication of a new type of textile sensor. The current level in these devices is directly dependent on the incident radiation. The achieved performance, although comparable in terms of response time and sensitivity to other examples of detectors already reported in the literature, are only a starting point for what may be a new area for radiation sensors. Improving the growth and integration of the various parts that compose the sensors will increase their main performance, thus reaching a device usable in real conditions. Finally, the feasibility of easily realising a sensing matrix with several pixels able to provide a sort of imaging opens the way to these new textile sensors for successful development in fields such as diagnostics and security.

# Chapter 6

## Further Works: textile thermoelectric generators

All the previous chapters reported the results of new examples of textile sensors, both employed to detect chemical and physical parameters. They used completely different physical or chemical principles to get the measurable electric signal needed to perform the detection. However, the low bias and low power consumption are the two main features that describe all the described sensors. In this frame, as a further and attractive aim, the desire to realize a fully wearable energy harvesting system has been followed. The present chapter collects the latest attempts in order to realize a single thread textile thermogenerator (STTT) able to harvest energy using the thermoelectric effect and the temperature difference between the body of the wearer and the surrounding environment. The results here reported are still preliminary but the reliability of the theoretical model, the first samples fabrication and their characterization pave the way for future promising results such as the possibility of being used together with the textile sensors as energy sources without employing external batteries that are stiff, rigid and with a limited lifetime.

## 6.1 Introduction

Nowadays, the energy supply problem is one of the most important and discussed issues in modern society. Not only the vast amount of energy requested by industries or cities has a relevant impact, but even the lower energy quantities requested by portable and wearable objects. In addition, in the era of wearable technology, the number of electronic devices able to operate at low voltage is rapidly increasing. There are several strategies to power wearable electronics using non-battery wearable power supplies that can harvest energy from different sources such as solar/light (small-scale solar cells, Figure 6.1.a), body movement (piezoelectric devices, Figure 6.1.b), and human body heat (thermoelectric generators, Figure 6.1.c).

Among the feasible technologies that have been discovered, thermoelectricity is one of the promising technologies as a clean power generator. A thermoelectric generator is a solid-state system that directly transforms heat into electrical energy induced by a temperature difference in the system involving two different conductive materials. The basic phenomenon of thermoelectric energy generation is known as the Seebeck effect. The thermoelectric generators have several advantages like having no moving parts or chemical reactions, are noiseless, renewable, environmentally friendly<sup>570-572</sup> and, can even operate oppositely: when an electrical current is applied to the thermoelectric circuit, one junction becomes hot, and the other becomes cold. This process is known as the Peltier effect.

In wearable technology, textiles are gaining much interests as an essential part of integrating electronic functionality, for example, yarn supercapacitors and triboelectric nanogenerators,<sup>573</sup> textile energy storage/batteries,<sup>20</sup> textile antenna,<sup>574</sup> textile-based transistors<sup>575</sup> and temperature sensors<sup>576</sup>, to name a few. Thermoelectric generators and thermoelectric cooling devices are made with the thermopile configuration in which many thermocouple junctions are connected in series to produce higher thermo-voltage, as illustrated in Figure 6.1.c-d. Several researchers have studied the possibility of using the thermopile principle in textile fabrics for heat flux sensors.<sup>577</sup> They used metal wire (copper-coated constantan wire) weaved into a common woven fabric and converted into a series of copper-constantan thermocouples. This kind of device, with metal wires integrated into the textile structure, decreases the textile product's flexibility and comfort properties.

Therefore, this overview aims to confirm previous results on this topic and further prove the feasibility of a textile-based thermoelectric device by using conductive textile yarns that can be directly integrated into fabrics for energy harvesting purposes. Hence, several steps are needed to achieve a prototype that addresses the primary request of wearable electronic devices like flexibility, comfortability, washability, and enough generated thermovoltage and thermopower. On the one hand, a theoretical model already reported by Hardianto et al.<sup>46</sup> is here extended to integrate different configurations and material combinations. The main scope is to find a model able to select the best conductive

## 6.2 Theoretical model

textile yarns that can be transformed into a series of thermocouples to function as a thermoelectric device. On the other hand, fabrication and testing of some pilot devices are presented to validate the theoretical framework.

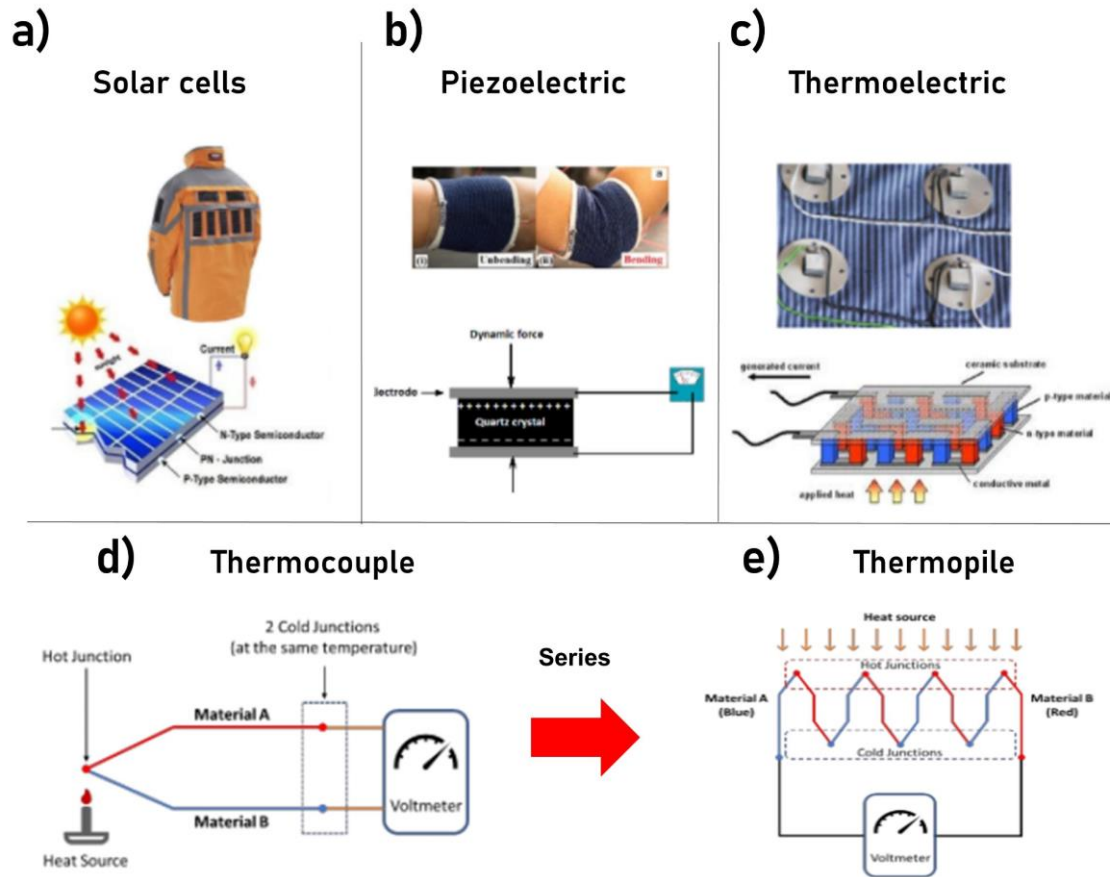


**Figure 6.1:** a) Textile solar cell device. b) Piezoelectric energy generator embedded in a wristband. c) Thermoelectric devices attached to a shirt with the wire connections sewed on the shirt.<sup>578</sup> d) Working principles of a thermocouple based on the Seebeck effect, and e) several thermocouples connected in series to form a four-fold thermopile.

## 6.2 Theoretical model

In order to find the best material combination and configuration to develop single thread textile thermopiles, a theoretical framework for predicting the best thermopower of a fibre-based thermocouple is firstly studied. As already reported, the idea is to realize a textile single yarn, periodically assembled or coated with different conductive materials, to create multiple junctions along the thread.<sup>15</sup> Figure 6.2.a shows the first application of this idea, in which the textile-thermoelectric generator thread is sewn into the fabric that has the

top and bottom sides at different temperatures. There are various configuration and fabrication solutions to realize such textile thermoelectric generators, which involves a different number of materials and geometry, like the following:

- 1) Two-material periodically adjacent (Figure 6.2.a);
- 2) Three-material: two periodically adjacent and the third one coated onto one material (Figure 6.2.b);
- 3) Two-material: the first in the core, and the second periodically coated on the shell (Figure 6.2.c);
- 4) Three-material: the first in the core, and the other two periodically coated onto the first one (Figure 6.2.d);

These combinations have a maximum thermoelectric voltage depending on the material properties like the conductivity, thread resistance, and the Seebeck coefficient. In order to estimate the best combination, various equations are derived from modelling the charge and heat transport through the thread sample. Here is reported the most general framework from which it is possible, under proper assumptions, to describe every system presented before. Even if the proposed combinations offer various degrees of realisation feasibility, mainly depending on the specific fabrication method used, it is helpful to provide a general and comprehensive explanation.

Starting from the work of Hardianto,<sup>579</sup> the generalized Ohm's law

$$J_i = \sigma_{ik} E_k - \sigma_{ik} \varepsilon_{km} \left( \frac{\partial T}{\partial x_m} \right) \quad (6.1)$$

can describe the current density through a system composed of two segments, one made by a single material and the other composed by a core-shell structure of two materials (Figure 6.2.b). They could be both metals or semiconductors, depending on the final scope, performances, and fabrication procedures used.

The junction and the extremities are set at different temperatures, and, exploiting the Seebeck effect, a potential gradient appears through the yarn. The current in segment one and segment two, assuming isotropy yarns, is described by the following equations:

$$i_1 = -\sigma_1 \left( \frac{d\varphi}{dx} - \varepsilon_1 \frac{dT}{dx} \right) S_1 \quad (6.2)$$

$$i_2 = -\sigma_{2i} \left( \frac{d\varphi}{dx} + \varepsilon_{2i} \frac{dT}{dx} \right) S_{2i} - \sigma_{2o} \left( \frac{d\varphi}{dx} + \varepsilon_{2o} \frac{dT}{dx} \right) S_{2o} \quad (6.3)$$

$\sigma$ ,  $\varepsilon$ ,  $S$  indicate the conductivity, Seebeck coefficient and section. Subscript 1 is referred to the first segment (on the left in the schemes of Figure 6.2) while subscript 2 to the second segment (on the right).  $i$  and  $o$  refer to the inner and outer material in the segment, respectively.  $\varphi$  and  $T$  indicate the potential and the temperature at a specific point along the thread.

## 6.2 Theoretical model

---

Following the model in Figure 6.2.b that indicates the temperatures and the potentials in the junctions, it is possible to combine equations 6.2 and 6.3. Assuming to use a voltmeter with high impedance,  $i_1 = i_2 \approx 0$ , is possible to extract the  $V_j$  expression (potential at the junction) from equation 6.2 and insert it into equation 6.3. Then, the final formula for the generated  $V_0$  with a temperature difference  $T_H - T_C$  is:

$$V_0 = \left( \frac{\sigma_{2i} S_{2i} (\varepsilon_{21} - \varepsilon_1) + \sigma_{2o} S_{2o} (\varepsilon_{2o} - \varepsilon_1)}{\sigma_{2i} S_{2i} + \sigma_{2o} S_{2o}} \right) (T_H - T_C) \quad (6.4)$$

expressed as a function of the materials' conductivities, sections, and Seebeck coefficients. Rewriting as a function of the resistances ( $R = \rho l / S = l / \sigma S$ ), it became:

$$V_0 = \left( \frac{R_{2o} (\varepsilon_{21} - \varepsilon_1) + R_{2i} (\varepsilon_{2o} - \varepsilon_1)}{R_{2o} + R_{2i}} \right) (T_H - T_C). \quad (6.5)$$

Using this framework it is possible to theoretically combine several materials to find the best configuration representing a trade-off between thermoelectric voltage and fabrication feasibility. This formula reports the maximum theoretical value of the thermopower of a thermocouple with the arrangement present in point (2) and schematized by Figure 6.2.b. As it is well-known, the thermocouples are an established device to measure temperature but the work here presented has not the pretension to develop a more precise or accurate measurement system. It attempts to use the inverse mechanism to achieve a novel thermoelectric textile generator that can produce a thermopower and integrate them in a fast and easy way directly on textile during their manufacturing. Realizing a textile single-yarn with a thermoelectric generation feature would represent a breakthrough in the wearable and electronic textile world.

The first step to applying the mathematical model result is to consider various metal materials (constantan, i.e., a Ni-Cu alloy, nickel, carbon, stainless steel, copper, silver) arranged in different dispositions to extract the theoretical thermopower. Figure 6.2.e shows the results exploiting the most straightforward configuration (1) between stainless steel and the various materials. These values are calculated using the physical constants  $\sigma$  and  $\varepsilon$  from the solid-state materials, but it is known that in the textile version (like coating a yarn with a particular metal), the values can change.

## 6.2 Theoretical model

More complex geometry, achievable by exploiting electrochemical or physical deposition methods, consists of the combination of three materials (configuration 2). Segment number one comprises a single conductive layer, while segment two is a core-shell structure. Figure 6.2.f reports the case in which segment one is stainless steel while segment 2 consists of all the different combinations of the materials proposed.

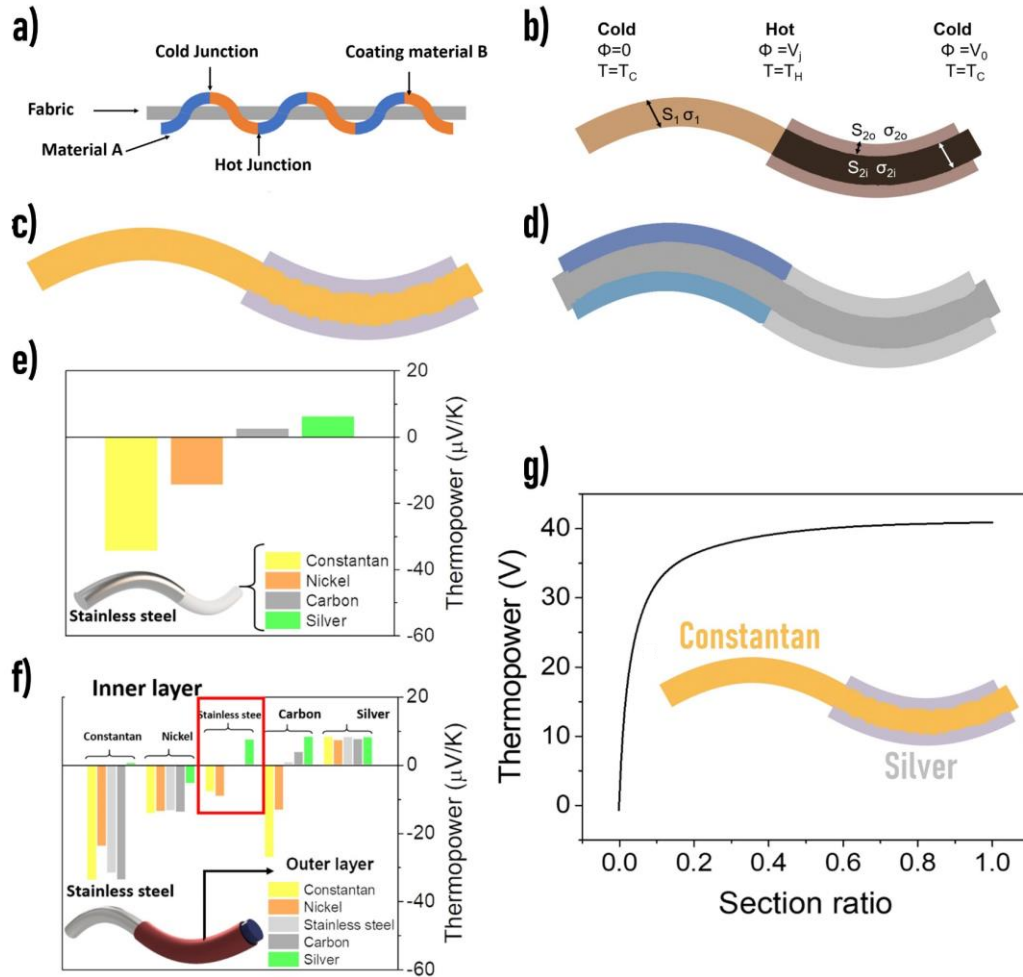


**Figure 6.2:** a) Scheme of the textile thermogenerator fibre sewn in a fabric. b) Illustration of a textile-thread formed by two different material connected together, with the right side covered by a third material. The middle junction has a different temperature respect to the extremities. e) Theoretical thermopower generated by all the combination of stainless steel yarn with the other materials. f) Thermopower calculated exploiting the third configuration. The ratio between the inner and outer section is chosen to be 0.14. Combinations with stainless steel fixed on one segment. g) Trend of the thermopower versus the section ratio of a thermocouple composed by a single constantan yarn as core, and a silver layer onto the second segment (configuration 3).

This figure also reports that the particular case (configuration 3) corresponds to the inner layer similar to the one present in the first segment (circle in red). It is possible to highlight that all the combinations using constantan present a higher thermopower and make this alloy a perfect candidate for developing textile thermoelectric generators. In this view, Figure 6.2.g shows the theoretical trend for the thermopower ( $V_0$  ( $\mu\text{V}/\text{K}$ )) versus the section ratio for a thermocouple made using configuration 3 with a constantan core and a silver coating on the shell.

### 6.2.1 Preliminary results

As a first validation of the theoretical framework developed so far, the first trial is done by realizing thermocouples combining metallic wire and yarns. A hotplate and a Peltier cooling system maintain the desired temperature difference between the textile thermocouple junction, and two commercial k-type thermocouples measured the real difference. The source meter Keithley 2600 acquires the sample's voltage signal generated through the sample. Figure 6.3.a shows the scheme of the set-up. Furthermore, a potentiometer is employed as the load sample to estimate the power produced by a series of multiple thermocouples connected together.

The main results of the thermovoltage reported in Figure 6.3.b from the connection of metal wire and textile yarn gave promising evidence about the feasibility of a final prototype. Combining a constantan wire with carbon and copper wire, or stainless steel and silver yarns results in a flexible, stable, and knittable system with thermovoltage sufficiently high to envisage a textile thermogenerator device. The experimental results are slightly different from the theoretical one, and it could be associated with the lower thermo- and electrical- conductance of textile samples, the custom connection between the materials and the unstable environment. These issues are well-known, and suitable protocols are still under implementation to enforce acquired data's reliability.

The values of the thermovoltage generated by a temperature difference between the top and bottom side of a fabric in which the textile thermogenerator thread is sewn are: Cst-Cu:  $24 \mu\text{V}/\text{K}$ , Cst-SS:  $52 \mu\text{V}/\text{K}$ ; Cst-C:  $37 \mu\text{V}/\text{K}$ ; Cst-Ag:  $32 \mu\text{V}/\text{K}$ . Moreover, a series of three thermocouples of Cst - SS is tested (Figure 6.3.c), and it shows the most important result that the final thermovoltage generated is directly proportional to the number of thermocouples (Figure 6.3.d). Finally, a measure connecting the thermopile with known resistances is made to determine the device's effective power. Applying a constant temperature difference of  $3\text{K}$  between the two faces of the fabric, the typical power plot is reported in Figure 6.3.e as a function of the flowing current. The maximum power value is strictly related to the internal resistance and the thermovoltage generated. The total amount of power per couple is  $0.2\text{nW}$  that, a part of its still low absolute value, is a significant step

### 6.3 Organic-inorganic textile thermogenerator device

forward compared to previously reported values for this type of thread-like thermogenerators.<sup>580,581</sup>

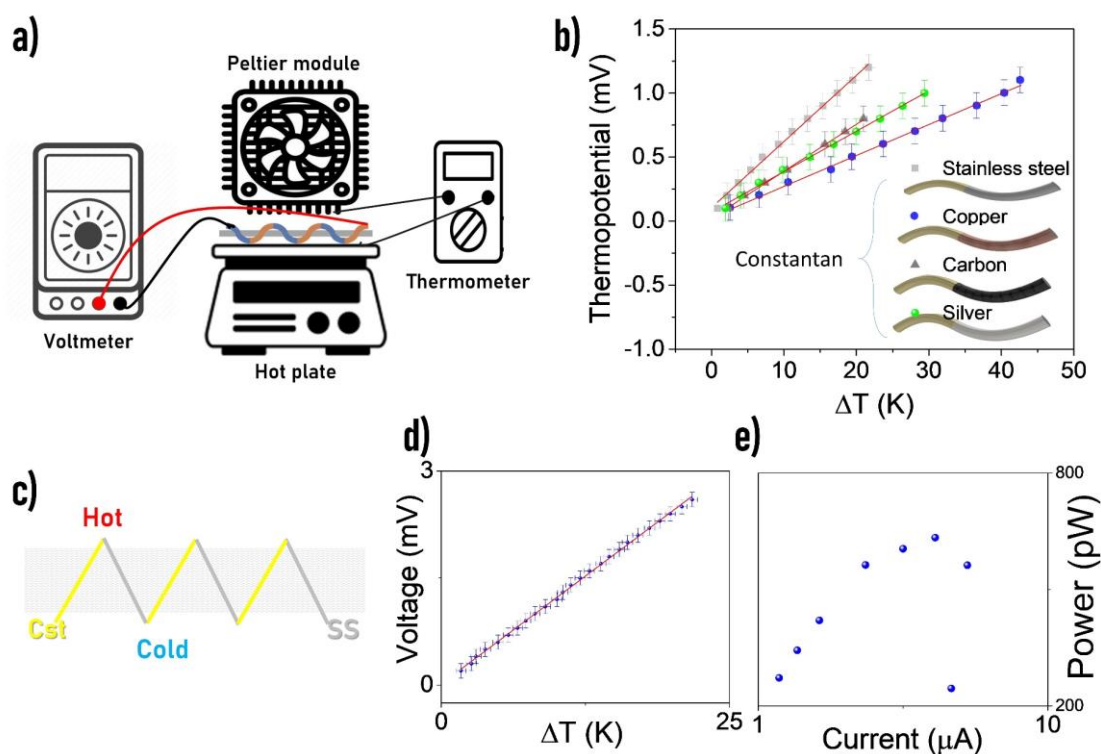


**Figure 6.3:** a) Schematic illustration of the experimental set-up for the textile thermoelectric generator. b) Experimental result for the measured voltage generated by the difference in temperature between fabric's top and bottom side. d) Simplified scheme of a thermopile with three junctions of constantan and stainless steel, and its thermopower (e) and absorbed power (f).

### 6.3 Organic-inorganic textile thermogenerator device

In order to develop a textile single-thread thermogenerator formed by a single yarn that can be sewn and integrated into a garment, the fourth configuration is also studied, combining organic semiconductor and inorganic semiconducting materials. The main idea is to coat a textile yarn with semiconducting polymers and then deposit onto it a periodical sequence of two different inorganic semiconducting materials with optimum thermoelectric properties.

### 6.3.1 Fabrication

In the present case, a polyester thread is coated with a conductive ink of PEDOT:PSS in the Clevious PH100 formulation plus 10% w/w of polyethylene glycol to enhance the resistance to cracks and delamination. The conductive mixture is warmed up in the oven at 70°C to increase the solution viscosity and allow a roll-to-roll-like deposition over the yarn (see section 2.3.1.3).

The thermoelectric materials used to harvest energy from the temperature difference along the thread are Bismuth telluride ( $\text{Bi}_2\text{Te}_3$ ) and Antimony telluride ( $\text{Sb}_2\text{Te}_3$ ), two of the most common thermoelectric materials used to realize solid-state thermocouples (see paragraph 2.2.7 for a detailed description). For this scope, they are adjacently electrodeposited onto the polyester-PEDOT:PSS yarn so that the junction and the extremities of a single thermocouple are kept at two different temperatures, a necessary condition to generate a potential difference by thermoelectric effect. Several parameters are varied and studied to deposit onto the PEDOT:PSS a metal layer with the required structure and stoichiometric coefficients. Electrolyte solutions based on HCl and  $\text{HNO}_3$  with different molarity are investigated, changing, in addition, the concentration of precursors (like Tellurium dioxide - $\text{TeO}_2$ , Bismuth (III) nitride - $\text{Bi}(\text{NO}_3)_3$ , Antimony (III) oxide - $\text{Sb}_2\text{O}_3$ , and Antimony trichloride -  $\text{SbCl}_3$ ), the deposition time and potential. SEM images and EDX spectrum allow the analysis of all the various samples realized by tuning all the possible variables, and the final electrolyte solution and procedure are reported in Table 6.1 both for  $\text{Bi}_2\text{Te}_3$  and  $\text{Sb}_2\text{Te}_3$ .

**Table 6.1:** Electrolyte solution composition and parameters for the electrochemical deposition of  $\text{Bi}_2\text{Te}_3$  and  $\text{Sb}_2\text{Te}_3$  onto polyester/PEDOT:PSS yarns. In both cases, the reference and counter electrodes are Ag/AgCl and Pt wire, respectively.

	<b>Bismuth Telluride (<math>\text{Bi}_2\text{Te}_3</math>)</b>	<b>Antimony Telluride (<math>\text{Sb}_2\text{Te}_3</math>)</b>
<b>Method/Potential</b>	Potentiostatic: -300mV	Potentiostatic: -500mV
<b>Electrolyte</b>	0,35 M HCl	2,5 M HCl
<b>Precursor</b>	14mM $\text{TeO}_2$ 11mM $\text{Bi}(\text{NO}_3)_3$	8,5mM $\text{TeO}_2$ 6,5M $\text{SbCl}_3$
<b>Time</b>	15 minutes	15 minutes

### 6.3 Organic-inorganic textile thermogenerator device

Figure 6.4.a shows a picture of the electrochemical cell employed to deposit the thermoelectric material onto the conductive textile yarns, while Figure 6.4.b reports an optical image of the polyester yarn electrochemically coated with  $\text{Bi}_2\text{Te}_3$  onto PEDOT:PSS. In addition, Figure 6.4.b-c reports the SEM image and the EDX analysis for  $\text{Bi}_2\text{Te}_3$ , while Figure 6.4.e-f for  $\text{Sb}_2\text{Te}_3$  thread realized using the best deposition parameters described in Table 6.1. Both images show that the coating is all-over the entire surface of the yarns and create an additional thick conductive layer.

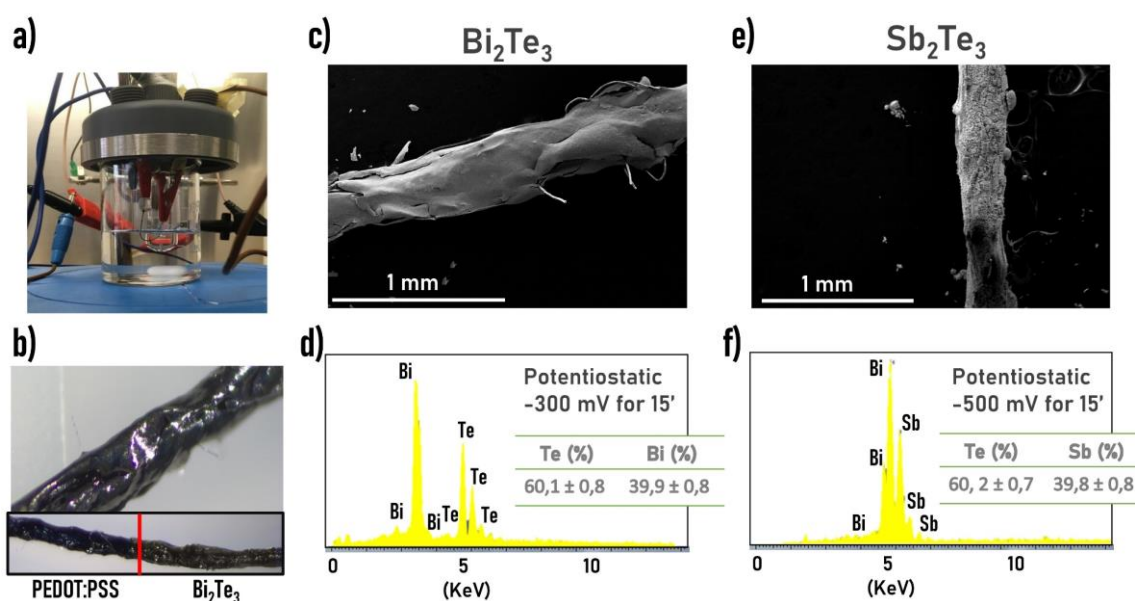


**Figure 6.4:** a) Picture of the electrochemical cell used to deposit metal layer onto Polyester/PEDOT:PSS. b) Optical image of a polyester thread cover with  $\text{Bi}_2\text{Te}_3$ . The inset shows on the left the thread covered only with PEDOT:PSS, while on the right the coating with  $\text{Bi}_2\text{Te}_3$  using the best parameters. SEM images and EDX analysis of yarns coated with c-d)  $\text{Bi}_2\text{Te}_3$  and e-f)  $\text{Sb}_2\text{Te}_3$ . Tables report the ratio of the materials highlighting the agreement with the desired material structure.

#### 6.3.2 Mathematical model

The mathematical framework presented in the previous paragraph can be slightly modified in order to describe the fourth configuration where three different materials are involved: one in the internal, or core, part and the others two cover it periodically so that they are in close contact, as reported by the schemes in Figure 6.5.a-b. Equations 6.2 and 6.3 are rewritten to take into account that the conductive core material is the same (subscript 1), in this case PEDOT:PSS, and the shell is composed of two materials ( $\text{Bi}_2\text{Te}_3$  and  $\text{Sb}_2\text{Te}_3$ ) (subscript 2 and 3). The new configuration can then be described by:

$$V_0 = \left( \frac{\sigma_1 S_1 \sigma_2 S_2 (\varepsilon_1 - \varepsilon_2) + \sigma_1 S_1 \sigma_3 S_3 (\varepsilon_3 - \varepsilon_1) + \sigma_3 S_3 \sigma_2 S_2 (\varepsilon_3 - \varepsilon_2)}{(\sigma_1 S_1 + \sigma_2 S_2) (\sigma_1 S_1 + \sigma_3 S_3)} \right) (T_H - T_C) \quad (6.5)$$

where  $\sigma$ ,  $\varepsilon$  and  $S$  are the conductivity, Seebeck coefficient and section of the three materials, and  $T_H$  and  $T_C$  are the hot and cold junction temperatures.

This expression is more complicated than the other one, but reasonable assumption allows to simplify its form. After writing it using the resistance per unit length, which is the easiest physical parameter accessible from a direct measure, it is possible to assume that the resistances of the outer materials are the same ( $R_2=R_3=R$ ). Introducing the variable  $x=R_1/R$ , that is the ratio between the internal and the external resistances, the final expression is:

$$V_0 = \frac{x}{(1+x)} (\varepsilon_3 - \varepsilon_2) (T_H - T_C) = k(x) (\varepsilon_3 - \varepsilon_2) (T_H - T_C) \quad (6.6)$$

with  $k(x)$  is the limited function reported in the graph of Figure 6.5.c The  $V_0$  thermopower is the potential difference generated by a single thermocouple where the temperature difference between the junction and the extremities is  $T_H-T_C$ . The inset in Figure 6.5.b schematizes the electrical resistance distribution, useful to extract the parameter  $x$  to compute the maximum  $V_0$ . After the deposition steps, a conductive polyester yarn long ( $4.0 \pm 0.1$ ) cm changes its resistance from  $R_{PEDOT:PSS} = (800 \pm 10) \Omega$ , where only PEDOT:PSS is present, to  $R_{coating} = (120 \pm 8) \Omega$ , when both metals are electrodeposited.

This means that assuming an equal contribution to the final resistance from both metal layers, the  $R$  value is  $(70 \pm 3) \Omega$ . From this value and the ones reported in the inset of Figure 6.5.c, it is possible to estimate the maximum thermovoltage  $V_0 = (140 \pm 7) \mu V K^{-1}$  for a thermocouple with the fourth configuration made by PEDOT:PSS,  $Bi_2Te_3$  and  $Sb_2Te_3$  in the ideal geometry modelled by equation 6.5.

#### 6.3.3 First results and further perspectives

Different samples are realised and characterised to measure the thermopower to prove the feasibility of this new type of textile thermogenerators. After the three fabrication steps, deposition of PEDOT:PSS, electrodeposition of  $Bi_2Te_3$  and  $Sb_2Te_3$ , the samples are characterised with the same set-up reported in Figure 6.3.a. The potential generated by one thermocouple is measured after the incremental variation of  $\Delta T$  between the junction (centre of the yarn) and the extremities, kept at the same temperature. Figure 6.5 d-e report on the potential trend versus time and the calibration curve to extract the thermopower coefficient of the thermocouple via a linear fit. The potential increment with  $\Delta T$  follow a perfect linear trend, but the absolute value is lower than the theoretical expectation.

### 6.3 Organic-inorganic textile thermogenerator device

---

This discrepancy could be related to several factors that are still under investigation. For example, the values for the Seebeck coefficients of the thermoelectric materials are the ones measured for solid-state and crystalline material. Although having the same stoichiometric ratio, it has to be considered that the layer of  $\text{Bi}_2\text{Te}_3$  and  $\text{Sb}_2\text{Te}_3$  can behave differently when electrodeposited on a textile thread. Another hypothesis that will be evaluated with a more detailed crystalline analysis by X-ray photoelectron spectroscopy, concern the thermoelectric nature of Bismuth Telluride. The deposited  $\text{Bi}_2\text{Te}_3$  structure, instead of being an n-type with a negative Seebeck coefficient, could be instead p-type presenting, therefore, a positive Seebeck coefficient that strongly decreases the theoretical value.<sup>582,583</sup> The thermoelectric properties of  $\text{Bi}_2\text{Te}_3$  strictly depend on the method used to deposit or synthesize the material.<sup>584</sup> Moreover, as reported by recent studies,<sup>585</sup> subjecting the samples to prolonged annealing treatments at high temperature, low pressure and in the presence of Argon could improve the device's performance. This, and other attempts will be the subject of further studies to improve the performance of these devices. However, it has been shown that they are potentially able to convert the thermal energy into an electrical potential which can charge, for example, textile supercapacitors.<sup>573,573,586,587</sup>

To investigate the consistency of the device reported so far, two different thermocouples are realized in series along the same conductive thread with the aim to form a simple thermopile (Figure 6.5.f). The characterization of the potential generated due to temperature variation shows a perfect linear correlation regardless of the mathematical sign of  $\Delta T$ . This aspect is highlighted by the negative value that the potential can assume when the junction has a lower temperature than the one present at the extremities of the two-fold thermopile. Calculating the thermopower through the linear fit allows one to extract a value for  $V_0$  that is double the one for the single thermocouple. This result paves the way for the future integration of multiple units in series. A measure of the power generated by the device is realized by measuring the current flowing on different load resistors when the textile thermopiles supply the circuit. The acquired curves are reported in Figure 6.5.g. By changing the constant  $\Delta T$  applied at the extremities of the device, different curves are obtained that present an increment in the maximum power value when the temperature increases. The maximum measured power allows obtaining the internal resistance of the device through the formula  $R_i = (V_0\Delta T)^2/4P_{max}$ . The value of  $R_i$  in the case of the two-fold thermopile results to be about 900  $\Omega$ , higher than the value expected. Since the internal resistance is a fundamental parameter to increment the power supplied by the thermogenerator device, solving the problem of this disagreement on the internal resistance is fundamental to proceed with further developments. Finally, it is worth mentioning that connecting several thermopiles in parallel makes it possible to increase the value of current that can flow on a load and, consequently, the power generated.

### 6.3 Organic-inorganic textile thermogenerator device

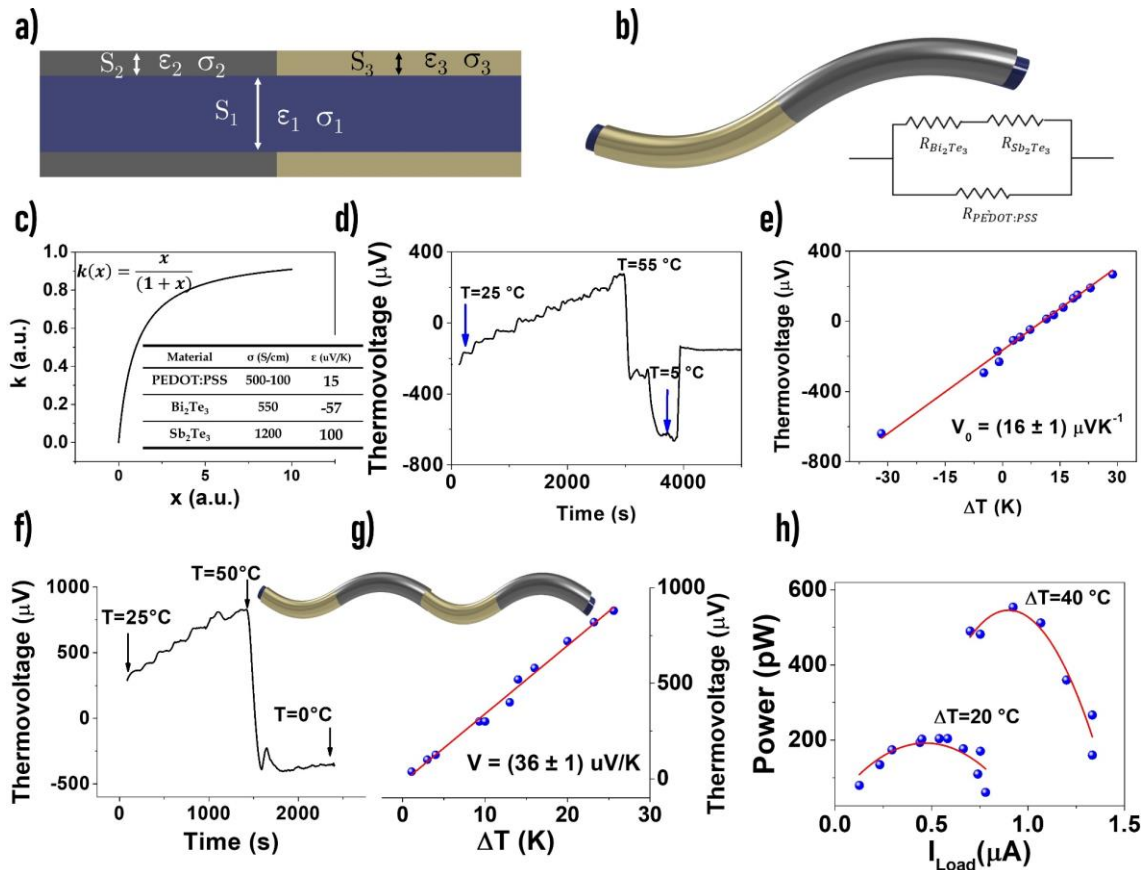


**Table 6.5:** a) Scheme of the fourth configuration with the physical parameters. b) Image of the final thermocouple structure with PEDOT:PSS as core material and  $\text{Bi}_2\text{Te}_3$  and  $\text{Sb}_2\text{Te}_3$  coated onto it. The inset shows the resistance arrangement. c) Graph of the  $k$  parameter versus the ratio between the internal and external resistance. The table reports the constants used in the mathematical model. d) Thermopotential versus time for one thermocouple when the  $\Delta T$  ( $T_{\text{centre}} - T_{\text{extremities}}$ ) varies. e) Linear trend of the thermocouple with  $\Delta T$ ; the slope is the thermopower. f-g) Characterisation curve for the thermocouples in series, highlighting the double value of the thermopower. h) Extraction of the generated power using a circuit with a variable load resistor.

In summary, this new textile device made on a textile single-thread by double deposition of an organic polymers semiconductor and two inorganic semiconductors represents a potential example for creating a system capable of collecting energy from the difference in temperature between the wearer's body and the surrounding, and thus power other textile sensors. Despite the further developments necessary to confirm the manufacturing technique and solve the problem of power loss due to high internal resistance, they represent a valid proof of concept for a new wearable, flexible and easy-to-integrate device that can recycle the lost thermal energy.



# Conclusion

This section will conclude the study by summarising the key research findings and results in relation to the smart textile sensors for healthcare monitoring and discussing the contribution and value thereof. It will also report the limitations of the research and propose opportunities for future studies.

This work aimed to investigate the possibility of realising a wearable, fully textile platform endowed with different types of sensors directly located on thread or fabric substrate to monitor the physiological and biometric parameters of the wearer. The physical and chemical sensors developed and reported in the previous chapter represent valid examples of a technological advancement through the achievement of wearable systems that are completely realised on a textile. This thesis reports, in detail, various important results achieved during the doctoral years, which are published in thirteen different publications. The resulting chapters of this work present the theoretical working principles, fabrication techniques, and characterisation methods for different physical and chemical textile sensors. The main conclusions can be summarised as follows:

- 1) The textile pH level and chloride concentration sensors in sweat are valuable tools for noninvasive monitoring of physiological parameters in humans. These devices are developed starting from a two-terminal pH and  $[\text{Cl}^-]$  sensors realised on glass substrates to fully comprehend the new electrochemical-gating effect originating from a transistor-like geometry and able to combine the intrinsically amplified response with a simple two-terminal electrical connection.

This results in a new composite material based on Ag/AgCl nanoparticles and PEDOT:PSS being designed, synthesised and exploited to fabricate  $[\text{Cl}^-]$  sensors inspired by organic electrochemical transistors. Ag/AgCl gate electrode is intrinsically integrated into the semiconducting polymer in the form of nanoparticles. The analytical signal is the flowing current in the composite polymer, and its variation is proportional to the logarithm of  $\text{Cl}^-$  concentration in the wide range  $10^{-4}$  to 1 M, with a limit of detection of 50  $\mu\text{M}$ , and a best sensitivity of  $(60 \pm 2) \cdot 10^{-3} \text{ dec}^{-1}$ .

The two-terminal pH sensor on rigid substrate exploits the chemiresistor-like geometry and the highly selective transduction due to the pH-sensitive bilayer organic structure (PEDOT:PSS/PEDOT:BTB) to achieve a label-free detection without the need for ion-selective membranes or rigid electrodes. The robustness of potentiometric-like transduction with the simple two-point probe device allows a sensor sensitivity of  $(8.3 \pm 0.2) \cdot 10^{-3} \text{ pH}^{-1}$  in the pH range from 2 to 7. By exploiting this new concept of

electrochemical transduction, a new example of multi-analyte textile platform is reported for continuous detection of pH and chloride in human sweat. Each sensor is a two-terminal device formed by a single textile thread, working in a liquid solution without reference or gate electrode. The sensitive yarns are fabricated utilising commercial natural and synthetic fibres, coated with the semiconducting polymer and functionalised to selectively detect pH level and  $[\text{Cl}^-]$  in artificial perspiration. The sensors show stability, repeatability, and reproducibility for all of the studied yarns. There are no significant differences between the fibres in terms of the overall performance, underlining the possibility of using the proper yarn in the final application. Their ability to work in parallel, without interfering and changing sensitivity, introduces the possibility for simultaneous and real-time pH level and  $[\text{Cl}^-]$  monitoring in body fluids. The sensitivities of  $(75 \pm 2) 10^{-3} \text{ dec}^{-1}$  and  $(17 \pm 3) 10^{-3} \text{ pH}^{-1}$  for the  $[\text{Cl}^-]$  and pH textile sensors, respectively, are in agreement, or even higher, with those of the devices realised on glass substrates.

- 2) The PEDOT:BTB compound employed as sensitive material in the two-terminal device for the detection of pH in sweat shows a limited linear trend up to pH 7. In order to extend the sensitive pH range to further work with other biofluids, as wound exudate, a new combination of the soft organic semiconductor PEDOT:PSS with the metal oxide potentiometric transducer IrOx has been introduced for the first time. It is demonstrated that the intimate interaction between IrOx particles and PEDOT:PSS creates a pH sensing feature that relies on electrochemical gating, allowing the fabrication of a two-terminal device. It benefits from the robustness of a potentiometric transduction regardless of its chemoresistor-like geometry and allows replication of the solid-state probe's fabrication procedure with textile substrates for flow and noninvasive analyses of pH level in a wound bed. The extensive studies of the device on a rigid substrate and the comprehension of the parabolic trend of the current with the pH value allows the realisation of a smart wound dressing operating with a small and continuous flow amount of artificial exudate. No statistical differences in analytical performances are found in the pH range relevant to wound healing (pH: 6–9) between the devices fabricated on glass and on fabric during a dynamic flow analysis using simulated wound exudate. The reported normalised sensitivity in the linear and relevant trend of the two-terminal sensor is  $(59 \pm 4) \mu\text{A pH}^{-1}$ , almost one order of magnitude higher than that reported using dye-doped PEDOT. Additionally, main advancements are achieved concerning the state-of-the-art in textile pH sensors that are mostly based on conventional potentiometric setup using PANi semiconductor. For example, the exclusion of a reference electrode and the adaptability to textile and flexible substrates without affecting the device reliability represents an important progress in smart textiles for biomedical applications.

Another example of textile sensors able to give information about the healing process of a wound has been developed combining commercial fabrics substrates regularly used for wound care and PEDOT:PSS. The screen-printed organic polymer on various fabrics with a precise pattern allows the design and implementation of a smart wound dressing that is able to monitor the wound's moisture conditions in real-time. Tunable features and performance can be obtained by combining the textile materials according to the wound type. For example, when a low amount of exudate is present, the gauze Rayon with the Absorbation layer C (cotton) represents the best combination to follow the wound healing stage. On the contrary, to observe the healing phase of a highly exuding wound (i.e., blisters or chronic wounds), gauze PET and Absorbation layer PE result in a more appropriate combination as it can store a large amount of exudate. This proves the possibility of connecting the smart textile patch to an RFID and NFC interface to passively monitor the wound moisture with the smart, disposable, and low-cost bandage in real-time.

- 3) This work also investigates textile physical sensors with particular attention to the effects of the addition of ethylene glycol to PEDOT:PSS conductive polymers and the fabric elastic features on the performance of textile pressure sensors. The sensing element consists of a PEDOT:PSS conductive ink deposited onto the fabric and the electrical connections realised with a conductive thread. The presence of EG decreases the electrical resistance of the textile sample up to one order of magnitude, and influences the piezoresistive properties and textile pressure sensor response. Samples with EG enhance their sensitivity in the low and medium pressure range (up to 50 kPa), while pristine PEDOT:PSS ink allows the sensor to cover a broader range of pressures (up to 100 kPa) but with a lower sensitivity. This behaviour can be ascribed to two different contributions related to fabric thickness variations during compression and the intrinsic piezoresistive features of the PEDOT:PSS film. In addition, the dynamic operation mode of such textile pressure sensors is reported exploiting four types of textile substrates with different materials (i.e., natural and synthetic fibres) and weaving structures. The elastic properties of the substrate have a relevant impact on the textile sensor performance: fabrics with high elastic properties and wide dynamic strain range during compression show higher sensitivities than the fabrics with poor elastic behaviour. However, it has been shown that this second type of substrate can be employed to realise textile pressure sensors with high reliability and stability in dynamic operation mode at the expense of a narrow strain dynamic range and limited sensitivity. As a result, implementing a sensorised glove with textile pressure sensors results in a conformable, unobtrusive, and low-cost device. The linear pressure range and sensitivity can be tuned according to the specific application varying conductive formulation and/or the textile material.

Another physical sensor has been reported involving the realisation and characterisation of a novel fully-textile, real-time, and direct X-ray detector (TX-RD). This device is formed by sewing together differently functionalised fabrics: cotton fabrics with screen printed PEDOT:PSS patterns, as electrodes, and silk-satin fabric embedded with perovskite crystals as the photo-active layer of the detector absorbing the X-ray radiation. The response to X-rays has been assessed to scale linearly with increasing dose rates and to be stable for a wide range of X-ray energies (40 kVp - 150kVp) and dose rates (from 500  $\mu\text{Gy s}^{-1}$  up to 8.0  $\text{mGy s}^{-1}$ ). The best sensitivity obtained by this new class of textile detectors is  $(12.2 \pm 0.6) \mu\text{C Gy}^{-1} \text{cm}^{-2}$  with a LoD down to 3  $\mu\text{Gy s}^{-1}$ . The low operating bias (down to 1V) and stable response over a period of twenty days, coupled with good flexibility and bendability behaviour, demonstrate the applicability of the aforementioned TX-RD as a wearable device. Additionally, the stacked configuration allows a scale up to a pixelated detector matrix with good reproducibility among different pixels. Finally, the employment of natural fabrics, such as cotton and silk-satin, represents an extra value in terms of recyclability, comfort, bio-compatibility, and breathability for the effective application of these new sensors directly onto smart garments.

- 4) As a further step toward achieving a fully textile wearable platform with several sensors, a new method, exploiting the thermoelectric effect, has been proposed to harvest the necessary energy to power the sensors. A single polyester thread coated entirely with PEDOT:PSS, and covered successively with alternating electrodeposited Bismuth Telluride and Antimony Telluride, led to a sewable textile thermocouple with a thermovoltage of  $V_0 = (16 \pm 1) \mu\text{VK}^{-1}$ . The temperature difference between the various junctions of a thermopile shows the scalability of the thermovoltage with the number of couples and the possibility of supplying power up to 600 pW with a  $\Delta T$  of 40°C when only two thermocouples are present on the thread. This pioneering work proves the feasibility of the fabrication technique and working principle, but further efforts are needed to enhance the figures of merit for such devices.

The main advantage of the textile sensors developed in this thesis is the capability of integration into clothes, but this strictly requires two main properties: wearability and washability. These two aspects need to be discussed and evaluated in order to further develop textile sensors. An encapsulation layer or protective coatings can also help to address this issue. Conformability is an essential requirement for wearable and on-body sensing devices to achieve the so-called *wear and forget* functionality. The resilience to mechanical stress should be investigated with more detail, focusing on bending tests, stress-strain, and stretchability studies. Additionally, a complete textile system includes the textile sensor and connections, readout electronics, and power supply. A common way to connect

## Conclusion

---

sensors with electronics includes the soldering of metallic wires, but this process is limited by the high temperature required (up to 280°C), which may damage most commercial fabrics. Alternative methods include mechanical gripping with rigid poppers, conductive adhesive, or RFID systems, as reported for the smart wound dressing. Furthermore, a critical aspect of wearable textile sensors is data validation, where the main challenges limiting commercialisation include sampling, calibration, selectivity, reliability, and correlation with other biological or biometrical parameters.

In the coming years, further improvements concerning new functionalisations, device structures (i.e., threads, planar fabric, or even 3D textiles), and signal acquisitions will be taken into account to lead the textile sensing field through a technological revolution.



# Bibliography

1. Hatamie, A. *et al.* Review – Textile Based Chemical and Physical Sensors for Healthcare Monitoring. *J. Electrochem. Soc.* **167**, 037546 (2020).
2. Islam, G. M. N., Ali, A. & Collie, S. Textile sensors for wearable applications: a comprehensive review. *Cellulose* vol. 27 6103–6131 (2020).
3. Gualandi, I. *et al.* Textile chemical sensors based on conductive polymers for the analysis of sweat. *Polymers* **13**, 894 (2021).
4. del Agua, I. *et al.* DVS-Crosslinked PEDOT:PSS Free-Standing and Textile Electrodes toward Wearable Health Monitoring. *Adv. Mater. Technol.* **3**, (2018).
5. Mariani, F. *et al.* Advanced Wound Dressing for Real-Time pH Monitoring. *ACS Sens.* **14**, acssensors.1c00552 (2021).
6. Tseghai, G. B. *et al.* PEDOT:PSS/PDMS-coated cotton fabric for ECG electrode. 2020 IEEE International Conference on Flexible and Printable Sensors and Systems (FLEPS) (2020). doi:10.1109/FLEPS49123.2020.9239526.
7. Pani, D. *et al.* Fully Textile, PEDOT:PSS Based Electrodes for Wearable ECG Monitoring Systems. *IEEE Trans. Biomed. Eng.* **63**, 540–549 (2016).
8. Bihar, E. *et al.* Fully Printed Electrodes on Stretchable Textiles for Long-Term Electrophysiology. *Adv. Mater. Technol.* **2**, 1600251 (2017).
9. Husain, M. D., Kennon, R. & Dias, T. Design and fabrication of Temperature Sensing Fabric. *J. Ind. Text.* **44**, 398–417 (2014).
10. Possanzini, L., Tessarolo, M., Mazzocchetti, L., Campari, E. G. & Fraboni, B. Impact of fabric properties on textile pressure sensors performance. *Sens. Switz.* **19**, (2019).
11. Tseghai, G. B., Malengier, B., Fante, K. A. & Langenhove, L. Van. PEDOT:PSS/PDMS-Coated Cotton Fabric for Strain and Moisture Sensors †. (2020) doi:10.3390/xxxxx.
12. Mariani, F. *et al.* Design of an electrochemically gated organic semiconductor for pH sensing. *Electrochem. Commun.* **116**, 106763 (2020).
13. Possanzini, L. *et al.* Textile sensors platform for the selective and simultaneous detection of chloride ion and pH in sweat. *Sci. Rep.* **10**, 17180 (2020).
14. Wang, L. *et al.* Weaving Sensing Fibers into Electrochemical Fabric for Real-Time Health Monitoring. *Adv. Funct. Mater.* **28**, (2018).
15. Hardianto, H., Malengier, B., De Mey, G., Van Langenhove, L. & Hertleer, C. Textile yarn thermocouples for use in fabrics. *J. Eng. Fibers Fabr.* **14**, 155892501983609 (2019).
16. Lund, A., Tian, Y., Darabi, S. & Müller, C. A polymer-based textile thermoelectric generator for wearable energy harvesting. *J. Power Sources* **480**, 228836 (2020).
17. Zhao, Z. *et al.* Machine-washable and breathable pressure sensors based on triboelectric nanogenerators enabled by textile technologies. *Nano Energy* **70**, 104528 (2020).
18. Jeerapan, I., Sempionatto, J. R., Pavinatto, A., You, J. M. & Wang, J. Stretchable biofuel cells as wearable textile-based self-powered sensors. *J. Mater. Chem. A* **4**, 18342–18353 (2016).
19. Lv, J. *et al.* Sweat-based wearable energy harvesting-storage hybrid textile devices †. *Energy Env. Sci* **11**, 3431 (2018).
20. Nuramdhani, I. *et al.* Charge-Discharge Characteristics of Textile Energy Storage Devices Having Different PEDOT:PSS Ratios and Conductive Yarns Configuration. *Polymers* **11**, 345 (2019).
21. Ashton, K. That ‘Internet of Things’ Thing. *RFID Journal* (2009).
22. Gao, W. *et al.* Fully integrated wearable sensor arrays for multiplexed in situ perspiration analysis. *Nature* **529**, 509–514 (2016).
23. Windmiller, J. R. & Wang, J. Wearable Electrochemical Sensors and Biosensors: A Review. *Electroanalysis* **25**, 29–46 (2013).

## Bibliography

---

24. Seshadri, D. R. *et al.* Wearable sensors for monitoring the physiological and biochemical profile of the athlete. *Npj Digit. Med.* **2**, (2019).
25. Tessarolo, M. *et al.* Adaptable pressure textile sensors based on a conductive polymer. *Flex. Print. Electron.* **3**, (2018).
26. Park, J. *et al.* Giant Tunneling Piezoresistance of Composite Elastomers with Interlocked Microdome Arrays for Ultrasensitive and Multimodal Electronic Skins. *ACS Nano* **8**, 4689–4697 (2014).
27. Wang, X., Gu, Y., Xiong, Z., Cui, Z. & Zhang, T. Silk-Molded Flexible, Ultrasensitive, and Highly Stable Electronic Skin for Monitoring Human Physiological Signals. *Adv. Mater.* **26**, 1336–1342 (2014).
28. Wang, Q., Jian, M., Wang, C. & Zhang, Y. Carbonized Silk Nanofiber Membrane for Transparent and Sensitive Electronic Skin. *Adv. Funct. Mater.* **27**, 1605657 (2017).
29. Schwartz, G. *et al.* Flexible polymer transistors with high pressure sensitivity for application in electronic skin and health monitoring. *Nat. Commun.* **4**, 1859 (2013).
30. Tee, B. C.-K., Wang, C., Allen, R. & Bao, Z. An electrically and mechanically self-healing composite with pressure- and flexion-sensitive properties for electronic skin applications. *Nat. Nanotechnol.* **7**, 825–832 (2012).
31. Choong, C.-L. *et al.* Highly Stretchable Resistive Pressure Sensors Using a Conductive Elastomeric Composite on a Micropyramid Array. *Adv. Mater.* **26**, 3451–3458 (2014).
32. Tessarolo, M., Gualandi, I. & Fraboni, B. Recent progress in wearable fully textile chemical sensors. *Adv. Mater. Technol.* **3**, (2018).
33. Carvalho, H., Yao, Y. & Gonçalves, L. M. Flexible force sensors for e-textiles. *IOP Conf. Ser. Mater. Sci. Eng.* **254**, 072007–072007 (2017).
34. Zhou, B., Sundholm, M., Cheng, J., Cruz, H. & Lukowicz, P. Measuring muscle activities during gym exercises with textile pressure mapping sensors. *Pervasive Mob. Comput.* **38**, 331–345 (2017).
35. Lin, X. & Seet, B.-C. Battery-Free Smart Sock for Abnormal Relative Plantar Pressure Monitoring. *IEEE Trans. Biomed. Circuits Syst.* **11**, 464–473 (2017).
36. Büscher, G. H., Kõiva, R., Schürmann, C., Haschke, R. & Ritter, H. J. Flexible and stretchable fabric-based tactile sensor. *Robot. Auton. Syst.* **63**, 244–252 (2015).
37. Kirthika, S. K., Ponraj, G. & Ren, H. Fabrication and Comparative Study on Sensing Characteristics of Soft Textile-Layered Tactile Sensors. *IEEE Sens. Lett.* **1**, 1–4 (2017).
38. Maziz, A. *et al.* Knitting and weaving artificial muscles. *Sci. Adv.* **3**, e1600327–e1600327 (2017).
39. Kinkeldei, T., Zysset, C., Cherenack, K. H. & Troster, G. A textile integrated sensor system for monitoring humidity and temperature. in *2011 16th International Solid-State Sensors, Actuators and Microsystems Conference* 1156–1159 (IEEE, 2011). doi:10.1109/TRANSDUCERS.2011.5969238.
40. Gualandi, I. *et al.* Textile Organic Electrochemical Transistors as a Platform for Wearable Biosensors. *Sci. Rep.* **6**, 33637–33637 (2016).
41. Gualandi, I. *et al.* Nanoparticle gated semiconducting polymer for a new generation of electrochemical sensors. *Sens. Actuators B Chem.* **273**, 834–841 (2018).
42. Jia, J. *et al.* Conductive Thread-Based Textile Sensor for Continuous Perspiration Level Monitoring. *Sensors* **18**, 3775–3775 (2018).
43. Pani, D. *et al.* Fully Textile, PEDOT:PSS Based Electrodes for Wearable ECG Monitoring Systems. *IEEE Trans. Biomed. Eng.* **63**, 540–549 (2016).
44. Pani, D., Achilli, A. & Bonfiglio, A. Survey on Textile Electrode Technologies for Electrocardiographic (ECG) Monitoring, from Metal Wires to Polymers. *Adv. Mater. Technol.* **3**, 1800008–1800008 (2018).
45. Zhang, Z. *et al.* A Lightweight Polymer Solar Cell Textile that Functions when Illuminated from Either Side. *Angew. Chem. Int. Ed.* **53**, 11571–11574 (2014).
46. Hardianto, H., Mey, G. D., Malengier, B. & Langenhove, L. V. Textile-based thermoelectric generator fabricated from carbon fibers. *J. Ind. Text.* 152808372091068–152808372091068 (2020) doi:10.1177/1528083720910686.
47. Sim, H. J. *et al.* Stretchable Triboelectric Fiber for Self-powered Kinematic Sensing Textile. *Sci. Rep.* **6**, 1–7 (2016).
48. Sun, H., Fu, X., Xie, S., Jiang, Y. & Peng, H. Electrochemical Capacitors with High Output Voltages that Mimic Electric Eels. *Adv. Mater.* **28**, 2070–2076 (2016).
49. Lu, L., Hu, Y. & Dai, K. The advance of fiber-shaped lithium ion batteries. *Mater. Today Chem.* **5**, 24–33 (2017).

## Bibliography

---

50. Kwon, S. *et al.* Weavable and Highly Efficient Organic Light-Emitting Fibers for Wearable Electronics: A Scalable, Low-Temperature Process. *Nano Lett* **18**, 356–356 (2018).
51. Sekar, M., Pandiaraj, M., Bhansali, S., Ponpandian, N. & Viswanathan, C. Carbon fiber based electrochemical sensor for sweat cortisol measurement. *Sci. Rep.* **9**, 1–14 (2019).
52. Zhou, G. *et al.* Highly Sensitive Wearable Textile-Based Humidity Sensor Made of High-Strength, Single-Walled Carbon Nanotube/Poly(vinyl alcohol) Filaments. *ACS Appl. Mater. Interfaces* **9**, 4788–4797 (2017).
53. Wang, R. *et al.* Stretchable gold fiber-based wearable electrochemical sensor toward pH monitoring. *J. Mater. Chem. B* **8**, 3655–3660 (2020).
54. Li, Z. & Wang, Z. L. Air/liquid-pressure and heartbeat-driven flexible fiber nanogenerators as a micro/nano-power source or diagnostic sensor. *Adv. Mater.* **23**, 84–89 (2011).
55. Liu, N. *et al.* Cable-type supercapacitors of three-dimensional cotton thread based multi-grade nanostructures for wearable energy storage. *Adv. Mater.* **25**, 4925–4931 (2013).
56. Gil, I., Fernández-García, R. & Tornero, J. A. Embroidery manufacturing techniques for textile dipole antenna applied to wireless body area network. *Text. Res. J.* **89**, 1573–1581 (2019).
57. Guo, L., Berglin, L. & Mattila, H. Improvement of electro-mechanical properties of strain sensors made of elastic-conductive hybrid yarns. *Text. Res. J.* **82**, 1937–1947 (2012).
58. Yun, Y. J., Hong, W. G., Kim, W. J., Jun, Y. & Kim, B. H. A novel method for applying reduced graphene oxide directly to electronic textiles from yarns to fabrics. *Adv. Mater.* **25**, 5701–5705 (2013).
59. Shim, B. S., Chen, W., Doty, C., Xu, C. & Kotov, N. A. Smart electronic yarns and wearable fabrics for human biomonitoring made by carbon nanotube coating with polyelectrolytes. *Nano Lett.* **8**, 4151–4157 (2008).
60. Gong, W. *et al.* Continuous and scalable manufacture of amphibious energy yarns and textiles. *Nat. Commun.* **10**, 1–8 (2019).
61. Lai, Y.-C. *et al.* Single-Thread-Based Wearable and Highly Stretchable Triboelectric Nanogenerators and Their Applications in Cloth-Based Self-Powered Human-Interactive and Biomedical Sensing. *Adv. Funct. Mater.* **27**, 1604462–1604462 (2017).
62. Choudhary, T., Rajamanickam, G. P. & Dendukuri, D. Woven electrochemical fabric-based test sensors (WEFTS): A new class of multiplexed electrochemical sensors. *Lab. Chip* **15**, 2064–2072 (2015).
63. Kim, S. J. *et al.* High Durability and Waterproofing rGO/SWCNT-Fabric-Based Multifunctional Sensors for Human-Motion Detection. *ACS Appl. Mater. Interfaces* **10**, 3921–3928 (2018).
64. Yin, L. *et al.* A self-sustainable wearable multi-modular E-textile bioenergy microgrid system. *Nat. Commun.* **2021** **12**, 1–12 (2021).
65. Konwar, A. *et al.* Tea-Carbon Dots-Reduced Graphene Oxide: An Efficient Conducting Coating Material for Fabrication of an E-Textile. *ACS Sustain. Chem. Eng.* **5**, 11645–11651 (2017).
66. Xu, Q. B. *et al.* Surface modification by carboxymethyl chitosan via pad-dry-cure method for binding Ag NPs onto cotton fabric. *Int. J. Biol. Macromol.* **111**, 796–803 (2018).
67. Takamatsu, S. *et al.* Direct patterning of organic conductors on knitted textiles for long-term electrocardiography. *Sci. Rep.* **5**, 1–7 (2015).
68. Takamatsu, S. *et al.* Wearable Keyboard Using Conducting Polymer Electrodes on Textiles. *Adv. Mater.* **28**, 4485–4488 (2016).
69. Tunáková, V., Grégr, J., Tunák, M. & Dohnal, G. Functional polyester fabric/polypyrrole polymer composites for electromagnetic shielding: Optimization of process parameters. *J. Ind. Text.* **47**, 686–711 (2018).
70. Bihar, E. *et al.* Fully Printed Electrodes on Stretchable Textiles for Long-Term Electrophysiology. *Adv. Mater. Technol.* **2**, 1600251–1600251 (2017).
71. Dąbrowska, A. K. *et al.* Materials used to simulate physical properties of human skin. *Skin Res. Technol.* **22**, 3–14 (2016).
72. Liu, X., Guo, R., Shi, Y., Deng, L. & Li, Y. Durable, Washable, and Flexible Conductive PET Fabrics Designed by Fiber Interfacial Molecular Engineering. *Macromol. Mater. Eng.* **301**, 1383–1389 (2016).
73. Du, D., Li, P. & Ouyang, J. Graphene coated nonwoven fabrics as wearable sensors. *J. Mater. Chem. C* **4**, 3224–3230 (2016).
74. Tchafa, F. M. & Huang, H. Microstrip patch antenna for simultaneous strain and temperature sensing. *Smart Mater. Struct.* **27**, 065019–065019 (2018).

## Bibliography

---

75. Lou, M. *et al.* Highly Wearable, Breathable, and Washable Sensing Textile for Human Motion and Pulse Monitoring. *ACS Appl. Mater. Interfaces* **12**, 19965–19973 (2020).
76. Lv, J. *et al.* Sweat-based wearable energy harvesting-storage hybrid textile devices †. *Energy Env. Sci* **11**, 3431–3431 (2018).
77. Zhang, J. *et al.* Fast and scalable wet-spinning of highly conductive PEDOT:PSS fibers enables versatile applications. *J. Mater. Chem. A* **7**, 6401–6410 (2019).
78. Tseghai, G. B., Mengistie, D. A., Malengier, B., Fante, K. A. & Van Langenhove, L. PEDOT:PSS-based conductive textiles and their applications. *Sens. Switz.* **20**, 1881–1881 (2020).
79. Onggar, T., Kruppke, I. & Cherif, C. Techniques and Processes for the Realization of Electrically Conducting Textile Materials from Intrinsically Conducting Polymers and Their Application Potential. *Polymers* **12**, (2020).
80. Bashir, T., Ali, M., Cho, S.-W., Persson, N.-K. & Skrifvars, M. OCVD polymerization of PEDOT: effect of pre-treatment steps on PEDOT-coated conductive fibers and a morphological study of PEDOT distribution on textile yarns. *Polym. Adv. Technol.* **24**, 210–219 (2013).
81. Trindade, I. G., Martins, F. & Baptista, P. High electrical conductance poly(3,4-ethylenedioxythiophene) coatings on textile for electrocardiogram monitoring. *Synth. Met.* **210**, 179–185 (2015).
82. Hong, K. H., Oh, K. W. & Kang, T. J. Preparation and properties of electrically conducting textiles by in situ polymerization of poly(3,4-ethylenedioxythiophene). *J. Appl. Polym. Sci.* **97**, 1326–1332 (2005).
83. Mariani, F. *et al.* Design of an electrochemically gated organic semiconductor for pH sensing. *Electrochem. Commun.* **116**, 106763–106763 (2020).
84. Mattana, G. *et al.* Organic electronics on natural cotton fibres. *Org. Electron.* **12**, 2033–2039 (2011).
85. Wang, L. *et al.* Application Challenges in Fiber and Textile Electronics. *Adv. Mater.* **32**, 1–25 (2020).
86. Donoval, M. *et al.* Relation between secondary doping and phase separation in PEDOT:PSS films. *Appl. Surf. Sci.* **395**, 86–91 (2017).
87. Vosgueritchian, M., Lipomi, D. J. & Bao, Z. Highly Conductive and Transparent PEDOT:PSS Films with a Fluorosurfactant for Stretchable and Flexible Transparent Electrodes. *Adv. Funct. Mater.* **22**, 421–428 (2012).
88. Buechley, L. & Eisenberg, M. Fabric PCBs, electronic sequins, and socket buttons: techniques for e-textile craft. *Pers. Ubiquitous Comput.* **13**, 133–150 (2009).
89. Leśnikowski, J. Research on poppers used as electrical connectors in high speed textile transmission lines. *Autex Res. J.* **16**, 228–235 (2016).
90. Li, Q. & Tao, X. M. Three-dimensionally deformable, highly stretchable, permeable, durable and washable fabric circuit boards. *Proc. R. Soc. Math. Phys. Eng. Sci.* **470**, (2014).
91. Siegel, A. C. *et al.* Foldable printed circuit boards on paper substrates. *Adv. Funct. Mater.* **20**, 28–35 (2010).
92. Han, J. W., Kim, B., Li, J. & Meyyappan, M. A carbon nanotube based ammonia sensor on cotton textile. *Appl. Phys. Lett.* **102**, 193104–193104 (2013).
93. Ozgit, D., Butler, T., Oluwasanya, P. W., Occhipinti, L. G. & Hiralal, P. “Wear and Forget” patch for ambient assisted living. in *2019 IEEE International Conference on Flexible and Printable Sensors and Systems (FLEPS)* 1–3 (2019). doi:10.1109/FLEPS.2019.8792270.
94. Zhang, Z. *et al.* A versatile, cost-effective, and flexible wearable biosensor for: In situ and ex situ sweat analysis, and personalized nutrition assessment. *Lab. Chip* **19**, 3448–3460 (2019).
95. Bandodkar, A. J. *et al.* Tattoo-based noninvasive glucose monitoring: A proof-of-concept study. *Anal. Chem.* **87**, 394–398 (2015).
96. Sears, M. E., Kerr, K. J. & Bray, R. I. Arsenic, Cadmium, Lead, and Mercury in Sweat: A Systematic Review. *J. Environ. Public Health* **2012**, (2012).
97. Huang, X. *et al.* Stretchable, wireless sensors and functional substrates for epidermal characterization of sweat. *Small* **10**, 3083–3090 (2014).
98. Hirokawa, T., Okamoto, H., Gosyo, Y., Tsuda, T. & Timerbaev, A. R. Simultaneous monitoring of inorganic cations, amines and amino acids in human sweat by capillary electrophoresis. *Anal. Chim. Acta* **581**, 83–88 (2007).
99. Patterson, M. J., Galloway, S. D. R. & Nimmo, M. A. Variations in Regional Sweat Composition in Normal Human Males. *Exp. Physiol.* **85**, 869–875 (2000).

## Bibliography

---

100. Sato, K., Kang, W. H., Saga, K. & Sato, K. T. Biology of sweat glands and their disorders. I. Normal sweat gland function. *J. Am. Acad. Dermatol.* **20**, 537–563 (1989).
101. Sato, K. & Sato, F. Na<sup>+</sup>, K<sup>+</sup>, H<sup>+</sup>, Cl<sup>-</sup>, and Ca<sup>2+</sup> concentrations in cystic fibrosis eccrine sweat in vivo and in vitro. *J. Lab. Clin. Med.* **115**, (1990).
102. Derbyshire, P. J., Barr, H., Davis, F. & Higson, S. P. J. Lactate in human sweat: A critical review of research to the present day. *J. Physiol. Sci.* **62**, 429–440 (2012).
103. Huang, C. T., Chen, M. L., Huang, L. L. & Mao, I. F. Uric acid and urea in human sweat. *Chin. J. Physiol.* **45**, 109–115 (2002).
104. Xu, H., Liao, C., Zuo, P., Liu, Z. & Ye, B. C. Magnetic-Based Microfluidic Device for On-Chip Isolation and Detection of Tumor-Derived Exosomes. *Anal. Chem.* **90**, 13451–13458 (2018).
105. Buono, M. J. *Sweat ethanol concentrations are highly correlated with co-existing blood values in humans. Experimental Physiology* vol. 84 401–404 (1999).
106. Barel, A. O., Paye, M., Maibach, H. I., Paye, M. & Maibach, H. I. *Handbook of Cosmetic Science and Technology*. (CRC Press, 2014). doi:10.1201/b16716.
107. Karpova, E. V. *et al.* Noninvasive diabetes monitoring through continuous analysis of sweat using flow-through glucose biosensor. *Anal. Chem.* **91**, 3778–3783 (2019).
108. Lee, H. *et al.* Wearable/disposable sweat-based glucose monitoring device with multistage transdermal drug delivery module. *Sci. Adv.* **3**, e1601314–e1601314 (2017).
109. Zhao, Y. *et al.* Highly Stretchable and Strain-Insensitive Fiber-Based Wearable Electrochemical Biosensor to Monitor Glucose in the Sweat. *Anal. Chem.* **91**, 35–35 (2019).
110. Liu, X. & Lillehoj, P. B. Embroidered electrochemical sensors for biomolecular detection. *Lab. Chip* **16**, 2093–2098 (2016).
111. Wang, Y. *et al.* The woven fiber organic electrochemical transistors based on polypyrrole nanowires/reduced graphene oxide composites for glucose sensing. *Biosens. Bioelectron.* **95**, 138–145 (2017).
112. He, J. *et al.* A thermoresponsive microfluidic system integrating a shape memory polymer-modified textile and a paper-based colorimetric sensor for the detection of glucose in human sweat. *RSC Adv.* **9**, 23957–23963 (2019).
113. Zhu, Y., Ji, X., Wu, Z. & Liu, Y. NiCo<sub>2</sub>S<sub>4</sub> hollow microsphere decorated by acetylene black for high-performance asymmetric supercapacitor. *Electrochimica Acta* **186**, 562–571 (2015).
114. Xu, W. *et al.* Direct growth of CuCo<sub>2</sub>S<sub>4</sub> nanosheets on carbon fiber textile with enhanced electrochemical pseudocapacitive properties and electrocatalytic properties towards glucose oxidation. *Nanoscale* **10**, 14304–14313 (2018).
115. Peng, Y., Lin, D., Justin Gooding, J., Xue, Y. & Dai, L. Flexible fiber-shaped non-enzymatic sensors with a graphene-metal heterostructure based on graphene fibres decorated with gold nanosheets. *Carbon* **136**, 329–336 (2018).
116. Wang, Y., Xu, H., Zhang, J. & Li, G. Electrochemical sensors for clinic analysis. *Sensors* **8**, 2043–2081 (2008).
117. Alam, F. *et al.* Lactate biosensing: The emerging point-of-care and personal health monitoring. *Biosens. Bioelectron.* **117**, 818–829 (2018).
118. Bio-sensing textiles to support health management. <https://cordis.europa.eu/project/id/16789> (2011).
119. Promphet, N. *et al.* Non-invasive textile based colorimetric sensor for the simultaneous detection of sweat pH and lactate. *Talanta* **192**, 424–430 (2019).
120. Jia, W. *et al.* Electrochemical tattoo biosensors for real-time noninvasive lactate monitoring in human perspiration. *Anal. Chem.* **85**, 6553–6560 (2013).
121. Baysal, G. *et al.* Microfluidic device on a nonwoven fabric: A potential biosensor for lactate detection. *Text. Res. J.* **84**, 1729–1741 (2014).
122. Zhang, Y. *et al.* Fiber organic electrochemical transistors based on multi-walled carbon nanotube and polypyrrole composites for noninvasive lactate sensing. *Anal. Bioanal. Chem.* **412**, 7515–7524 (2020).
123. Douglas, B. L. & Mauri, E. K. Cystic Fibrosis: Does CFTR Malfunction Alter pH Regulation? in *Genetic Disorders* (InTech, 2013). doi:10.5772/52342.
124. Moyer, J., Wilson, D., Finkelshtein, I., Wong, B. & Potts, R. Correlation between sweat glucose and blood glucose in subjects with diabetes. *Diabetes Technol. Ther.* **14**, 398–402 (2012).

## Bibliography

---

125. Patterson, M. J., Galloway, S. D. R. & Nimmo, M. A. Effect of induced metabolic alkalosis on sweat composition in men. *Acta Physiol. Scand.* **174**, 41–46 (2002).
126. Sonner, Z. *et al.* The microfluidics of the eccrine sweat gland, including biomarker partitioning, transport, and biosensing implications. *Biomicrofluidics* **9**, 1–19 (2015).
127. Manjakkal, L., Dervin, S. & Dahiya, R. Flexible potentiometric pH sensors for wearable systems. *RSC Adv.* **10**, 8594–8617 (2020).
128. Giachet, F. T. *et al.* Reversible and washing resistant textile-based optical pH sensors by dyeing fabrics with curcuma. *Fibers Polym.* **18**, 720–730 (2017).
129. Park, J. B., Kim, S. H. & Bae, J. S. Quinaldine and Indole based pH sensitive Textile chemosensor. *Fibers Polym.* **12**, 696–699 (2011).
130. Van Der Schueren, L., Mollet, T., Ceylan, Ö. & De Clerck, K. The development of polyamide 6.6 nanofibres with a pH-sensitive function by electrospinning. *Eur. Polym. J.* **46**, 2229–2239 (2010).
131. Van Der Schueren, L. *et al.* Novel cellulose and polyamide halochromic textile sensors based on the encapsulation of Methyl Red into a sol-gel matrix. *Sens. Actuators B Chem.* **162**, 27–34 (2012).
132. Kianfar, P. *et al.* Surface Functionalization of Cotton Fabrics by Photo-Grafting for pH Sensing Applications. *Front. Mater.* **7**, 1–9 (2020).
133. Morris, D. *et al.* Bio-sensing textile based patch with integrated optical detection system for sweat monitoring. *Sens. Actuators B Chem.* **139**, 231–236 (2009).
134. Caldara, M. *et al.* Low power textile-based wearable sensor platform for pH and temperature monitoring with wireless battery recharge. *Proc. IEEE Sens.* 6–9 (2012) doi:10.1109/ICSENS.2012.6411146.
135. Caldara, M., Colleoni, C., Guido, E., Re, V. & Rosace, G. Optical monitoring of sweat pH by a textile fabric wearable sensor based on covalently bonded litmus-3-glycidoxypropyltrimethoxysilane coating. *Sens. Actuators B Chem.* **222**, 213–220 (2016).
136. Caldara, M., Colleoni, C., Guido, E., Re, V. & Rosace, G. Development of a textile-optoelectronic pH meter based on hybrid xerogel doped with Methyl Red. *Sens. Actuators B Chem.* **171–172**, 1013–1021 (2012).
137. Zamora, M. L. *et al.* Potentiometric textile-based pH sensor. *Sens. Actuators B Chem.* **260**, 601–608 (2018).
138. Manjakkal, L., Dang, W., Yogeswaran, N. & Dahiya, R. Textile-Based Potentiometric Electrochemical pH Sensor for Wearable Applications. *Biosensors* **9**, 14–14 (2019).
139. Reid, D. O., Smith, R. E., Garcia-Torres, J., Watts, J. F. & Crean, C. Solvent treatment of wet-spun PEDOT: PSS fibers for fiber-based wearable pH sensing. *Sens. Switz.* **19**, 1–10 (2019).
140. Yoon, J. H. *et al.* Highly self-healable and flexible cable-type pH sensors for real-time monitoring of human fluids. *Biosens. Bioelectron.* **150**, 1–7 (2020).
141. Lieberman, J. Cyclic Fluctuation of Sweat Electrolytes in Women: Effect of Polythiazide Upon Sweat Electrolytes. *JAMA J. Am. Med. Assoc.* **195**, 629–635 (1966).
142. Bergeron, M. F. Heat cramps: Fluid and electrolyte challenges during tennis in the heat. *J. Sci. Med. Sport* **6**, 19–27 (2003).
143. Schwart, I. L. & Thaysen, J. H. Excretion of sodium and potassium in human sweat. *J. Clin. Invest.* **35**, 114–120 (1956).
144. Medbø, J. I. & Sejersted, O. M. Plasma potassium changes with high intensity exercise. *J. Physiol.* **421**, 105–122 (1990).
145. Newmark, S. R. & Dluhy, R. G. Hyperkalemia and Hypokalemia. *JAMA J. Am. Med. Assoc.* **231**, 631–633 (1975).
146. Parrilla, M., Ferré, J., Guinovart, T. & Andrade, F. J. Wearable Potentiometric Sensors Based on Commercial Carbon Fibres for Monitoring Sodium in Sweat. *Electroanalysis* **28**, 1267–1275 (2016).
147. Parrilla, M., Cánovas, R., Jeerapan, I., Andrade, F. J. & Wang, J. A Textile-Based Stretchable Multi-Ion Potentiometric Sensor. *Adv. Healthc. Mater.* **5**, 996–1001 (2016).
148. Yun, S. Y. *et al.* Potentiometric Properties of Ion-Selective Electrode Membranes Based on Segmented Polyether Urethane Matrices. *Anal. Chem.* **69**, 868–873 (1997).
149. Guinovart, T., Parrilla, M., Crespo, G. A., Rius, F. X. & Andrade, F. J. Potentiometric sensors using cotton yarns, carbon nanotubes and polymeric membranes. *Analyst* **138**, 5208–5215 (2013).

## Bibliography

---

150. Mousavi, Z. *et al.* Comparison of Multi-walled Carbon Nanotubes and Poly(3-octylthiophene) as Ion-to-Electron Transducers in All-Solid-State Potassium Ion-Selective Electrodes. *Electroanalysis* **23**, 1352–1358 (2011).
151. Yoon, J. H. *et al.* Extremely Fast Self-Healable Bio-Based Supramolecular Polymer for Wearable Real-Time Sweat-Monitoring Sensor. *ACS Appl. Mater. Interfaces* **11**, 46165–46175 (2019).
152. Tarabella, G. *et al.* A single cotton fiber organic electrochemical transistor for liquid electrolyte saline sensing. *J. Mater. Chem.* **22**, 23830–23834 (2012).
153. Coppedè, N. *et al.* Ion selective textile organic electrochemical transistor for wearable sweat monitoring. *Org. Electron.* **78**, 105579–105579 (2020).
154. Wang, L. *et al.* Weaving Sensing Fibers into Electrochemical Fabric for Real-Time Health Monitoring. *Adv. Funct. Mater.* **28**, (2018).
155. He, W. *et al.* Integrated textile sensor patch for real-time and multiplex sweat analysis. *Sci. Adv.* **5**, 1–9 (2019).
156. Terse-Thakoor, T. *et al.* Thread-based multiplexed sensor patch for real-time sweat monitoring. *Npj Flex. Electron.* **4**, 1–10 (2020).
157. Menke, N. B., Ward, K. R., Witten, T. M., Bonchev, D. G. & Diegelmann, R. F. Impaired wound healing. *Clin. Dermatol.* **25**, 19–25 (2007).
158. Qin, M., Guo, H., Dai, Z., Yan, X. & Ning, X. Advances in flexible and wearable pH sensors for wound healing monitoring. *J. Semicond.* **40**, (2019).
159. Tonnesen, M. G., Feng, X. & Clark, R. A. F. Angiogenesis in wound healing. *J. Investig. Dermatol. Symp. Proc.* **5**, 40–46 (2000).
160. Lazarus, G. S. *et al.* Definitions and guidelines for assessment of wounds and evaluation of healing. *Wound Repair Regen. Off. Publ. Wound Heal. Soc. Eur. Tissue Repair Soc.* **2**, 165–70 (1994).
161. Cukjati, D., Reberšek, S., & Miklavčič. A reliable method of determining wound healing rate. *Med. Biol. Eng. Comput.* **39**, 263–271 (2001).
162. A clinimetric analysis of wound measurement tools.
163. Brown, M. S., Ashley, B. & Koh, A. Wearable technology for chronic wound monitoring: Current dressings, advancements, and future prospects. *Front. Bioeng. Biotechnol.* **6**, 1–21 (2018).
164. Fonder, M. A. *et al.* Treating the chronic wound: A practical approach to the care of nonhealing wounds and wound care dressings. *J. Am. Acad. Dermatol.* **58**, 185–206 (2008).
165. Dabiri, G., Damstetter, E. & Phillips, T. Choosing a Wound Dressing Based on Common Wound Characteristics. *Adv. Wound Care* **5**, 32–41 (2016).
166. Gianino, E., Miller, C. & Gilmore, J. Smart wound dressings for diabetic chronic wounds. *Bioengineering* **5**, 51–51 (2018).
167. Power, G., Moore, Z. & O'Connor, T. Measurement of pH, exudate composition and temperature in wound healing: A systematic review. *J. Wound Care* **26**, 381–397 (2017).
168. Nocke, A., Schröter, A., Cherif, C. & Gerlach, G. Miniaturized textile-based multi-layer pH-sensor for wound monitoring applications. *Autex Res. J.* **12**, 20–22 (2012).
169. Schneider, L. A., Korber, A., Grabbe, S. & Dissemond, J. Influence of pH on wound-healing: A new perspective for wound-therapy? *Arch. Dermatol. Res.* **298**, 413–420 (2007).
170. Parvaneh, S. *et al.* Stressing the dressing: Assessing stress during wound care in real-time using wearable sensors. *Wound Med.* **4**, 21–26 (2014).
171. Cutting, K. F. Wound exudate: composition and functions. *Br. J. Community Nurs.* **8**, S4–S9 (2003).
172. Trengove, N. J., Langton, S. R. & Stacey, M. C. Biochemical analysis of wound fluid from nonhealing and healing chronic leg ulcers. *Wound Repair Regen.* **4**, 234–239 (1996).
173. Brem, H. & Tomic-canic, M. Cellular and molecular basis of wound healing in diabetes Find the latest version : Cellular and molecular basis of wound healing in diabetes. **117**, 1219–1222 (2007).
174. Kassal, P. *et al.* Smart bandage with wireless connectivity for uric acid biosensing as an indicator of wound status. *Electrochem. Commun.* **56**, 6–10 (2015).
175. Tu, C., Zhang, R. dong, Yan, C., Guo, Y. & Cui, L. A pH indicating carboxymethyl cellulose/chitosan sponge for visual monitoring of wound healing. *Cellulose* **26**, 4541–4552 (2019).
176. Cui, L. *et al.* Smart pH response flexible sensor based on calcium alginate fibers incorporated with natural dye for wound healing monitoring. *Cellulose* **27**, 6367–6381 (2020).

## Bibliography

---

177. Gorji, M., Sadeghianmaryan, A., Rajabinejad, H., Nasherolahkam, S. & Chen, X. Development of highly pH-sensitive hybrid membranes by simultaneous electrospinning of amphiphilic nanofibers reinforced with graphene oxide. *J. Funct. Biomater.* **10**, (2019).
178. Pakolpakçil, A. *et al.* Halochromic composite nanofibrous mat for wound healing monitoring. *Mater. Res. Express* **6**, (2019).
179. Steyaert, I., Vancoillie, G., Hoogenboom, R. & De Clerck, K. Dye immobilization in halochromic nanofibers through blend electrospinning of a dye-containing copolymer and polyamide-6. *Polym. Chem.* **6**, 2685–2694 (2015).
180. Schoolaert, E. *et al.* Blend electrospinning of dye-functionalized chitosan and poly( $\epsilon$ -caprolactone): Towards biocompatible pH-sensors. *J. Mater. Chem. B* **4**, 4507–4516 (2016).
181. Mohr, G. J. & Müller, H. Tailoring colour changes of optical sensor materials by combining indicator and inert dyes and their use in sensor layers, textiles and non-wovens. *Sens. Actuators B Chem.* **206**, 788–793 (2015).
182. Schaude, C. *et al.* The development of indicator cotton swabs for the detection of pH in wounds. *Sens. Switz.* **17**, (2017).
183. Del Mercato, L. L., Moffa, M., Rinaldi, R. & Pisignano, D. Ratiometric Organic Fibers for Localized and Reversible Ion Sensing with Micrometer-Scale Spatial Resolution. *Small* **11**, 6417–6424 (2015).
184. Jankowska, D. A. *et al.* Simultaneous detection of pH value and glucose concentrations for wound monitoring applications. *Biosens. Bioelectron.* **87**, 312–319 (2017).
185. Tamayol, A. *et al.* Flexible pH-Sensing Hydrogel Fibers for Epidermal Applications. *Adv. Healthc. Mater.* **5**, 711–719 (2016).
186. Kassal, P. *et al.* Smart bandage with wireless connectivity for optical monitoring of pH. *Sens. Actuators B Chem.* **246**, 455–460 (2017).
187. Shukla, V. K., Shukla, D., Tiwary, S. K., Agrawal, S. & Rastogi, A. Evaluation of pH measurement as a method of wound assessment. *J. Wound Care* **16**, 291–294 (2007).
188. Dargaville, T. R. *et al.* Sensors and imaging for wound healing: A review. *Biosens. Bioelectron.* **41**, 30–42 (2013).
189. Loffler, M., Schmohl, M., Schneiderhan-Marra, N. & Beckert, S. Wound Fluid Diagnostics in Diabetic Foot Ulcers. *Glob. Perspect. Diabet. Foot Ulcerations* (2011) doi:10.5772/30002.
190. Beidler, S. K. *et al.* Inflammatory cytokine levels in chronic venous insufficiency ulcer tissue before and after compression therapy. *J. Vasc. Surg.* **49**, 1013–1020 (2009).
191. Schreml, S. *et al.* Oxygen in acute and chronic wound healing. *Br. J. Dermatol.* **163**, 257–268 (2010).
192. Guinovart, T., Valdés-Ramírez, G., Windmiller, J. R., Andrade, F. J. & Wang, J. Bandage-Based Wearable Potentiometric Sensor for Monitoring Wound pH. *Electroanalysis* **26**, 1345–1353 (2014).
193. Smith, R. E. *et al.* Development of a novel highly conductive and flexible cotton yarn for wearable pH sensor technology. *Sens. Actuators B Chem.* **287**, 338–345 (2019).
194. Punjiya, M., Nejad, H. R., Mostafalu, P. & Sonkusale, S. PH sensing threads with CMOS readout for Smart Bandages. *Proc. - IEEE Int. Symp. Circuits Syst.* 10–13 (2017) doi:10.1109/ISCAS.2017.8050730.
195. Karperien, L. *et al.* Smart Thread Based pH Sensitive Antimicrobial Wound Dressing. *2019 IEEE Int. Flex. Electron. Technol. Conf. IFETC 2019* 8–12 (2019) doi:10.1109/IFETC46817.2019.9073705.
196. Collins, G. E. & Buckley, L. J. Conductive polymer-coated fabrics for chemical sensing. *Synth. Met.* **78**, 93–101 (1996).
197. McColl, D., Cartlidge, B. & Connolly, P. Real-time monitoring of moisture levels in wound dressings in vitro: An experimental study. *Int. J. Surg.* **5**, 316–322 (2007).
198. Milne, S. D. *et al.* A wearable wound moisture sensor as an indicator for wound dressing change: An observational study of wound moisture and status. *Int. Wound J.* **13**, 1309–1314 (2016).
199. Randeniya, L. K., Martin, P. J., Bendavid, A. & McDonnell, J. Ammonia sensing characteristics of carbon-nanotube yarns decorated with nanocrystalline gold. *Carbon* **49**, 5265–5270 (2011).
200. Qi, J., Xu, X., Liu, X. & Lau, K. T. Fabrication of textile based conductometric polyaniline gas sensor. *Sens. Actuators B Chem.* **202**, 732–740 (2014).
201. Lmberis, A. & Dittmar, A. Advanced Wearable Health Systems and Applications - Research and Development Efforts in the European Union. *IEEE Eng. Med. Biol. Mag.* **26**, 29–33 (2007).
202. Baig, M. M., Gholamhosseini, H. & Connolly, M. J. A comprehensive survey of wearable and wireless ECG monitoring systems for older adults. *Med. Biol. Eng. Comput.* **51**, 485–495 (2013).

## Bibliography

---

203. Di Rienzo, M. *et al.* Textile Technology for the Vital Signs Monitoring in Telemedicine and Extreme Environments. *IEEE Trans. Inf. Technol. Biomed.* **14**, 711–717 (2010).
204. Coosemans, J., Hermans, B. & Puers, R. Integrating wireless ECG monitoring in textiles. in *The 13th International Conference on Solid-State Sensors, Actuators and Microsystems, 2005. Digest of Technical Papers. TRANSDUCERS '05.* vol. 1 228–232 Vol. 1 (2005).
205. Nigusse, A. B., Malengier, B., Mengistie, D. A., Tseghai, G. B. & Van Langenhove, L. Development of Washable Silver Printed Textile Electrodes for Long-Term ECG Monitoring. *Sensors* **20**, 6233 (2020).
206. K, A., AK, W. & AP, A. Textile Electrocardiogram (ECG) Electrodes for Wearable Health Monitoring. *Sensors* **20**, (2020).
207. Saenz-Cogollo, J., Pau, M., Fraboni, B. & Bonfiglio, A. Pressure Mapping Mat for Tele-Home Care Applications. *Sensors* **16**, 365–365 (2016).
208. Hauke, A. *et al.* Complete validation of a continuous and blood-correlated sweat biosensing device with integrated sweat stimulation. *Lab. Chip* **18**, 3750–3759 (2018).
209. Meyer, J., Lukowicz, P. & Troster, G. Textile Pressure Sensor for Muscle Activity and Motion Detection. in *2006 10th IEEE International Symposium on Wearable Computers* 69–72 (IEEE, 2006). doi:10.1109/ISWC.2006.286346.
210. Schall, M. C., Sesek, R. F. & Cavuoto, L. A. Barriers to the Adoption of Wearable Sensors in the Workplace: A Survey of Occupational Safety and Health Professionals. *Hum. Factors* **60**, 351–362 (2018).
211. Chen, L. *et al.* Textile-Based Capacitive Sensor for Physical Rehabilitation via Surface Topological Modification. *ACS Nano* **14**, 8191–8201 (2020).
212. Lian, Y., Yu, H., Wang, M., Yang, X. & Zhang, H. Ultrasensitive Wearable Pressure Sensors Based on Silver Nanowire-Coated Fabrics. *Nanoscale Res. Lett.* **2020 151** **15**, 1–8 (2020).
213. Mokhtari, F. *et al.* Wearable Electronic Textiles from Nanostructured Piezoelectric Fibers. *Adv. Mater. Technol.* **5**, 1900900 (2020).
214. Carpi, F. & De Rossi, D. Electroactive polymer-based devices for e-textiles in biomedicine. *IEEE Trans. Inf. Technol. Biomed.* **9**, 295–318 (2005).
215. Li, P. *et al.* A wearable and sensitive graphene-cotton based pressure sensor for human physiological signals monitoring. *Sci. Rep.* **2019 91** **9**, 1–8 (2019).
216. Ray, T. *et al.* Soft, skin-interfaced wearable systems for sports science and analytics. *Curr. Opin. Biomed. Eng.* **9**, 47–56 (2019).
217. Yang, Y. *et al.* Flexible piezoelectric pressure sensor based on polydopamine-modified BaTiO<sub>3</sub>/PVDF composite film for human motion monitoring. *Sens. Actuators Phys.* **301**, 111789–111789 (2020).
218. Jiajun Guo, Min Nie, & Qi Wang. A piezoelectric poly(vinylidene fluoride) tube featuring highly-sensitive and isotropic piezoelectric output for compression. *RSC Adv.* **11**, 1182–1186 (2021).
219. Li, H. *et al.* Facile Strategy for Fabrication of Flexible, Breathable, and Washable Piezoelectric Sensors via Welding of Nanofibers with Multiwalled Carbon Nanotubes (MWCNTs). *ACS Appl. Mater. Interfaces* **11**, 38023–38030 (2019).
220. Kim, H. J. & Kim, Y. J. High performance flexible piezoelectric pressure sensor based on CNTs-doped 0–3 ceramic-epoxy nanocomposites. *Mater. Des.* **151**, 133–140 (2018).
221. Zhang, L. *et al.* Thiolated Graphene@Polyester Fabric-Based Multilayer Piezoresistive Pressure Sensors for Detecting Human Motion. *ACS Appl. Mater. Interfaces* **10**, 41784–41792 (2018).
222. Tian, M. *et al.* A Pillow-Shaped 3D Hierarchical Piezoresistive Pressure Sensor Based on Conductive Silver Components-Coated Fabric and Random Fibers Assembly. (2019) doi:10.1021/acs.iecr.9b00035.
223. Choudhry, N. A., Rasheed, A., Ahmad, S., Arnold, L. & Wang, L. Design, Development and Characterization of Textile Stitch-Based Piezoresistive Sensors for Wearable Monitoring. *IEEE Sens. J.* **20**, 10485–10494 (2020).
224. Cunguang, L. & Xiuling, L. A Graphene-Based Flexible Pressure Sensor with Applications to Plantar Pressure Measurement and Gait Analysis. *Materials* **10**, 1068 (2017).
225. Lee, J. *et al.* Conductive Fiber-Based Ultrasensitive Textile Pressure Sensor for Wearable Electronics. *Adv. Mater.* **27**, 2433–2439 (2015).

## Bibliography

---

226. Chhetry, A., Yoon, H. & Park, J. Y. A flexible and highly sensitive capacitive pressure sensor based on conductive fibers with a microporous dielectric for wearable electronics. *J. Mater. Chem. C* **5**, 10068–10076 (2017).
227. Li, S. *et al.* Capacitive pressure sensor inlaid a porous dielectric layer of superelastic polydimethylsiloxane in conductive fabrics for detection of human motions. *Sens. Actuators Phys.* **312**, 112106–112106 (2020).
228. Hatamie, A. *et al.* Review – Textile Based Chemical and Physical Sensors for Healthcare Monitoring. *J. Electrochem. Soc.* **167**, 037546–037546 (2020).
229. Islam, G. M. N., Ali, A. & Collie, S. Textile sensors for wearable applications: a comprehensive review. *Cellulose* **27**, 6103–6131 (2020).
230. del Agua, I. *et al.* DVS-Crosslinked PEDOT:PSS Free-Standing and Textile Electrodes toward Wearable Health Monitoring. *Adv. Mater. Technol.* **3**, (2018).
231. Tseghai, G. B. *et al.* PEDOT:PSS/PDMS-coated cotton fabric for ECG electrode. *2020 IEEE Int. Conf. Flex. Printable Sens. Syst. FLEPS* (2020) doi:10.1109/FLEPS49123.2020.9239526.
232. Husain, M. D., Kennon, R. & Dias, T. Design and fabrication of Temperature Sensing Fabric. *J. Ind. Text.* **44**, 398–417 (2014).
233. Possanzini, L., Tessarolo, M., Mazzocchetti, L., Campari, E. G. & Fraboni, B. Impact of Fabric Properties on Textile Pressure Sensors Performance. *Sensors* **19**, 4686–4686 (2019).
234. Hardianto, H., Malengier, B., De Mey, G., Van Langenhove, L. & Hertleer, C. Textile yarn thermocouples for use in fabrics. *J. Eng. Fibers Fabr.* **14**, 155892501983609–155892501983609 (2019).
235. Lund, A., Tian, Y., Darabi, S. & Müller, C. A polymer-based textile thermoelectric generator for wearable energy harvesting. *J. Power Sources* **480**, 228836–228836 (2020).
236. Zhao, Z. *et al.* Machine-washable and breathable pressure sensors based on triboelectric nanogenerators enabled by textile technologies. *Nano Energy* **70**, 104528–104528 (2020).
237. Jeerapan, I., Sempionatto, J. R., Pavinatto, A., You, J. M. & Wang, J. Stretchable biofuel cells as wearable textile-based self-powered sensors. *J. Mater. Chem. A* **4**, 18342–18353 (2016).
238. Nuramdhani, I. *et al.* Charge-Discharge Characteristics of Textile Energy Storage Devices Having Different PEDOT:PSS Ratios and Conductive Yarns Configuration. *Polymers* **11**, 345–345 (2019).
239. Ciavatti, A. *et al.* Boosting Direct X-Ray Detection in Organic Thin Films by Small Molecules Tailoring. *Adv. Funct. Mater.* **29**, 1806119–1806119 (2019).
240. Thirimanne, H. M. *et al.* High sensitivity organic inorganic hybrid X-ray detectors with direct transduction and broadband response. *Nat. Commun.* **9**, 1–10 (2018).
241. Griffith, M. J., Cottam, S., Stamenkovic, J., Posar, J. A. & Petasecca, M. Printable Organic Semiconductors for Radiation Detection: From Fundamentals to Fabrication and Functionality. *Front. Phys.* **8**, 22–22 (2020).
242. Basiricò, L., Ciavatti, A. & Fraboni, B. Solution-Grown Organic and Perovskite X-Ray Detectors: A New Paradigm for the Direct Detection of Ionizing Radiation. *Adv. Mater. Technol.* **6**, (2021).
243. Li, Z. *et al.* Halide perovskites for high-performance X-ray detector. *Mater. Today* (2021) doi:10.1016/j.mattod.2021.01.028.
244. Wei, H. & Huang, J. Halide lead perovskites for ionizing radiation detection. *Nat. Commun.* **10**, 1–12 (2019).
245. Kaltenbrunner, M. *et al.* Ultrathin and lightweight organic solar cells with high flexibility. *Nat. Commun.* **3**, 1–7 (2012).
246. Kaltenbrunner, M. *et al.* Flexible high power-per-weight perovskite solar cells with chromium oxide-metal contacts for improved stability in air. *Nat. Mater.* **14**, 1032–1039 (2015).
247. Jung, J. W., Bae, J. H., Ko, J. H. & Lee, W. Fully solution-processed indium tin oxide-free textile-based flexible solar cells made of an organic-inorganic perovskite absorber: Toward a wearable power source. *J. Power Sources* **402**, 327–332 (2018).
248. Legge, K. *et al.* Technical note: TROG 15.01 SPARK trial multi-institutional imaging dose measurement. *J. Appl. Clin. Med. Phys.* **18**, 358–363 (2017).
249. Demchyshyn, S. *et al.* Designing Ultraflexible Perovskite X-Ray Detectors through Interface Engineering. *Adv. Sci.* **7**, 1–11 (2020).
250. Brivio, D. *et al.* Nanoporous aerogel-based periodic high-energy electron current x-ray sensors. (2020).

## Bibliography

---

251. Yakunin, S. *et al.* Detection of X-ray photons by solution-processed lead halide perovskites. *Nat. Photonics* **9**, 444–449 (2015).
252. Wang, X. *et al.* Wire-shaped perovskite solar cell based on TiO<sub>2</sub> nanotubes. *Nanotechnology* **27**, 1–6 (2016).
253. Li, R., Xiang, X., Tong, X., Zou, J. & Li, Q. Wearable Double-Twisted Fibrous Perovskite Solar Cell. *Adv. Mater.* **27**, 3831–3835 (2015).
254. Qiu, L., Deng, J., Lu, X., Yang, Z. & Peng, H. Integrating Perovskite Solar Cells into a Flexible Fiber. *Angew. Chem. Int. Ed.* **53**, 10425–10428 (2014).
255. Lam, J. Y. *et al.* A stable, efficient textile-based flexible perovskite solar cell with improved washable and deployable capabilities for wearable device applications. *RSC Adv.* **7**, 54361–54368 (2017).
256. Liu, W., Song, M. S., Kong, B. & Cui, Y. Flexible and Stretchable Energy Storage: Recent Advances and Future Perspectives. *Adv. Mater.* **29**, 1603436–1603436 (2017).
257. Yin, L., Seo, J. K., Kurniawan, J., Kumar, R., Lv, J., Xie, L., Liu, X., Xu, S., Meng, Y. S., Wang, J. Highly Stable Battery Pack via Insulated, Reinforced, Buckling-Enabled Interconnect Array. *Small* **14**, 1800938–1800938 (2018).
258. Kumar, R. *et al.* All-Printed, Stretchable Zn-Ag<sub>2</sub>O Rechargeable Battery via Hyperelastic Binder for Self-Powering Wearable Electronics. *Adv. Energy Mater.* **7**, 1602096–1602096 (2017).
259. Yahiro, A. T., Lee, S. M. & Kimble, D. O. Bioelectrochemistry: I. Enzyme utilizing bio-fuel cell studies. *Biochim. Biophys. Acta BBA - Spec. Sect. Biophys. Subj.* **88**, 375–383 (1964).
260. Hardianto, H., De Mey, G., Ciesielska-Wróbel, L., Hertleer, C. & Van Langenhove, L. Seebeck Coefficient of Thermocouples from Nickel-Coated Carbon Fibers: Theory and Experiment. *Materials* **11**, 922–922 (2018).
261. Kim, S. J., We, J. H. & Cho, B. J. A wearable thermoelectric generator fabricated on a glass fabric. *Energy Environ. Sci.* **7**, 1959–1965 (2014).
262. Kim, M. K., Kim, M. S., Lee, S., Kim, C. & Kim, Y. J. Wearable thermoelectric generator for harvesting human body heat energy. *Smart Mater. Struct.* **23**, (2014).
263. Kim, M. *et al.* Wearable thermoelectric generator for human clothing applications. *2013 Transducers Eurosensors XXVII 17th Int. Conf. Solid-State Sens. Actuators Microsyst. TRANSDUCERS EUROSENSORS XXVII* (2013) doi:10.1109/TRANSDUCERS.2013.6627034.
264. Lu, Z., Zhang, H., Mao, C. & Li, C. M. Silk fabric-based wearable thermoelectric generator for energy harvesting from the human body. *Appl. Energy* **164**, 57–63 (2016).
265. Park, Y. W., Han, W. K., Choi, C. H. & Shirakawa, H. Metallic nature of heavily doped polyacetylene derivatives: Thermopower. *Phys. Rev. B* **30**, 5847–5851 (1984).
266. Pukacki, W., Płocharski, J. & Roth, S. Anisotropy of thermoelectric power of stretch-oriented new polyacetylene. (1994) doi:10.1016/0379-6779(94)90213-5.
267. Shi, H. *et al.* Electrochemical Fabrication and Thermoelectric Performance of the PEDOT:PSS Electrode Based Bilayered Organic Nanofilms. *Int. J. Electrochem. Sci.* **9**, 7629–7643 (2014).
268. Wu, J., Sun, Y., Xu, W. & Zhang, Q. Investigating thermoelectric properties of doped polyaniline nanowires. *Synth. Met.* **189**, 177–182 (2014).
269. Tsai, T.-C., Chang, H.-C., Chen, C.-H. & Whang, W.-T. Widely variable Seebeck coefficient and enhanced thermoelectric power of PEDOT:PSS films by blending thermal decomposable ammonium formate. *Org. Electron.* **12**, 2159–2164 (2011).
270. Wei, Q., Mukaida, M., Kirihaara, K., Naitoh, Y. & Ishida, T. Recent Progress on PEDOT-Based Thermoelectric Materials. *Materials* **8**, 732–750 (2015).
271. Du, Y. *et al.* Multifold enhancement of the output power of flexible thermoelectric generators made from cotton fabrics coated with conducting polymer. *RSC Adv.* **7**, 43737–43742 (2017).
272. Kemp, N. *et al.* Thermoelectric power and conductivity of different types of polypyrrole. (1999) doi:10.1002/(SICI)1099-0488(19990501)37:9<953::AID-POLB7>3.0.CO;2-L.
273. Sparavigna, A. C., Florio, L., Avloni, J. & Henn, A. Polypyrrole Coated PET Fabrics for Thermal Applications. *Mater. Sci. Appl.* **1**, 253–259 (2010).
274. Bounioux, C. *et al.* Thermoelectric composites of poly(3-hexylthiophene) and carbon nanotubes with a large power factor. *Energy Environ. Sci.* **6**, 918–925 (2013).
275. Hynynen, J., Kiefer, D. & Müller, C. Influence of crystallinity on the thermoelectric power factor of P3HT vapour-doped with F4TCNQ. *RSC Adv.* **8**, 1593–1599 (2018).

## Bibliography

---

276. Hynynen, J. *et al.* Enhanced Thermoelectric Power Factor of Tensile Drawn Poly(3-hexylthiophene). *ACS Macro Lett.* **8**, 70–76 (2019).
277. Thermoelectric Fabrics: Toward Power Generating Clothing | Scientific Reports. <https://www.nature.com/articles/srep06411>.
278. Choi, J. *et al.* Flexible and Robust Thermoelectric Generators Based on All-Carbon Nanotube Yarn without Metal Electrodes. *ACS Nano* **11**, 7608–7614 (2017).
279. Ito, M., Koizumi, T., Kojima, H., Saito, T. & Nakamura, M. From materials to device design of a thermoelectric fabric for wearable energy harvesters. *J. Mater. Chem. A* **5**, 12068–12072 (2017).
280. Ryan, J. D. *et al.* All-Organic Textile Thermoelectrics with Carbon-Nanotube-Coated n-Type Yarns. *ACS Appl. Energy Mater.* **1**, 2934–2941 (2018).
281. Cave, I. D. & Walker, J. C. F. Stiffness of wood in fast-grown plantation softwoods: the influence of microfibril angle. *For. Prod. J. USA* (1994).
282. Hearle, J. W. S. 2 - Physical structure and properties of cotton. in *Cotton* (eds. Gordon, S. & Hsieh, Y.-L.) 35–67 (Woodhead Publishing, 2007). doi:10.1533/9781845692483.1.35.
283. Nevell, T. P. Cellulose: structure, properties and behaviour in the dyeing process. *Cellul. Dye.* 1–80 (1995).
284. Segal, L. & Wakelyn, P. J. Cotton fibres. 11–23 (2012) doi:10.1533/9780857095503.1.9.
285. Various Authors. *Handbook of Natural Fibres. Processing and Applications.* vol. Vol: 2 529 (Woodhead Publishing, 2012).
286. Naraporn Indarit, Yong-Hoon Kim, Nattasamon Petchsang, & Rawat Jaisutti. Highly sensitive polyaniline-coated fiber gas sensors for real-time monitoring of ammonia gas. *RSC Adv.* **9**, 26773–26779 (2019).
287. Malshe, P., Mazlumpour, M., El-Shafei, A. & Hauser, P. Functional military textile: Plasma-induced graft polymerization of dadmac for antimicrobial treatment on nylon-cotton blend fabric. *Plasma Chem. Plasma Process.* **32**, 833–843 (2012).
288. Kothari, V. K. Polyester and polyamide fibres – apparel applications. *Polyest. Polyam.* 419–440 (2008) doi:10.1533/9781845694609.3.419.
289. Ruwan D. Sumanasinghe & Martin W. King. New trends in biotextiles - The challenge of tissue engineering. *J. Text. Appar. Technol. Manag.* **3**, (2003).
290. Le, T.-H., Kim, Y. & Yoon, H. Electrical and Electrochemical Properties of Conducting Polymers. *Polymers* **9**, 150 (2017).
291. Guo, B. & Ma, P. X. Conducting Polymers for Tissue Engineering. *Biomacromolecules* **19**, 1764–1782 (2018).
292. Inal, S., Rivnay, J., Suiu, A.-O., Malliaras, G. G. & McCulloch, I. Conjugated Polymers in Bioelectronics. *Acc. Chem. Res.* **51**, 1368–1376 (2018).
293. Ibanez, J. G. *et al.* Conducting Polymers in the Fields of Energy, Environmental Remediation, and Chemical-Chiral Sensors. *Chem. Rev.* **118**, 4731–4816 (2018).
294. Das, T. K. & Prusty, S. Review on Conducting Polymers and Their Applications. *Polym.-Plast. Technol. Eng.* **51**, 1487–1500 (2012).
295. Singh, S., Solanki, P. R., Pandey, M. K. & Malhotra, B. D. Cholesterol biosensor based on cholesterol esterase, cholesterol oxidase and peroxidase immobilized onto conducting polyaniline films. *Sens. Actuators B Chem.* **1**, 534–541 (2006).
296. Gualandi, I. *et al.* Selective detection of dopamine with an all PEDOT:PSS Organic Electrochemical Transistor. *Sci. Rep.* **6**, 35419–35419 (2016).
297. Organic electrochemical transistors as impedance biosensors | MRS Communications | Cambridge Core. <https://www.cambridge.org/core/journals/mrs-communications/article/organic-electrochemical-transistors-as-impedance-biosensors/AECB7F581025DF916D56B85AED4C1828>.
298. Heeger, A. J. Semiconducting and Metallic Polymers: The Fourth Generation of Polymeric Materials. *J. Phys. Chem. B* **105**, 8475–8491 (2001).
299. Müller, H. K., Hocker, J., Menke, K., Ehinger, K. & Roth, S. Long-term conductivity decrease in polyacetylene samples. *Synth. Met.* **10**, 273–280 (1985).
300. Elschner, A., Kirchmeyer, S., Lovenich, W., Merker, U. & Reuter, K. *PEDOT: Principles and Applications of an Intrinsically Conductive Polymer.* (CRC Press, 2010). doi:10.1201/b10318.

## Bibliography

---

301. Yamato, H., Kai, K., Ohwa, M., Wernet, W. & Matsumura, M. Mechanical, electrochemical and optical properties of poly(3,4-ethylenedioxythiophene)/sulfated poly( $\beta$ -hydroxyethers) composite films. (1997) doi:10.1016/S0013-4686(96)00442-2.
302. Yamato, H. *et al.* Synthesis of free-standing poly(3,4-ethylenedioxythiophene) conducting polymer films on a pilot scale. *Synth. Met.* **83**, 125–130 (1996).
303. Yamato, H., Ohwa, M. & Wernet, W. Stability of polypyrrole and poly(3,4-ethylenedioxythiophene) for biosensor application. *J. Electroanal. Chem.* **397**, 163–170 (1995).
304. Guha, P. C. & Attem, B. H. I. Attempts towards the synthesis of cantharidin- partII. **P.C. Guha, B. H. I. Attempts towards the synthesis of cantharidin-partII. J. Indian Inst Sci 21A, 115–118 (1938).**, 115–118 (1938).
305. Gogte, V. N., Shah, L. G., Tilak, B. D., Gadekar, K. N. & Sahasrabudhe, M. B. Synthesis of potential anticancer agents – I: Synthesis of substituted thiophenes. *Tetrahedron* **23**, 2437–2441 (1967).
306. Groenendaal, L., Jonas, F., Freitag, D., Pielartzik, H. & Reynolds, J. R. Poly(3,4-ethylenedioxythiophene) and Its Derivatives: Past, Present, and Future. *Adv. Mater.* **12**, 481–494 (2000).
307. Wang, H., Barrett, M., Duane, B., Gu, J. & Zenhausern, F. Materials and processing of polymer-based electrochromic devices. *Mater. Sci. Eng. B* **228**, 167–174 (2018).
308. Jonas, F. & Morrison, J. T. 3,4-polyethylenedioxythiophene (PEDT): Conductive coatings technical applications and properties. *Synth. Met.* **85**, 1397–1398 (1997).
309. de Leeuw, D. M., Kraakman, P. A., Bongaerts, P. F. G., Mutsaers, C. M. J. & Klaassen, D. B. M. Electroplating of conductive polymers for the metallization of insulators. *Synth. Met.* **66**, 263–273 (1994).
310. Yamamoto, T. & Koizumi, T. Synthesis of  $\pi$ -conjugated polymers bearing electronic and optical functionalities by organometallic polycondensations and their chemical properties. *Polymer* **48**, 5449–5472 (2007).
311. Yamamoto, T.  $\pi$ -Conjugated Polymers Bearing Electronic and Optical Functionalities. Preparation by Organometallic Polycondensations, Properties, and Their Applications. *Bull. Chem. Soc. Jpn.* **72**, 621–638 (1999).
312. Electrochemically Induced Volume Changes in Poly(3,4-ethylenedioxythiophene) | Chemistry of Materials. <https://pubs.acs.org/doi/abs/10.1021/cm9600034>.
313. Randriamahazaka, H., Noël, V. & Chevrot, C. Nucleation and growth of poly(3,4-ethylenedioxythiophene) in acetonitrile on platinum under potentiostatic conditions. *J. Electroanal. Chem.* **472**, 103–111 (1999).
314. Sakmeche, N. *et al.* Application of sodium dodecylsulfate (SDS) micellar solution as an organized medium for electropolymerization of thiophene derivatives in water. *Synth. Met.* **84**, 191–192 (1997).
315. Sakmeche, N. *et al.* Anionic micelles; a new aqueous medium for electropolymerization of poly(3,4-ethylenedioxythiophene) films on Pt electrodes. (1996) doi:10.1039/CC9960002723.
316. Lima, A., Schottland, P., Sadki, S. & Chevrot, C. Electropolymerization of 3,4-ethylenedioxythiophene and 3,4-ethylenedioxythiophene methanol in the presence of dodecylbenzenesulfonate. *Synth. Met.* **93**, 33–41 (1998).
317. Wang, Y. Research progress on a novel conductive polymer–poly(3,4-ethylenedioxythiophene) (PEDOT). *J. Phys. Conf. Ser.* **152**, 012023 (2009).
318. Reynolds, J. *et al.* Unique variable-gap polyheterocycles for high-contrast dual polymer electrochromic devices. (1997) doi:10.1016/S0379-6779(97)80248-2.
319. Cornil, J., Dos Santos, D. A., Beljonne, D. & Bredas, J. L. Electronic Structure of Phenylene Vinylene Oligomers: Influence of Donor/Acceptor Substitutions. *J. Phys. Chem.* **99**, 5604–5611 (1995).
320. Dietrich, M., Heinze, J., Heywang, G. & Jonas, F. Electrochemical and spectroscopic characterization of polyalkylenedioxythiophenes. *J. Electroanal. Chem.* **369**, 87–92 (1994).
321. Kirchmeyer, S. & Reuter, K. Scientific importance, properties and growing applications of poly(3,4-ethylenedioxythiophene). *J. Mater. Chem.* **15**, 2077–2088 (2005).
322. Hwang, J., Tanner, D. B., Schwendeman, I. & Reynolds, J. R. Optical properties of nondegenerate ground-state polymers: Three dioxothiophene-based conjugated polymers. *Phys. Rev. B* **67**, 115205 (2003).

## Bibliography

---

323. Aasmundtveit, K. E. *et al.* Structure of thin films of poly(3,4-ethylenedioxythiophene). *Synth. Met.* **101**, 561–564 (1999).
324. Zotti, G. *et al.* Electrochemical and XPS Studies toward the Role of Monomeric and Polymeric Sulfonate Counterions in the Synthesis, Composition, and Properties of Poly(3,4-ethylenedioxythiophene). *Macromolecules* **36**, 3337–3344 (2003).
325. Rivnay, J. *et al.* Structural control of mixed ionic and electronic transport in conducting polymers. *Nat. Commun.* **7**, 1–9 (2016).
326. Nitta, A., Chosa, N. & Takeda, K. Effect of Surfactant Addition on Organic Transparent Conductive Films Fabricated by Inkjet Printing Method. *Electron. Mater.* **2**, 536–544 (2021).
327. Pingree, L. S. C., MacLeod, B. A. & Ginger, D. S. The Changing Face of PEDOT:PSS Films: Substrate, Bias, and Processing Effects on Vertical Charge Transport. *J. Phys. Chem. C* **112**, 7922–7927 (2008).
328. Ouyang, J. *et al.* On the mechanism of conductivity enhancement in poly(3,4-ethylenedioxythiophene):poly(styrene sulfonate) film through solvent treatment. (2004) doi:10.1016/j.polymer.2004.10.001.
329. Krebs, F. C. Fabrication and processing of polymer solar cells: A review of printing and coating techniques. *Sol. Energy Mater. Sol. Cells* **93**, 394–412 (2009).
330. Hohnholz, D. & MacDiarmid, A. G. Line patterning of conducting polymers: New horizons for inexpensive, disposable electronic devices. *Synth. Met.* **121**, 1327–1328 (2001).
331. Ogawa, S. *et al.* High-Resolution Three-Dimensional Computed Tomography Analysis of the Clinical Efficacy of Cultured Autogenous Periosteal Cells in Sinus Lift Bone Grafting. *Clin. Implant Dent. Relat. Res.* **18**, 707–716 (2016).
332. Paetzold, R. *et al.* Performance of flexible polymeric light-emitting diodes under bending conditions. *Appl. Phys. Lett.* **82**, 3342–3344 (2003).
333. MacDiarmid, A. G. & Epstein, A. J. The concept of secondary doping as applied to polyaniline. *Synth. Met.* **65**, 103–116 (1994).
334. Jönsson, S. K. M. *et al.* The effects of solvents on the morphology and sheet resistance in poly(3,4-ethylenedioxythiophene)–polystyrenesulfonic acid (PEDOT–PSS) films. *Synth. Met.* **139**, 1–10 (2003).
335. Timpanaro, S., Kemerink, M., Touwslager, F. J., De Kok, M. M. & Schrader, S. Morphology and conductivity of PEDOT/PSS films studied by scanning–tunneling microscopy. *Chem. Phys. Lett.* **394**, 339–343 (2004).
336. Huang, J. *et al.* Investigation of the Effects of Doping and Post-Deposition Treatments on the Conductivity, Morphology, and Work Function of Poly(3,4-ethylenedioxythiophene)/Poly(styrene sulfonate) Films. *Adv. Funct. Mater.* **15**, 290–296 (2005).
337. Kim, J. Y., Jung, J. H., Lee, D. E. & Joo, J. Enhancement of electrical conductivity of poly(3,4-ethylenedioxythiophene)/poly(4-styrenesulfonate) by a change of solvents. *Synth. Met.* **126**, 311–316 (2002).
338. X. Crispin, \*, † *et al.* The Origin of the High Conductivity of Poly(3,4-ethylenedioxythiophene)–Poly(styrenesulfonate) (PEDOT–PSS) Plastic Electrodes. (2006) doi:10.1021/CM061032+.
339. Zhang, S. *et al.* Solvent-induced changes in PEDOT:PSS films for organic electrochemical transistors. *APL Mater.* **3**, 014911–014911 (2015).
340. Thomas, J. P., Zhao, L., McGillivray, D. & Leung, K. T. High-efficiency hybrid solar cells by nanostructural modification in PEDOT:PSS with co-solvent addition. *J. Mater. Chem. A* **2**, 2383–2389 (2014).
341. Kergoat, L. *et al.* Detection of glutamate and acetylcholine with organic electrochemical transistors based on conducting polymer/platinum nanoparticle composites. *Adv. Mater. Deerfield Beach Fla* **26**, 5658–5664 (2014).
342. Nardes, A. M. *et al.* Conductivity, work function, and environmental stability of PEDOT:PSS thin films treated with sorbitol. *Org. Electron.* **9**, 727–734 (2008).
343. David, V., Viñas, C. & Teixidor, F. Poly(3,4-ethylenedioxythiophene) doped with a non-extrudable metallacarborane anion electroactive during synthesis. *Polymer* **47**, 4694–4702 (2006).
344. Adamczyk, L. *et al.* Effective Charge Transport in Poly(3,4-ethylenedioxythiophene) Based Hybrid Films Containing Polyoxometallate Redox Centers. *J. Electrochem. Soc.* **152**, E98 (2005).

## Bibliography

---

345. Visy, C., Bencsik, G., Németh, Z. & Vértés, A. Synthesis and characterization of chemically and electrochemically prepared conducting polymer/iron oxalate composites. *Electrochimica Acta* **53**, 3942–3947 (2008).
346. Balamurugan, A., Chen, Z.-W. & Chen, S.-M. Electrochemical Preparation of Bromo Thymol Blue-PEDOT Composite Electrode and Characterization. *J. Electrochem. Soc.* **155**, E151–E156 (2008).
347. Mariani, F., Gualandi, I., Tessarolo, M., Fraboni, B. & Scavetta, E. PEDOT: Dye-Based, Flexible Organic Electrochemical Transistor for Highly Sensitive pH Monitoring. *ACS Appl. Mater. Interfaces* **10**, 22474–22484 (2018).
348. Spectrometric Identification of Organic Compounds, 8th Edition | Wiley. *Wiley.com* <https://www.wiley.com/en-us/Spectrometric+Identification+of+Organic+Compounds%2C+8th+Edition-p-9780470616376>.
349. Massonnet, N. *et al.* Improvement of the Seebeck coefficient of PEDOT:PSS by chemical reduction combined with a novel method for its transfer using free-standing thin films. *J. Mater. Chem. C* **2**, 1278–1283 (2014).
350. Polarons, bipolarons, and solitons in conducting polymers | Accounts of Chemical Research. <https://pubs.acs.org/doi/10.1021/ar00118a005>.
351. Wöhler, L. & Witzmann, W. Die Oxyde Des Iridiums. *Z Anorg Chem* **57**, 323–352 (1908).
352. Yamanaka, K. Anodically Electrodeposited Iridium Oxide Films (AEIROF) from Alkaline Solutions for Electrochromic Display Devices. *Jpn. J. Appl. Phys.* **28**, 632 (1989).
353. Efficient Electro-Oxidation of Water near Its Reversible Potential by a Mesoporous IrO<sub>x</sub> Nanoparticle Film | The Journal of Physical Chemistry C. <https://pubs.acs.org/doi/10.1021/jp9060076>.
354. Zhao, Y., Vargas-Barbosa, N. M., Hernandez-Pagan, E. A. & Mallouk, T. E. Anodic deposition of colloidal iridium oxide thin films from hexahydroxyiridate(IV) solutions. *Small Wein. Bergstr. Ger.* **7**, 2087–2093 (2011).
355. Chandra, D. *et al.* Highly Efficient Electrocatalysis and Mechanistic Investigation of Intermediate IrO<sub>x</sub>(OH)<sub>y</sub> Nanoparticle Films for Water Oxidation. *ACS Catal.* **6**, 3946–3954 (2016).
356. Characterization and Analysis of Self-Assembly of a Highly Active Colloidal Catalyst for Water Oxidation onto Transparent Conducting Oxide Substrates | The Journal of Physical Chemistry C. <https://pubs.acs.org/doi/10.1021/jp7098416>.
357. Large-scale layer-by-layer inkjet printing of flexible iridium-oxide based pH sensors - ScienceDirect. <https://www.sciencedirect.com/science/article/pii/S157266571730810X>.
358. Mariani, F. *et al.* Advanced Wound Dressing for Real-Time pH Monitoring. *ACS Sens.* **14**, acssensors.1c00552-acssensors.1c00552 (2021).
359. Sambhy, V., MacBride, M. M., Peterson, B. R. & Sen, A. Silver bromide nanoparticle/polymer composites: dual action tunable antimicrobial materials. *J. Am. Chem. Soc.* **128**, 9798–9808 (2006).
360. Castellano, J. J. *et al.* Comparative evaluation of silver-containing antimicrobial dressings and drugs. *Int. Wound J.* **4**, 114–122 (2007).
361. The bactericidal effect of silver nanoparticles - PubMed. <https://pubmed.ncbi.nlm.nih.gov/20818017/>.
362. García-Barrasa, J., López-de-Luzuriaga, J. & Monge, M. Silver nanoparticles: synthesis through chemical methods in solution and biomedical applications. *Open Chem.* **9**, 7–19 (2011).
363. Kim, S. & Ryu, D.-Y. Silver nanoparticle-induced oxidative stress, genotoxicity and apoptosis in cultured cells and animal tissues. *J. Appl. Toxicol. JAT* **33**, 78–89 (2013).
364. Gajbhiye, S. & Sakharwade, S. Silver Nanoparticles in Cosmetics. *J. Cosmet. Dermatol. Sci. Appl.* **6**, 48–53 (2016).
365. Facile Synthesis of Silver Chloride Nanocubes and Their Derivatives -Bulletin of the Korean Chemical Society | Korea Science. <https://www.koreascience.or.kr/article/JAKO201030560144830.page>.
366. Synthesis and Characterization of AgCl Nanoparticles Under Various Solvents by Ultrasound Method | SpringerLink. <https://link.springer.com/article/10.1007/s10904-012-9774-9>.
367. Chandrappa, C. P. *et al.* Endophytic synthesis of silver chloride nanoparticles from *Penicillium* sp. of *Calophyllum apetalum*. *Adv. Nat. Sci. Nanosci. Nanotechnol.* **7**, 025016 (2016).
368. Facet-dependent photovoltaic efficiency variations in single grains of hybrid halide perovskite | Nature Energy. <https://www.nature.com/articles/nenergy201693>.

## Bibliography

---

369. Low-temperature solution-processed wavelength-tunable perovskites for lasing | *Nature Materials*. <https://www.nature.com/articles/nmat3911>.
370. High Photoluminescence Efficiency and Optically Pumped Lasing in Solution-Processed Mixed Halide Perovskite Semiconductors | *The Journal of Physical Chemistry Letters*. <https://pubs.acs.org/doi/abs/10.1021/jz5005285>.
371. Kojima, A., Teshima, K., Shirai, Y. & Miyasaka, T. Organometal Halide Perovskites as Visible-Light Sensitizers for Photovoltaic Cells | *Journal of the American Chemical Society*. *J Am Chem Soc* **131**, 6050–6051 (2009).
372. Mingzhen, L., Johnston, M. B. & Snaith, H. J. Efficient planar heterojunction perovskite solar cells by vapour deposition | *Nature*. *Nature* **501**, 395–398 (2013).
373. Baikie, T. *et al.* Synthesis and crystal chemistry of the hybrid perovskite (CH<sub>3</sub>NH<sub>3</sub>)PbI<sub>3</sub> for solid-state sensitised solar cell applications. *J. Mater. Chem. A* **1**, 5628–5641 (2013).
374. Ponseca, C. S. *et al.* Organometal Halide Perovskite Solar Cell Materials Rationalized: Ultrafast Charge Generation, High and Microsecond-Long Balanced Mobilities, and Slow Recombination. *J. Am. Chem. Soc.* **136**, 5189–5192 (2014).
375. B. Mitzi, D. Templating and structural engineering in organic–inorganic perovskites. *J. Chem. Soc. Dalton Trans.* **0**, 1–12 (2001).
376. Stoumpos, C. C., Malliakas, C. D. & Kanatzidis, M. G. Semiconducting Tin and Lead Iodide Perovskites with Organic Cations: Phase Transitions, High Mobilities, and Near-Infrared Photoluminescent Properties. *Inorg. Chem.* **52**, 9019–9038 (2013).
377. Stranks, S. D. *et al.* Electron-Hole Diffusion Lengths Exceeding 1 Micrometer in an Organometal Trihalide Perovskite Absorber. *Science* (2013) doi:10.1126/science.1243982.
378. Grätzel, M. The light and shade of perovskite solar cells. *Nat. Mater.* 2014 139 **13**, 838–842 (2014).
379. Kim, H. *et al.* Enhanced Stability of MAPbI<sub>3</sub> Perovskite Solar Cells using Poly(p-chloro-xylylene) Encapsulation. *Sci. Rep.* **9**, 15461 (2019).
380. Wei, H. *et al.* Sensitive X-ray detectors made of methylammonium lead tribromide perovskite single crystals. *Nat. Photonics* **10**, 333–339 (2016).
381. Heo, J. H. *et al.* Efficient inorganic–organic hybrid heterojunction solar cells containing perovskite compound and polymeric hole conductors. *Nat. Photonics* **7**, 486–491 (2013).
382. Shen, H., Nan, R., Jian, Z. & Li, X. Defect step controlled growth of perovskite MAPbBr<sub>3</sub> single crystal. *J. Mater. Sci.* **54**, 11596–11603 (2019).
383. Witting, I. T. *et al.* The Thermoelectric Properties of Bismuth Telluride. *Adv. Electron. Mater.* **5**, 1800904 (2019).
384. Zeier, W. G. *et al.* Thinking Like a Chemist: Intuition in Thermoelectric Materials. *Angew. Chem. Int. Ed.* **55**, 6826–6841 (2016).
385. Austin, I. G. The Optical Properties of Bismuth Telluride. *Proc. Phys. Soc.* **72**, 545–552 (1958).
386. Liu, T. *et al.* Improved capacity of redox-active functional carbon cathodes by dimension reduction for hybrid supercapacitors. *J. Mater. Chem. A* **6**, 3367–3375 (2018).
387. Tan, J. *et al.* Thermoelectric properties of bismuth telluride thin films deposited by radio frequency magnetron sputtering. *Proc. Smart Sens. Actuators MEMS II* **5836**, 711–718 (2005).
388. Zheng, Z., Fan, P., Luo, J., Liang, G. & Zhang, D. Enhanced Thermoelectric Properties of Antimony Telluride Thin Films with Preferred Orientation Prepared by Sputtering a Fan-Shaped Binary Composite Target. *J. Electron. Mater.* **42**, 3421–3425 (2013).
389. Realization of a vertical topological p–n junction in epitaxial Sb<sub>2</sub>Te<sub>3</sub>/Bi<sub>2</sub>Te<sub>3</sub> heterostructures | *Nature Communications*. <https://www.nature.com/articles/ncomms9816>.
390. Zhang, Z., Wu, Y., Zhang, H., Zeng, Z. & Hu, Z. Enhancement of Seebeck coefficient in Sb-rich Sb<sub>2</sub>Te<sub>3</sub> thin film. *J. Mater. Sci. Mater. Electron.* **26**, 1619–1624 (2015).
391. Ahmed, A. & Seungwoo, H. Optimizing the Structural, Electrical and Thermoelectric Properties of Antimony Telluride Thin Films Deposited on Aluminum Nitride-coated Stainless Steel Foil | *Scientific Reports*. *Sci. Rep.* **10**, 6978 (2020).
392. Mehta, R. J. *et al.* Seebeck and Figure of Merit Enhancement in Nanostructured Antimony Telluride by Antisite Defect Suppression through Sulfur Doping. *Nano Lett.* **12**, 4523–4529 (2012).

## Bibliography

---

393. Zybala, R. Synthesis and Characterization of Antimony Telluride for Thermoelectric and Optoelectronic Applications - Archives of Metallurgy and Materials - PAS Journals Repository. *Arch Met. Mater* **62**, 1067–1070 (2017).
394. Scavetta, E. *et al.* Dopamine amperometric detection at a ferrocene clicked PEDOT:PSS coated electrode. *J. Mater. Chem. B* **2**, 2861–2867 (2014).
395. Dang, Y. *et al.* Bulk crystal growth of hybrid perovskite material CH<sub>3</sub>NH<sub>3</sub>PbI<sub>3</sub>. *CrystEngComm* **17**, 665–670 (2014).
396. Shi, D. *et al.* Low trap-state density and long carrier diffusion in organolead trihalide perovskite single crystals. *Science* (2015) doi:10.1126/science.aaa2725.
397. Bard, A. J. & Faulkner, L. R. *Electrochemical Methods: Fundamentals and Applications, 2nd Edition* | Wiley. (2000).
398. Marken, F., Neudeck, A. & Bond, A. M. Cyclic Voltammetry. in *Electroanalytical Methods: Guide to Experiments and Applications* (eds. Scholz, F. *et al.*) 57–106 (Springer, 2010). doi:10.1007/978-3-642-02915-8\_4.
399. Oldham, K. & Myland, J. *Fundamentals of Electrochemical Science*. (1993).
400. Mironov., V. L. *Fundamentals of scanning probe microscopy*. (Nizhniy Novgorod, 2004).
401. Lanza, M. *Conductive Atomic Force Microscopy: Applications in Nanomaterials* | Wiley. (2017).
402. Yanev, V., Erlbacher, T., Rommel, M., Bauer, A. J. & Frey, L. Comparative study between conventional macroscopic IV techniques and advanced AFM based methods for electrical characterization of dielectrics at the nanoscale. *Microelectron. Eng.* **86**, 1911–1914 (2009).
403. Rommel, M. *et al.* Influence of parasitic capacitances on conductive AFM I-V measurements and approaches for its reduction. *J. Vac. Sci. Technol. B* **31**, 01A108 (2013).
404. Experimental Methods. in *Infrared Spectroscopy: Fundamentals and Applications* 15–44 (John Wiley & Sons, Ltd, 2004). doi:10.1002/0470011149.ch2.
405. Infrared Spectroscopy: Fundamentals and Applications | Analytical Techniques in the Sciences. <https://onlinelibrary.wiley.com/doi/book/10.1002/0470011149>.
406. Almoselhy, R. I. M. Applications of Differential Scanning Calorimetry (DSC) in Oils and Fats Research. A Review. *Am. Res. J. Agric.* **6**, 1–9 (2020).
407. Rahman, M. M. *et al.* Chloride ion sensors based on low-dimensional  $\alpha$ -MnO<sub>2</sub>-Co<sub>3</sub>O<sub>4</sub> nanoparticles fabricated glassy carbon electrodes by simple I-V technique. *Electrochimica Acta* **103**, 143–150 (2013).
408. Sempionatto, J. R. *et al.* Skin-worn Soft Microfluidic Potentiometric Detection System. *Electroanalysis* **31**, 239–245 (2019).
409. Xu, H. Disposable blood potassium sensors based on screen-printed thick film electrodes Related content. *Meas. Sci. Technol.* **21**, 055802–055802 (2010).
410. Sekine, Y. *et al.* A fluorometric skin-interfaced microfluidic device and smartphone imaging module for: In situ quantitative analysis of sweat chemistry. *Lab. Chip* **18**, 2178–2186 (2018).
411. Vázquez-Guardado, A. *et al.* Enzyme-Free Plasmonic Biosensor for Direct Detection of Neurotransmitter Dopamine from Whole Blood. *Nano Lett.* **19**, 449–454 (2019).
412. Coppedè, N. *et al.* Human stress monitoring through an organic cotton-fiber biosensor. *J. Mater. Chem. B* **2**, 5620–5626 (2014).
413. Martín, A. *et al.* Epidermal Microfluidic Electrochemical Detection System: Enhanced Sweat Sampling and Metabolite Detection. *ACS Sens.* **2**, 1860–1868 (2017).
414. Teymourian, H. *et al.* Microneedle-Based Detection of Ketone Bodies along with Glucose and Lactate: Toward Real-Time Continuous Interstitial Fluid Monitoring of Diabetic Ketosis and Ketoacidosis. *Anal. Chem.* **92**, 2291–2300 (2020).
415. Rahman, M. M. *et al.* Facile and efficient 3-chlorophenol sensor development based on photoluminescent core-shell CdSe/ZnS quantum dots. *Sci. Rep.* **10**, 1–10 (2020).
416. Zhou, Y. *et al.* Real-time colorimetric hydration sensor for sport activities. *Mater. Des.* **90**, 1181–1185 (2016).
417. McKenna, M. J. The Roles of Ionic Processes in Muscular Fatigue During Intense Exercise. *Sports Med. Int. J. Appl. Med. Sci. Sport Exerc.* **13**, 134–145 (1992).
418. Strakosas, X. *et al.* A Bioelectronic Platform Modulates pH in Biologically Relevant Conditions. *Adv. Sci.* **6**, 1800935–1800935 (2019).

## Bibliography

---

419. Nyein, H. Y. Y. *et al.* A Wearable Electrochemical Platform for Noninvasive Simultaneous Monitoring of Ca<sup>2+</sup> and pH. *ACS Nano* **10**, 7216–7224 (2016).
420. Villeneuve, P.-M. & Bagshaw, S. M. Assessment of Urine Biochemistry. *Crit. Care Nephrol.* **55**, (2019).
421. Xu, G. *et al.* Smartphone-based battery-free and flexible electrochemical patch for calcium and chloride ions detections in biofluids. *Sens. Actuators B Chem.* **297**, 126743–126743 (2019).
422. Kim, Y. *et al.* Organic electrochemical transistor-based channel dimension-independent single-strand wearable sweat sensors. *NPG Asia Mater.* **10**, 1086–1095 (2018).
423. Bujes-Garrido, J., Izquierdo-Bote, D., Heras, A., Colina, A. & Arcos-Martínez, M. J. Determination of halides using Ag nanoparticles-modified disposable electrodes. A first approach to a wearable sensor for quantification of chloride ions. *Anal. Chim. Acta* **1012**, 42–48 (2018).
424. White, H., Kittlesen, G. & Wrighton, M. Chemical derivatization of an array of three gold microelectrodes with polypyrrole: Fabrication of a molecule-based transistor. (1984) doi:10.1021/JA00330A070.
425. Basiricò, L., Cosseddu, P., Fraboni, B. & Bonfiglio, A. Inkjet printing of transparent, flexible, organic transistors. *Thin Solid Films* **520**, 1291–1294 (2011).
426. Gualandi, I. *et al.* A simple all-PEDOT:PSS electrochemical transistor for ascorbic acid sensing. *J. Mater. Chem. B* **3**, 6753–6762 (2015).
427. Ion-Sensitive Properties of Organic Electrochemical Transistors | ACS Applied Materials & Interfaces. <https://pubs.acs.org/doi/10.1021/am100154e>.
428. Khodagholy, D. *et al.* Organic electrochemical transistor incorporating an ionogel as a solid state electrolyte for lactate sensing. *J. Mater. Chem.* **22**, 4440–4443 (2012).
429. Rivnay, J. *et al.* Organic electrochemical transistors for cell-based impedance sensing. *Appl. Phys. Lett.* **106**, 043301 (2015).
430. In vivo recordings of brain activity using organic transistors | Nature Communications. <https://www.nature.com/articles/ncomms2573>.
431. van de Burgt, Y. *et al.* A non-volatile organic electrochemical device as a low-voltage artificial synapse for neuromorphic computing. *Nat. Mater.* **16**, 414–418 (2017).
432. Kergoat, L., Piro, B., Berggren, M., Horowitz, G. & Pham, M.-C. Advances in organic transistor-based biosensors: from organic electrochemical transistors to electrolyte-gated organic field-effect transistors. *Anal. Bioanal. Chem.* **402**, 1813–1826 (2012).
433. Rivnay, J. *et al.* Organic electrochemical transistors. *Nat. Rev. Mater.* **3**, 1–14 (2018).
434. Proctor, C. M., Rivnay, J. & Malliaras, G. G. Understanding volumetric capacitance in conducting polymers. *J. Polym. Sci. Part B Polym. Phys.* **54**, 1433–1436 (2016).
435. Lin, F. & Lonergan, M. C. Gate electrode processes in an electrolyte-gated transistor: Non-Faradaically versus Faradaically coupled conductivity modulation of a polyacetylene ionomer. *Appl. Phys. Lett.* **88**, 133507 (2006).
436. Tarabella, G. *et al.* New opportunities for organic electronics and bioelectronics: ions in action. *Chem Sci* **4**, 1395–1409 (2013).
437. Lin, P., Yan, F. & Chan, H. L. W. Ion-Sensitive Properties of Organic Electrochemical Transistors. *ACS Appl. Mater. Interfaces* **2**, 1637–1641 (2010).
438. Cicoira, F. *et al.* Influence of Device Geometry on Sensor Characteristics of Planar Organic Electrochemical Transistors. *Adv. Mater.* **22**, 1012–1016 (2010).
439. Rivnay, J. *et al.* High-performance transistors for bioelectronics through tuning of channel thickness. *Sci. Adv.* **1**, e1400251–e1400251 (2015).
440. Khodagholy, D. *et al.* High transconductance organic electrochemical transistors. *Nat. Commun.* **4**, 2133 (2013).
441. Bernardis, D. A. & Malliaras, G. G. Steady-State and Transient Behavior of Organic Electrochemical Transistors. *Adv. Funct. Mater.* **17**, 3538–3544 (2007).
442. Stenger-Smith, J. D. *et al.* Poly(3,4-alkylenedioxythiophene)-Based Supercapacitors Using Ionic Liquids as Supporting Electrolytes. *J. Electrochem. Soc.* **149**, A973 (2002).
443. Makris, E. A., Gomoll, A. H., Malizos, K. N., Hu, J. C. & Athanasiou, K. A. Repair and tissue engineering techniques for articular cartilage. *Nat. Rev. Rheumatol.* **11**, 21–34 (2015).
444. Bernardis, D. A. *et al.* Enzymatic sensing with organic electrochemical transistors. *J Mater Chem* **18**, 116–120 (2008).

## Bibliography

---

445. Rivnay, J. *et al.* Organic electrochemical transistors with maximum transconductance at zero gate bias. *Adv. Mater.* **25**, 7010–7014 (2013).
446. Zhang, M., Höfle, S., Czolk, J., Mertens, A. & Colsmann, A. All-solution processed transparent organic light emitting diodes. *Nanoscale* **7**, 20009–20014 (2015).
447. Ma, X., Dai, Y., Guo, M., Zhu, Y. & Huang, B. Insights into the adsorption and energy transfer of Ag clusters on the AgCl(100) surface. *Phys Chem Chem Phys* **15**, 8722–8731 (2013).
448. Michaelson, H. B. The work function of the elements and its periodicity. *J. Appl. Phys.* **48**, 4729–4733 (1977).
449. Jadoon, S. *et al.* Recent Developments in Sweat Analysis and Its Applications. *Int. J. Anal. Chem.* **2015**, e164974 (2015).
450. Heikenfeld, J. Non-invasive Analyte Access and Sensing through Eccrine Sweat: Challenges and Outlook circa 2016. *Electroanalysis* **28**, 1242–1249 (2016).
451. Morgan, R. M., Patterson, M. J. & Nimmo, M. A. Acute effects of dehydration on sweat composition in men during prolonged exercise in the heat. *Acta Physiol. Scand.* **182**, 37–43 (2004).
452. Curto, V. F. *et al.* Real-time sweat pH monitoring based on a wearable chemical barcode micro-fluidic platform incorporating ionic liquids. *Sens. Actuators B Chem.* **171–172**, 1327–1334 (2012).
453. Oncescu, V., O'Dell, D. & Erickson, D. Smartphone based health accessory for colorimetric detection of biomarkers in sweat and saliva. *Lab. Chip* **13**, 3232–3238 (2013).
454. Marzocchi, M. *et al.* Physical and Electrochemical Properties of PEDOT:PSS as a Tool for Controlling Cell Growth. *ACS Appl. Mater. Interfaces* **7**, 17993–18003 (2015).
455. Kittlesen, G. P., White, H. S. & Wrighton, M. S. Chemical derivatization of microelectrode arrays by oxidation of pyrrole and N-methylpyrrole: fabrication of molecule-based electronic devices. *ACS Publ.* **106**, 7389–7396 (1984).
456. Paul, E. W., Ricco, A. J. & Wrighton, M. S. Resistance of polyaniline films as a function of electrochemical potential and the fabrication of polyaniline-based microelectronic devices. *J. Phys. Chem.* **89**, 1441–1447 (1985).
457. Gualandi, I. *et al.* Organic Electrochemical Transistors as Versatile Analytical Potentiometric Sensors. *Front. Bioeng. Biotechnol.* **7**, 354–354 (2019).
458. Sonner, Z. *et al.* The microfluidics of the eccrine sweat gland, including biomarker partitioning, transport, and biosensing implications. *Biomicrofluidics* **9**, 31301–31301 (2015).
459. Chlahawi, A. A., Narakathu, B. B., Emamian, S., Bazuin, B. J. & Atashbar, M. Z. Development of printed and flexible dry ECG electrodes. *Sens. Bio-Sens. Res.* **20**, 9–15 (2018).
460. Li, G. & Al -, E. Towards emerging EEG applications: a novel printable flexible Ag/AgCl dry electrode array for robust recording of EEG signals at forehead sites Recent citations Titania/Electro-Reduced Graphene Oxide Nanohybrid as an Efficient Electrochemical Sensor for t. *J. Neural Eng.* **17**, 026001–026001 (2020).
461. Samberg, M. E., Oldenburg, S. J. & Monteiro-Riviere, N. A. Evaluation of silver nanoparticle toxicity in skin in vivo and keratinocytes in vitro. *Environ. Health Perspect.* **118**, 407–413 (2010).
462. Sakharov, D. A. *et al.* Relationship between Lactate Concentrations in Active Muscle Sweat and Whole Blood. *Bull. Exp. Biol. Med.* **150**, 94–96 (2010).
463. Possanzini, L. *et al.* Textile sensors platform for the selective and simultaneous detection of chloride ion and pH in sweat. *Sci. Rep.* **10**, 17180–17180 (2020).
464. Pan, N., Qin, J., Feng, P., Li, Z. & Song, B. Color-changing smart fibrous materials for naked eye real-time monitoring of wound pH. *J. Mater. Chem. B* **7**, 2626–2633 (2019).
465. Prabhu, P. Nanofibers for Medical Diagnosis and Therapy. in *Handbook of Nanofibers* (eds. Barhoum, A., Bechelany, M. & Makhoulouf, A. S. H.) 831–867 (Springer International Publishing, 2019). doi:10.1007/978-3-319-53655-2\_48.
466. Pillay, V. *et al.* A Review of the Effect of Processing Variables on the Fabrication of Electrospun Nanofibers for Drug Delivery Applications. *J. Nanomater.* **2013**, 789289 (2013).
467. Sen, C. K. *et al.* Human skin wounds: A major and snowballing threat to public health and the economy. *Wound Repair Regen.* **17**, 763–771 (2009).
468. Qin, M., Guo, H., Dai, Z., Yan, X. & Ning, X. Advances in flexible and wearable pH sensors for wound healing monitoring. *J Semicond* 111607–111607 (2019) doi:10.1088/1674-4926/40/11/111607.

## Bibliography

---

469. Li, H. *et al.* Poly(N-isopropylacrylamide)/poly(l-lactic acid-co- $\epsilon$ -caprolactone) fibers loaded with ciprofloxacin as wound dressing materials. *Mater. Sci. Eng. C* **79**, 245–254 (2017).
470. Okan, D., Woo, K., Ayello, E. A. & Sibbald, G. The Role of Moisture Balance in Wound Healing. *Adv. Skin Wound Care* **20**, 39–53 (2007).
471. Schoolaert, E., Hoogenboom, R. & De Clerck, K. Colorimetric Nanofibers as Optical Sensors - Schoolaert - 2017 - Advanced Functional Materials - Wiley Online Library. *Adv. Funct. Mater.* **27**, 1702646 (2017).
472. Yu, L., Yang, Z. & An, M. Lab on the eye: A review of tear-based wearable devices for medical use and health management. *Biosci. Trends* **13**, 308–313 (2019).
473. Kim, J., Campbell, A. S., de Ávila, B. E. F. & Wang, J. Wearable biosensors for healthcare monitoring. *Nat. Biotechnol.* **37**, 389–406 (2019).
474. Gualandi, I. *et al.* Textile Chemical Sensors Based on Conductive Polymers for the Analysis of Sweat. *Polym. 2021 Vol 13 Page 894* **13**, 894–894 (2021).
475. Farooqui, M. F. & Shamim, A. Low Cost Inkjet Printed Smart Bandage for Wireless Monitoring of Chronic Wounds. *Sci. Rep.* **6**, 1–13 (2016).
476. Galliani, M. *et al.* Flexible Printed Organic Electrochemical Transistors for the Detection of Uric Acid in Artificial Wound Exudate. *Adv. Mater. Interfaces* **7**, (2020).
477. Schneider, L. A., Korber, A., Grabbe, S. & Dissemond, J. Influence of pH on wound-healing: A new perspective for wound-therapy? *Arch. Dermatol. Res.* **298**, 413–420 (2007).
478. Lambers, H., Piessens, S., Bloem, A., Pronk, H. & Finkel, P. Natural skin surface pH is on average below 5, which is beneficial for its resident flora. *Int. J. Cosmet. Sci.* **28**, 359–370 (2006).
479. Salvo, P., Dini, V., Di Francesco, F. & Romanelli, M. The role of biomedical sensors in wound healing. *Wound Med.* **8**, 15–18 (2015).
480. Lyu, B., Punjiya, M., Matharu, Z. & Sonkusale, S. An improved pH mapping bandage with thread-based sensors for chronic wound monitoring. *Proc. - IEEE Int. Symp. Circuits Syst.* **2018-May**, 2018–2021 (2018).
481. Ochoa, M., Rahimi, R. & Ziaie, B. Flexible sensors for chronic wound management. *IEEE Rev. Biomed. Eng.* **7**, 73–86 (2014).
482. Devaux, E., Aubry, C., Campagne, C., Rochery, M. & Ensait, F. PLA/Carbon Nanotubes Multifilament Yarns for Relative Humidity Textile Sensor. *J. Eng. Fibers Fabr.* **6**, 13–13 (2011).
483. Ma, L. *et al.* Full-Textile Wireless Flexible Humidity Sensor for Human Physiological Monitoring. *Adv. Funct. Mater.* **29**, 1–9 (2019).
484. Li, B. *et al.* A flexible humidity sensor based on silk fabrics for human respiration monitoring. *J. Mater. Chem. C* **6**, 4549–4554 (2018).
485. Choi, K. H., Sajid, M., Aziz, S. & Yang, B.-S. Wide range high speed relative humidity sensor based on PEDOT:PSS-PVA composite on an IDT printed on piezoelectric substrate. *Sens. Actuators Phys.* **228**, 40–49 (2015).
486. Benchirouf, A. *et al.* Electrical properties of multi-walled carbon nanotubes/PEDOT:PSS nanocomposites thin films under temperature and humidity effects. *Sens. Actuators B Chem.* **224**, 344–350 (2016).
487. Hossein-Babaei, F. & Akbari, T. Direct current powered humidity sensor based on a polymer composite with humidity sensitive electronic conduction. *Appl. Phys. Lett.* **117**, (2020).
488. Fog, A. & Buck, R. P. Electronic semiconducting oxides as pH sensors. *Sens. Actuators* **5**, 137–146 (1984).
489. Wang, M., Yao, S. & Madou, M. A long-term stable iridium oxide pH electrode. *Sens. Actuators B Chem.* **81**, 313–315 (2002).
490. Sun, Z., Ma, Q., Wang, Y. & Pan, Y. Effects of Structures on the Sensing Properties of Long-Term Stable IrO<sub>x</sub> pH Electrodes. *J. Electrochem. Soc.* **167**, 047501 (2020).
491. Liu, B. & Zhang, J. A ruthenium oxide and iridium oxide coated titanium electrode for pH measurement. *RSC Adv* **10**, 25952–25957 (2020).
492. Chung, H.-J. *et al.* Stretchable, Multiplexed pH Sensors With Demonstrations on Rabbit and Human Hearts Undergoing Ischemia. *Adv. Healthc. Mater.* **3**, 59–68 (2014).
493. Marzouk, S. A. M. *et al.* Electrodeposited Iridium Oxide pH Electrode for Measurement of Extracellular Myocardial Acidosis during Acute Ischemia. *Anal. Chem.* **70**, 5054–5061 (1998).

## Bibliography

---

494. Ges, I. A. *et al.* Thin-film IrO<sub>x</sub> pH microelectrode for microfluidic-based microsystems. *Biosens. Bioelectron.* **21**, 248–256 (2005).
495. Bause, S. *et al.* Development of an iridium-based pH sensor for bioanalytical applications. *J. Solid State Electrochem.* **22**, 51–60 (2018).
496. Weltin, A. *et al.* Cell culture monitoring for drug screening and cancer research: a transparent, microfluidic, multi-sensor microsystem. *Lab Chip* **14**, 138–146 (2014).
497. Pásztor, K., Sekiguchi, A., Shimo, N., Kitamura, N. & Masuhara, H. Iridium oxide-based microelectrochemical transistors for pH sensing. (1993) doi:10.1016/0925-4005(93)80023-5.
498. Scheiblin, G., Coppard, R., Owens, R. M., Mailley, P. & Malliaras, G. G. Referenceless pH Sensor using Organic Electrochemical Transistors. *Adv. Mater. Technol.* **2**, 1600141 (2017).
499. Yang, X., Chawang, K. & Chiao, J.-C. Wearable Iridium Oxide pH Sensors for Sweat pH Measurements. in *2019 IEEE SENSORS 1–4* (2019). doi:10.1109/SENSORS43011.2019.8956832.
500. Anastasova, S. *et al.* A wearable multisensing patch for continuous sweat monitoring. *Biosens. Bioelectron.* **93**, 139–145 (2017).
501. Marsh, P. *et al.* Flexible Iridium Oxide Based pH Sensor Integrated With Inductively Coupled Wireless Transmission System for Wearable Applications. *IEEE Sens. J.* **20**, 5130–5138 (2020).
502. Mazzaracchio, V., Fiore, L., Nappi, S., Marocco, G. & Arduini, F. Medium-distance affordable, flexible and wireless epidermal sensor for pH monitoring in sweat - ScienceDirect. *Talanta* **222**, 121502 (2021).
503. Zhao, Y., Hernandez-Pagan, E. A., Vargas-Barbosa, N. M., Dysart, L. & Mallouk, T. E. A High Yield Synthesis of Ligand-Free Iridium Oxide Nanoparticles with High Electrocatalytic Activity | The Journal of Physical Chemistry Letters. *J Phys Chem Lett* **2**, 402–406 (2011).
504. Yuen, M. F., Lauks, I. & Dautremont-Smith, W. C. pH dependent voltammetry of iridium oxide films. *Solid State Ion.* **11**, 19–29 (1983).
505. Rivera, J. F., Pignot-Paintrand, I., Pereira, E., Rivas, B. L. & Moutet, J.-C. Electrosynthesized iridium oxide-polymer nanocomposite thin films for electrocatalytic oxidation of arsenic(III). *Electrochimica Acta* **110**, 465–473 (2013).
506. Dickhaus, B. N. & Priefer, R. Determination of polyelectrolyte pK<sub>a</sub> values using surface-to-air tension measurements. *Colloids Surf. Physicochem. Eng. Asp.* **488**, 15–19 (2016).
507. Brewer, S. H. & Franzen, S. Investigation of the electrical and optical properties of iridium oxide by reflectance FTIR spectroscopy and density functional theory calculations - ScienceDirect. *Chem. Phys.* **313**, 25–31 (2005).
508. Chalamala, B. R., Wei, Y. & Reuss, R. H. Effect of growth conditions on surface morphology and photoelectric work function characteristics of iridium oxide thin films: Applied Physics Letters: Vol 74, No 10. *Appl Phys Lett* **74**, 1394 (1999).
509. Kinlen, P. J., Heider, J. E. & Hubbard, D. E. A solid-state pH sensor based on a Nafion-coated iridium oxide indicator electrode and a polymer-based silver chloride reference electrode. *Sens. Actuators B Chem.* **22**, 13–25 (1994).
510. Haris, D. C. *Quantitative Chemical Analysis.* (W. H. Freeman and Company, 2016).
511. Yang, J. *et al.* Digital pH Test Strips for In-Field pH Monitoring Using Iridium Oxide-Reduced Graphene Oxide Hybrid Thin Films. *ACS Publications* <https://pubs.acs.org/doi/pdf/10.1021/acssensors.6b00385> (2016) doi:10.1021/acssensors.6b00385.
512. Potentiometric RuO<sub>2</sub>-Ta<sub>2</sub>O<sub>5</sub> pH sensors fabricated using thick film and LTCC technologies. *Talanta* **147**, 233–240 (2016).
513. Dealey, C., Cameron, J. & Arrowsmith, M. A study comparing two objective methods of quantifying the production of wound exudate. *J. Wound Care* **15**, 149–153 (2006).
514. Cramer, T. *et al.* Passive radiofrequency x-ray dosimeter tag based on flexible radiation-sensitive oxide field-effect transistor. *Sci. Adv.* **4**.
515. Takala, E.-P. *et al.* Systematic evaluation of observational methods assessing biomechanical exposures at work. *Scand. J. Work. Environ. Health* **36**, 3–24 (2010).
516. Comparison of measurement methods for quantifying hand force: Ergonomics: Vol 48, No 8. <https://www.tandfonline.com/doi/full/10.1080/00140130500120841>.
517. Chkeir, A., Jaber, R., Hewson, D. J. & Duchene, J. Estimation of grip force using the Grip-ball dynamometer - ScienceDirect. *Med. Eng. Phys.* **35**, 1698–1702 (2013).

## Bibliography

---

518. Trindade, I. *et al.* Design and Evaluation of Novel Textile Wearable Systems for the Surveillance of Vital Signals. *Sensors* **16**, 1573–1573 (2016).
519. Lamberti, F., Sanna, A. & Rokne, J. Sensors for Entertainment. *Sensors* **16**, 1102–1102 (2016).
520. Hwang, B.-U. *et al.* A transparent stretchable sensor for distinguishable detection of touch and pressure by capacitive and piezoresistive signal transduction. *NPG Asia Mater.* **11**, 23–23 (2019).
521. Jacobs, J. V. *et al.* Employee acceptance of wearable technology in the workplace. *Appl. Ergon.* **78**, 148–156 (2019).
522. Neumann, S., Kwisda, S., Krettek, S. & Gaulke, R. Comparison of the Grip Strength Using the Martin-Vigorimeter and the JAMAR-Dynamometer: Establishment of Normal Values | In Vivo. *In Vivo* **31**, 917–924 (2017).
523. Mühldorfer-Fodor, M. *et al.* Grip force monitoring on the hand: Manugraphy system versus Jamar dynamometer. *Arch. Orthop. Trauma Surg.* **134**, 1179–1188 (2014).
524. Gao, Y. *et al.* Wearable Microfluidic Diaphragm Pressure Sensor for Health and Tactile Touch Monitoring. *Adv. Mater.* **29**, 1701985 (2017).
525. Garratt, A. & Lacour, S. Elastomeric Electronic Skin for Prosthetic Tactile Sensation - Gerratt - 2015 - Advanced Functional Materials - Wiley Online Library. *Adv Funct Mater* **25**, 2287–2295 (2015).
526. Zang, Y., Zhang, F., Di, C. & Zhu, D. Advances of flexible pressure sensors toward artificial intelligence and health care applications. *Mater Horiz* **2**, 140–156 (2015).
527. Mannsfeld, S. C. B. *et al.* Highly sensitive flexible pressure sensors with microstructured rubber dielectric layers. *Nat. Mater.* **9**, 859–864 (2010).
528. Yang, T., Xie, D., Li, Z. & Zhu, H. Recent advances in wearable tactile sensors: Materials, sensing mechanisms, and device performance. *Mater. Sci. Eng. R Rep.* **115**, 1–37 (2017).
529. Recent progresses on flexible tactile sensors - ScienceDirect. <https://www.sciencedirect.com/science/article/pii/S2542529317301001?via%3Dihub>.
530. Chen, S., Zhuo, B. & Guo, X. Large Area One-Step Facile Processing of Microstructured Elastomeric Dielectric Film for High Sensitivity and Durable Sensing over Wide Pressure Range | ACS Applied Materials & Interfaces. *ACS Appl Mater Interfaces* **8**, 20364–20370 (2016).
531. Peratech. *Peratech* <https://www.peratech.com/>.
532. Silva, D. C., Medola, F. O., Bonfim, G. H. C. & Paschoarelli, L. C. Using a Pressure Mapping System to Evaluate Contact Pressure on Hands During Use of Axillary Crutches. *Assist. Technol.* 432–439 (2015) doi:10.3233/978-1-61499-566-1-432.
533. Jonnalagedda, P. *et al.* An instrumented glove for improving spasticity assessment. in *2016 IEEE Healthcare Innovation Point-Of-Care Technologies Conference (HI-POCT)* 167–170 (2016). doi:10.1109/HIC.2016.7797723.
534. Wang, J.-C., Karmakar, R. S., Lu, Y.-J., Huang, C.-Y. & Wei, K.-C. Characterization of Piezoresistive PEDOT:PSS Pressure Sensors with Inter-Digitated and Cross-Point Electrode Structures. *Sensors* **15**, 818–831 (2015).
535. Shi, H., Liu, C., Jiang, Q. & Xu, J. Effective Approaches to Improve the Electrical Conductivity of PEDOT:PSS: A Review. *Adv. Electron. Mater.* **1**, 1500017 (2015).
536. Kim, Y. H. & Leo, K. Highly Conductive PEDOT:PSS Electrode with Optimized Solvent and Thermal Post-Treatment for ITO-Free Organic Solar Cells - Kim - 2011 - Advanced Functional Materials - Wiley Online Library. *Adv. Funct. Mater.* **21**, 1076–1081 (2011).
537. Wei, Q., Mukaida, M., Naitoh, Y. & Ishida, T. Morphological Change and Mobility Enhancement in PEDOT:PSS by Adding Co-solvents. *Adv. Mater.* **25**, 2831–2836 (2013).
538. Tadesse, M. G. *et al.* Effect of liquid immersion of PEDOT: PSS-coated polyester fabric on surface resistance and wettability. *Smart Mater. Struct.* **26**, 065016 (2017).
539. A wearable and highly sensitive pressure sensor with ultrathin gold nanowires | Nature Communications. <https://www.nature.com/articles/ncomms4132>.
540. Pizarro, F. *et al.* Easy-to-Build Textile Pressure Sensor. *Sensors* **18**, 1190–1190 (2018).
541. He, Y. *et al.* A Novel Method for Fabricating Wearable, Piezoresistive, and Pressure Sensors Based on Modified-Graphite/Polyurethane Composite Films. *Materials* **10**, 684–684 (2017).
542. Horrocks, A. R. & Anand, S. C. *Handbook of Technical Textiles - 2nd Edition.* (2016).
543. Strain, I. N. *et al.* Electrospinning of recycled PET to generate tough mesomorphic fibre membranes for smoke filtration. *J Mater Chem A* **3**, 1632–1640 (2015).

## Bibliography

---

544. Kennedy, J. Neurologic Injuries in Cycling and Bike Riding. *Phys. Med. Rehabil. Clin. N. Am.* **20**, 241–248 (2009).
545. Ciavatti, A. *et al.* Boosting Direct X-Ray Detection in Organic Thin Films by Small Molecules Tailoring. *Adv. Funct. Mater.* **29**, 1806119 (2019).
546. Thirimanne, H. M. *et al.* High sensitivity organic inorganic hybrid X-ray detectors with direct transduction and broadband response. *Nat. Commun.* **9**, 1–10 (2018).
547. Griffith, M. J., Cottam, S., Stamenkovic, J., Posar, J. A. & Petasecca, M. Printable Organic Semiconductors for Radiation Detection: From Fundamentals to Fabrication and Functionality. *Frontiers in Physics* vol. 8 22 (2020).
548. Basicicò, L., Ciavatti, A. & Fraboni, B. Solution-Grown Organic and Perovskite X-Ray Detectors: A New Paradigm for the Direct Detection of Ionizing Radiation. *Advanced Materials Technologies* vol. 6 2000475 (2021).
549. Li, Z. *et al.* Halide perovskites for high-performance X-ray detector. *Materials Today* (2021) doi:10.1016/j.mattod.2021.01.028.
550. Wei, H. & Huang, J. Halide lead perovskites for ionizing radiation detection. *Nature Communications* vol. 10 1–12 (2019).
551. Kaltenbrunner, M. *et al.* Ultrathin and lightweight organic solar cells with high flexibility. *Nat. Commun.* **3**, 1–7 (2012).
552. Kaltenbrunner, M. *et al.* Flexible high power-per-weight perovskite solar cells with chromium oxide-metal contacts for improved stability in air. *Nat. Mater.* **14**, 1032–1039 (2015).
553. Tessarolo, M., Gualandi, I. & Fraboni, B. Recent progress in wearable fully textile chemical sensors. *Adv. Mater. Technol.* **3**, (2018).
554. Jung, J. W., Bae, J. H., Ko, J. H. & Lee, W. Fully solution-processed indium tin oxide-free textile-based flexible solar cells made of an organic-inorganic perovskite absorber: Toward a wearable power source. *J. Power Sources* **402**, 327–332 (2018).
555. Basicicò, L. *et al.* Medical Applications of Tissue-Equivalent, Organic-Based Flexible Direct X-Ray Detectors. *Front. Phys.* **8**, 1–11 (2020).
556. Basicicò, L. *et al.* Detection of X-Rays by Solution-Processed Cesium-Containing Mixed Triple Cation Perovskite Thin Films. *Adv. Funct. Mater.* **29**, 1–9 (2019).
557. Yakunin, S. *et al.* Detection of gamma photons using solution-grown single crystals of hybrid lead halide perovskites. *Nat. Photonics* **10**, 585–589 (2016).
558. Wei, H. *et al.* Sensitive X-ray detectors made of methylammonium lead tribromide perovskite single crystals. *Nat. Photonics* **10**, 333–339 (2016).
559. Liu, J. *et al.* Flexible, Printable Soft-X-Ray Detectors Based on All-Inorganic Perovskite Quantum Dots. *Adv. Mater.* **31**, (2019).
560. Ciavatti, A. *et al.* High-Sensitivity Flexible X-Ray Detectors based on Printed Perovskite Inks. *Adv. Funct. Mater.* **2009072**, 1–9 (2021).
561. Mescher, H. *et al.* Flexible Inkjet-Printed Triple Cation Perovskite X-ray Detectors. *Cite This ACS Appl Mater Interfaces* **12**, 15774–15784 (2020).
562. Legge, K. *et al.* Technical note: TROG 15.01 SPARK trial multi-institutional imaging dose measurement. *J. Appl. Clin. Med. Phys.* **18**, 358–363 (2017).
563. Zhao, J. *et al.* Perovskite-filled membranes for flexible and large-area direct-conversion X-ray detector arrays. *Nat. Photonics* **14**, 612–617 (2020).
564. Brivio, D. *et al.* Nanoporous aerogel-based periodic high-energy electron current x-ray sensors. (2020).
565. Yakunin, S. *et al.* Detection of X-ray photons by solution-processed lead halide perovskites. *Nat. Photonics* **9**, 444–449 (2015).
566. Wang, K. H., Li, L. C., Shellaiah, M. & Sun, K. W. Structural and Photophysical Properties of Methylammonium Lead Tribromide (MAPbBr<sub>3</sub>) Single Crystals. *Sci. Rep.* **7**, (2017).
567. Kasap, S. *Springer Handbook of Electronic and Photonic Materials.* (Springer US, 2007).
568. Long, G. L. & Winefordner, J. D. Limit of Detection: A Closer Look at the IUPAC Definition. *Anal. Chem.* **55**, 712A–724A (1983).
569. Billinger, J., Nowotny, R. & Homolka, P. Diagnostic reference levels in pediatric radiology in Austria. *Eur. Radiol.* **20**, 1572–1579 (2010).

## Bibliography

---

570. Hamid Elsheikh, M. *et al.* A review on thermoelectric renewable energy: Principle parameters that affect their performance. *Renewable and Sustainable Energy Reviews* vol. 30 337–355 (2014).
571. Thermoelectrics Handbook: Macro to Nano - 1st Edition - D.M. Rowe - H. <https://www.routledge.com/Thermoelectrics-Handbook-Macro-to-Nano/Rowe/p/book/9780849322648>.
572. He, W. *et al.* Recent development and application of thermoelectric generator and cooler. *Applied Energy* vol. 143 1–25 (2015).
573. Pu, X. *et al.* Wearable Self-Charging Power Textile Based on Flexible Yarn Supercapacitors and Fabric Nanogenerators. *Adv. Mater.* **28**, 98–105 (2016).
574. Lemey, S., Declercq, F. & Rogier, H. Textile antennas as hybrid energy-harvesting platforms. *Proc. IEEE* **102**, 1833–1857 (2014).
575. Van Genabet, B. *et al.* Synthesis and characterization of copper, polyimide and TIPS-pentacene layers for the development of a solution processed fibrous transistor. *AIP Adv.* **1**, 042119 (2011).
576. Lugoda, P., Hughes-Riley, T., Morris, R. & Dias, T. A Wearable Textile Thermograph. *Sensors* **18**, 2369 (2018).
577. Gidik, H., Bedek, G., Dupont, D. & Codau, C. Impact of the textile substrate on the heat transfer of a textile heat flux sensor. *Sensors and Actuators, A: Physical* vol. 230 25–32 (2015).
578. Leonov, V. Thermoelectric Energy Harvesting of Human Body Heat for Wearable Sensors. *Artic. IEEE Sens. J.* **13**, (2013).
579. Hardianto, H., De Mey, G., Ciesielska-Wróbel, I., Hertleer, C. & Van Langenhove, L. Seebeck Coefficient of Thermocouples from Nickel-Coated Carbon Fibers: Theory and Experiment. *Materials* **11**, 922 (2018).
580. Hardianto, H., Mey, G. De, Malengier, B. & Langenhove, L. Van. Textile-based thermoelectric generator fabricated from carbon fibers. *J. Ind. Text.* 152808372091068 (2020) doi:10.1177/1528083720910686.
581. Ryan, J. D. *et al.* All-Organic Textile Thermoelectrics with Carbon-Nanotube-Coated n-Type Yarns. *ACS Appl. Energy Mater.* **1**, 2934–2941 (2018).
582. Kim, T.-S. & Chun, B.-S. Microstructure and thermoelectric properties of n- and p-type Bi<sub>2</sub>Te<sub>3</sub> alloys by rapid solidification processes. *J. Alloys Compd.* **437**, 225–230 (2007).
583. Li, D., Sun, R. & Qin, X. Improving thermoelectric properties of p-type Bi<sub>2</sub>Te<sub>3</sub>-based alloys by spark plasma sintering. *Prog. Nat. Sci. Mater. Int.* **21**, 336–340 (2011).
584. P. Westbroek, Tseles, D., Van Langenhove, L., & Piromalis. A flexible Peltier element composed of textile yarns for cooling applications. in *Proceedings of 2nd International Scientific Conference eRA-2*, (2007).
585. Morgan, K. A., Zeimpekis, I., Feng, Z. & Hewak, D. Enhancing thermoelectric properties of bismuth telluride and germanium telluride thin films for wearable energy harvesting. *Thin Solid Films* **741**, 139015 (2022).
586. Liu, M. *et al.* High-Energy Asymmetric Supercapacitor Yarns for Self-Charging Power Textiles. *Adv. Funct. Mater.* **29**, 1806298–1806298 (2019).
587. J. Varma, S., Sambath Kumar, K., Seal, S., Rajaraman, S. & Thomas, J. Fiber-Type Solar Cells, Nanogenerators, Batteries, and Supercapacitors for Wearable Applications. *Adv. Sci.* **5**, (2018).

# Acknowledgement

At the end of this very important period of my life, just briefly summarized with this thesis, I want to thank all the people that supported me making this journey smooth and special. First of all, I would like to thank my supervisor, the Prof. Beatrice Fraboni, for giving me the opportunity to start the PhD programme and join her amazing research group. Her leadership, wisdom advices, and always-present support provided during these three years guided me through the several projects and researches that I have done in this work.

I would never achieved this goal without the constant presence of all the collaborators from the Department of Physics and Astronomy at the University of Bologna. A special thank to Dott. Marta Tessarolo, Dott. Laura Basiricò, Dott. Andrea Ciavatti and Prof. Tobias Cramer for their unfailing support, patience and positivity that helped me overcoming every obstacles. Also, I would like to thank all my colleagues from Bologna: Francesco, Alberto, Ilaria, Matteo, Filippo, Giovanni, Ferdinand, Luca and Pierpaolo that were my second family. I would also thank the group of Prof. Erika Scavetta from the Department of Industrial Chemistry of the University of Bologna for the fruitfull and meaningful collaboration. In particular, a sincere thank to Isacco Gualandi, Federica Mariani and Danilo Arcangeli for their ever-present help and suggestions.

I acknowledge the Marco Polo project of the Department of Physics and Astronomy of the University of Bologna for the financial support given for my research period abroad during the 2<sup>nd</sup> year. I really thank Prof. Lieva Van Langenhoven from the Department of Materials, Textiles and Chemical Engineering at the Ghent University, for giving me the opportunity to do my secondment in her group, working in her laboratories as a visiting PhD student. A special thanks to her collaborator, Dott. Benny Malengier for warmly welcoming me into his research group (and not only) and constantly making me felt at home. That period strongly improved my abilities as a researcher and word-discover, and also allow me to start a new adventure and career in Belgium. I also thank the amazing people I have met in Ghent, especially Magdalena, Irene, Robin, Billy, Kate, Simone, Katia, Vlad and Tim (my favourite Belgian).

A true thank goes to my family: to my mother Antonina and my father Enzo who gave me the opportunity to follow this path and have always believed in me. I know that I will never be alone wherever I'll be. Thanks to my sister Francesca, Giuseppe and my nieces Caterina, Giorgia and Gemma who always shown me their closeness. A huge hug to my *real second family* Tommaso, Cinzia and Jacopo for their support, estimation and trust. I would like to thank all my friends with whom, during these youthful years, I likely shared hundreds of experiences: Gigio, Orlio, Dinu, Bibo, Gango, Michi, Dary, Picci e Anto.

Last, but certainly not least, I must thank my constant companion, Sofia, for her endless support and encouragement in all adventures personal, professional, and academic. These PhD years would not have been as manageable or meaningful without you, and I am so grateful to have you in my life.

